Dmitri Visser

Electrospinning of biomimetic scaffolds:
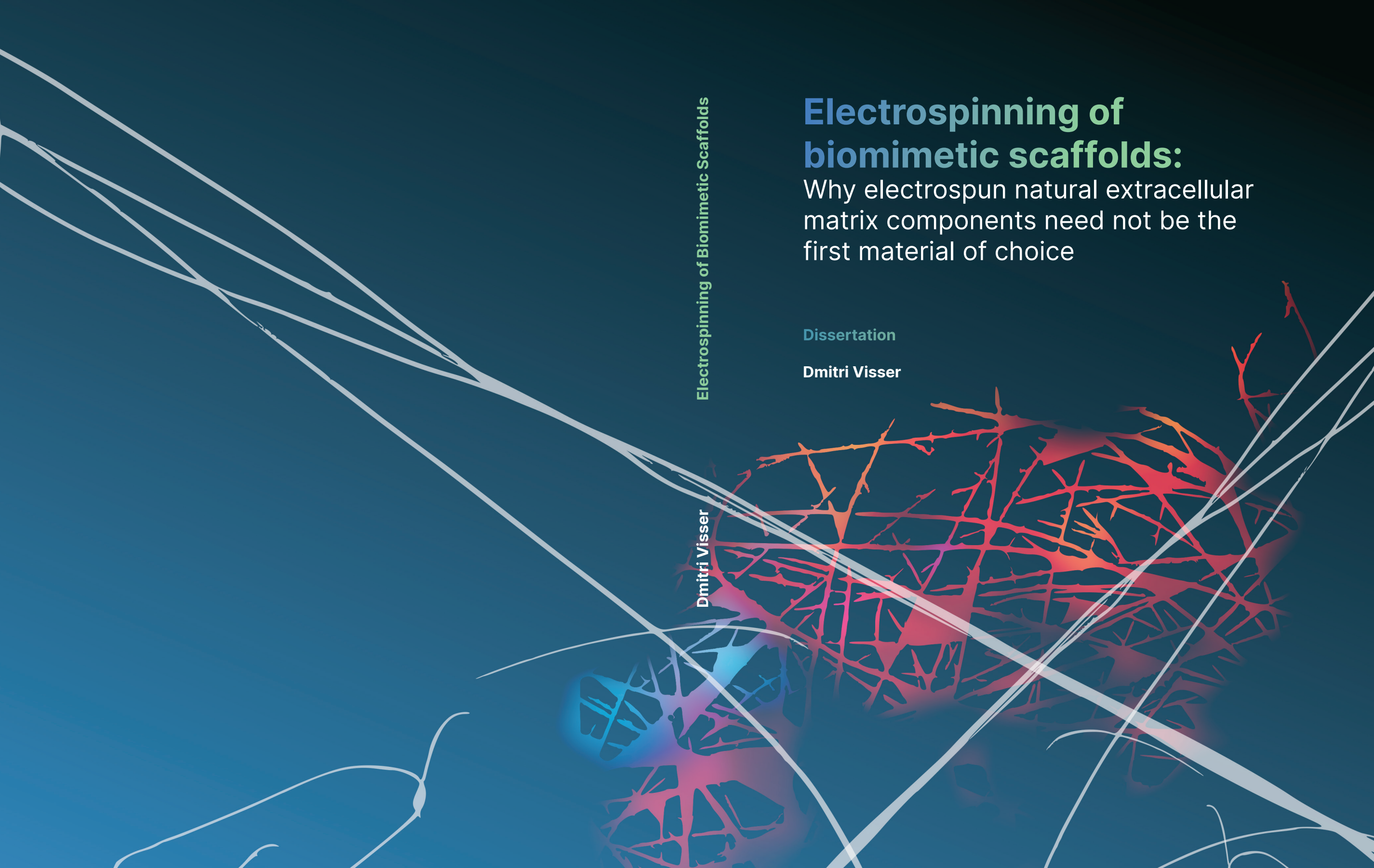
Why electrospun natural extracellular matrix components need not be the first material of choice

Dissertation

Dmitri Visser

Electrospinning of biomimetic scaffolds: Why electrospun natural extracellular matrix components need not be the first material of choice

Dissertation

der Mathematisch-Naturwissenschaftlichen Fakultät

der Eberhard Karls Universität Tübingen

zur Erlangung des Grades eines

Doktors der Naturwissenschaften

(Dr. rer. nat.)

vorgelegt von

Dmitri Visser M.Sc.

aus Capelle aan den IJssel, den Niederlanden

Tübingen

2023

Gedruckt mit Genehmigung der Mathematisch-Naturwissenschaftlichen Fakultät der Eberhard Karls Universität Tübingen.

Tag der mündlichen Qualifikation: 15.11.2023

Dekan: Prof. Dr. Thilo Stehle
1. Berichterstatterin: Prof. Dr. Katja Schenke-Layland
2. Berichterstatter: Prof. Dr. Peter Loskill

Abstract

The increasing prevalence of age-related diseases has created an unprecedented demand for organ replacement solutions. Adequate transplant material is scarce, fuelling the need for treatments that do not rely on organ transplantation. Electrospinning has seen a rapid emergence in the field of regenerative medicine, for its ability to create porous scaffolds that mimick the native extracellular matrix (ECM). In addition to synthetic polymers, the technique also allows the processing of natural ECM proteins, essentially paving the way for *de novo* engineering of fully functional fibrous tissues. Although a wide range of materials has been electrospun into fibrous scaffolds, the question of whether synthetic polymers or natural ECM proteins should be used as the primary scaffold material remains an ongoing debate.

The use of collagen is tempting as it is the major constituent of the ECM in connective tissues, yet gets denatured during the electrospinning processes and yields a product, which does not biochemically represent native collagen anymore. Although fluorinated solvents have long been suspected as the culprit, the work in this thesis provides evidence that this denaturation might occur irrespective of the choice of electrospinning solvent. A mixture of acetic acid and ethanol also left electrospun collagen with a disordered and unravelled triple helix, as was confirmed by a combination of circular dichroism, Raman spectroscopy, multiphoton microscopy, and enzymatic digestion. *In vitro* cell-material interaction studies did not uncover the inflicted damage, which has often been used in the literature as an indicator of biocompatibility.

Thermoplastic polyurethanes have a long standing reputation as relatively inert materials with outstanding biocompatibility. The synthesis of polyurethanes, however, still often necessitates the use of hazardous and toxic isocyanates, which becomes an increasingly unviable synthesis route in the light of the emerging green chemistry. Secondly, the electrospinning of polyurethane often requires solvents that pose health risks towards the operator. Here, we presented electrospun high molecular weight non-isocyanate polycarbonate-based polyurethane for use as biocompatible porous scaffolds and with potential application in cardiovascular tissue engineering. The electrospun NIPUs had excellent biocompatibility, even without a collagen coating, which matched that of the electrospun collagen mats.

This does not necessarily imply that the use of natural ECM components and adhesion proteins in electrospuns is no longer justified. These proteins can indeed perform a pivotal role in facilitating the *in situ* regeneration of implanted electrospun grafts. For instance, we evaluated an electrospun vascular graft that was coated with decorin and fibronectin within a modular bioreactor system under dynamic flow conditions and found that endothelialisation might benefit from such biofunctionalisation. These findings rather suggest that biocompatible synthetic materials, such as polyurethanes, could serve as a more strategic choice for the primary material in electrospun grafts. However, where appropriate, the regenerative process could be enhanced by the incorporation of natural components. It was also shown, that it may be necessary to simulate physiological conditions more comprehensively in order to determine the additional benefits of incorporating natural proteins.

Zusammenfassung

Die zunehmende Zahl altersbedingter Krankheiten hat zu einer ungekannten Nachfrage nach Lösungen für den Organersatz geführt. Es mangelt an geeignetem Transplantationsmaterial, was den Bedarf an Behandlungen, die nicht auf Organtransplantationen beruhen, weiter erhöht. Im Bereich der regenerativen Medizin hat das Elektrospinnverfahren einen raschen Aufschwung erlebt, da es poröse Gerüste erzeugen kann, die die natürliche extrazelluläre Matrix (ECM) nachbilden. Neben synthetischen Polymeren ermöglicht die Technik auch die Verarbeitung natürlicher ECM-Proteine und ist somit ein erster Schritt auf dem Weg zum De-novo-Engineering voll funktionsfähiger, faseriger Gewebe. Obwohl bereits eine Vielzahl von Materialien zu faserartigen Scaffolds elektrogesponnen wurde, bleibt die Frage, ob synthetische Polymere oder natürliche ECM-Proteine als primäres Scaffold-Material verwendet werden sollten, weiterhin umstritten.

Verlockend ist vor allem die Verwendung von Kollagen, dem Hauptbestandteil der ECM in Bindegeweben, das jedoch während des Elektrospinnprozesses denaturiert - es entsteht ein Produkt, das biochemisch betrachtet nicht mehr dem natürlichen Kollagen entspricht. Zwar wurde lange Zeit der Verdacht geäußert, dass die Verwendung fluorierter Lösemittel dafür verantwortlich ist, doch in dieser Arbeit wird gezeigt, dass diese Denaturierung möglicherweise unabhängig von der Wahl des Elektrospinn-Lösungsmittels auftritt. Eine Mischung aus Essigsäure und Ethanol führte ebenfalls zu einer ungeordneten und entfalteten Tripelhelix in elektrogesponnenem Kollagen, was durch eine Kombination aus Zirkulardichroismus, Raman-Spektroskopie, Multiphotonenmikroskopie und enzymatischen Verdauungsversuchen bestätigt wurde. Die Zell-Material-Interaktionsstudien haben die entstandenen Schäden auf molekularer Ebene nicht aufgedeckt, die jedoch in der Literatur häufig als Indikator für die Biokompatibilität angesehen werden.

Thermoplastische Polyurethane haben seit langem eine ausgezeichnete Reputation als relativ inerte Materialien mit hervorragender Biokompatibilität. Die Synthese von Polyurethanen erfordert jedoch immer noch häufig die Verwendung gefährlicher und giftiger Isocyanate, was angesichts der aufkommenden grünen Chemie ein zunehmend schwer vertretbarer Syntheseweg wird. Zweitens werden für das Elektrospinnen von Polyurethan häufig Lösemittel benötigt, die ein Gesundheitsrisiko für den Anwender darstellen. Hier haben wir elektrogesponnenes, hochmolekulares Polycarbonat auf Basis von Nicht-Isocyanat-Polyurethan vorgestellt, das als biokompatibles poröses Trägersubstrat verwendet werden kann und eine Anwendung im kardiovaskulären Tissue Engineering ermöglicht. Die elektrogesponnenen NIPUs wiesen, auch ohne Kollagenbeschichtung, eine hervorragende Biokompatibilität auf, die mit der von elektrogesponnenen Kollagenfasermatten vergleichbar war.

Dies bedeutet nicht unbedingt, dass die Verwendung natürlicher ECM-Komponenten und Adhäsionsproteine in elektrogesponnenen Scaffolds gar keine Berechtigung mehr hat. Diese Proteine können durchaus eine entscheidende Rolle bei der Förderung der Regeneration von elektrogesponnenen Implantaten spielen. So haben wir beispielsweise ein elektrogesponnenes Gefäßimplantat, das mit Decorin und Fibronektin beschichtet war, in einem modularen Bioreaktorsystem unter dynamischen Flussbedingungen untersucht und festgestellt, dass die

Endothelialisierung von einer solchen Biofunktionalisierung profitieren könnte. Diese Erkenntnisse deuten aber eher darauf hin, dass der Einsatz biokompatibler, synthetischer Materialien, wie z.B. Polyurethane, in elektrogesponnenen Implantaten als primäres Material eine strategischere Wahl darstellen könnte. Gegebenenfalls könnte der Regenerationsprozess jedoch durch die Einbindung natürlicher Komponenten verbessert werden. Es wurde auch gezeigt, dass es notwendig sein könnte, physiologische Bedingungen umfassender zu simulieren, um die zusätzlichen Vorteile der Einbeziehung von natürlichen Proteinen zu ermitteln.

Samenvatting

De toenemende prevalentie van leeftijdsgerelateerde ziekten heeft een ongekende vraag naar oplossingen voor orgaanvervanging gecreëerd. Geschikt transplantatiemateriaal is schaars, waardoor de behoefte aan behandelingen die niet afhankelijk zijn van orgaantransplantatie, toeneemt. Elektrospinning heeft een snelle opkomst op het gebied van regeneratieve geneeskunde doorgemaakt, aangezien het in staat is poreuze scaffolds te maken die de natuurlijke extracellulaire matrix (ECM) nabootsen. Naast synthetische polymeren is het met deze techniek ook mogelijk om natuurlijke ECM-eiwitten te verwerken, wat in wezen de weg vrijmaakt voor de *de novo*-ontwikkeling van volledig functioneel vezelachtig weefsel. Hoewel een breed scala aan materialen tot vezelachtige scaffolds is elektrogesponnen, blijft de vraag of synthetische polymeren of natuurlijke ECM-eiwitten als het primaire scaffoldmateriaal moeten worden gebruikt een voortdurende discussie.

Het gebruik van collageen is aantrekkelijk, omdat het het hoofdbestanddeel van de ECM in bindweefsel is, maar het wordt tijdens het elektrospinnen gedenatureerd – het levert een product op dat biochemisch gezien niet meer overeenkomt met natuurlijk collageen. Fluorhoudende oplosmiddelen werden lange tijd verdacht als de boosdoener, maar het werk in dit proefschrift levert het bewijs dat deze denaturatie ongeacht de keuze van het elektrospinoplosmiddel kan optreden. Een mengsel van azijnzuur en ethanol liet ook elektrogesponnen collageen met een ongeordende en ontvouwde drievoudige helix achter, hetgeen werd bevestigd door een combinatie van circulair dichroïsme, Raman spectroscopie, multifotonmicroscopie en enzymatische afbraak. *In vitro* onderzoek naar cel-materiaalinteracties kon de toegebrachte schade niet aan het licht brengen, wat echter in de literatuur vaak als aanwijzing voor de biocompatiliteit is gebruikt.

Thermoplastische polyurethanen hebben een lang gevestigde reputatie als relatief inerte materialen met een uitstekende biocompatibiliteit. Voor de synthese van polyurethanen is echter nog steeds vaak het gebruik van gevaarlijke en giftige isocyanaten nodig, wat in het kader van de opkomst van milieuvriendelijke chemie een steeds minder levensvatbare syntheseroute wordt. Ten tweede zijn voor het elektrospinnen van polyurethaan vaak oplosmiddelen nodig die gezondheidsrisico's voor de gebruiker met zich meebrengen. In dit werk toonden we een elektrogesponnen niet-isocyanaat-polyurethaan (NIPU) op basis van polycarbonaat met een hoog molecuulgewicht voor gebruikt als biocompatibele poreuze scaffolds met potentiële toepassing in de cardiovasculaire tissue engineering. De elektrogesponnene NIPU's hadden ook zonder collageencoating een uitstekende biocompatibiliteit, die overeenkwam met de elektrogesponnene collageenscaffolds.

Dit hoeft niet te betekenen dat het gebruik van natuurlijke ECM-componenten en hechtingseiwitten in elektrogesponnene scaffolds in zijn geheel niet meer nodig is. Deze eiwitten kunnen wel degelijk een cruciale rol spelen bij het faciliteren van de *in situ*-regeneratie van geïmplanteerde elektrogesponnene transplantaten. We evalueerden bijvoorbeeld een elektrogesponnen bloedvatimplantaat dat gecoat was met decorine en fibronectine, in een modulair bioreactorsysteem onder dynamische stromingsomstandigheden en ontdekten dat endotheelvorming mogelijk baat heeft bij een dergelijke biofunctionalisatie. Dit bewijs suggereert echter wel, dat het gebruik van synthetische

materialen, zoals polyurethanen, als het primaire materiaal in elektrogesponnene transplantaten een strategischere keuze kan zijn. Waar nodig zou het regeneratieve proces echter verbeterd kunnen worden door de toevoeging van natuurlijke componenten. Er werd ook aangetoond dat het nodig kan zijn om fysiologische omstandigheden uitgebreider te simuleren om de extra voordelen van het gebruik van natuurlijke eiwitten vast te stellen.

Contents

Notation

This chapter provides an overview and a reference for the notation and abbreviations used throughout the thesis.

Abbreviations

CCD	charge-couple device
CD	circular dichroism
CFD	computational fluid dynamics
δ	bending (molecular vibrational state)
DMF	N,N-dimethylformamide
ECM	extracellular matrix
EPCs	endothelial progenitor cells
FAD(P)H	flavine adenine dinucleotide (phosphate)
FLIM	fluorescence lifetime imaging microscopy
Gly	glycine
HFIP	hexafluoroisopropanol / 1,1,1,3,3,3-hexafluoropropan-2-ol
Hyp	hydroxyproline
MTT	3-(4,5-dimethylthiazol-2-yl)-2,5-diphenyltetrazolium bromide
NAD(P)H	nicotinamide adenine dinucleotide (phosphate)
NIPU	non-isocyanate polyurethane
ν_s	symmetric stretching (molecular vibrational state)
ν_a	asymmetric stretching (molecular vibrational state)
PCA	principal component analysis
PCDL	polycarbonate diol
PCL	polycaprolactone
PLA	poly(lactic acid)
PLGA	poly(lactic-*co*-glycolic acid)
Pro	proline
PU	polyurethane
SDS	sodium dodecyl sulphate
SDS-PAGE	sodium dodecyl sulphate-polyacrylamide gel electrophoresis
SEM	scanning electron microscopy
SHG	second harmonics generation
TEVG	tissue-engineered vascular graft
THF	tetrahydrofuran
TPU	thermoplastic polyurethane
TPCU	thermoplastic polycarbonate urethane
vECs	vascular endothelial cells

Algebraic Notation

a	a **scalar** number
$\mathbf{A}$	a **matrix**
$\mathbf{A}^{\mathrm{T}}$	**transpose** of the matrix $\mathbf{A}$
$\mathbf{A}^{-1}$	**inverse** of the matrix $\mathbf{A}$
e	Euler's number

Symbols and Units

c	$\mathrm{m\,s^{-1}}$	speed of light
d	cm	tip-to-collector distance
d	µm	fibre diameter
E	eV or J	energy
F_{b}	$\mathrm{kg\,m\,s^{-2}}$ or N	force at failure
h	$\mathrm{m^2\,kg\,s^{-1}}$ or $\mathrm{J\,Hz^{-1}}$	Planck's constant: $6.62607015 \cdot 10^{-34}\,\mathrm{J\,Hz^{-1}}$
I	–	intensity (arbitrary units)
M_{w}	kDa	molecular weight
P_{b}	mmHg	burst pressure
RH	%	relative air humidity
U	kV	electric potential
s_{b}	mm	strain at failure
T	°C	temperature
t	s	time
α_i	–	(relative) occurrence of component i (arbitrary units)
λ	nm	wavelength
ν	Hz or $\mathrm{s^{-1}}$	frequency
$\tilde{\nu}$	$\mathrm{cm^{-1}}$	wavenumber, Raman shift
φ	$\mathrm{mL\,h^{-1}}$	flow speed
σ	$\mathrm{µS\,cm^{-1}}$	electric conductivity
τ	s	lifetime, half-time; for photonic events, usually expressed in picoseconds (ps)

List of Figures

List of Tables

Preface

The world population is experiencing an unprecedented rapid ageing. By the end of this decade, 1 in 6 people worldwide will be aged 60 years or older (1). Although the increase in lifespan brings with it many opportunities, many of the additional years are spent in poor health. Older age is accompanied by the emergence of multiple and complex conditions simultaneously, which makes population ageing an increasing burden for both society and healthcare systems. Circulatory diseases and ischaemia are the most prevalent ageing-associated diseases and have surpassed other causes of death worldwide (1). Current treatment techniques often rely on the use of autologous and homologous grafts (2). As the number of diseased people is rising rapidly, graft material remains scarce, causing transplantations to become an increasingly unviable treatment (3). Regenerative medicine currently focusses on novel treatments and implants that bear the potential to replace organ transplantation (4). This, in turn, is driving demand for innovative, and in some cases yet-to-be-developed, materials that meet the high demands (4).

This thesis will concentrate on the development of electrospun scaffolds for applications in regenerative medicine, including the optimisation of electrospinning parameters, characterisation of the resulting scaffolds and evaluation of their biocompatibility and functionality in vitro. In particular, it will focus on whether natural components, such as collagen, are a viable material for the creation of such scaffolds. Hence, the name of this thesis.

Structure of this Thesis

- ▶ **Chapter 1** is an introduction to the biological concepts and the analytical methods used in the present study. The purpose of this chapter is to provide the reader with an overview of the background and objectives of this thesis, and to have a better understanding of the results and discussion of this thesis.
- ▶ **Chapter 3** provides an overview of the main findings on the feasability of the green electrospinning of polyurethanes and their biocompatibility. The contents of this chapter are based on the contents of the following peer-reviewed article:

Visser, **D.** et al. (2022). Green Chemistry for Biomimetic Materials: Synthesis and Electrospinning of High-Molecular-Weight Polycarbonate-Based Nonisocyanate Polyurethanes. *ACS Omega* **7**, 39772–39781

▶ **Chapter 4** explores the feasability and pitfalls of the direct electrospinning of collagen. It covers multiple stages of the production of such electrospun fibers; including solubilisation and electrospinning, material characterisation, and study of cell-material interactions *in vitro*. The contents of this chapter ar based on: **Visser**, **D.** et al. (2023). Electrospinning of collagen: Enzymatic and spectroscopical analyses reveal solvent-independent disruption of the triple-helical structure. *Journal of Materials Chemistry B* **11**, 2207–2218

▶ **Chapter 5** presents a possible approach to a more comprehensive *in vitro* study of electrospun scaffolds under conditions that more closely mimic *in vivo* dynamic conditions, namely the use of bioreactors. The contents of this chapter are based on Daum, R. et al. (2020). Fibronectin adsorption on electrospun synthetic vascular grafts attracts endothelial progenitor cells and promotes endothelialization in dynamic in vitro culture. *Cells* **9**, 778

▶ **Chapter 6** discusses the main findings of the publications in comparison to the current literature. It also states the possible implications for the electrospinning of both synthetic polymers and natural ECM components.

List of Publications

1. Daum, R., **Visser**, **D.**, Wild, C., Kutuzova, L., Schneider, M., Lorenz, G., Weiss, M., Hinderer, S., Stock, U. A., Seifert, M. and Schenke-Layland, K. (2020). Fibronectin adsorption on electrospun synthetic vascular grafts attracts endothelial progenitor cells and promotes endothelialization in dynamic in vitro culture. *Cells* **9**, 778

2. **Visser**, **D.**, Bakhshi, H., Rogg, K., Fuhrmann, E., Wieland, F., Schenke-Layland, K., Meyer, W. and Hartmann, H. (2022). Green Chemistry for Biomimetic Materials: Synthesis and Electrospinning of High-Molecular-Weight Polycarbonate-Based Nonisocyanate Polyurethanes. *ACS Omega* **7**, 39772–39781

3. **Visser**, **D.**, Rogg, K., Fuhrmann, E., Marzi, J., Schenke-Layland, K. and Hartmann, H. (2023). Electrospinning of collagen: Enzymatic and spectroscopical analyses reveal

solvent-independent disruption of the triple-helical structure. *Journal of Materials Chemistry B* **11**, 2207–2218

The contributions to these publications are given in **Table 1**.

Table 1: **The candidate's contributions to the publications.** S = scientific ideas generated by the candidate, D = data generated by the candidate, A = analysis and interpretation by the candidate, P = paper writing by the candidate.

No.	Accepted	No. of authors	Candidate pos.	S	D	A	P
1	yes	11	2	25%	15%	25%	20%
2	yes	8	1	40%	40%	40%	50%
3	yes	6	1	60%	60%	70%	70%

Introduction | 1

1.1 Extracellular Matrix

The extracellular matrix (ECM) is the major component of connective tissues and can be considered as a highly sophisticated 'structural fabric' of the body. It is largely composed of extracellular macromolecules and minerals in varying compositions. These macromolecules include proteoglycans, glycosaminoglycans, and fibrous proteins, such as collagen and elastin. Stiffer types of ECM, e.g. the connective tissue in bones, also comprise minerals, such as hydroxyapatite. The remainder of the ECM includes interstitial fluid and cell adhesion proteins, including fibronectin and laminin. (*8*, *9*)

Due to its diverse nature and variable composition, the ECM serves multiple purposes, but in most body parts it is responsible for the structural support, segregation, and regulation of different tissues. The ECM has an impressively wide array of modes of action at its disposal to accomplish these tasks. The varying degrees of stiffness and elasticity secure its supporting function, but also act as a means to direct adjacent cell behaviour, cellular differentiation, and migration (*8–10*). The ECM further augments its regulatory role by mediating intercellular communication and by the storage and release of growth factors (*11*, *12*).

Collagen

Collagen is the major load-bearing constituent of the ECM and is the most abundant protein in all animals (*14*). Modern research on collagen at the molecular level has led to the identification of twenty-eight different types of collagen, each denoted by a roman numeral (*15*). The occurrence of the three most abundant collagen types are given in **Table 1.1**. The collagen numbering system partially reflects the relative abundance of the various types, as more abundant collagen type were identified earlier (*16*). Of all collagens found in the body, fibril-forming collagens are quantitatively the most important of the collagen family. This

Table 1.1: The distribution of the most common types of collagen (*13*).

Type	Distribution
I	skin, bone, tendon, blood vessels, cornea
II	cartilage, intervertebral disk
III	blood vessels, fetal skin

5

group of collagens includes collagen type I, which accounts for 70% of the total ([17]).

The archetypal structure of collagen[1] is characterised by the unique arrangement of three parallel polypeptide chains, of which the sequential residues each form a *left-handed*, polyproline-II (PPII) helix. These strands, in turn, coil with a single-residue stagger about each other in a tightly packed *right-handed* triple helix ([18], [19]). The dense packing of the helices requires that the inward-facing residues be glycine (Gly) for its small sidechain. As the PPII helix completes one turn after every three residues, the three chains all feature a repeating Gly-X-Y motif, where X and Y can be any amino acid. Though in the case of most collagen types, proline (Pro) and hydroxyproline (Hyp) usually take the place of these two positions in the repeating motif, making Gly-Pro-Hyp the most common triplet. The hydroxyproline and glycine residues in adjacent chains stabilise the supercoiled arrangement through hydrogen bonds (**Figure 1.1**) ([19]).

Collagen I is composed of two identical chains, which are denoted as α1(I), and a slightly longer third chain, denoted α2(I). Although the α1(I) and α2(I) are highly similar, the molecular weights are sufficiently different for the chains to be separable by sodium dodecyl sulphate-polyacrylamide gel electrophoresis (SDS-PAGE). The molecular weight of the three alpha chains accumulate to approximately 285 kD. This rod-shaped triple helix, referred to as tropocollagen, forms the basic constituent monomer of collagen fibrils. Typical collagen fibrils have diameters ranging from 10 to 200 nm depending on their tissue of origin. ([14], [16])

Native collagen fibrils are insoluble in aqueous media due to crosslinking of the tropocollagen monomers, which are linked to other constituents by intermolecular aldimine-type crosslinks. These acid-labile crosslinks are easily broken by dilute acidic solvents, but under appropriate in vitro conditions, separated tropocollagen molecules will spontaneously self-assemble and return into insoluble collagen fibrils ([20]). The unique combination of the high proteolytic resistance of the triple helix and solubility at acid pH sets collagen apart from virtually all other proteins. At physiological temperatures, pepsin is only able to cleave the non-helical telopeptides. The triple-helical domain is generally resistant to most degrading enzymes, aside from certain matrix metalloproteinases and bacterial collagenase. However, when the native triple helical conformation is compromised, other degrading enzymes gain access to cleavage sites within the helical domain, rendering collagen susceptible to proteolytic degradation.

1: For the sake of simplicity, I will omit less abundant non-fibrillar collagen types and continue for collagen I, of which the structure is roughly shared by the most abundant fibril forming collagen types.
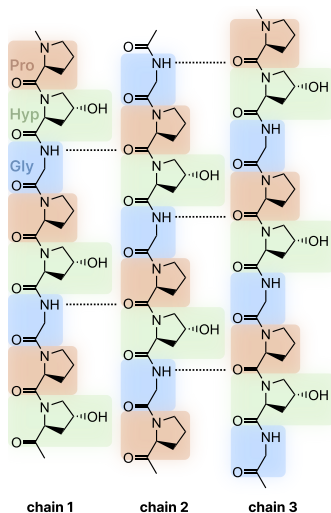

Figure 1.1: Structural schematic of repeating motifs and interchain hydrogen bonding of collagen. Notice the single-residue stagger between the chains. Red = proline, green = hydroxyproline, blue = glycine. The schematic representation has been adapted from Bella et al. ([19])

One of the most studied collagen denaturation processes is the heating of collagen above physiological temperatures, which causes the triple helix to undergo an irreversible helix-to-coil transition. (*21*, *22*)

As a result, heat-denaturated collagen is easily degraded by enzymes, including pepsin and trypsin, and is left in a water-soluble state. The insoluble fibrils cannot be recovered anymore without the use of additional chemical crosslinking steps. (*23*)

1.2   Tissue Engineering

The ECM's multifaceted role makes it challenging to replace. For most of human history, the capacity of human repair and replacement was limited to the use of simple non-living materials. The nineteenth and twentieth century oversaw the advance of regenerative medicine, as tissue repair strategies were augmented by the possibility of tissue transplantation. Essentially, a living structure is moved from a site of normal, healthy tissue to a defect site. The use of such autologous and homologous grafts is still considered to be the gold standard in certain procedures to this day (*24*, *25*). However, the scarcity of source material is severely hampering this strategy and will become even more so in the near future (*3*). The combination of twentieth century medicine, science, and engineering has recently culminated in the emerging field of **tissue engineering**. This new approach focusses on the creation and improvement of functional *biomaterials* that have the potential to partially or fully restore, maintain or improve diseased tissue function. (*26*, *27*)

1.2.1   Biomaterials

Biomaterials should meet certain requirements in order to be classified as *biocompatible*. Although the term 'biocompatibility' is frequently used in biomaterials science, the underlying mechanisms and phenomena that collectively constitute biocompatibility remain poorly understood. Even more so, there exists no unified theory on what is encompassed by biocompatibility and the precise definition of the term has been subject to constant change.[2] The biomaterials that are used in tissue engineering are, by definition, foreign to the recipient. However, biomaterials are distinguished from any other material by their ability to coexist

2: In an attempt to provide a concise definition, Williams (*28*) defined 'biocompatibility' as:
"Biocompatibility is the ability of a biomaterial to perform its desired function with respect to a medical therapy, without eliciting any undesirable local or systemic effects in the recipient or beneficiary of that therapy, but generating the most appropriate beneficial cellular or tissue response in that specific situation, and optimising the clinically relevant performance of that therapy."

with tissues of the human body without evoking undesired reactions in the host. (*28*)

Biomaterials assist in tissue engineering by imparting shape to the tissue under regeneration and by stimulating the host's innate regenerative capacity through molecular and/or mechanical signals. The two prevailing paradigms in tissue engineering differ on the issue, whether a majority of this process should take place *in vivo* or *ex vivo*. In the former case, tissue engineering takes a more bare-bones approach, focusing on the biomaterial itself, whereas in the latter case, seeded cells form an integral part of the tissue-engineered construct, as they serve the formation of fully-developed tissue before implantation. (*29*)

The various aspects of biomaterials, such as the material type, mechanics, and degradability, allow for multiple classification systems. The distinction between biomaterials of *synthetic* and *natural* origin is one of the principally used classifications to subdivide biomaterials, although blends of synthetic and natural polymers also exist (*30*). The group of synthetic biomaterials comprise a wide variety of materials, including metals, ceramics, and (synthetic) polymers. Polymers are extensively used in the creation of biomaterials for tissue engineering, as they can be tailored to meet specific requirements, including mechanical properties and degradability, depending on the application (*31*). Some synthetic polymers are designed to break down within a limited time window (*32*). Degradable synthetic polymers, such as polycaprolactone (PCL), poly(lactic acid) (PLA) and poly(lactic-*co*-glycolic acid) (PLGA) have found wide application in the biocompatible and bioabsorbable medical device market as shape memory polymers, drug release sutures, and wound dressings (*32–34*). In the case of tissue engineering, non-degradable polymers are intended to stay in the body after implantation and have the advantage that they are relatively inert and, hence, are less likely to elicit an immune response.

Polyurethane

Thermoplastic polyurethanes (TPUs) are an often used and widely commercially available class of biomaterials, which can be found in various biomedical applications including scaffolds, catheters, and wound dressings (*35*, *36*). It is important to note that TPUs form a class of polymers, rather than a single polymer. Their common feature is the linear segmentation of hard and soft segments (**Figure 1.2**). The soft segment usually consists of polyester,
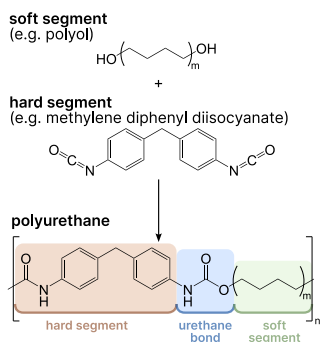
Figure 1.2: Simplified synthesis route of a polyurethane. This scheme presents a simplified sysnthesis route for polyurethanes showing a simple polyol as the soft segment and methylene diphenyl diisocyanate (MDI) as the hard segment.

polyether, or polycarbonate. Polycarbonate-based TPUs have a superior haemocompatibility and high hydrolysis and oxidation resistance compared to other TPUs, which favours the use of polycarbonate-based TPUs in long-term implants and medical devices that have blood contact (*37–40*). Although TPUs are considered to be the most biocompatible and stable elastomers for use as biomaterials currently available, they can still be subject to hydrolytic and oxidative degradation (*39–41*). Depending on the hard-segment chemistry, this may raise concerns about the compounds released in the body. The regular synthesis route of TPUs comprises the use of isocyanates that form the hard segment in TPUs. Diisocyanates, especially the aromatic diisocyanates, are known to be toxic substances (*42–44*). Attempts have been made to replace aromatic diisocyanates with aliphatic diisocyanates, or to eliminate the use of isocyanates in polyurethane synthesis altogether, in order to reduce the risk of release of harmful hard segment degradation products. The latter class of polyurethanes, called *non-isocyanate polyurethanes* (NIPUs), are a novel type of polyurethanes and are further explored in **Chapter 3** (*45*, *46*).

1.2.2 Biomimetic Scaffolds

Advancements have been made to modify or process biomaterials into **biomimetic** scaffolds, in order to better simulate the properties of the native ECM. Such modifications or processing methods serve the purpose to enable cellular adhesion, migration, and differentiation, analogous to the functions of the native ECM (*47*). The development of biomimetic materials can be roughly subdivided into three general strategies:

1) **Creation of an ECM-mimicking microstructure.** This strategy aspires to foster cell adhesion and tissue formation through modulation of structurally-governed processes.
2) **Surface modification of biomaterials.** Biomaterials have been shown to be optimised by chemical modification (e.g. acetylation or plasma treatment) of the surface or by surface immobilisation (usually by coating) of peptide sequences or entire ECM proteins, including fibronectin, collagen and laminin (*48–50*).
3) **Incorporation and release of bioactive molecules.** This strategy can be achieved through the incorporation and controlled release of molecules that actively modulate tissue formation and regeneration, such as growth factors (*51*).

The last two strategies are collectively referred to as *biofunctional-isation* of materials.

1.3 Electrospinning

One of the most versatile methods to create biomimetic fibrous structures, pursuing the first strategy **(1)** in the previous section (**Section** 1.2.2), is by means of the **electrospinning method**, which allows for the production of fibres with diameters in the nano- and micrometre range (52). The rediscovery[3] and subsequent boom of the electrospinning method was pioneered by Doshi and Reneker in 1995 (56). They were also the first to envisage possible biomedical applications of this method, albeit only as a wound dressing material. In the following decades, electrospinning emerged as one of the most versatile method to create threedimensional nano-fibrous materials with a plethora of possible applications in tissue engineering (57, 58).

1.3.1 Fibre Formation

The rapid initial expansion of the electrospinning method can be attributed to the convenience of producing nanofibres out of different polymers with inexpensive machinery that can be found in most laboratories. A typical electrospinning set-up consists of a syringe with conductive capillary, a high-voltage source and a grounded collector (**Figure 1.3**). The capillary is connected to the high-voltage source (usually capable of delivering an electrical potential of up to tens of kilovolts) to create an electrical field between the capillary and the collector. Dissolved or molten polymer is pumped through the capillary and gets collected in a small droplet at the tip of the capillary. In the absence of any external actors, this droplet favours a spherical shape, in which the

3: The origins of the electrospinning method can be traced back much further in time (53). Formhals described the production of thin fibres using electrostatic repulsion forces in a patent published in 1934 and claimed potential application in the textile industry (54). Interestingly, the formation of liquid jets due to electrical forces was observed even earlier by Zeleni in a publication in 1917, in which he referred to a *"long known experiment"* (55). It remains unclear what this referenced experiment ought to be.
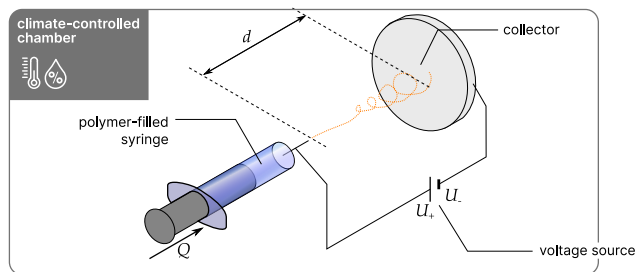

Figure 1.3: Schematic represenation of a typical electrospinning set-up. Some of the relevant electrospinning parameters that influence fibre formation are shown as well, including the flow speed Q, tip-to-collector distance d, and electric potential U.

surface area per unit mass is minimised. When the high voltage is applied on the capillary, an electrical potential is induced on the fluid surface, in which repulsing charges act directly opposite to the surface tension. This causes an elongation of the droplet into a conical shape (referred to as the *Taylor cone*) and the ejection of a charged fluid jet. (*52*, *59*, *60*)

The fluid jet starts with a straight segment, of which the diameter monotonically decreases with the distance from the capillary. The straight segment quickly transforms into a coiled path (*61*). The onset of the bending instability is explained by coulomb repulsion forces, which impel perturbed segments radially outwards. The bended path starts out as a coiled trajectory, which grows in size and is envelloped by a cone (*60*). Higher-order bending instabilities can be observed as well, which manifest as coiling of the coiled trajectory. These bending instabilities enable a substantial elongation of the fluid jet path by multiple orders of magnitude within a confined space. In turn, the elongation causes a reduction of the fibre diameter (*60*).

1.3.2 Electrospun Meshes

The perturbed trajectory of the fluid jet underlies the seemingly random deposition of nanofibres on the collector plate. The deposited electrospun fibres collectively form a distinctive nanofibrous mesh (**Figure 1.4**). The exact morphology of the polymer mesh arises from a complex interplay of multiple electrospinning process parameters (*52*, *58*). The rheology of the polymer solution or melt and the impeded electrical potential affect the trajectory of the fluid jet and, hence, the morphology of the deposited fibres. In addition to that, environmental parameters, such as temperature and relative air humidity, also influence the evaporation of the solvent and alter the fibre morphology (*62*). Flow speed and capillary diameter change the initial diameter of the fluid jet, which, in turn, affects all aforementioned phenomena (*57*). Modification of the electrical field (e.g. by the introduction of insulators) (*63*), adding magnetic fields (*64*), or the use of rotating or moving collectors (*65*, *66*) can be used to aid the deposition of fibres in a preferred alignment (*67*). The process parameters listed here are just a nonexhaustive overview, that demonstrate the great versatility of the electrospinning process to control the morphology of nanofibrous meshes.

The mechanical properties of the electrospun product are by a large degree determined by the polymer selection. Additional fine
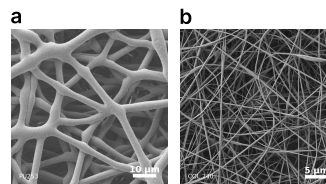

Figure 1.4: SEM images of electrospun meshes. a) Electrospun polyurethane. **b)** Electrospun collagen.

control of the mechanical properties is provided by the parameters of the electrospinning process. Changing the fibre diameter can give different elastic moduli and tensile strengths for the same polymer (*68*, *69*). Fibre alignment can be exploited to achieve anisotropic mechanical properties, which are key to mimic the mechanical properties of certain tissues (*70*, *71*).

Scaffold design is an important aspect of achieving a biomimetic scaffold and is known to strongly influence various aspects of cell behaviour. Morphological aspects such as scaffold porosity, fibre diameter and fibre orientation can influence or regulate cell adhesion, migration, differentiation, growth, proliferation and also the expression of ECM components (*58*). A well explored type of scaffold in this regard are tissue-engineered vascular grafts (TEVGs). To maximise potential success as an implant, an ideal biomimetic electrospun TEVG should mimic the highly structurally organised tunicae (blood vessel layers). Cells rearrange in the direction of flow with well-developed cytoskeletal organisation when seeded directly onto unidirectionally oriented electrospun fibres (*66*).

1.3.3 Electrospinning of Synthetic Polymers

Over the past decades, it has been shown that a large array of different polymers can effectively be processed with electrospinning (*72*). For a polymer to be spinnable, it must meet at least the following two basic requirements: (i) the polymer should have a sufficiently high molecular weight (M_w) and (ii) it should be soluble in an appropriate solvent. When the first condition is not met, fibre formation will not occur or the electrospun fibres will contain beads (*60*). Most synthetic polymers, however, can be synthesised in such way, that their molecular weight is sufficiently high for electrospinning. As such, practically all polymers that have previously been used as biomaterials can be processed using the electrospinning technique.

Biocompatible and degradable polymers, including those mentioned in **Section 1.2.1**, have been spun into various resorbable scaffolds for tissue engineering with the intention to provide a temporary scaffold and prevent postoperative surgery after implantation (*73*). Another main application of electrospun degradable products is found in the fabrication of drug delivery systems. The electrospinning of these degradable polymers provides additional control over the drug release kinetics, as the electrospinning technique allows for many different drug loading and

encapsulation techniques (*74*). PCL was one of the first materials to be employed in electrospinning and has been often spun in biomimetic scaffolds for various applications, ranging from blood vessel (*75*) to bone tissue engineering (*76*). To overcome the early onset of plastic deformation of PCL, TPUs have become a promising elastic material for electrospun scaffolds for soft tissue engineering (*36*, *77*). Due to their superior mechanical properties, electrospun TPUs have been investigated as tissue-engineered vascular grafts (*78–80*), heart valves (*81–83*), and cardiac patches (*84–86*).

1.3.4 Electrospinning of Collagen

The idea of electrospinning collagen directly is not that far-fetched, as electrospun fibres have similar diameter dimensions to native collagen fibrils found in vivo (*16*, *87*). Secondly, as explained in section 1.2.2, collagen is part of the natural ECM and provides numerous cues to cells that can be exploited by electrospinning collagen directly into a fibrous scaffold to develop a biomimetic construct and hence promote tissue formation (*58*).

Highly volatile fluorinated solvents, such as hexafluoroisopropanol (HFIP) and trifluoroethanol (TFE), were used in the first attempts to electrospin collagen (*70*, *88–90*). As these solvents had a proven track record in the electrospinning of synthetic polymers, they were initially simply transferred to collagen. These fluorinated solvents were found to be indeed effective in the solubilisation of collagen and the production of collagen fibres. However, their use was met with increasing concern about the potential denaturation of the native structure of collagen, as they had previously been found to denaturate non-collageneous proteins (*91*, *92*). A similar, devastating effect on collagen was confirmed in a study by Zeugolis et al. (*93*) who showed that after solubilisation in HFIP and subsequent electrospinning, rat tail collagen lost its crystalline and fibrillar structure, resulting in a water-soluble product that was more similar to gelatin.

To maintain collagen integrity, recent efforts have focused on replacing fluorinated solvents with milder solvents (*94–98*). Solvent substitutes include concentrated buffered salines (*99–101*), acetic acid (*95*, *99*), and hydrochloric acid (*102*, *103*). While there is no doubt that these alternative solvents have a lower environmental impact and raise less concern for health during handling, few studies have thoroughly investigated the collagen structure after

electrospinning. Some of the studies included cross-linking with glutaraldehyde or carbodiimides after electrospinning, which more or less negates the success of using alternative solvents in the first place (*97*, *100*, *104*).

1.4 Material Characterisation

The characterisation of materials is an essential facet of materials science, by which the structure and properties of a material are examined. These characterisations are particularly relevant when studying electrospun collagen, as collagen is modified by the various processing steps involved in creating a biomimetic scaffold. Different techniques exist that can unveil a wealth of information regarding the alterations that are inflicted upon collagen. The following sections explain the characterisation techniques relevant to this thesis.

1.4.1 Circular Dichroism

Figure 1.5: Visualisation of different states of polarisation of an electromagnetic wave. The blue and green waves represent orthogonal components of the electromagnetic wave and the resulting wave is shown in red.**a)** Circularly polarised light. **b)** Linearly polarised light. This image has been released into the public domain on Wikimedia Commons and is not subject to copyright in this thesis.

Circular dichroism (CD) spectroscopy is a spectroscopic technique which makes use of the optical activity of chiral molecules. It is particularly useful for studying protein secondary structure.

Light, as well as any other electromagnetic wave for that matter, can have different states of polarisation (**Figure 1.5**) (*105*). When light is circularly polarised, the electromagnetic field rotates in a plane perpendicular to the direction of the light wave. The resulting wave can be left- or right-circularly polarised. When circularly polarised light interacts with a chiral molecule, left- and right-circularly polarised waves will interact differently depending on the chirality of the sample, as the electric and magnetic dipoles of the electrons in chiral molecules are not symmetrically distributed. This results in a different absorption of left and right circularly polarised light, which can be detected in the CD spectrum as circular dichroism. (*106*)

The secondary structure of proteins imparts distinct CD spectra in the medium to far ultraviolet range (180 – 260 nm) of the electromagnetic spectrum. The characteristic triple-helical structure of collagen gives rise to a very strong negative band at 195 nm and slightly weaker specific band at 220 nm (*107*). CD spectroscopy has been shown to be a powerful tool for assessing the degree of helical unfolding in collagen, as the intensities of these two

bands attenuate with increasing degree of collagen denaturation (*99*, *108*).

1.4.2 Raman Spectroscopy

Raman spectroscopy is a popular vibrational spectroscopical technique that can be used to characterise single molecular compounds, materials, and even whole cells (*109*, *110*). It allows for the acquisition of a highly detailed molecular signature, thus permitting the detection of minor molecular changes. Unlike many other analytical techniques, Raman spectroscopy offers a non-invasive and non-destructive approach to studying materials, conferring it with a great benefit in materials science. In addition, its relative insensitivity to water allows the measurement of biological solutes in dilute aqueous solutions, which is of particular interest to the pharmaceutical and biomedical sciences (*111*, *112*). In recent years, Raman spectroscopy has also been extensively studied to distinguish healthy and diseased tissues in biomedical research (*113*, *114*).

Raman scattering

Raman spectroscopy is based on the determination of vibrational modes of molecules by studying inelastically scattered light. This is explained best by the underlying principle of the *conservation of energy* (**Figure 1.6**). When a molecule is hit by photons from an incoming light source, these photons can be scattered either elastically or inelastically. Most photons will be scattered elastically, that is, the scattered photon has the same energy (E) as the incident photon. The molecule is only briefly excited to a very short-lived electronic energy level before returning to the same state it had before excitation. Because of this, the re-emitted photon also has the same wavelength (λ) and frequency (ν) as the incident photon, as the energy of a photon depends only on its frequency or reciprocally, its wavelength:

$$E = h\nu = \frac{hc}{\lambda},\qquad(1.1)$$

where c is the speed of light and h Planck's constant. This commonly observed phenomenon is called *Rayleigh scattering*.

A small fraction (approximately one in 10^7) of photons is scattered inleastically, which is referred to as *Raman scattering* (*109*, *110*).
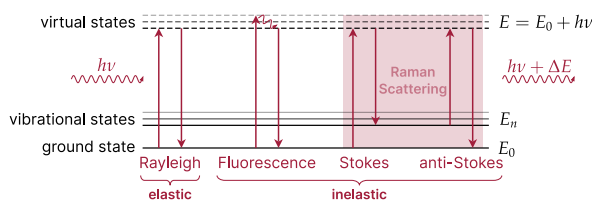
This occurs when re-emission of the photon leads to a change in vibrational energy of the molecules, which is higher in the case of Stokes Raman scattering and lower in the case of anti-Stokes Raman scattering. Since the change of energy has to be conserved and the final state has the same electronic energy as the initial state, the change in vibrational energy is equal to the difference in energy between the incident and scattered photon. The energy change is observed as a wavelength shift and commonly expressed as the *Raman shift* in terms of wavenumbers, where the wavenumber $\tilde{\nu}$ is given by

$$\tilde{\nu} = \frac{\nu}{c} = \frac{1}{\lambda}. \tag{1.2}$$

The possible vibrational states depend on the possible vibrational modes of the atomic bonds within the molecule, such as symmetric (ν_s) and asymmetric (ν_a) stretching and bending (δ). Principally, the wavenumbers of the Stokes and anti-Stokes transitions form a symmetric pattern around zero. However, the principles of thermodynamics dictate that the lower energy states, i.e. those that are closer to the ground state, are more populated at physiologically relevant temperatures, which is why Stokes events are observed much more frequently than anti-Stokes events (*115*).
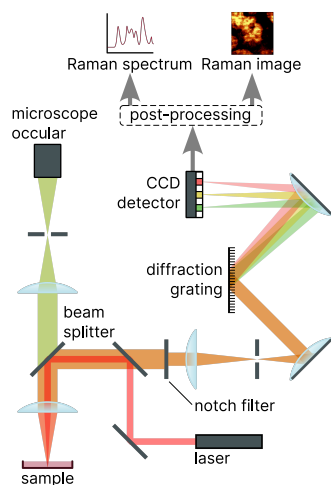
Instrumentation and Interpretation

The instrumentation for Raman spectroscopy has become significantly smaller and simpler to operate with advances in laser and detector technology (*109*). Modern spontaneous Raman spectroscopy nearly always involves the use of a laser to excite the sample. Commonly used laserwavelengths include 488 and 532 nm in the visible and 785 and 1064 nm in the near-infrared range (*112*, *118*). Additional microscopic instrumentation can be used to determine the focal plane or to be used in combination with Raman spectroscopy, referred to as Raman *microspectroscopy*. Scattered light from the sample is directed through a notch filter to block the

much stronger Rayleigh scattering. A diffraction grating diffracts the remaining Raman-scattered light, separating the wavelengths over the length of a CCD array, which counts the scattered photons (**Figure 1.7**). A motorised sample scanning stage allows for raster scanning of the sample to obtain a spectral map with spectral recordings for every pixel. (*109*)

The acquired Raman spectra will contain numerous peaks with varying position, height and shape. Although for smaller molecules the peaks can be individually traced back to well-known vibrational modes of molecular bonds, most samples yield feature-rich Raman spectra that contain a large number of overlapping bands. Additionally, factors such as noise, variations in the sample, and instrumentation can affect the spectra, which can make it difficult to compare data between samples. *Principal component analysis* (PCA) is a popular statistical technique that is used to reduce the dimensionality of datasets by identifying the most important features (the principal components) within a dataset. As such, PCA can help to extract meaningful information from the complex spectra. (*119*, *120*)

Suppose we have obtained 9 recordings, each represented by a spectrum that is described by the photon counts for 6 wavenumbers (**Figure 1.8**a). How do we represent the (combination of) bands that are responsible for the biggest variance within our observations by, say, just two components? Assume the recorded data is contained in a matrix $\mathbf{X}$ with every row one spectral recording and columns as the variables, i.e. the intensities for every wavenumber. Then this data can be represented by the linear combination

$$\mathbf{X} = \mathbf{Z}\mathbf{V}^\mathrm{T} + \mathbf{E}, \tag{1.3}$$

where $\mathbf{V}^\mathrm{T}$ contains the principal components of the dataset. The matrix $\mathbf{Z}$, referred to as the scores matrix, can be regarded as the weighing of these principal components that constitute the dataset (*119*). Since the scores and loadings are typically obtained numerically, the residuals ($\mathbf{E}$) explain the difference between the original data matrix and the numerically computed *decomposition*.[4] The implications of **Equation 1.3** are more intuitively visualised in **Figure 1.8**.

Of course, actual Raman spectral recordings contain considerably more wavenumbers and hence have a much higher dimensionality. PCA can, however, robustly reduce this dimensionality and expose separations that are otherwise impossible to see at first sight. The multivariate analysis of the spectral data has been performed
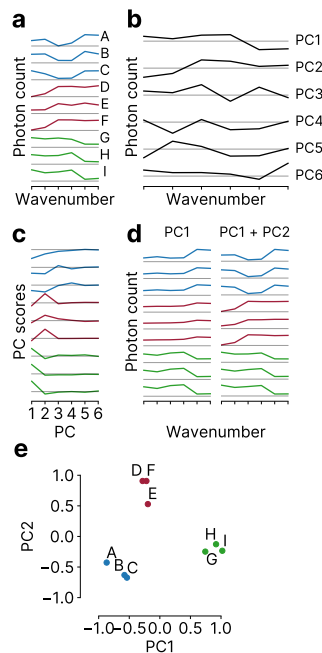
Figure 1.8: Visualisation of PCA reduction of nine observations from six to two dimensions. (a) Nine recordings (A-I) across six wavenumbers. **(b)** PC1-PC6 of the recordings in **a**. **(c)** PC scores show most of the variance is explained by the first two principal components. **(d)** Reconstruction of the original data analogously to **Equation 1.3** using the PCs from **b** and weighings from **c**. **(e)** The scores of the first two PCs from **c** plotted as 2D coordinates. The schematic representation has been adapted from Lever et al. (*120*)

4: The term *decomposition* refers to the numerical method that underlies PCA to obtain these matrices: *singular value decomposition*. This decomposition states that every matrix $\mathbf{X}$ can be decomposed as $\mathbf{X} = \mathbf{U\Sigma V}^\mathrm{T}$. There exist multiple numerical algorithms that compute this factorisation (*121*).

using the RaMAT toolbox **Appendix B**.

Applications of Raman spectroscopy in collagen analysis

It wasn't until advances in laser technology in the 1960s that biological macromolecules could be studied using Raman spectroscopy ([122]). Raman spectroscopy has made it possible to study changes in the secondary structure of macromolecules, which usually arise as a result of protein denaturation or a pH-induced conformational change ([123]). The amide III band (between 1200 and 1300 cm^{-1}) in Raman spectra was suggested to be indicative of the unfolding of small helical polypeptides ([124], [125]). Subsequent spectroscopical analysis of collagen with improved signal-to-noise ratios soon revealed that the amide III band can also be used to detect collagen denaturation, as collagen that had been heated to 70 °C, featured an attenuation, shifting, and widening of the peak within this band ([22]). Further peak assignments were collected in subsequent studies, of which the most relevant peaks for collagen analysis are listed in **Table A.1**.

5: The physics underlying the optical second-harmonic activity of such orderly molecules is rather complicated and reaches beyond the scope of this thesis. If the reader is, however, further interested in this subject, they are referred to the treatise by Bloembergen ([129]) on nonlinear optics and the publication by Roth and Freund ([130]), which touches on the physics of SHG as applied to intact collagen samples.

1.4.3 Second–Harmonic Generation Imaging

Decades before the exact structure of collagen was elucidated through high-resolution x-ray crystallography, it was well known that collagen must have a highly ordered structure ([18], [126]). This realisation led to pioneering investigations of structurally organised tissues with optical **second-harmonic generation** (SHG) by Roth, Freund, and colleagues ([127], [128]). SHG is a physical technique that is sensitive to orientational order of molecules.[5] Since only molecules that feature a *noncentrosymmetric* organisation, it was herefore postulated that collagen must exhibit SHG as well, given its helical structure that gives rise to such symmetry ([130]). SHG is an interesting non-linear optical phenomenon, by which two incident photons are annihilated to produce a single photon at double the frequency (**Figure 1.9**). As gelatin constitutes the unorderly state of collagen fibrils, it is devoid of any structural symmetry and, hence, loses the ability to exhibit SHG. As a result, structurally intact collagen can be distinguished from denaturated and unorderly gelatin ([131]).

virtual state $\cdots\cdots\cdots$ $E = E_0 + 2h\nu$
$h\nu$
virtual state $\longrightarrow$ $E = E_0 + h\nu$ $2h\nu$
$h\nu$
ground state $\longrightarrow$ E_0
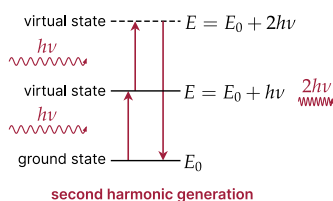
second harmonic generation

Figure 1.9: Schematic engergy diagram visualising the principle of SHG. Notice how the emitted photon has twice the energy and thus half the wavelength of the incident two photons.

1.5 Studying Cell-Material Interaction

The understanding of cell-material interactions is critical in the development of biomaterials, as this comprehension enables a prediction of the performance of the biomaterials within the body. In this section, two aspects of cell-material interaction studies are discussed: firstly, the simulation of the physiological conditions for *in vitro* cell culture using bioreactors, and secondly, the analysis of cell-material interactions of these *in vitro* studies using novel imaging techniques.

1.5.1 Bioreactor Systems in Tissue Engineering

Bioreactors for tissue engineering are designed to offer a controlled environment that simulates the *in vivo* conditions of the target tissue. This is a significant improvement over regular static *in vitro* cell culture, as these systems not only provide the necessary nutrients and biochemical factors, but can also expose cells to predefined and controlled mechanical stimuli, improve cell seeding, and promote cell proliferation and migration (*132*, *133*).

Following the two tissue engineering paradigms introduced in **Section** 1.2.1, a bioreactor system can be designed and used for two purposes. It can either act as a 'preconditioner', providing the ideal conditions for the development of functional tissue architecture prior to implantation, or it can be used to study the tissue formation processes that may occur within the host after implantation by simulating the *in situ* conditions. By eliminating the need for costly and time-consuming animal studies, the latter approach has proven to be critical in achieving more accurate predictions of implant success rates faster and at lower cost. (*133*, *134*)

Bioreactor Systems for Cardiovascular Tissue Engineering

Bioreactor systems perform an important role in cardiovascular tissue engineering as they are able to overcome the specific challenges encountered in this field, such as replicating mechanical and haemodynamic cues. These conditions are typically achieved through the design of a perfusion bioreactor, which typically consists of a pump, tubing, media reservoir and a specially designed flow chamber in which the graft is placed (*135*). Depending on the

target organ, different design variants exist. Heart valve bioreactors focus on the replication of complex cyclic haemodynamics of native heart valves ([136], [137]). Bioreactors for TEVGs are designed to replicate physiological blood flow of the target vessel and are devised as perfusion bioreactors with a flow chamber in which the TEVG is exposed to a well-defined *intraluminal*[6] flow ([140–144]).

6: The *intraluminal* flow is defined as the flow through the *lumen* of a blood vessel, i.e. the inner part of a tubular structure. Certain bioreactors also feature a completely separated circulation for the *extraluminal* environment ([138], [139]).

1.5.2 Cell-Material Assessment

Numerous methods have been developed to provide insight into how cells interact with biomaterials. The reader of this thesis is assumed to be familiar with most of these techniques, such as cell viability assays by MTT[7] assay or live/dead staining and the study of cell spreading and cytoskeletal organisation by immunofluorescence staining. The evaluation of cytotoxicity typically follows the guidelines outlined in ISO 10993-5 and 10993-12 ([145], [146]). This protocol requires cells to be cultured in extracts derived from the material under investigation. Following this incubation period, MTT, a compound that is metabolised exclusively by viable cells, is added to the system. This metabolic process results in an observable colorimetric change reflecting cell viability. In the following section, I shall focus on one (label-free) microscopy method of particular interest.

7: 3-(4,5-dimethylthiazol-2-yl)-2,5-diphenyltetrazolium bromide

Fluorescence Lifetime Imaging

Fluorescence Lifetime Imaging (FLIM) is a microscopy technique that is based on the decay of fluorescence of fluorophores in biological samples ([147]). Although FLIM is not inherently label-free, it is increasingly being used to study the endogenous autofluorescent coenzymes nicotinamide adenine dinucleotide (NADH) and flavine adenine dinucleotide (FADH), which allows for the label-free visualisation of biological samples without the use of exogenous dyes and also provides information on the metabolic state of cells ([148], [149]).

Fluorophores that have been excited by a photon will return to their ground states with a certain probability that is dependent on their chemistry and micro-environment ([147], [150]). In the *ensemble*[8] description, the emitted fluorescence I of a fluorophore decays exponentially with time. This decay is described by

8: In physics, an *ensemble* refers to a statistical model, which describes a large number of copies of a system or an event. In this case, we are looking at multiple thousands of photons all at once, for which the ensemble description holds true.

$$I(t) = I_0 e^{-\frac{t}{\tau}} \tag{1.4}$$

where I_0 is the initial fluorescence, t is time, and τ is the fluorescence lifetime (147). This implies that the number of excited states decays to 36.8% of its original value after one fluorescence lifetime τ, analogous to the concept of radioactive decay. The autofluorescent coenzymes NADH and FADH both exist in a free and protein-bound form, both of which have slightly different fluorescence lifetimes (148). Since both states are observed simultaneously in a cell, the resulting fluorescence will be a superposition of two exponential decay curves. Assuming both coenzymes have a similar intrinsic initial fluorescence, the resulting biexponential decay equation

$$I\left(t\right) = \alpha_1 e^{-\frac{t}{\tau_1}} + \alpha_2 e^{-\frac{t}{\tau_2}} \qquad (1.5)$$

also holds the relative amounts α_1 and α_2 of each coenzyme. By performing a biexponential fit to an observed decay curve, we can deduce how much of the coenzymes are present in the free form (typically found in the cytosol) and how much is present in the protein-bound form (found in the mitochondria).

The relative distribution of free and protein-bound forms of the coenzymes provide a nondestructive optical interrogation of the metabolic state of a cell (151). Pioneering work by Britton Chance has identified NAD(P)H and FAD(P)H as reliable indicators of cell metabolism, which are reflected by a change in the autofluorescent properties of the metabolic coenzymes (152–154).

Objectives of this Thesis | 2

The scope of this thesis encompasses several key aspects of electrospun tissue-engineered cardiovascular graft materials. This thesis aims to address some of the current challenges in the development process of such grafts, from material selection to the *in vitro* testing.

The first aspect is concerned with the use of one of the most commonly used source materials for the production of cardiovascular implants: polyurethane. A novel class of polyurethanes is explored, using an alternative synthesis route that omits hazardous and toxic isocyanates. The first objective of this thesis was to investigate whether these NIPUs can be electrospun and can be a viable biomaterial for use in electrospun grafts in terms of the biocompatibility. This study considered both bare NIPU fibres and biofunctionalised fibres with collagen.

As introduced in **Section** 1.3.4, collagen is also an interesting choice as the main material in electrospun tissue-engineered grafts. The second study explores the pitfalls of this approach, which are involved in the direct electrospinning of collagen. The aim of this study was to investigate the impact of solubilisation and electrospinning on collagen, using non-fluorinated electrospinning solvents. Furthermore, the cell-material interaction was studied *in vitro* and the results of these studies were correlated to the investigation of the secondary structure of electrospun collagen.

The aforementioned studies raise the question, what material is preferred in the production of tissue-engineered vascular grafts. In the last study, the *in vitro* simulation of *in situ* regenerative processes on the surface of a biofunctionalised electrospun vascular graft made from polyurethane was performed using a perfusion bioreactor. The aim of this study was to investigate the additional benefits of biological surface functionalisation under dynamic flow conditions, which were unlikely to be detected in the static cell culture experiments of the second study.

Results I
Electrospinning of high-molecular-weight
polycarbonate-based nonisocyanate polyurethanes

3

The contents of this chapter are based on

Visser, D., Bakhshi, H., Rogg, K., Fuhrmann, E., Wieland, F., Schenke-Layland, K., Meyer, W. and Hartmann, H. (2022). Green Chemistry for Biomimetic Materials: Synthesis and Electrospinning of High-Molecular-Weight Polycarbonate-Based Nonisocyanate Polyurethanes. *ACS Omega* **7**, 39772–39781

As mentioned in **Section** 1.2.1, the conventional synthesis route for TPUs involves the use of harmful diisocyanates for the hard segment chemistry. The risks associated with using these are two-fold. The isocyanates are often not completely consumed during the polymerisation process, causing environmental damage and posing a health risk to operators during synthesis (*42–44*). Another risk arises after implantation. Implanted biomaterials can be subjected to hydrolytic activity during an inflammatory reaction, for example by cholesterol esterase, or to oxidative activity during a foreign body reaction by hydrogen peroxide (H_2O_2) (*155–159*). The hard segments that are incorporated into the polyurethanes might be released into the body upon this degradation. Another problem with conventional TPUs is formed by toxic tin-based catalysts, which are not fully removed after the polymerisation process (*160*, *161*).

3.1 Electrospinning of NIPUs

Alternative synthesis routes for TPUs that omit the use isocyanates and tin-based catalysts of the conventional polyurethane chemistry have recently gained much interest (*45*, *46*, *162–164*). One such alternative route for the synthesis of non-isocyanate polyurethanes (NIPUs) is the transurethanisation reaction between bis-carbamates and polyols, which results in a structure and properties similar to those of classic TPUs (*165–167*).

Even though water-soluble polymers have already made a successful contribution to improving the environmental sustainability of electrospinning, the green electrospinning of polyurethanes still remains an unexplored field. Most studies so far have only

focussed on the electrospinning of TPUs based on conventional synthesis routes. The electrospinning of polyether-based NIPUs, synthesised from cyclic carbonate methyl esters, and their potential for biomedical applications has recently been reported by Aduba et al. (*45*) However, these polyether-based NIPUs fall short of the classic TPUs in terms of their mechanical properties. Therefore, an electrospinning process for PC-based NIPUs was established.

The synthesis of the NIPU was carried out at the Fraunhofer Institute for Applied Polymer Research IAP. For the creation of polycarbonate-based NIPU with varying molecular weights, different polycarbonate diols (PCDL) with molecular weights of 500, 1000, and 2000 g mol^{-1} were used at various stochiometry, temperatures, and vacuum pressures. These PCDLs were reacted with 1,6-hexanedicarbamate, obtained from a reaction between 1,6-hexanediamine and dimethyl carbonate (Visser et al., **Appendix C**, **Scheme 1**). The resulting NIPUs had molecular weights ranging between 14 500 and 58 600 g mol^{-1} (Visser et al., **Appendix C**, **Table 1**), which were all tested for spinnability, to find the appropriate molecular weight that facilitated the electrospinning process.

While all of the synthesised NIPUs were soluble in common electrospinning solvents like DMF, THF, and HFIP, their solubility decreased as their molecular weight increased. Conversely, the electrospinning of NIPUs with lower molecular weights usually yielded bead-containing fibrous morphologies and was prone a premature halt, especially in combination with DMF and THF. NIPUs based on PCDLs with M_w = 500 g mol^{-1} were successfully spun into fibrous mats. Generally, the electrospinnability of these NIPU formulations improved with increasing molecular weight and increasing solution concentration. It was observed, that the reduction of bead formation and increase in fibre diameter positively correlated with these process parameters. Following similar observations in the electrospinning of conventional TPUs (*168*) and other polymers (*169–171*), the suppression of bead formation and the increase in fibre diameter in NIPUs with higher molecular weight and solution concentration can be attributed to the rheological properties of the electrospinning solution. The NIPU with the highest molecular weight (58 600 g mol^{-1}), called NIPU-D hereafter, was successfully spun into fibres at polymer concentrations between 25 wt % and 35 wt %. It was noted, that increasing the solvent conductivity to 10 µS cm^{-1} through supplemention with sodium carbonate, fibre formation could be

Table 3.1: Electrospinning parameters and resulting fibre diameter of NIPU-D fibre mats that were used for cell-material interaction studies. U: electrical potential, φ: flow speed, CID: cannula inner diameter, rH: relative humidity, T: temperature, and d: tip-to-collector distance. The average values refer to the mean of the fibre diameters and the inter-sample standard deviation ($n = 3$) and the spread refers to the mean of the standard deviation of the intra-sample fibre distributions.

sample		electrospinning parameters						fibre diameter	
conc.	σ	U	φ	CID	rH	T	d	average	spread
	$\mu S\,cm^{-1}$	kV	$mL\,h^{-1}$	mm	%	°C	cm	μm	μm
25 wt %	10	23	0.4	0.5	20	35	28	1.11 ± 0.03	0.34

further improved. In comparison to the NIPU mats electrospun from unsupplemented HFIP, the fibres were more segregated and had more well-defined round cross-sections (Visser et al., **Appendix C**, **Figure 4c,d**). The intra-sample fibre diameter spread was also narrowed and the fibre mats contained a few melted fibres. Electrospun NIPU-D mats contained fibres with a diameter of 1.11 ± 0.03 µm when spun out of a 25 wt % solution. Since electrospinning of NIPU-D at 25 wt % in supplemented HFIP was found to be the most stable electrospinning process with the smallest intra-sample fibre diameter spread (0.34 ± 0.01 µm), these process parameters (**Table 3.1** and Visser et al., **Appendix C**, **Table 2**) were selected for the preparation of electrospun mats for biocompatibility testing.

3.2 Biocompatibility of electrospun NIPUs

In an initial assessment of potential cytotoxicity caused by the NIPUs or any possible solvent residues, L929 cells were cultured in medium extracts according to ISO 10993-5 and -12 norms (*145*, *146*). Based on the relative viability of these cells, measured by means of an MTT assay, neither the NIPU-D granulate nor the electrospun NIPU-D mats were considered cytotoxic. The corollary of this observation is that no cytotoxic leachables or extractables of the NIPUs can be detected within a 24 hour incubation period and vacuum drying is sufficient to remove any remaining HFIP remnants after electrospinning.

Since these NIPUs were synthesised and electrospun with the primary intention of achieving enhanced biocompatibility, the ability of the mats to facilitate fibroblast and epithelial cell adhesion and proliferation was assessed after 24 h and 7 days of static *in vitro* culture. To simulate the conditions of use as a pericardial

substitute, the cells chosen for this evaluation were epithelial cells obtained from the pleural mesothelial membrane, which consists of squamous epithelial cells. Similar cells also line the outermost layer of the pericardium towards the serous cavity (*172–174*).

For such cell-material interaction studies, it is often helpful to modify polyurethane surfaces by surface immobilisation of bio-molecules to improve interfacial properties, as most polycarbonate-based polyurethanes lack natural cell recognition sites and are notoriously hydrophobic (*175*). Therefore, the electrospun NIPU-D mats were coated with collagen, which despite a minimal contact angle reduction from $101 \pm 6°$ to $98 \pm 2°$, effectively bio-functionalised the mat surface as immunological staining against collagen I confirmed successful surface adsorption (Visser et al., **Appendix C**, **Figure S6,S7**).

After both 24 h and 7 days, both cell types were predomin-antly stained calcein-positive on both the functionalised and non-functionalised electrospun NIPU (Visser et al., **Appendix C**, **Figure 5a**). Morphologies and arrangement of either cell type on the bare and collagen-functionalised electrospun NIPU mats mirrored those on the glass, which acted as the negative control. The cobblestone morphology of the epithelial cells and the ten-dency to form a tightly packed monolayer were especially evident in SEM images (Visser et al., **Appendix C**, **Figure 5b**). These observations proved that, in spite of the high contact angles, the mats provided a highly biocompatible substrate for the cultured cells regardless of functionalisation. As such, the electrospun NIPU mats are well suited for use as a three-dimensional scaffold without any further processing.

The contents of this chapter are based on

Visser, D., Rogg, K., Fuhrmann, E., Marzi, J., Schenke-Layland, K. and Hartmann, H. (2023). Electrospinning of collagen: Enzymatic and spectroscopical analyses reveal solvent-independent disruption of the triple-helical structure. *Journal of Materials Chemistry B* **11,** 2207–2218

A full copy of this publication can be found in **Appendix D**.

4.1 Electrospinning of Collagen

As a major constituent of the natural ECM, collagen has always been an interesting candidate for use in electrospinning to produce biomimetic constructs with natural ECM components. Initial efforts to electrospin collagen were attempted using the same solvents that had previously been used to establish electrospinning processes for synthetic polymers, in particular highly volatile fluorinated solvents such as hexafluoroisopropanol (HFIP) and trifluoroethanol (TFE) (*70*, *88–90*). **Section 1.3.4** briefly touched on the potential drawbacks of these 'conventional' electrospinning solvents, which denature the secondary structure of collagen, and introduced the alternative solvent substitutes that have seen more intensive investigation since the seminal work by Zeugolis et al. (*93*).

With so many publications claiming successful electrospinning of collagen using alternative solvents, the suggestion has taken hold that these alternatives may better preserve the secondary structure of collagen. Indeed, some promising advances have been made. Dems et al. (*102*) presented evidence for the preservation of the native triple helical structure using a mixture of hydrochloric acid and ethanol, followed by crosslinking with ammonia vapour. Nevertheless, most other studies fail to unequivocally demonstrate the preservation of the structural integrity and proteolytic resistance of collagen after electrospinning, nor do they propose a possible mechanism of collagen denaturation in cases where the results suggest that collagen has been compromised in the process. On the contrary, some publications mention the cross-linking of

electrospun mats, which is only necessitated by structural damage to the otherwise water-insoluble collagen fibres (*97*, *100*, *104*). Liu et al. (*98*) even presented the first explicit evidence of collagen denaturation by acetic acid, which was almost indiscernible from the damage inflicted by HFIP.

These conflicting observations and claims raise the debate as to whether it is worth the effort to electrospin pure collagen fibres under all circumstances. For this very reason, the collagen in the present study was investigated more thoroughly for possible denaturation and its effects of cell-material interaction after electrospinning with the aforementioned alternative 'gentle' solvents. For this, collagen was isolated from rat tail tendons, lyophilised and dissolved in various solutions at 4 °C (Visser et al., **Appendix D**, **Figure 1a**). Indeed, there is a wide range of fibre morphologies that are possible upon expansion of the solvent spectrum (Visser et al., **Appendix D**, **Figure 1b**). The combination of acetic acid and ethanol, especially when the ethanol content was increased to a ratio of 1:2, provided the most reproducible results and yielded well defined and uniformly shaped fibre meshes over a wide range of collagen concentrations (Visser et al., **Appendix D**, **Figure 1c**). This solvent was then used to spin collagen at 20, 25, and 30 °C for further characterisation. For comparison against denaturated collagen, a control was spun out of a collagen solution in HFIP.

4.2 Characterisation of ES Collagen

The electrospun collagen was analysed using CD spectroscopy, SDS-PAGE, Raman spectroscopy and SHG to determine whether the electrospun collagen still comprised an intact secondary protein structure.

As previously observed by Liu et al. (*98*) and Kazanci (*96*), circular dichroism revealed the attenuating effect of electrospinning with acetic acid on the optical activity of collagen. The least damage was inflicted when collagen was spun in acetic acid/ethanol at 20 °C, the lowest temperature achieved. Though even at these conditions, only 15.7 ± 2.0% of the polyproline-II helix remained in the folded state (Visser et al., **Appendix D**, **Figure 2d**). These figures support the previously reported findings by Burck et al. (*99*). Although acetic acid unfolded collagen to a lesser extent than HFIP, both solvents left collagen partially unfolded after electrospinning. As unfolding further increased with increasing

electrospinning temperature (Visser et al., **Appendix D**, **Figure 2d**), the denaturation temperature of collagen may be a common underlying factor for the observed denaturation, with the electrospinning process or certain solvents being the main actors that lower the denaturation temperature.

Native and electrospun collagen were also examined by gel electrophoresis (Visser et al., **Appendix D**, **Figure 3**). Although α_1 and α_2 monomers were clearly identified in all electrospun collagen samples, this observation alone is inadequate to detect denaturation without including a comparison of enzyme digestion resistance ([176]). The denaturation surfaced after a brief α-chymotrypsin digestion, as only native collagen I retained discernable α bands. The near total loss of these bands and the presence of digestion fragments of lower molecular weight in the digested electrospun samples are clear indications that electrospun collagen has gained accessible cleavage sites in the helical domain.

The sudden access to cleavage sites strongly suggests a change in the helical structure of collagen. The simultaneously observed loss of SHG signal after electrospinning (Visser et al., **Appendix D**, **Figure S1**) raises the hypothesis of an ordered triple helix transitioning to a disordered state ([177], [178]). Conformational changes could also be inferred from Raman spectroscopic analysis. Electrospun and thermally denatured collagen showed subtle yet clear differences in their spectral fingerprints compared to native collagen (Visser et al., **Appendix D**, **Figure 4**). Some more subtle differences were revealed by PCA. The amide III band (1240 – 1249 cm^{-1}) reflected changes that were present in all processed collagen samples. The maximum height of the amide III band was lowered, its peak position shifted to higher wavenumbers, and its width increased due to the formation of shoulders. These changes are archetypal of conformational changes of the alpha helix and have been linked to collagen heat denaturation ([22]). More specifically, these conformational changes are likely to be the transition of α-helices to β-sheets, as is implied by the location of the newly formed shoulders around 1220 cm^{-1}, changes in the amide II region at 1409 cm^{-1} and loss of bands in the proline and hydroxyproline region between 936 and 940 cm^{-1} ([179], [180]). Interestingly, all processed collagen samples were significantly ($p < 0.01$) separated from native collagen by PCA, but not statistically separated from each other. The corollary to this is that the above mentioned modes of denaturation seem to occur independently of the solvent used for electrospinning.

It is not obvious to pinpoint the direct cause of denaturation. The

high ethanol content seems to be a common factor in the studies which present a denaturated collagen product. It should be noted that the denature temperature of collagen can be reduced from 40 to 34 °C by using aqueous ethanol solutions with concentrations as low as 40% (*181*). Electrospinning solutions, however, generally exist at much higher ethanol concentrations (*99*).

4.3 Cell–Material Interactions on ES Collagen

In the present study, it was investigated whether the often emphasised advantages of an electrospun scaffold remain valid in spite of evidence that the collagen no longer represents native collagen from a biochemical perspective. To analyse the cell interaction with the collagen material after different processing steps, electrospun NIPU (as mentioned in **Chapter 3**) without collagen (ES-PU), with collagen coating (ES-PU+COL) or with collagen electrospun on top (ES-PUCOL) were compared by F-actin staining, SEM, live/dead staining and FLIM. After 7 days of cell culture on electrospun collagen and electrospun polyurethane, both epithelial cells and fibroblasts achieved an organised organisation of their cytoskeleton, similar to those cultured on glass (Visser et al., **Appendix D**, **Figure 5**). Live/Dead stainings confirmed high viability of cultured cells on electrospun scaffolds irrespective of any collagen contact. Live cell studies of cell metabolism using FLIM were in line with aforementioned studies (Visser et al., **Appendix D**, **Figure 6**). The positive control with DMSO was the only condition that consistently yielded significant differences in free NAD(P)H quantities (α_1) and free NAD(P)H fluorescence lifetimes (τ_1) relative to glass in both cell types after 24 hours ($p < 0.05$) and 7 days ($p < 0.01$). Electrospun collagen showed no advantage over other electrospun substrates, and fibroblasts even showed evidence of a slightly elevated metabolic stress on electrospun collagen, albeit not significant. Based on these observations, cell-material interaction studies are not likely to reveal the damage inflicted upon the triple helix structure of collagen.

The contents of this chapter are based on

Daum, R., **Visser, D.**, Wild, C., Kutuzova, L., Schneider, M., Lorenz, G., Weiss, M., Hinderer, S., Stock, U. A., Seifert, M. and Schenke-Layland, K. (2020). Fibronectin adsorption on electrospun synthetic vascular grafts attracts endothelial progenitor cells and promotes endothelialization in dynamic in vitro culture. *Cells* **9**, 778

A full copy of this publication can be found in **Appendix E**.

Effective therapies to replace small-diameter grafts (<6 mm) are still lacking, as currently available synthetic TEVGs in this diameter range are associated with elevated thrombosis risk and donor site morbidity (*182*, *183*). Electrospinning is a promising technique for the production of novel TEVGs, because electrospun TEVGs manage to capture several characteristics of an ideal vascular replacement, such as: (a) mechanical strength, (b) biocompatibility, and (c) ease of handling (*182*, *184*). In **Chapter 3** and **Chapter 4**, several tests were presented to assess the biocompatibility and cell-material interaction of electrospun grafts under static *in vitro* conditions. A further step in the development of medical devices is the replication of physiological conditions, e.g. through the use of tissue-engineering bioreactors.[9] Numerous designs of perfusion bioreactors for TEVGs have been proposed that replicate the haemodynamics of blood vessels (*138*–*140*, *142*). However, most designs are non-modular and cumbersome to assemble and operate, with some studies explicitly stating the need for simplicity (*143*, *144*). The aim of the study of this chapter was twofold: to demonstrate a newly devised modular bioreactor that allows for the simulation of *in situ* regenerative processes in TEVGs, and to construct and test an electrospun TEVG, which was biofunctionalised with adhesion proteins.

9: This strategy has gained traction in the light of the recently introduced *3Rs* principles of animal testing: replace, reduce and refine. By immitating *in vivo* conditions, a large number of animal trials can be avoided in the development of medical devices.

5.1 Electrospinning and Material Characterisation of a TEVG

TPCU dissolved in HFIP was electrospun into 110 mm-long tubular scaffolds with an inner diameter of 5 mm (Daum et al., **Appendix E**, **Table 1** and **Figure 3a**). A wall thickness of 0.40 ± 0.06 mm was achieved and fibre diameters and pore sizes were measured to be 775.8 ± 162.5 nm and $0.09 \pm 0.03\ \mu m^2$ respectively. Despite the larger fibre diameters compared to typical collagen fibres in blood vessels, similarly sized electrospun fibres have proven sufficient for the development of a functional endothelium, whereas smaller fibre sizes often correlate with smaller pore sizes that hinder cellular infiltration (*68*, *185*). Following the second strategy introduced in **Section** 1.2.2 for the production of biomimetic scaffolds, the electrospun tubular scaffolds were biofunctionalised with decorin and fibronectin through protein adsorption. Successful protein adsorption was confirmed by immunofluorescence staining and SEM analysis, and pore sizes were not significantly affected by the coating (Daum et al., **Appendix E**, **Figure 3b–e**).

The electrospun tubular graft was cut and stretched using a uniaxal tensile testing device until rupture. The registered force at rupture, F_b was translated using the ultime strain s_b into the more clinically relevant quantity of the burst pressure, P_b, using the equation provided by Laterreur et al. (*186*) as follows:

$$P_b = \frac{F_b \pi}{L_0 d_{pin}\left(\pi + 2\right) + 2L_0 s_b},\qquad(5.1)$$

where d_{pin} is the diameter of the pins and L_0 the length of the test samples (**Figure 5.1**).
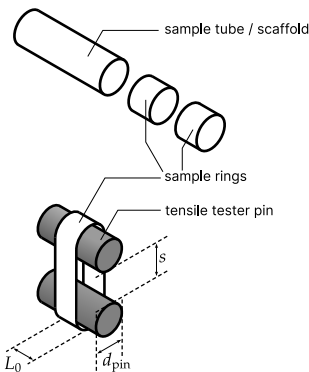
Figure 5.1: Schematic illustration of the ring tensile test. Relevant dimensions are included in the illustration, such as length of the sample rings L_0, tensile test pin diameter d_{pin} and elongation length s.

The TEVG had a comparable elastic modulus (4.8 ± 0.6 MPa) and burst pressure (3326 ± 78 mmHg) to those of a saphenous vein (*187*), which is still considered the conduit of choice for arterial bypass operations (*2*). Mechanical properties were not significantly altered by protein adsorption (Daum et al., **Appendix E**, **Figure 3e**)

5.2 Bioreactor System for TEVGs

A previously custom-designed tissue-engineered vascular graft (TEVG) bioreactor system was assembled, offering a versatile solution for cell seeding, *in vitro* endothelialisation and mechanical characterisation under physiologically accurate dynamic flow conditions (*188*). By utilising modular reconfiguration, this single system was easily adapted for the study of cell-material interaction at different stages of the tissue engineering of a TEVG (Daum et al., **Appendix E**, **Figure 2**). The core part of the system consists of a graft frame that holds the TEVG and is enclosed in a 250 mL glass bottle. Flexible silicone tubing linked the graft frame to medium reservoirs in a closed circuit, only separated from the external environment through sterile gas filters. Medium circulation was driven by a multichannel roller pump.

Biomechanical cues, particularly shear stress, significantly impact cell behavior. Applying controlled shear stress in bioreactors can promote cellular rearrangement(*189*, *190*), extracellular matrix protein expression(*191*), and tissue formation(*142*), making wall shear stress a critical consideration in bioreactor design. Since we are considering a bioreactor for vascular grafts, the idea of shear forces can be intuitively explained by an idealised laminar flow profile through a tubular hollow structure (**Figure 5.2**). The fluid flow takes on a parabolic velocity distribution, u, leading to a linear velocity gradient that reaches its maximum near the walls. The shear stress, τ, is obtained by multiplying this gradient with the fluid's viscosity μ:

$$\tau = \mu \frac{\partial u}{\partial x}. \tag{5.2}$$

Usually, however, the exact flow velocity within a tube is unkown. Therefore, the wall shear stress is generally approximated by a modified version of the Hagen-Poiseuille equation:

$$\tau = \frac{4\mu Q}{\pi r^3}, \tag{5.3}$$

which relates the wall shear stress to the flow rate, Q, and the internal tube radius r (*192*). This approximation was numerically confirmed by computational fluid dynamics (CFD) simulations, taking the entire threedimensional geometry of the graft frame into consideration.
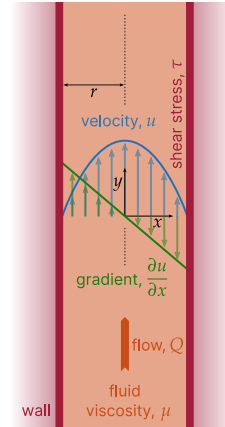

Figure 5.2: Schematic visualisation of the shear force by an idealised laminar flow profile through a hollow structure.

5.3 *In Vitro* Endothelialisation under Flow

The functionality and regenerative potential of the biofunction-alisation with fibronectin and decorin was tested with two endothelialisation processes. First the attraction, also called *homing* of endothelial progenitor cells (EPCs) was simulated. This is a crucial step for the formation of new blood vessels (*193*). Fibronectin coating increased endothelial progenitor homing, whereas decorin coating did not affect this process (Daum et al., **Appendix E**, **Figure 5**, **6**). Secondly, endothelialisation under physiological shear stress was simulated with vascular endothelial cells (vECs). vECs, isolated from human foreskin biopsies, were seeded onto fibronectin-coated tubular scaffolds. The scaffolds were then inserted into the graft chamber followed by assembly of the bioreactor. After three days of static conditions, the flow rate was steadily increased to $25\,\text{mL}\,\text{min}^{-1}$. Taking the viscosity of cell culture media of $0.82 \cdot 10^{-3}\,\text{Pa}\,\text{s}$(*194*), the cells were subject to a shear stress of about $0.3\,\text{Pa}$. Although this shear stress is lower than common arterial shear stress(*195*, *196*), CFD simulations showed that, increasing the flow rate further would most likely induce flow recirculation patterns, effectively reducing the shear stress.

After 7 days of cell culture under flow conditions, a confluent layer of vECs had formed with a unidirectional cell orientation aligned with the direction of flow (Daum et al., **Appendix E**, **Figure 8**). A functional endothelium is primarily characterised by cell-cell junctions and the expression of PECAM-1, a crucial component for maintaining permeability barriers. PECAM-1 expression (Daum et al., **Appendix E**, **Figure 8b**) proved, the cells cultured under flow conditions had formed a functional endothelium.

Discussion and Outlook | 6

6.1 Current State of Electrospinning in Tissue Engineering

The pioneering work by Doshi and Reneker (56) sparked a surge in academic interest in the electrospinning technique. At the time of writing, the abstract and citation database Scopus® lists 45.951 entries with the keyword "electrospinning" and the annual number has risen steadily since 1996, when the first publications appeared. The capability of producing ultra-thin fibres from a variety of materials has opened the door to new designs and the further development of high-performance materials, particularly for use in drug delivery systems, tissue engineering, nanocomposites, and filtration technologies (57, 72).

Electrospinning is particularly suitable for tissue engineering because of its ability to produce scaffolds that mimic the natural nanofibrous structure of the extracellular matrix. Soon, the idea emerged that electrospinning might allow the construction of the whole ECM from scratch. This approach is called *de novo* engineering. Early electrospinning research in the field of tissue engineering was quick to adopt the strategy of incorporating natural extracellular matrix (ECM) components, demonstrating grafts purely composed of electrospun collagen and elastin. This perhaps slightly over-optimistic enthusiasm was somewhat curtailed after Zeugolis et al. (93) provided clear evidence of the detrimental impact of the electrospinning process on native collagen.

Despite the challenges, the integration of natural ECM components into electrospun materials continues to attract considerable academic attention and remains a subject of intense research (50). The main driver behind this interest is the lack of cell recognition sites on synthetic materials (197). Therefore, the feasibility of the incorporation of whole ECM proteins into tissue-engineered constructs either by means of electrospinning or by surface adsorption continues to be a focus of investigation.

6.2 Synthetic vs. Natural Materials

The use of synthetic or natural materials in electrospinning for tissue-engineered constructs doesn't have to represent a strict dichotomy. It is rather a spectrum of possibilities. In practice, it's entirely possible to combine both synthetic and natural materials to create hybrid constructs that benefit from the advantages of both. Electrospinning achieves biomimicry mainly by mimicking the nanostructure of natural ECM, but electrospinning is also readily amenable to include the other biomimetic strategies mentioned in **Section** 1.2.2, such as surface modification of the fibres and the incorporation and release of bioactive molecules. Each additional biological component, however, raises the product's complexity, potentially leading to significantly increased regulatory challenges if the product is classified as an Advanced Therapy Medicinal Product (ATMP) (*198*). Biological components generally also reduce the reproducibility and consistency of the product.

One of the main issues explored in this thesis is the extent to which the synthetic or natural approach is preferable. For this purpose, the investigation was limited to two materials commonly used in tissue engineering: polyurethane and collagen.

In the case of polyurethane, the new class of non-isocyanate polyurethanes, NIPUs, was evaluated for use in electrospinning. The first study (**Chapter 3**) demonstrated that such NIPUs can be successfully synthesised by transurethanisation. The NIPUs exposed two challenges that are associated with the electrospinning of polyurethanes: the solubility and the high molecular weight. Typically, as molecular weight increases, solubility tends to decrease. However, a higher molecular weight also benefits the electrospinning process by reducing bead formation and has been shown to assist in the production of well-separated and defect-free fibres (*168–171*). NIPUs of different molecular weights were obtained. In our study, the NIPUs could be synthesised at a molecular weight that was sufficient to ensure a stable, fibre-yielding electrospinning process.

Despite high contact angles of electrospun NIPU, the bare NIPU mats matched the performance of the collagen-coated mats, suggesting cells were not hindered by the lack of cell recognition sites. Hgh contact angles do not necessarily impede cell adhesion per se (*199*), although conventional TPUs have often been modified through surface immobilisation of adhesion proteins or co-electrospun with proteins on the assumption it benefits the

cell attachment (*200–202*). However, one comparative study with electrospun, protein-modified PU suggested that the microarchitecture of the scaffold plays a predominant role in influencing the cellular response, more so than the presence of adhesion protein coatings, given that the electrospun morphology matches the dimensions of the ECM fibres (*203*).

Although more difficult to prove, another possible factor explaining the good biocompatibility performance of the electrospun NIPU mats may be the inherent properties of the NIPU itself compared to conventional TPUs. The biocompatibility assays used in this study are unlikely to reveal any difference in biocompatibility between NIPUs and commercially available TPUs (*45*). Such differences are more likely to be observed in long-term degradation studies, since TPUs typically have good biocompatibility due to their high stability (*39*). Over time TPUs can partially degrade, particularly when their hard segment chemistry is modified to be more susceptible to hydrolytic degradation (*38*, *204*) or when they are exposed to hydrolytic conditions for extended periods. As implanted biomaterials are likely to be exposed to such conditions during an inflammatory response, this is an important aspect to consider when developing biomaterials (*155–157*). Although it should be noted that aromatic diisocyanates are unlikely to spontaneously reform during hydrolytic degradation, our NIPUs lower the risk that potentially harmful hard segment degradation products are released into the body (*205*).

Eliminating isocyanates from the synthesis process also simultaneously addresses another concern. It significantly improves the environmental footprint and reduces potential health concerns for operators during the synthesis process. This trend has been termed *green chemistry* (*206*). The trend has recently gained momentum, driven by an increasing number of safety and environmental regulations, some of which also affect established electrospinning protocols and necessitate continuous advancements in the field. A case in point is the recent REACH[10] amendment published by the European Commission, which restricts the use of N,N-dimethylformamide (DMF) – an aprotic solvent widely used to solubilise TPUs for electrospinning – from 12 December 2023 in relation to general use and in 2025 in relation to electrospinning processes (*207*). Analogously to DMF, HFIP is also associated with liver and developmental toxicity and is classified as potentially toxic to reproduction (*208*). Solutions for the further advancement of polyurethane-based biomaterials may include solvent-free electrospinning techniques, such as melt electrospinning (*209*,

10: The *Registration, Evaluation, Authorisation and Restriction of Chemicals* (REACH) is a regulatory framework of the European Union addressing the producing and use of chemicals.

210), and the synthesis of polyurethanes, which are soluble in alternative solvents.

In the case of collagen, the search for other electrospinning solvents has long since become inevitable. Several alternative solvents – most of which binary solvents, containing ethanol – have been proposed and successfully used to electrospin collagen into fibrous scaffolds (*95–104*, *176*, *211–215*). Avoiding potential collagen denaturation is often cited as the main reason for solvent selection. Yet, the majority of studies lack compelling evidence to confirm the preservation of the structural integrity and proteolytic resistance of collagen following the electrospinning process. Even in cases where findings suggest that collagen has been compromised during the process, an explanation of a potential mechanism which may have lead to the denaturation of the collagen is often not provided (*96*, *98*). The collagen, which is otherwise – when harvested from adult animals – insoluble in water(*216*), was processed into fibres that required additional cross-linking in the post-processing stage (*97*, *98*, *100*, *104*, *215*, *217*).

The search for suitable alternative solvents proves particularly challenging in the context of collagen electrospinning, as ideally the solvent should evaporate rapidly. Acidic solvents are often mixed with ethanol(*95*, *99*, *102*, *103*) or used in highly concentrated solutions(*96*, *176*) to facilitate this evaporation. Both methods, however, come at a substantial cost. Highly concentrated collagen solutions often require thermal or mechanical input during solubilisation, risking collagen denaturation and unfolding. Our observations (**Chapter 4**), consistent with the existing literature(*96*, *98*, *99*), suggest that ethanol also unravels the polyproline-II helix, even without thermal input at relatively low temperatures such as 20 °C. The observation that α-chymotrypsin was able to access the cleavage sites supports the hypothesis of a disrupted and unravelled helix. This is particularly significant because α-chymotrypsin is only able to cleave the non-helical telopeptides when collagen's triple-helical structure is not disrupted (*218*). The suggestion of conformational changes in the collagen triple helix was further supported by both Raman spectroscopic analysis and the loss of the SHG signal.

Ethanol could be the culprit, as it may affect the denaturation temperature of collagen or its ability to refold and re-nature, both of which vary considerably depending on the organisational state of collagen. One study has shown that a 40% aqueous ethanol solution can reduce the denaturation temperature of collagen from 40 to 34 °C (*181*). Although this temperature is still higher than that

typically used in most electrospinning processes, it's plausible that in many studies the collagen denaturation temperature was further reduced by using even higher ethanol concentrations, ranging from 60%(*99*) to 75%(*102*). A recently proposed two-step approach, in which ethanol was used only for solubilisation and not for electrospinning, yielded a significantly reduced triple helix content, with a further decrease with increasing ethanol content (*212*). A second explanation could be derived from the supposition that the denaturation does not have to be caused by the solvent per se, but rather by the combination of the solvent and the electrospinning process. This is supported by PCA of the Raman analysis, suggesting that the detected conformational changes occurred independently of the solvent used for electrospinning. Promising CD results indicating the retention of the triple helix have also been shown when collagen was spun at very low concentrations in a combination of ethanol and hydrochloric acid (*102*).

6.3 Assessment of Cell–Material Interaction

Following our observations of the material investigation, a pivotal question emerges concerning the biocompatibility of electrospun grafts: to what extent does the material composition of these grafts affect cell behaviour? In the case of collagen, our observations challenge the frequently cited attribution, that biocompatibility is enhanced due to the biochemical mimicry of the native ECM. Strictly speaking, this attribution appears flawed as electrospun collagen biochemically no longer constitutes native collagen anymore. Our data indicate that cell-material interaction studies will probably not be able to uncover the damage that has been made to the triple helical structure of collagen. Some publications are more conservative in their assumptions, citing in particular the nano-structure and three-dimensionality of electrospun scaffolds as potential factors for improved cell penetration and vascularisation (*74*, *219–221*). This perspective aligns with the previously referenced study, which proposed that microstructure may hold more significance than biofunctionalisation with adhesion proteins (*203*).

However, this observation does not invalidate the widely accepted notion that adhesion proteins play an important role in mediating cell attachment and behaviour. Under physiological conditions,

cells rarely directly interact with the surface of an implant and instead only perceive the adsorbed protein layer (*222*, *223*). This layer may already form simply by adsorption of the adhesion proteins present in serum-supplemented cell culture media (*199*). This could explain the good performance of the uncoated NIPU in **Chapter 3**. One example of an important interaction with adhesion proteins is the homing of endothelial progenitor cells, which bind to ECM proteins such as decorin, collagen, and fibronectin, and concecutively enable the early formation of functional epithelium (*224*, *225*). Indirect cell-material interactions play a crucial role in *in situ* tissue engineering, as the surface protein layer can be exploited as a mediator to stimulate and control the desired biological responses in the host (*226*).

Thorough evaluation of the success of *in situ* regenerative processes remains a time-consuming and costly process, which is the main reason for the slow approval of new ATMPs (*227*). The primary source of the substantial level of investment is attributable to the conduct of *in vivo* studies. In fact, many remodeling processes can be replicated *in vitro*, which carries huge potential to – at least partially – obviate animal trials. However, the *in vitro* testing of cardiovascular implants presents particular challenges due to the highly dynamic flow regime, and test setups for these applications are often complex and difficult to operate (*138*, *140*, *143*).

In our study (**Chapter 5**), a simplified and modular bioreactor system for TEVGs was demonstrated. This system, which can be partially assembled from common laboratory equipment, allows the testing of a broad spectrum of *in situ* regenerative processes. Here, EPC homing and endothelialisation were simulated using fibronectin- and decorin-coated electrospun TPCU vascular grafts. The fibronectin coating was shown to be effective in increasing the attachment of EPCs and to promote endothelialisation *in vitro*. It has also been shown that this bioreactor system can be used to study a much wider range of regenerative processes and to demonstrate the efficacy of biological functionalisations otherwise improbable with static cell culture tests.

6.4 Conclusion

The field of electrospinning continues to evolve. Although the electrospinning process itself is well established, there is still considerable potential for innovation. This potential is particularly

evident in areas such as the development of novel scaffold designs, improvements in synthesis and processing techniques, and the continuous improvement of *in vitro* models. In addition, the emergence of green chemistry has further increased the attractiveness of using polyurethane in electrospun grafts by addressing the major limitations of this versatile polymer.

A lot of research is also devoted to advance the incorporation of biological materials. However, the first two chapters of these thesis may leave a bitter aftertaste when it comes to the use of natural materials as the primary scaffold material in electrospinning. A closer look at the studies in which collagen was electrospun suggests that electrospinning of natural ECM components doesn't seem to be quite the biomedical panacea it was once claimed to be. In fact, collagen gets biochemically compromised during currently established electrospinning processes, making it, so far, little more than 'just an expensive way to create gelatin' (93).

Though this tongue-in-cheek statement may be underselling the use of collagen in electrospun grafts. This work has suggested that leaving out ethanol of the equation could potentially preserve the denaturation temperature, thus allowing collagen to be electrospun without denaturation. Secondly, the studies under dynamic flow conditions demonstrated that surface adhesion proteins do play an important role in regenerative processes. Although the improved biocompatibility of collagen-coated NIPUs may have been negligible in static in vitro tests, dynamic simulations of endothelialisation processes under flow revealed the added benefit of biofunctionalisation. In light of these observations, it seems reasonable to use polyurethane – or any other biocompatible synthetic polymer – as a starting point for electrospinning, and then add biological components where necessary.

Bibliography

(1) World Health Organization Ageing and health https://www.who.int/news-room/fact-sheets/detail/ageing-and-health (accessed 22nd Nov. 2022).

(2) Caliskan, E., De Souza, D. R., Boening, A., Liakopoulos, O. J., Choi, Y.-H., Pepper, J., Gibson, C. M., Perrault, L. P., Wolf, R. K., Kim, K.-B. et al. (2020). Saphenous vein grafts in contemporary coronary artery bypass graft surgery. *Nature Reviews Cardiology* **17**, 155–169.

(3) Vacanti, J. P., Otte, J.-B. and Wertheim, J. A. In *Regenerative Medicine Applications in Organ Transplantation*, Orlando, G., Lerut, J., Soker, S. and Stratta, R. J., Eds.; Academic Press: Boston, 2014, pp 1–15.

(4) Mao, A. S. and Mooney, D. J. (2015). Regenerative medicine: Current therapies and future directions. *Proceedings of the National Academy of Sciences* **112**, 14452–14459.

(5) **Visser, D.**, Bakhshi, H., Rogg, K., Fuhrmann, E., Wieland, F., Schenke-Layland, K., Meyer, W. and Hartmann, H. (2022). Green Chemistry for Biomimetic Materials: Synthesis and Electrospinning of High-Molecular-Weight Polycarbonate-Based Nonisocyanate Polyurethanes. *ACS Omega* **7**, 39772–39781.

(6) **Visser, D.**, Rogg, K., Fuhrmann, E., Marzi, J., Schenke-Layland, K. and Hartmann, H. (2023). Electrospinning of collagen: Enzymatic and spectroscopical analyses reveal solvent-independent disruption of the triple-helical structure. *Journal of Materials Chemistry B* **11**, 2207–2218.

(7) Daum, R., **Visser, D.**, Wild, C., Kutuzova, L., Schneider, M., Lorenz, G., Weiss, M., Hinderer, S., Stock, U. A., Seifert, M. and Schenke-Layland, K. (2020). Fibronectin adsorption on electrospun synthetic vascular grafts attracts endothelial progenitor cells and promotes endothelialization in dynamic in vitro culture. *Cells* **9**, 778.

(8) Marieb, E. N. and Hoehn, K., *Human anatomy & physiology*; Pearson education: 2007.

(9) Frantz, C., Stewart, K. M. and Weaver, V. M. (2010). The extracellular matrix at a glance. *Journal of cell science* **123**, 4195–4200.

(10) Järveläinen, H., Sainio, A., Koulu, M., Wight, T. N. and Penttinen, R. (2009). Extracellular matrix molecules: potential targets in pharmacotherapy. *Pharmacological reviews* **61**, 198–223.

(11) Nathan, C. and Sporn, M. (1991). Cytokines in context. *The Journal of cell biology* **113**, 981–986.

(12) Border, W. A. and Noble, N. A. (1994). Transforming growth factor β in tissue fibrosis. *New England journal of medicine* **331**, 1286–1292.

(13) Eyre, D. R. (1980). Collagen: molecular diversity in the body's protein scaffold. *Science* **207**, 1315–1322.

(14) Linsenmayer, T. In *Cell biology of extracellular matrix*, Hay, E. D., Ed.; Springer: 1991, pp 7–44.

(15) Shoulders, M. D. and Raines, R. T. (2009). Collagen structure and stability. *Annu Rev Biochem* **78**, 929–58.

(*16*) Kielty, C. M. and Grant, M. E. (2002). The collagen family: structure, assembly, and organization in the extracellular matrix. *Connective tissue and its heritable disorders: molecular, genetic, and medical aspects*, 159–221.

(*17*) Kühn, K. In Mayne, R. and Burgeson, R., Eds.; Structure and Function of Collagen Types, Vol. 5, 1987.

(*18*) Rich, A. and Crick, F. (1961). The molecular structure of collagen. *Journal of molecular biology* **3**, 483–IN4.

(*19*) Bella, J., Eaton, M., Brodsky, B. and Berman, H. M. (1994). Crystal and molecular structure of a collagen-like peptide at 1.9 Å resolution. *Science* **266**, 75–81.

(*20*) Trelstad, R. L. In *Immunochemistry of the extracellular matrix*, Furthmayr, H., Ed.; CRC Press Boca Raton, FL: 1982; Vol. 1, pp 32–39.

(*21*) Engel, J. (1962). Investigation of the denaturation and renaturation of soluble collagen by light scattering. *Archives of Biochemistry and Biophysics* **97**, 150–158.

(*22*) Frushour, B. G. and Koenig, J. L. (1975). Raman scattering of collagen, gelatin, and elastin. *Biopolymers: Original Research on Biomolecules* **14**, 379–391.

(*23*) Meyer, M. (2019). Processing of collagen based biomaterials and the resulting materials properties. *Biomed Eng Online* **18**, 24.

(*24*) Fayon, A., Menu, P. and El Omar, R. (2021). Cellularized small-caliber tissue-engineered vascular grafts: looking for the ultimate gold standard. *NPJ Regenerative medicine* **6**, 46.

(*25*) Schmidt, A. H. (2021). Autologous bone graft: Is it still the gold standard? *Injury* **52**, S18–S22.

(*26*) Langer, R. and Vacanti, J. P. (1993). Tissue engineering. *Science* **260**, 920–926.

(*27*) Kelleher, C. M. and Vacanti, J. P. (2010). Engineering extracellular matrix through nano-technology. *J. R. Soc. Interface* **7**, S717–29.

(*28*) Williams, D. F. (2008). On the mechanisms of biocompatibility. *Biomaterials* **29**, 2941–2953.

(*29*) Williams, D. F. (2006). To engineer is to create: the link between engineering and regeneration. *Trends Biotechnol.* **24**, 4–8.

(*30*) Sionkowska, A. (2011). Current research on the blends of natural and synthetic polymers as new biomaterials. *Progress in polymer science* **36**, 1254–1276.

(*31*) Gunatillake, P. A., Adhikari, R. and Gadegaard, N. (2003). Biodegradable synthetic polymers for tissue engineering. *European Cells and Materials* **5**, 1–16.

(*32*) Nair, L. S. and Laurencin, C. T. (2007). Biodegradable polymers as biomaterials. *Progress in polymer science* **32**, 762–798.

(*33*) Lendlein, A. and Kelch, S. (2002). Shape-memory polymers. *Angewandte Chemie International Edition* **41**, 2034–2057.

(*34*) Brannigan, R. P. and Dove, A. P. (2017). Synthesis, properties and biomedical applications of hydrolytically degradable materials based on aliphatic polyesters and polycarbonates. *Biomaterials science* **5**, 9–21.

(*35*) Lamba, N. M. K., Woodhouse, K. A. and Cooper, S. L. In *Polyurethanes in Biomedical Applications*, 1st ed.; CRC Press: 2017, pp 5–25.

(*36*) Kucinska-Lipka, J., Gubanska, I., Janik, H. and Sienkiewicz, M. (2015). Fabrication of polyurethane and polyurethane based composite fibres by the electrospinning technique for soft tissue engineering of cardiovascular system. *Mater Sci Eng C Mater Biol Appl* **46**, 166–76.

(*37*) Santerre, J., Labow, R., Duguay, D., Erfle, D. and Adams, G. (1994). Biodegradation evaluation of polyether and polyester-urethanes with oxidative and hydrolytic enzymes. *Journal of biomedical materials research* **28**, 1187–1199.

(*38*) Santerre, J., Woodhouse, K., Laroche, G. and Labow, R. (2005). Understanding the bio-degradation of polyurethanes: from classical implants to tissue engineering materials. *Biomaterials* **26**, 7457–7470.

(*39*) Khan, I., Smith, N., Jones, E., Finch, D. S. and Cameron, R. E. (2005). Analysis and evaluation of a biomedical polycarbonate urethane tested in an in vitro study and an ovine arthroplasty model. Part I: Materials selection and evaluation. *Biomaterials* **26**, 621–631.

(*40*) Pinchuk, L. (1995). A review of the biostability and carcinogenicity of polyurethanes in medicine and the new generation of'biostable'polyurethanes. *Journal of Biomaterials Science, Polymer Edition* **6**, 225–267.

(*41*) Parins, D. J., McCoy, K. D., Horvath, N. and Olson, R. W. In *Corrosion and Degradation of Implant Materials: Second Symposium*, 1985, pp 322–339.

(*42*) Lockey, J. E., Redlich, C. A., Streicher, R., Pfahles-Hutchens, A., Hakkinen, P. J., Ellison, G. L., Harber, P., Utell, M., Holland, J. and Comai, A. (2015). Isocyanates and human health: Multi-stakeholder information needs and research priorities. *Journal of occupational and environmental medicine/American College of Occupational and Environmental Medicine* **57**, 44.

(*43*) Redlich, C., Bello, D. and Wisnewski, A. In *Environmental and occupational medicine*, Rom, W. and Markowitz, S., Eds., 4th; Lippincott Williams & Wilkins: 2007, pp 502–515.

(*44*) Allport, D. C., Gilbert, D. S. and Outterside, S., *MDI and TDI: safety, health and the environment: a source book and practical guide*; John Wiley & Sons: 2003.

(*45*) Aduba, D. C., Zhang, K., Kanitkar, A., Sirrine, J. M., Verbridge, S. S. and Long, T. E. (2018). Electrospinning of plant oil-based, non-isocyanate polyurethanes for biomedical applications. *Journal of Applied Polymer Science* **135**.

(*46*) Pramanik, S. K., Sreedharan, S., Singh, H., Khan, M., Tiwari, K., Shiras, A., Smythe, C., Thomas, J. A. and Das, A. (2018). Mitochondria targeting non-isocyanate-based polyureth-ane nanocapsules for enzyme-triggered drug release. *Bioconjugate Chemistry* **29**, 3532–3543.

(*47*) Rahmany, M. B. and Van Dyke, M. (2013). Biomimetic approaches to modulate cellular adhesion in biomaterials: A review. *Acta biomaterialia* **9**, 5431–5437.

(*48*) Seitz, T., Noonan, K. D., Hench, L. L. and Noonan, N. E. (1982). Effect of fibronectin on the adhesion of an established cell line to a surface reactive biomaterial. *Journal of biomedical materials research* **16**, 195–207.

(*49*)   Lewandowska, K., Pergament, E., Sukenik, C. N. and Culp, L. A. (1992). Cell-type-specific adhesion mechanisms mediated by fibronectin adsorbed to chemically derivatized substrata. *Journal of biomedical materials research* **26**, 1343–1363.

(*50*)   Tallawi, M., Rosellini, E., Barbani, N., Cascone, M. G., Rai, R., Saint-Pierre, G. and Boccaccini, A. R. (2015). Strategies for the chemical and biological functionalization of scaffolds for cardiac tissue engineering: a review. *J R Soc Interface* **12**, 20150254.

(*51*)   Murray, M. M., Rice, K., Wright, R. and Spector, M. (2003). The effect of selected growth factors on human anterior cruciate ligament cell interactions with a three-dimensional collagen-GAG scaffold. *Journal of orthopaedic research* **21**, 238–244.

(*52*)   Reneker, D. H. and Yarin, A. L. (2008). Electrospinning jets and polymer nanofibers. *Polymer* **49**, 2387–2425.

(*53*)   Reneker, D. H. and Fong, H. In *Polymeric nanofibers*, Reneker, D. H. and Fong, H., Eds.; ACS Publications: 2006, pp 1–6.

(*54*)   Formhals, A. Process and apparatus for preparing artificial threads, US Patent 1 975 504, 1934.

(*55*)   Zeleny, J. (1917). Instability of Electrified Liquid Surfaces. *Phys. Rev.* **10**, 1–6.

(*56*)   Doshi, J. and Reneker, D. H. (1995). Electrospinning process and applications of electrospun fibers. *Journal of Electrostatics* **35**, 151–160.

(*57*)   Schiffman, J. D. and Schauer, C. L. (2008). A review: electrospinning of biopolymer nanofibers and their applications. *Polymer reviews* **48**, 317–352.

(*58*)   Khorshidi, S., Solouk, A., Mirzadeh, H., Mazinani, S., Lagaron, J. M., Sharifi, S. and Ramakrishna, S. (2016). A review of key challenges of electrospun scaffolds for tissue-engineering applications. *Journal of tissue engineering and regenerative medicine* **10**, 715–738.

(*59*)   Taylor, G. I. (1964). Disintegration of water drops in an electric field. *Proceedings of the Royal Society of London. Series A. Mathematical and Physical Sciences* **280**, 383–397.

(*60*)   Reneker, D., Yarin, A., Zussman, E. and Xu, H. In Aref, H. and van der Giessen, E., Eds.; Advances in Applied Mechanics, Vol. 41; Elsevier: 2007, pp 43–346.

(*61*)   Taylor, G. I. (1969). Electrically driven jets. *Proceedings of the Royal Society of London. A. Mathematical and Physical Sciences* **313**, 453–475.

(*62*)   Putti, M., Simonet, M., Solberg, R. and Peters, G. W. M. (2015). Electrospinning poly(ϵ-caprolactone) under controlled environmental conditions: Influence on fiber morphology and orientation. *Polymer* **63**, 189–195.

(*63*)   Li, D., Wang, Y. and Xia, Y. (2003). Electrospinning of polymeric and ceramic nanofibers as uniaxially aligned arrays. *Nano letters* **3**, 1167–1171.

(*64*)   Yang, D., Zhang, J., Zhang, J. and Nie, J. (2008). Aligned electrospun nanofibers induced by magnetic field. *Journal of applied polymer science* **110**, 3368–3372.

(*65*)   Theron, A., Zussman, E. and Yarin, A. (2001). Electrostatic field-assisted alignment of electrospun nanofibres. *Nanotechnology* **12**, 384.

(66) Whited, B. M. and Rylander, M. N. (2014). The influence of electrospun scaffold topography on endothelial cell morphology, alignment, and adhesion in response to fluid flow. *Biotechnology and bioengineering* **111**, 184–195.

(67) Teo, W. E. and Ramakrishna, S. (2006). A review on electrospinning design and nanofibre assemblies. *Nanotechnology* **17**, R89.

(68) Ju, Y. M., Choi, J. S., Atala, A., Yoo, J. J. and Lee, S. J. (2010). Bilayered scaffold for engineering cellularized blood vessels. *Biomaterials* **31**, 4313–21.

(69) Wong, S.-C., Baji, A. and Leng, S. (2008). Effect of fiber diameter on tensile properties of electrospun poly (ε-caprolactone). *Polymer* **49**, 4713–4722.

(70) Matthews, J. A., Wnek, G. E., Simpson, D. G. and Bowlin, G. L. (2002). Electrospinning of Collagen Nanofibers. *Biomacromolecules* **3**, 232–238.

(71) McClure, M., Sell, S., Ayres, C., Simpson, D. and Bowlin, G. (2009). Electrospinning-aligned and random polydioxanone–polycaprolactone–silk fibroin-blended scaffolds: geometry for a vascular matrix. *Biomedical Materials* **4**, 055010.

(72) Xue, J., Wu, T., Dai, Y. and Xia, Y. (2019). Electrospinning and Electrospun Nanofibers: Methods, Materials, and Applications. *Chemical Reviews* **119**, 5298–5415.

(73) Dong, Y., Liao, S., Ngiam, M., Chan, C. K. and Ramakrishna, S. (2009). Degradation behaviors of electrospun resorbable polyester nanofibers. *Tissue Engineering - Part B: Reviews* **15**, 333–351.

(74) Sill, T. J. and von Recum, H. A. (2008). Electrospinning: Applications in drug delivery and tissue engineering. *Biomaterials* **29**, 1989–2006.

(75) Wu, H., Fan, J., Chu, C.-C. and Wu, J. (2010). Electrospinning of small diameter 3-D nanofibrous tubular scaffolds with controllable nanofiber orientations for vascular grafts. *Journal of Materials Science: Materials in Medicine* **21**, 3207–3215.

(76) Phipps, M. C., Clem, W. C., Grunda, J. M., Clines, G. A. and Bellis, S. L. (2012). Increasing the pore sizes of bone-mimetic electrospun scaffolds comprised of polycaprolactone, collagen I and hydroxyapatite to enhance cell infiltration. *Biomaterials* **33**, 524–534.

(77) Caracciolo, P. C., Thomas, V., Vohra, Y. K., Buffa, F. and Abraham, G. A. (2009). Electrospinning of novel biodegradable poly(ester urethane)s and poly(ester urethane urea)s for soft tissue-engineering applications. *J. Mater. Sci. Mater. Med.* **20**, 2129–2137.

(78) Kidoaki, S., Kwon, I. K. and Matsuda, T. (2005). Mesoscopic spatial designs of nano-and microfiber meshes for tissue-engineering matrix and scaffold based on newly devised multilayering and mixing electrospinning techniques. *Biomaterials* **26**, 37–46.

(79) Baudis, S., Ligon, S. C., Seidler, K., Weigel, G., Grasl, C., Bergmeister, H., Schima, H. and Liska, R. (2012). Hard-block degradable thermoplastic urethane-elastomers for electrospun vascular prostheses. *Journal of Polymer Science Part A: Polymer Chemistry* **50**, 1272–1280.

(80) Stankus, J. J., Guan, J., Fujimoto, K. and Wagner, W. R. (2006). Microintegrating smooth muscle cells into a biodegradable, elastomeric fiber matrix. *Biomaterials* **27**, 735–744.

(81) Amoroso, N. J., D'Amore, A., Hong, Y., Rivera, C. P., Sacks, M. S. and Wagner, W. R. (2012). Microstructural manipulation of electrospun scaffolds for specific bending stiffness for heart valve tissue engineering. *Acta Biomaterialia* **8**, 4268–4277.

(*82*) Puperi, D. S., Kishan, A., Punske, Z. E., Wu, Y., Cosgriff-Hernandez, E., West, J. L. and Grande-Allen, K. J. (2016). Electrospun polyurethane and hydrogel composite scaffolds as biomechanical mimics for aortic valve tissue engineering. *ACS Biomaterials Science and Engineering* **2**, 1546–1558.

(*83*) Motiwale, S., Russell, M. D., Conroy, O., Carruth, J., Wancura, M., Robinson, A., Cosgriff-Hernandez, E. and Sacks, M. S. (2022). Anisotropic elastic behavior of a hydrogel-coated electrospun polyurethane: Suitability for heart valve leaflets. *Journal of the Mechanical Behavior of Biomedical Materials* **125**.

(*84*) Şenel Ayaz, H. G., Perets, A., Ayaz, H., Gilroy, K. D., Govindaraj, M., Brookstein, D. and Lelkes, P. I. (2014). Textile-templated electrospun anisotropic scaffolds for regenerative cardiac tissue engineering. *Biomaterials* **35**, 8540–8552.

(*85*) D'Amore, A., Yoshizumi, T., Luketich, S. K., Wolf, M. T., Gu, X., Cammarata, M., Hoff, R., Badylak, S. F. and Wagner, W. R. (2016). Bi-layered polyurethane – Extracellular matrix cardiac patch improves ischemic ventricular wall remodeling in a rat model. *Biomaterials* **107**, 1–14.

(*86*) Tao, Z. W., Jarrell, D. K., Robinson, A., Cosgriff-Hernandez, E. M. and Jacot, J. G. (2021). A prevascularized polyurethane-reinforced fibrin patch improves regenerative remodeling in a rat right ventricle replacement model. *Advanced Healthcare Materials* **10**.

(*87*) Silver, F. H., Freeman, J. W. and Seehra, G. P. (2003). Collagen self-assembly and the development of tendon mechanical properties. *Journal of biomechanics* **36**, 1529–1553.

(*88*) Telemeco, T. A., Ayres, C., Bowlin, G. L., Wnek, G. E., Boland, E. D., Cohen, N., Baumgarten, C. M., Mathews, J. and Simpson, D. G. (2005). Regulation of cellular infiltration into tissue engineering scaffolds composed of submicron diameter fibrils produced by electrospinning. *Acta Biomaterialia* **1**, 377–385.

(*89*) Huang, L., Nagapudi, K., Apkarian, R. P. and Chaikof, E. L. (2001). Engineered collagen-PEO nanofibers and fabrics. *Journal of biomaterials science. Polymer edition* **12**, 979–993.

(*90*) Heydarkhan-Hagvall, S., Schenke-Layland, K., Dhanasopon, A. P., Rofail, F., Smith, H., Wu, B. M., Shemin, R., Beygui, R. E. and MacLellan, W. R. (2008). Three-dimensional electrospun ECM-based hybrid scaffolds for cardiovascular tissue engineering. *Biomaterials* **29**, 2907–14.

(*91*) Hong, D.-P., Hoshino, M., Kuboi, R. and Goto, Y. (1999). Clustering of Fluorine-Substituted Alcohols as a Factor Responsible for Their Marked Effects on Proteins and Peptides. *Journal of the American Chemical Society* **121**, 8427–8433.

(*92*) Kundu, A. and Kishore, N. (2004). 1, 1, 1, 3, 3, 3-hexafluoroisopropanol induced thermal unfolding and molten globule state of bovine α-lactalbumin: Calorimetric and spectroscopic studies. *Biopolymers: Original Research on Biomolecules* **73**, 405–420.

(*93*) Zeugolis, D. I., Khew, S. T., Yew, E. S., Ekaputra, A. K., Tong, Y. W., Yung, L. Y., Hutmacher, D. W., Sheppard, C. and Raghunath, M. (2008). Electro-spinning of pure collagen nano-fibres - just an expensive way to make gelatin? *Biomaterials* **29**, 2293–305.

(*94*) Castilla-Casadiego, D. A., Rivera-Martínez, C. A., Quiñones-Colón, B. A. and Almodóvar, J. In *Electrospun Biomaterials and Related Technologies*, 2017, pp 21–55.

(*95*)   Montalbano, G., Tomasina, C., Fiorilli, S., Camarero-Espinosa, S., Vitale-Brovarone, C. and Moroni, L. (2021). Biomimetic Scaffolds Obtained by Electrospinning of Collagen-Based Materials: Strategies to Hinder the Protein Denaturation. *Materials (Basel)* **14**.

(*96*)   Kazanci, M. (2014). Solvent and temperature effects on folding of electrospun collagen nanofibers. *Materials Letters* **130**, 223–226.

(*97*)   Elamparithi, A., Punnoose, A. M. and Kuruvilla, S. (2016). Electrospun type 1 collagen matrices preserving native ultrastructure using benign binary solvent for cardiac tissue engineering. *Artif Cells Nanomed Biotechnol* **44**, 1318–25.

(*98*)   Liu, T., Teng, W. K., Chan, B. P. and Chew, S. Y. (2010). Photochemical crosslinked electrospun collagen nanofibers: synthesis, characterization and neural stem cell interactions. *J Biomed Mater Res A* **95**, 276–82.

(*99*)   Burck, J., Heissler, S., Geckle, U., Ardakani, M. F., Schneider, R., Ulrich, A. S. and Kazanci, M. (2013). Resemblance of electrospun collagen nanofibers to their native structure. *Langmuir* **29**, 1562–72.

(*100*) Baek, J., Sovani, S., Glembotski, N. E., Du, J., Jin, S., Grogan, S. P. and D'Lima, D. D. (2016). Repair of Avascular Meniscus Tears with Electrospun Collagen Scaffolds Seeded with Human Cells. *Tissue Eng Part A* **22**, 436–48.

(*101*) Dong, B., Arnoult, O., Smith, M. E. and Wnek, G. E. (2009). Electrospinning of collagen nanofiber scaffolds from benign solvents. *Macromol Rapid Commun* **30**, 539–42.

(*102*) Dems, D., Rodrigues da Silva, J., Hélary, C., Wien, F., Marchand, M., Debons, N., Muller, L., Chen, Y., Schanne-Klein, M.-C., Laberty-Robert, C., Krins, N. and Aimé, C. (2020). Native Collagen: Electrospinning of Pure, Cross-Linker-Free, Self-Supported Membrane. *ACS Applied Bio Materials* **3**, 2948–2957.

(*103*) Jiang, Q., Reddy, N., Zhang, S., Roscioli, N. and Yang, Y. (2012). Water-stable electrospun collagen fibers from a non-toxic solvent and crosslinking system. *J Biomed Mater Res A* **101**, 1237–47.

(*104*) Castilla-Casadiego, D. A., Ramos-Avilez, H. V., Herrera-Posada, S., Calcagno, B., Loyo, L., Shipmon, J., Acevedo, A., Quintana, A. and Almodovar, J. (2016). Engineering of a Stable Collagen Nanofibrous Scaffold with Tunable Fiber Diameter, Alignment, and Mechanical Properties. *Macromolecular Materials and Engineering* **301**, 1064–1075.

(*105*) Griffiths, D. J. (2021). Introduction to electrodynamics. 382–435.

(*106*) Johnson Jr, W. C. (1988). Secondary structure of proteins through circular dichroism spectroscopy. *Annual review of biophysics and biophysical chemistry* **17**, 145–166.

(*107*) Berova, N., Ellestad, G. A. and Harada, N. In *Comprehensive Chiroptical Spectroscopy, Volume 2: Applications in Stereochemical Analysis of Synthetic Compounds, Natural Products, and Biomolecules*, Berova, N., Polavarapu, P., Nakanishi, K. and Woody, R., Eds.; Elsevier Ltd: 2010; Vol. 2, pp 499–544.

(*108*) Yang, L., Fitie, C. F., van der Werf, K. O., Bennink, M. L., Dijkstra, P. J. and Feijen, J. (2008). Mechanical properties of single electrospun collagen type I fibers. *Biomaterials* **29**, 955–62.

(*109*) Smith, E. and Dent, G., *Modern Raman spectroscopy: a practical approach*; John Wiley & Sons: 2019.

(*110*) Larkin, P., *Infrared and Raman spectroscopy: principles and spectral interpretation*; Elsevier: 2017.

(*111*) McCreery, R. L., *Raman spectroscopy for chemical analysis*; John Wiley & Sons: 2005.

(*112*) De Beer, T., Burggraeve, A., Fonteyne, M., Saerens, L., Remon, J. P. and Vervaet, C. (2011). Near infrared and Raman spectroscopy for the in-process monitoring of pharmaceutical production processes. *International journal of pharmaceutics* **417**, 32–47.

(*113*) Brauchle, E., Kasper, J., Daum, R., Schierbaum, N., Falch, C., Kirschniak, A., Schäffer, T. E. and Schenke-Layland, K. (2018). Biomechanical and biomolecular characterization of extracellular matrix structures in human colon carcinomas. *Matrix Biology* **68**, 180–193.

(*114*) Bergholt, M. S., Serio, A. and Albro, M. B. (2019). Raman Spectroscopy: Guiding Light for the Extracellular Matrix. *Front Bioeng Biotechnol* **7**, 303.

(*115*) Schroeder, D., *An Introduction to Thermal Physics*; Oxford University Press: 2021.

(*116*) Schmid, T. and Dariz, P. (2019). Raman microspectroscopic imaging of binder remnants in historical mortars reveals processing conditions. *Heritage* **2**, 1662–1683.

(*117*) Marzi, J., Brauchle, E. M., Schenke-Layland, K. and Rolle, M. W. (2019). Non-invasive functional molecular phenotyping of human smooth muscle cells utilized in cardiovascular tissue engineering. *Acta biomaterialia* **89**, 193–205.

(*118*) Rygula, A., Majzner, K., Marzec, K. M., Kaczor, A., Pilarczyk, M. and Baranska, M. (2013). Raman spectroscopy of proteins: a review. *Journal of Raman Spectroscopy* **44**, 1061–1076.

(*119*) Abdi, H. and Williams, L. J. (2010). Principal component analysis. *Wiley interdisciplinary reviews: computational statistics* **2**, 433–459.

(*120*) Lever, J., Krzywinski, M. and Altman, N. (2017). Points of significance: Principal component analysis. *Nature methods* **14**, 641–643.

(*121*) Trefethen, L. and Bau, D., *Numerical Linear Algebra*; Other Titles in Applied Mathematics; Society for Industrial and Applied Mathematics: 1997.

(*122*) Walton, A., Deveney, M. and Koenig, J. (1970). Raman spectroscopy of calcified tissue. *Calcified tissue research* **6**, 162–167.

(*123*) Ashton, L. and Blanch, E. W. (2010). pH-induced conformational transitions in α-lactalbumin investigated with two-dimensional Raman correlation variance plots and moving windows. *Journal of Molecular Structure* **974**, 132–138.

(*124*) Yu, T.-J., Lippert, J. L. and Peticolas, W. L. (1973). Laser Raman studies of conformational variations of poly-L-lysine. *Biopolymers: Original Research on Biomolecules* **12**, 2161–2176.

(*125*) Lippert, J. L., Tyminski, D. and Desmeules, P. J. (1976). Determination of the secondary structure of proteins by laser Raman spectroscopy. *Journal of the American Chemical Society* **98**, 7075–7080.

(*126*) *Treatise on Collagen*; Ramachandran, G., Ed.; Academic Press, New York: 1967.

(*127*) Roth, S. and Freund, I. (1981). Optical second-harmonic scattering in rat-tail tendon. *Biopolymers: Original Research on Biomolecules* **20**, 1271–1290.

(*128*) Freund, I., Deutsch, M. and Sprecher, A. (1986). Connective tissue polarity. Optical second-harmonic microscopy, crossed-beam summation, and small-angle scattering in rat-tail tendon. *Biophysical journal* **50**, 693–712.

(129) *Nonlinear Optics: A Lecture Note and Reprint Volume*; Bloembergen, N., Ed.; New York: W.A. Benjamin: 1965.

(130) Roth, S. and Freund, I. (1979). Second harmonic generation in collagen. *The Journal of chemical physics* **70**, 1637–1643.

(131) Theodossiou, T. A., Thrasivoulou, C., Ekwobi, C. and Becker, D. L. (2006). Second harmonic generation confocal microscopy of collagen type I from rat tendon cryosections. *Biophysical journal* **91**, 4665–4677.

(132) Barron, V., Lyons, E., Stenson-Cox, C., McHugh, P. and Pandit, A. (2003). Bioreactors for cardiovascular cell and tissue growth: a review. *Annals of biomedical engineering* **31**, 1017–1030.

(133) Pörtner, R., Nagel-Heyer, S., Goepfert, C., Adamietz, P. and Meenen, N. M. (2005). Bioreactor design for tissue engineering. *Journal of bioscience and bioengineering* **100**, 235–245.

(134) Peroglio, M., Gaspar, D., Zeugolis, D. I. and Alini, M. (2018). Relevance of bioreactors and whole tissue cultures for the translation of new therapies to humans. *Journal of Orthopaedic Research®* **36**, 10–21.

(135) Martin, I., Wendt, D. and Heberer, M. (2004). The role of bioreactors in tissue engineering. *TRENDS in Biotechnology* **22**, 80–86.

(136) Hinderer, S., Seifert, J., Votteler, M., Shen, N., Rheinlaender, J., Schäffer, T. E. and Schenke-Layland, K. (2014). Engineering of a bio-functionalized hybrid off-the-shelf heart valve. *Biomaterials* **35**, 2130–2139.

(137) Mela, P., Hinderer, S., Kandail, H. S., Bouten, C. V. and Smits, A. I. In *Principles of heart valve engineering*; Elsevier: 2019, pp 123–176.

(138) Maschhoff, P., Heene, S., Lavrentieva, A., Hentrop, T., Leibold, C., Wahalla, M.-N., Stanislawski, N., Blume, H., Scheper, T. and Blume, C. (2017). An intelligent bioreactor system for the cultivation of a bioartificial vascular graft. *Engineering in Life Sciences* **17**, 567–578.

(139) Tosun, Z. and McFetridge, P. S. (2013). Improved recellularization of ex vivo vascular scaffolds using directed transport gradients to modulate ECM remodeling. *Biotechnology and bioengineering* **110**, 2035–2045.

(140) Diamantouros, S. E., Hurtado-Aguilar, L. G., Schmitz-Rode, T., Mela, P. and Jockenhoevel, S. (2013). Pulsatile perfusion bioreactor system for durability testing and compliance estimation of tissue engineered vascular grafts. *Annals of biomedical engineering* **41**, 1979–1989.

(141) Engbers-Buijtenhuijs, P., Buttafoco, L., Poot, A. A., Dijkstra, P. J., de Vos, R. A., Lotus, M. T., Geelkerken, R. H., Vermes, I., Feijen, J. et al. (2006). Biological characterisation of vascular grafts cultured in a bioreactor. *Biomaterials* **27**, 2390–2397.

(142) Melchiorri, A. J., Bracaglia, L. G., Kimerer, L. K., Hibino, N. and Fisher, J. P. (2016). In vitro endothelialization of biodegradable vascular grafts via endothelial progenitor cell seeding and maturation in a tubular perfusion system bioreactor. *Tissue Engineering Part C: Methods* **22**, 663–670.

(143) Piola, M., Prandi, F., Bono, N., Soncini, M., Penza, E., Agrifoglio, M., Polvani, G., Pesce, M. and Fiore, G. B. (2016). A compact and automated ex vivo vessel culture system for the pulsatile pressure conditioning of human saphenous veins. *Journal of tissue engineering and regenerative medicine* **10**, E204–E215.

(144) Wolf, F., Rojas González, D. M., Steinseifer, U., Obdenbusch, M., Herfs, W., Brecher, C., Jockenhoevel, S., Mela, P. and Schmitz-Rode, T. (2018). VascuTrainer: a mobile and disposable bioreactor system for the conditioning of tissue-engineered vascular grafts. *Annals of Biomedical Engineering* **46**, 616–626.

(145) ISO 10993-5:2009 Biological evaluation of medical devices – Part 5: Tests for in vitro cytotoxicity, Standard, Geneva, CH: International Organization for Standardization, 2009.

(146) ISO 10993-12:2021 Biological evaluation of medical devices – Part 5: Tests for in vitro cytotoxicity, Standard, Geneva, CH: International Organization for Standardization, 2021.

(147) Gerritsen, H., Draaijer, A., Van Den Heuvel, D. and Agronskaia, A. In *Handbook Of Biological Confocal Microscopy*, Pawley, J., Ed., 2006; Chapter 27, pp 519–534.

(148) Blacker, T. S., Mann, Z. F., Gale, J. E., Ziegler, M., Bain, A. J., Szabadkai, G. and Duchen, M. R. (2014). Separating NADH and NADPH fluorescence in live cells and tissues using FLIM. *Nature Communications* **5**, 3936.

(149) Skala, M. C., Riching, K. M., Bird, D. K., Gendron-Fitzpatrick, A., Eickhoff, J., Eliceiri, K. W., Keely, P. J. and Ramanujam, N. (2007). In vivo multiphoton fluorescence lifetime imaging of protein-bound and free nicotinamide adenine dinucleotide in normal and precancerous epithelia. *Journal of biomedical optics* **12**, 024014–024014.

(150) Nakabayashi, T., Wang, H.-P., Kinjo, M. and Ohta, N. (2008). Application of fluorescence lifetime imaging of enhanced green fluorescent protein to intracellular pH measurements. *Photochemical & photobiological sciences* **7**, 668–670.

(151) Kolenc, O. I. and Quinn, K. P. (2019). Evaluating Cell Metabolism Through Autofluorescence Imaging of NAD(P)H and FAD. *Antioxid Redox Signal* **30**, 875–889.

(152) Chance, B. (1952). Spectra and reaction kinetics of respiratory pigments of homogenized and intact cells. *Nature* **169**, 215–221.

(153) Chance, B., Cohen, P., Jobsis, F. and Schoener, B. (1962). Intracellular Oxidation-Reduction States in Vivo: The microfluorometry of pyridine nucleotide gives a continuous measurement of the oxidation state. *Science* **137**, 499–508.

(154) Chance, B., Schoener, B., Oshino, R., Itshak, F. and Nakase, Y. (1979). Oxidation-reduction ratio studies of mitochondria in freeze-trapped samples. NADH and flavoprotein fluorescence signals. *Journal of Biological Chemistry* **254**, 4764–4771.

(155) Christenson, E. M., Patel, S., Anderson, J. M. and Hiltner, A. (2006). Enzymatic degradation of poly (ether urethane) and poly (carbonate urethane) by cholesterol esterase. *Biomaterials* **27**, 3920–3926.

(156) Labow, R. S., Meek, E. and Santerre, J. P. (1999). Synthesis of cholesterol esterase by monocyte-derived macrophages: a potential role in the biodegradation of poly (urethane)s. *Journal of biomaterials applications* **13**, 187–205.

(*157*) Tang, Y., Labow, R. and Santerre, J. (2001). Enzyme-induced biodegradation of polycarbonate-polyurethanes: Dependence on hard-segment chemistry. *Journal of Biomedical Materials Research: An Official Journal of The Society for Biomaterials, The Japanese Society for Biomaterials, and The Australian Society for Biomaterials and the Korean Society for Biomaterials* **57**, 597–611.

(*158*) Ward, R., Anderson, J., McVenes, R. and Stokes, K. (2006). In vivo biostability of shore 55D polyether polyurethanes with and without fluoropolymer surface modifying endgroups. *Journal of Biomedical Materials Research Part A* **79**, 836–845.

(*159*) Wiggins, M. J., Wilkoff, B., Anderson, J. M. and Hiltner, A. (2001). Biodegradation of polyether polyurethane inner insulation in bipolar pacemaker leads. *Journal of Biomedical Materials Research: An Official Journal of The Society for Biomaterials, The Japanese Society for Biomaterials, and The Australian Society for Biomaterials and the Korean Society for Biomaterials* **58**, 302–307.

(*160*) Nath, M. (2008). Toxicity and the cardiovascular activity of organotin compounds: A review. *Applied Organometallic Chemistry* **22**, 598–612.

(*161*) Tanzi, M. C., Verderio, P., Lampugnani, M. G., Resnati, M., Dejana, E. and Sturani, E. (1994). Cytotoxicity of some catalysts commonly used in the synthesis of copolymers for biomedical use. *Journal of Materials Science: Materials in Medicine* **5**, 393–396.

(*162*) Zhao, Y., Xia, X., Zhou, J., Huang, Z., Lei, F., Tan, X., Yu, D., Zhu, Y. and Xu, H. (2021). Thermoresponsive behavior of non-isocyanate poly(hydroxyl)urethane for biomedical composite materials. *Advanced Composites and Hybrid Materials* **5**, 843–852.

(*163*) Ghasemlou, M., Daver, F., Ivanova, E. P. and Adhikari, B. (2020). Synthesis of green hybrid materials using starch and non-isocyanate polyurethanes. *Carbohydrate Polymers* **229**.

(*164*) Matsumoto, K., Kokai, A. and Endo, T. (2016). Synthesis and properties of novel poly-(hydroxyurethane) from difunctional alicyclic carbonate and m-xylylenediamine and its possibility as gas barrier materials. *Polymer Bulletin* **73**, 677–686.

(*165*) Shen, Z., Zhang, J., Zhu, W., Zheng, L., Li, C., Xiao, Y., Liu, J., Wu, S. and Zhang, B. (2018). A solvent-free route to non-isocyanate poly(carbonate urethane) with high molecular weight and competitive mechanical properties. *European Polymer Journal* **107**, 258–266.

(*166*) Deng, Y., Li, S., Zhao, J., Zhang, Z., Zhang, J. and Yang, W. (2014). Crystallizable and tough aliphatic thermoplastic poly(ether urethane)s synthesized through a non-isocyanate route. *RSC Advances* **4**, 43406–43414.

(*167*) Wołosz, D., Parzuchowski, P. G. and Świderska, A. (2021). Synthesis and characterization of the non-isocyanate poly(carbonate-urethane)s obtained via polycondensation route. *European Polymer Journal* **155**.

(*168*) Mi, H.-Y., Jing, X., Jacques, B. R., Turng, L.-S. and Peng, X.-F. (2013). Characterization and properties of electrospun thermoplastic polyurethane blend fibers: Effect of solution rheological properties on fiber formation. *Journal of Materials Research* **28**, 2339–2350.

(*169*) Veleirinho, B., Rei, M. F. and Lopes-Da-Silva, J. A. (2008). Solvent and concentration effects on the properties of electrospun poly(ethylene terephthalate) nanofiber mats. *Journal of Polymer Science Part B: Polymer Physics* **46**, 460–471.

(*170*) Filip, P. and Peer, P. (2019). Characterization of poly(ethylene oxide) nanofibers—mutual relations between mean diameter of electrospun nanofibers and solution characteristics. *Processes* **7**.

(*171*) Kim, K. W., Lee, K. H., Khil, M. S., Ho, Y. S. and Kim, H. Y. (2004). The effect of molecular weight and the linear velocity of drum surface on the properties of electrospun poly (ethylene terephthalate) nonwovens. *Fibers and Polymers* **5**, 122–127.

(*172*) Whitaker, D., Papadimitriou, J. M. and Walters, M. N. I. (1982). The mesothelium and its reactions: A review. *Critical Reviews in Toxicology* **10**, 81–144.

(*173*) Mutsaers, S. E. (2004). The mesothelial cell. *The International Journal of Biochemistry & Cell Biology* **36**, 9–16.

(*174*) Lachaud, C. C., Rodriguez-Campins, B., Hmadcha, A. and Soria, B. (2015). Use of mesothelial cells and biological matrices for tissue engineering of simple epithelium surrogates. *Frontiers in Bioengineering and Biotechnology* **3**, 117.

(*175*) Ren, X., Feng, Y., Guo, J., Wang, H., Li, Q., Yang, J., Hao, X., Lv, J., Ma, N. and Li, W. (2015). Surface modification and endothelialization of biomaterials as potential scaffolds for vascular tissue engineering applications. *Chemical Society Reviews* **44**, 5680–5742.

(*176*) Sizeland, K. H., Hofman, K. A., Hallett, I. C., Martin, D. E., Potgieter, J., Kirby, N. M., Hawley, A., Mudie, S. T., Ryan, T. M., Haverkamp, R. G. et al. (2018). Nanostructure of electrospun collagen: Do electrospun collagen fibers form native structures? *Materialia* **3**, 90–96.

(*177*) Sun, Y., Chen, W.-L., Lin, S.-J., Jee, S.-H., Chen, Y.-F., Lin, L.-C., So, P. T. C. and Dong, C.-Y. (2006). Investigating Mechanisms of Collagen Thermal Denaturation by High Resolution Second-Harmonic Generation Imaging. *Biophysical Journal* **91**, 2620–2625.

(*178*) Kim, B.-M., Eichler, J., Reiser, K. M., Rubenchik, A. M. and Da Silva, L. B. (2000). Collagen structure and nonlinear susceptibility: Effects of heat, glycation, and enzymatic cleavage on second harmonic signal intensity. *Lasers in Surgery and Medicine* **27**, 329–335.

(*179*) Stone, N., Kendall, C., Smith, J., Crow, P. and Barr, H. (2004). Raman spectroscopy for identification of epithelial cancers. *Faraday discussions* **126**, 141–157.

(*180*) Fields, M., Spencer, N., Dudhia, J. and McMillan, P. F. (2017). Structural changes in cartilage and collagen studied by high temperature Raman spectroscopy. *Biopolymers* **107**.

(*181*) Gopinath, A., Reddy, S. M., Madhan, B., Shanmguam, G. and Rao, J. R. (2014). Effect of aqueous ethanol on the triple helical structure of collagen. *Eur Biophys J* **43**, 643–52.

(*182*) Ercolani, E., Del Gaudio, C. and Bianco, A. (2015). Vascular tissue engineering of small-diameter blood vessels: reviewing the electrospinning approach. *Journal of tissue engineering and regenerative medicine* **9**, 861–888.

(*183*) Ravi, S., Qu, Z. and Chaikof, E. L. (2009). Polymeric materials for tissue engineering of arterial substitutes. *Vascular* **17**, 45–54.

(*184*) Isenberg, B. C., Williams, C. and Tranquillo, R. T. (2006). Small-diameter artificial arteries engineered in vitro. *Circulation research* **98**, 25–35.

(185) Rnjak-Kovacina, J., Wise, S. G., Li, Z., Maitz, P. K., Young, C. J., Wang, Y. and Weiss, A. S. (2011). Tailoring the porosity and pore size of electrospun synthetic human elastin scaffolds for dermal tissue engineering. *Biomaterials* **32**, 6729–6736.

(186) Laterreur, V., Ruel, J., Auger, F. A., Vallières, K., Tremblay, C., Lacroix, D., Tondreau, M., Bourget, J.-M. and Germain, L. (2014). Comparison of the direct burst pressure and the ring tensile test methods for mechanical characterization of tissue-engineered vascular substitutes. *Journal of the mechanical behavior of biomedical materials* **34**, 253–263.

(187) Stekelenburg, M., Rutten, M. C., Snoeckx, L. H. and Baaijens, F. P. (2009). Dynamic straining combined with fibrin gel cell seeding improves strength of tissue-engineered small-diameter vascular grafts. *Tissue Engineering Part A* **15**, 1081–1089.

(188) Visser, D. Creating a simplified and standardised bioreactor system for tissue-engineered vascular graft culturing and characterisation, MA thesis, Delft, The Netherlands: Delft University of Technology, 2018.

(189) Dewey, J., C. F., Bussolari, S. R., Gimbrone, J., M. A. and Davies, P. F. (1981). The Dynamic Response of Vascular Endothelial Cells to Fluid Shear Stress. *Journal of Biomechanical Engineering* **103**, 177–185.

(190) Inoguchi, H., Tanaka, T., Maehara, Y. and Matsuda, T. (2007). The effect of gradually graded shear stress on the morphological integrity of a huvec-seeded compliant small-diameter vascular graft. *Biomaterials* **28**, 486–495.

(191) Hinderer, S., Shen, N., Ringuette, L.-J., Hansmann, J., Reinhardt, D. P., Brucker, S. Y., Davis, E. C. and Schenke-Layland, K. (2015). In vitro elastogenesis: instructing human vascular smooth muscle cells to generate an elastic fiber-containing extracellular matrix scaffold. *Biomedical Materials* **10**, 034102.

(192) van den Akker, H. and Mudde, R., *Transport Phenomena – The Art of Balancing*, 1st ed.; Delft Academic Press: Delft, 2014.

(193) Caiado, F. and Dias, S. (2012). Endothelial progenitor cells and integrins: adhesive needs. *Fibrogenesis & tissue repair* **5**, 1–13.

(194) Raimondi, M. T., Boschetti, F., Falcone, L., Fiore, G. B., Remuzzi, A., Marinoni, E., Marazzi, M. and Pietrabissa, R. (2002). Mechanobiology of engineered cartilage cultured under a quantified fluid-dynamic environment. *Biomechanics and modeling in mechanobiology* **1**, 69–82.

(195) Ford, M. D., Alperin, N., Lee, S. H., Holdsworth, D. W. and Steinman, D. A. (2005). Characterization of volumetric flow rate waveforms in the normal internal carotid and vertebral arteries. *Physiological measurement* **26**, 477.

(196) Rittgers, S. E., Karayannacos, P. E., Guy, J. F., Nerem, R. M., Shaw, G. M., Hostetler, J. R. and Vasko, J. S. (1978). Velocity distribution and intimal proliferation in autologous vein grafts in dogs. *Circulation research* **42**, 792–801.

(197) Lavik, E. and Langer, R. (2004). Tissue engineering: current state and perspectives. *Applied microbiology and biotechnology* **65**, 1–8.

(198) Iglesias-Lopez, C., Agustí, A., Obach, M. and Vallano, A. (2019). Regulatory framework for advanced therapy medicinal products in Europe and United States. *Frontiers in pharmacology* **10**, 921.

(199) Grinnell, F. and Feld, M. K. (1982). Fibronectin adsorption on hydrophilic and hydrophobic surfaces detected by antibody binding and analyzed during cell adhesion in serum-containing medium. *Journal of Biological Chemistry* **257**, 4888–4893.

(200) Chen, R., Qiu, L., Ke, Q., He, C. and Mo, X. (2009). Electrospinning thermoplastic polyurethane-contained collagen nanofibers for tissue-engineering applications. *Journal of Biomaterials Science, Polymer Edition* **20**, 1513–1536.

(201) Jia, L., Prabhakaran, M. P., Qin, X., Kai, D. and Ramakrishna, S. (2013). Biocompatibility evaluation of protein-incorporated electrospun polyurethane-based scaffolds with smooth muscle cells for vascular tissue engineering. *Journal of Materials Science* **48**, 5113–5124.

(202) Tomecka, E., Wojasinski, M., Jastrzebska, E., Chudy, M., Ciach, T. and Brzozka, Z. (2017). Poly (l-lactic acid) and polyurethane nanofibers fabricated by solution blow spinning as potential substrates for cardiac cell culture. *Materials Science and Engineering: C* **75**, 305–316.

(203) Gustafsson, Y., Haag, J., Jungebluth, P., Lundin, V., Lim, M. L., Baiguera, S., Ajalloueian, F., Del Gaudio, C., Bianco, A., Moll, G., Sjöqvist, S., Lemon, G., Teixeira, A. I. and MacChiarini, P. (2012). Viability and proliferation of rat MSCs on adhesion protein-modified PET and PU scaffolds. *Biomaterials* **33**, 8094–8103.

(204) Tanzi, M. C., Mantovani, D., Petrini, P., Guidoin, R. and Laroche, G. (1997). Chemical stability of polyether urethanes versus polycarbonate urethanes. *Journal of Biomedical Materials Research: An Official Journal of The Society for Biomaterials and The Japanese Society for Biomaterials* **36**, 550–559.

(205) Delebecq, E., Pascault, J.-P., Boutevin, B. and Ganachaud, F. (2013). On the versatility of urethane/urea bonds: reversibility, blocked isocyanate, and non-isocyanate polyurethane. *Chemical reviews* **113**, 80–118.

(206) Sheldon, R. A. (2018). Metrics of Green Chemistry and Sustainability: Past, Present, and Future. *ACS Sustainable Chemistry and Engineering* **6**, 32–48.

(207) Council of European Union (2021) Commission Regulation (EU) 2021/2030 of 19 November 2021 amending Annex XVII to Regulation (EC) No 1907/2006 of the European Parliament and of the Council concerning the Registration, Evaluation, Authorisation and Restriction of Chemicals (REACH) as regards N,N-dimethylformamide, *Official Journal of the European Union, L 415/16*
http://data.europa.eu/eli/reg/2021/2030/oj.

(208) Council of European Union (2008) REGULATION (EC) No 1272/2008 OF THE EUROPEAN PARLIAMENT AND OF THE COUNCIL of 16 December 2008 on classification, labelling and packaging of substances and mixtures, amending and repealing Directives 67/548/EEC and 1999/45/EC, and amending Regulation (EC) No 1907/2006, *Official Journal of the European Union, L 353/1*
http://data.europa.eu/eli/reg/2008/1272/oj.

(209) Brown, T. D., Dalton, P. D. and Hutmacher, D. W. (2016). Melt electrospinning today: An opportune time for an emerging polymer process. *Progress in Polymer Science* **56**, 116–166.

(*210*) Hutmacher, D. W. and Dalton, P. D. (2011). Melt electrospinning. *Chemistry–An Asian Journal* **6**, 44–56.

(*211*) Bürck, J., Aras, O., Bertinetti, L., Ilhan, C. A., Ermeydan, M. A., Schneider, R., Ulrich, A. S. and Kazanci, M. (2018). Observation of triple helix motif on electrospun collagen nanofibers and its effect on the physical and structural properties. *Journal of Molecular Structure* **1151**, 73–80.

(*212*) Wakuda, Y., Nishimoto, S., Suye, S. I. and Fujita, S. (2018). Native collagen hydrogel nanofibres with anisotropic structure using core-shell electrospinning. *Sci Rep* **8**, 6248.

(*213*) Anaya Mancipe, J. M., Boldrini Pereira, L. C., de Miranda Borchio, P. G., Dias, M. L. and da Silva Moreira Thire, R. M. (2023). Novel polycaprolactone (PCL)-type I collagen core-shell electrospun nanofibers for wound healing applications. *Journal of Biomedical Materials Research Part B: Applied Biomaterials* **111**, 366–381.

(*214*) Anaya Mancipe, J. M., Lopes Dias, M. and Moreira Thiré, R. M. D. S. (2022). Type I collagen–poly (vinyl alcohol) electrospun nanofibers: FTIR study of the collagen helical structure preservation. *Polymer-Plastics Technology and Materials* **61**, 846–860.

(*215*) Baek, J., Chen, X., Sovani, S., Jin, S., Grogan, S. P. and D'Lima, D. D. (2015). Meniscus tissue engineering using a novel combination of electrospun scaffolds and human meniscus cells embedded within an extracellular matrix hydrogel. *J Orthop Res* **33**, 572–83.

(*216*) Veis, A., Anesey, J. and Cohen, J. (1961). The long range reorganization of gelatin to the collagen structure. *Archives of biochemistry and biophysics* **94**, 20–31.

(*217*) Jiang, S., Schmalz, H., Agarwal, S. and Greiner, A. (2020). Electrospinning of ABS nanofibers and their high filtration performance. *Advanced Fiber Materials* **2**, 34–43.

(*218*) Bornstein, P., Kang, A. H. and Piez, K. A. (1966). The Limited Cleavage of Native Collagen with Chymotrypsin, Trypsin, and Cyanogen Bromide*. *Biochemistry* **5**, 3803–3812.

(*219*) Kishan, A. P. and Cosgriff-Hernandez, E. M. (2017). Recent advancements in electrospinning design for tissue engineering applications: A review. *Journal of Biomedical Materials Research Part A* **105**, 2892–2905.

(*220*) Hasan, A., Memic, A., Annabi, N., Hossain, M., Paul, A., Dokmeci, M. R., Dehghani, F. and Khademhosseini, A. (2014). Electrospun scaffolds for tissue engineering of vascular grafts. *Acta Biomaterialia* **10**, 11–25.

(*221*) Salvatore, L., Gallo, N., Natali, M. L., Terzi, A., Sannino, A. and Madaghiele, M. (2021). Mimicking the hierarchical organization of natural collagen: Toward the development of ideal scaffolding material for tissue regeneration. *Frontiers in Bioengineering and Biotechnology* **9**, 644595.

(*222*) Baier, R. E. and Dutton, R. C. (1969). Initial events in interactions of blood with a foreign surface. *Journal of biomedical materials research* **3**, 191–206.

(*223*) Wilson, C. J., Clegg, R. E., Leavesley, D. I. and Pearcy, M. J. (2005). Mediation of biomaterial–cell interactions by adsorbed proteins: a review. *Tissue engineering* **11**, 1–18.

(*224*) Jana, S. (2019). Endothelialization of cardiovascular devices. *Acta biomaterialia* **99**, 53–71.

(225) Hinderer, S., Sudrow, K., Schneider, M., Holeiter, M., Layland, S. L., Seifert, M. and Schenke-Layland, K. (2018). Surface functionalization of electrospun scaffolds using recombinant human decorin attracts circulating endothelial progenitor cells. *Scientific Reports* **8**, 1–14.

(226) Li, S., Sengupta, D. and Chien, S. (2014). Vascular tissue engineering: from in vitro to in situ. *Wiley Interdisciplinary Reviews: Systems Biology and Medicine* **6**, 61–76.

(227) Yu, T. T., Gupta, P., Ronfard, V., Vertès, A. A. and Bayon, Y. (2018). Recent progress in European advanced therapy medicinal products and beyond. *Frontiers in bioengineering and biotechnology* **6**, 130.

(228) Cheng, W. T., Liu, M. T., Liu, H. N. and Lin, S. Y. (2005). Micro-Raman spectroscopy used to identify and grade human skin pilomatrixoma. *Microsc Res Tech* **68**, 75–9.

(229) Huang, Z., McWilliams, A., Lui, H., McLean, D. I., Lam, S. and Zeng, H. (2003). Near-infrared Raman spectroscopy for optical diagnosis of lung cancer. *International journal of cancer* **107**, 1047–1052.

(230) Stone, N., Kendall, C., Shepherd, N., Crow, P. and Barr, H. (2002). Near-infrared Raman spectroscopy for the classification of epithelial pre-cancers and cancers. *Journal of Raman Spectroscopy* **33**, 564–573.

(231) Talari, A. C. S., Movasaghi, Z., Rehman, S. and Rehman, I. u. (2014). Raman Spectroscopy of Biological Tissues. *Applied Spectroscopy Reviews* **50**, 46–111.

(232) Zhang, Q., Andrew Chan, K. L., Zhang, G., Gillece, T., Senak, L., Moore, D. J., Mendelsohn, R. and Flach, C. R. (2011). Raman microspectroscopic and dynamic vapor sorption characterization of hydration in collagen and dermal tissue. *Biopolymers* **95**, 607–15.

(233) Dong, R., Yan, X., Pang, X. and Liu, S. (2004). Temperature-dependent Raman spectra of collagen and DNA. *Spectrochimica Acta Part A: Molecular and Biomolecular Spectroscopy* **60**, 557–561.

(234) McColl, I. H., Blanch, E. W., Gill, A. C., Rhie, A. G., Ritchie, M. A., Hecht, L., Nielsen, K. and Barron, L. D. (2003). A new perspective on β-sheet structures using vibrational Raman optical activity: from poly (L-lysine) to the prion protein. *Journal of the American Chemical Society* **125**, 10019–10026.

(235) Gullekson, C., Lucas, L., Hewitt, K. and Kreplak, L. (2011). Surface-Sensitive Raman Spectroscopy of Collagen I Fibrils. *Biophysical Journal* **100**, 1837–1845.

(236) Murphy, R., Turcott, A., Banuelos, L., Dowey, E., Goodwin, B. and Cardinal, K. O. (2020). SIMPoly: A matlab-based image analysis tool to measure electrospun polymer scaffold fiber diameter. *Tissue Eng Part C Methods* **26**, 628–636.

Acknowledgements

This thesis would not have been possible without the help of some amazing people, to whom I would like to express my sincere gratitude.

First and foremost, I am grateful to my promotor and supervisor at the University of Tübingen, Prof. Dr. Katja Schenke-Layland. We have worked together for about five years, the first of which have been in Stuttgart, where I joined the group as an intern. I can still remember how excited you were at one of our meetings with Ruben about a coloured SEM image of electrospun fibres. The cover of this thesis is a little nod to that very first meeting of ours.

I would like to thank the other members of the defence committee: Prof. Dr. Peter Loskill, Prof. Dr. Dirk Schwarzer, and Prof. Dr. Jennifer Ewald. I really appreciate your interest in this work and the time and effort spent evaluating this thesis.

I also want to thank my daily supervisor at the NMI, Dr. Hanna Hartmann. Thank you for your 'adopting' me, when my research group was dissolved. Thank you for the scientific and organisational support, and for the possibility to always knock on your door. I would also like to thank everyone else involved in the PolyKARD project, without whom this collaboration would not have been possible, especially Wolfdietrich and Hadi from the Fraunhofer IAP in Potsdam. Thanks to everyone who supported the PolyKARD project, with technical, organisational, and scientific assistance, at the NMI: Ellena, Katharina, and Elsa.

I would particularly like to thank the members of the *'Spinner'* group. A more fitting name could not have been chosen, best left untranslated: *'Wir spinnen, sowohl als auch.'*. From dawn to dusk, with each careful measurement, we spun science. Though, between the experiments and research, we wove memories more lasting than that. We had a lot more in common than just electrospinning. We shared our humour and laughter. We enjoyed many get-togethers, parties, and hikes. Thank you, Ruben, Kathrin, Nora, Lisa, Johannes, Adrian, Katharina, Florian, Isabelle, Oktay. You made the time worth it.

I would like to extend my gratitude to all staff members who supported me at the NMI, especially to Simon, Kai, Steffen, and Eberhard. Thank you for your help with the lab renovation, for the assistance when I knocked on your door, for the numerous lunch talks. Thank you Thoralf and Desi for the many spontaneous gatherings both inside and outside the NMI. I also want to highlight my gratitude to Jenny at the NMI. Thank you.

Furthermore, I would like to thank all members of the Schenke-Layland Lab group at the laboratory in Tübingen, especially Julia, Simone, and Daniel for whenever I needed something in the lab or when I had spontaneously booked the Raman spectroscope.

Finally, I would like to thank all those who have helped me personally during this time with unconditional and heartfelt support.

Declaration

Ich erkläre hiermit, dass ich die zur Promotion eingereichte Arbeit mit dem Titel: *"Electrospinning of biomimetic scaffolds: Why electrospun natural extracellular matrix components need not be the first material of choice"* selbständig verfasst, nur die angegebenen Quellen und Hilfsmittel benutzt und wörtlich oder inhaltlich übernommene Zitate als solche gekennzeichnet habe. Ich erkläre, dass die Richtlinien zur Sicherung guter wissenschaftlicher Praxis der Universität Tübingen beachtet wurden. Ich versichere an Eides statt, dass diese Angaben wahr sind und dass ich nichts verschwiegen habe. Mir ist bekannt, dass die falsche Angabe einer Versicherung an Eides statt mit Freiheitsstrafe bis zu drei Jahren oder mit Geldstrafe bestraft wird.

Dmitri Visser

Appendix

Raman Peak Assignments A

Raman Shift	Assignment	Refs.
Proline and Hydroxyproline Region		
814	proline, hydroxyproline	(*228*)
854	ring breathing, tyrosine, ν(C-C), proline	(*179*)
858	proline, hydroxyproline	(*228*)
858	tyrosine	(*118*, *179*)
875, 880	ν(C-C), hydroxyproline	(*229*)
923	ν(C-C), proline, hydroxyproline	(*179*, *230*, *231*)
936	C-C vibrations, carbonyl	(*180*, *232*)
936	ν(C-C), proline, α-helix	(*229*)
936	ν(C-C), α-helix, proline, hydroxyproline	(*228*, *231*)
1005	ν_s(C-C), phenylalanine	(*118*)
1030, 1035	phenylalanine	(*118*, *228*)
Amide Region		
1220	amide III, β-sheet	(*179*)
1240 – 1248	amide III, α-helix	(*22*, *125*)
1310 – 1368	amide III shoulder, γ(CH3, CH2)	(*22*)
1409	heat denaturation in cartilage	(*180*)
1453	amide II, ν(C-N), N-H bending	(*231*)
1440 – 1444	δ(CH3, CH2) in collagen	(*233*)
1648	amide I, α-helix	(*179*, *234*)
1668	amide I, α-helix	(*118*, *229*)
1672	amide I, β-sheet	(*234*, *235*)

Table A.1: Raman peak assignments with corresponding references. The peaks are given as wave shifts (in cm^{-1})

Software | B

Some of the software used in this thesis has been developed by me during this doctoral project. These are publicly available via the open access repository host GitHub.

RaMAT

`RaMAT` is a MATLAB-based toolbox which allows rapid analysis, spectral correction and plotting of spectroscopic Raman data. It has the additional advantage that Raman measurements from WiTEC spectroscopes can be directly imported in their native proprietary format using the `WitIO` toolbox written by Joonas T. Holmi. The `RaMAT` toolbox is the result of my observation that the traditional workflow involved many proprietary software packages and multiple steps, which hindered rapid analysis and visualisation of measurements. `RaMAT` allows for the management of measurements, baseline correction, and multivariate data analysis of Raman spectroscopical measurements. It supersedes many of the 'write-once-use-once' MATLAB scripts previously used in our lab, because it stores data in the polymorphic `SpecData` class, which can handle both single spectral measurements and multidimensional spectral measurements (so-called 'large-area scans'). The toolbox can be retrieved at: https://github.com/ksllabtue/ramat

FibreSEM

`FibreSEM` is a small python repository to analyse SEM images of fibrous materials. I wrote this software to analyse the fibre diameters in batch using the SIMPoly algorithm developed by Murphy et al. (236) and to uniformly annotate the images that have been taken with the Zeiss Auriga. The repository can be retrieved at https://github.com/dvtxc/fibresem. It is distributed at PyPi and can be installed in python using:

```
py -m pip install fibresem
```

Article

Green Chemistry for Biomimetic Materials: Synthesis and Electrospinning of High-Molecular-Weight Polycarbonate-Based Nonisocyanate Polyurethanes

Dmitri Visser,* Hadi Bakhshi,* Katharina Rogg, Ellena Fuhrmann, Franziska Wieland, Katja Schenke-Layland, Wolfdietrich Meyer, and Hanna Hartmann

Read Online

ACCESS | Metrics & More | Article Recommendations | SI Supporting Information

ABSTRACT: Conventional synthesis routes for thermoplastic polyurethanes (TPUs) still require the use of isocyanates and tin-based catalysts, which pose considerable safety and environmental hazards. To reduce both the ecological footprint and human health dangers for nonwoven TPU scaffolds, it is key to establish a green synthesis route, which eliminates the use of these toxic compounds and results in biocompatible TPUs with facile processability. In this study, we developed high-molecular-weight nonisocyanate polyurethanes (NIPUs) through transurethanization of 1,6-hexanedicarbamate with polycarbonate diols (PCDLs). Various molecular weights of PCDL were employed to maximize the molecular weight of NIPUs and consequently facilitate their electrospinnability. The synthesized NIPUs were characterized by nuclear magnetic resonance, Fourier-transform infrared spectroscopy, gel permeation chromatography, and differential scanning calorimetry. The highest achieved molecular weight (M_w) was 58,600 g/mol. The NIPUs were consecutively electrospun into fibrous scaffolds with fiber diameters in the submicron range, as shown by scanning electron microscopy (SEM). To assess the suitability of electrospun NIPU mats as a possible biomimetic load-bearing pericardial substitute in cardiac tissue engineering, their cytotoxicity was investigated in vitro using primary human fibroblasts and a human epithelial cell line. The bare NIPU mats did not need further biofunctionalization to enhance cell adhesion, as it was not outperformed by collagen-functionalized NIPU mats and hence showed that the NIPU mats possess a great potential for use in biomimetic scaffolds.
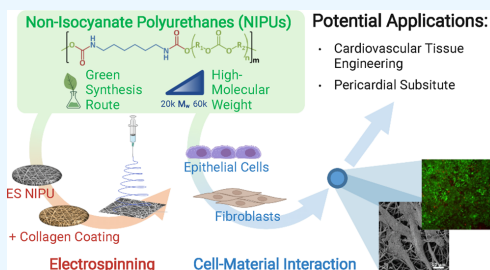
1. INTRODUCTION

Thermoplastic polyurethanes (TPUs) are linear segmented polymers with a wide range of applications because of their superior mechanical properties and feasible processability. TPUs are generally synthesized through the reaction of isocyanates, polyols, and chain extenders, in the presence of tin-based catalysts. The principal limitation of this route is the high toxicity of isocyanate compounds causing irreversible environmental and human health damage.[1−3] Isocyanates are not completely consumed during the polymerization process, and traces of isocyanate residues were detected in the final polyurethanes.[4,5] Tin-based catalysts, for example, dibutyl-tin-dilaurate (DBTDL), are not removed after the polymerization process and can result in toxicity.[6,7] Therefore, synthesis routes for TPUs excluding isocyanates and tin-based catalysts have attracted great interest, especially for the fabrication of biomedical materials,[8−10] food packaging,[11,12] and children products.

One route for synthesizing nonisocyanate polyurethanes (NIPUs) is through the transurethanization reaction between bis-carbamates and polyols, leading to a structure and characteristics similar to classic TPUs but through solvent-free and green chemistry.[13−15] TPUs can be synthesized using polyether, polyester, or polycarbonate (PC) polyols. PC-based TPUs exhibit superior hydrolysis and oxidation resistance, biostability, and biocompatibility compared to the polyether- and polyester-based ones and consequently have greater potential for long-term biomedical applications.[16]

Electrospinning is a versatile technique to process a wide variety of polymers into fibrous mats.[17] Typically, a charged jet of polymer melt or solution is induced by a strong electric field and driven in a spinning motion toward a metal collector, while the jet solidifies. Electrospinning allows for the fabrication of nonwoven fibrous materials with fiber diameters ranging from

tens of nanometers to several microns. As such, this technique has found its way into many applications, especially the production of functional materials that require an extremely high surface-to-volume ratio, such as sensors[18−20] and filtration membranes.[21,22] In the last two decades, the interest in the electrospinning technique for biomedical applications surged because of the high resemblance of mechanical and structural properties of electrospun materials to those of native tissues.[23−26]

The highly variable chemistry of TPUs allows for tailored physio-chemical and biodegradable properties.[27,28] Especially for long-term implants, TPUs have a long-standing reputation as biomaterials with good biocompatibility, which do not elicit inflammatory reactions. Additionally, the anti-thrombogenic properties of TPUs make them excellent biomaterials that come into contact with blood.[28] This has led to the investigation of electrospun TPUs as tissue-engineered vascular grafts,[29−33] heart valves,[34−36] and cardiac patches.[37−39] However, most studies have only considered the electro-spinning of TPUs based on isocyanate synthesis. Although water-soluble polymers have successfully raised the bar in making electrospinning more environmentally friendly, green electrospinning of NIPUs is still uncharted territory. Aduba et al.[8] recently reported the electrospinning of polyether-based NIPUs, which were synthesized from cyclic carbonate methyl esters, and their potential for biomedical applications. To our knowledge, the present study is the first to present the electrospinning of PC-based NIPUs, which more closely resemble the classical TPUs.

This work aimed to synthesize high-molecular-weight PC-based NIPUs using nontoxic chemicals and green procedures, which are suitable for the electrospinning process as well as to establish and optimize the electrospinning process to obtain bead-free fibers with potential for biomedical applications. The NIPUs were synthesized by employing 1,6-hexanedicarbamate (1,6-HDC) as a green substitute for diisocyanates. The synthesized NIPUs were fully characterized before electro-spinning and after electrospinning in biological tests.

2. EXPERIMENTAL SECTION

2.1. Materials. 1,6-Hexanediamine (1,6-HDA, 99.5%), dimethyl carbonate (DMC, 99%), sodium acetate, absolute methanol, chloroform, tetra butyl titanate (TBT), N,N-dimethylformamide (DMF), and sodium carbonate were obtained from Sigma Aldrich. Tetrahydrofuran (THF, 99.9%) was obtained from Carl Roth. Eternacoll UH50 (PCDL500, OH#: 224, 500 g/mol), Eternacoll UH100 (PCDL1000, OH#: 110, 1000 g/mol), and Eternacoll UH200 (PCDL2000, OH#: 56, 2000 g/mol) as aliphatic polycarbonate diols (PCDLs) were kindly supplied from UBE Corporation Europe. 1,1,1,3,3,3-Hexafluoroisopropanol (HFIP) was obtained from Iris Biotech GmbH.

2.2. Synthesis of 1,6-HDC. 1,6-HDC was synthesized from DMC and 1,6-HDA according to a reported procedure[40] with some modifications. 1,6-HDA (23.24 g, 200 mmol), DMC (18.02 mL, 400 mmol), sodium acetate (4.00 g, 48.8 mmol), and absolute methanol (100 mL) were added in a 500 mL three-neck round-bottomed flask equipped with a condenser, a magnetic stirrer, and an Ar inlet. The temperature was raised to 75 °C and the reaction mixture was stirred overnight. Over time, white floccules disappeared and turned the clear reaction mixture into a white dispersion. After cooling to room temperature, the reaction mixture was diluted with an

excess amount of HCl solution (2 N, 400 mL) and extracted with chloroform twice. The chloroform phases were combined and washed with distilled water. Removal of chloroform on a vacuum rotary evaporator yielded a white solid, which was purified through the recrystallization from the methanol/water mixture (1/1, 100 mL) at 80 °C and vacuum-drying overnight (23.45 g, 50% yield).

2.3. Transurethanization Polymerization. NIPUs were synthesized through the transurethanization reaction of PCDLs and 1,6-HDC according to a reported procedure[8] with some modifications. PCDLs (43.0 mmol), 1,6-HDC (43,0 mmol), and TBT (0.2−0.3 wt %) were added in a 100 mL three-neck round-bottomed flask equipped with a condenser, a mechanical stirrer, an N_2 inlet, and a vacuum outlet. The mixture was heated at 170 °C and stirred mechanically to form a homogeneous melt, first under an N_2 atmosphere and then under reduced pressure. Later, the reaction mixture was transferred to a vacuum oven and heated at 170 °C under a dynamic vacuum. The reaction parameters for selected samples are summarized in Table S1. The product was dissolved in DMF (80 mL) at 70 °C, precipitated in methanol (2 L), and dried in a vacuum oven at 40 °C overnight.

2.4. Electrospinning of NIPUs. NIPUs were dissolved in DMF, THF, or HFIP at various concentrations (20−50 wt %) and temperatures up to 50 °C under stirring. For selected experiments, the conductivity of solutions was adjusted to 10 μS/cm by the supplementation of sodium carbonate,[41] as measured with a conductivity meter (GMH 3431-LTG, Greisinger). The electrospinning process was done using a climate-controlled EC-CLI electrospinning setup (IME Technologies) with a flat collector plate, which allows for temperature control between 20 and 45 °C. All experiments were conducted with a 21G cannula corresponding to an inner diameter of 0.5 mm. The temperature and the relative humidity of the electrospinning chamber were kept at 35 °C and 20%, respectively, for all experiments. The remaining electrospinning parameters (voltage, flow rate, and tip-to-collector distance) were varied until a stable, fiber-yielding process was established. After electrospinning, the fibrous mats were dried in a vacuum oven at <5 mbar overnight to remove all solvent residues.

2.5. Instruments. Fourier transform infrared (FTIR) spectroscopy was done using a Thermo Fisher Scientific instrument (Nicolet iS20) equipped with an attenuated total reflection (ATR) unit (PIKE Technologies, GladiATR).

An nuclear magnetic resonance (NMR) spectrometer (Varian, Unity Inova 500 NB) was employed for recording the ^{1}H- and ^{13}C-NMR spectra at 25 °C using CDCl$_3$ and DMF-d_7 as solvents.

The molecular weight distributions of samples were determined by gel permeation chromatography (GPC) in DMF containing LiBr (0.1%) using PSS GRAM Guard (8 × 50 mm), PSS GRAM 1000 Å (300 × 7.5 mm), PSS GRAM 1000 Å (300 × 7.5 mm), and PSS GRAM 30 Å (300 × 7.5 mm) columns (PSS Polymer Standards Service) and an SEC-3010 reflect index detector (WGE Dr. Bures GmbH) with a flow rate of 1 mL/min at 50 °C. The data were evaluated by ParSEC CPC/SEC software (Brookhaven Instruments) using polystyrenes with molecular weights of 265−2,570,000 g/mol (PSS Polymer Standards Service) as the standards.

A differential scanning calorimetry (DSC) instrument (Netzsch, DSC 204 F1 Phoenix) operating in a range of −50 to 200 °C with a heating rate of 10 °C/min under a N_2

atmosphere was used to study the thermal transition of samples. The glass transition (T_g), crystallization (T_c), cold crystallization (T_{cc}), and melting (T_m) temperatures were extracted from the middle point of the baseline change and corresponding peak maximums, respectively, in the second heating cycle.

The morphology of the electrospun NIPU mats was studied on a scanning electron microscopy (SEM) instrument (Zeiss, Auriga 40) operating at an electron gun voltage of 3 kV using a secondary electron detector. The mats were coated with gold−palladium in a sputtering system (Balzers, SCD-040) for 20 s before microscopy. Cell-loaded mats were fixed in a three-step process; first with paraformaldehyde (PFA, 4%) in Dulbecco's phosphate-buffered saline (DPBS) for 30 min, thereafter in PFA (4%) and glutaraldehyde (2%) in DPBS for 1 h, and consequently dehydrated with isopropanol through critical point drying. Fiber diameters were assessed in MATLAB using an adapted version of the Simpoly algorithm from Murphy et al.[42] The source code of the used algorithm is available online at github.com/dvtxc/fibresem.

The surface hydrophilicity of the electrospun NIPU mats was assessed by measuring the water contact angle with the DSA25 drop-shape analyzer (Krüss). A photograph was taken 20 s after applying 2 μL of deionized water onto the mats.

2.6. Biofunctionalization. The biofunctionalization of the electrospun NIPU mats was performed with rat tail collagen, type I (rCol I). Collagen was extracted from rat tail tendons using acid-based isolation and lyophilized for long-term storage. The collagen integrity after extraction was confirmed with electrophoretic assays and circular dichroism. Before biofunctionalization, the collagen lyophilisate was solubilized in acetic acid (0.1 M) at a concentration of 0.1 mg/mL. The mats were incubated in the collagen solution at 37 °C for 2 h before aspirating the excess solution and left to dry at 4 °C overnight. The collagen functionalization was confirmed with contact angle measurements and immunohistochemical staining against collagen I.

2.7. Biocompatibility Assays. The MTT assay was done to study the cytotoxicity of NIPU granulates and electrospun NIPU mats according to ISO 10993-5 and ISO 10993-12 norms. NIPU granulates were obtained after the polymerization. Mats were dried in a vacuum at 50 °C and <5 mbar to remove all HFIP residues. Additional mats were washed three times in phosphate-buffered saline (PBS) for 10 min. Samples were incubated in the supplemented media at an extraction ratio of 3 cm²/mL. The L929 cells were cultured in minimal essential media supplemented with fetal bovine serum (FBS, 10%, 10270-106, Gibco), L-glutamine (4 mM, 2051024, Gibco), and penicillin−streptomycin (1%, 15070-063, Gibco) at 37 °C in a 5% CO_2 atmosphere. The cell viability was assessed with 1 mg/mL 3-(4,5-dimethylthiazol-2-yl)-2,5-diphenyltetrazolium bromide (MTT, M2128, Sigma-Aldrich) by measuring the absorbance at 570 nm with respect to the absorbance of the blank samples. The samples were considered to be cytotoxic when the relative cell viability was less than 70%. The positive control was a polyurethane film containing 0.1% zinc diethyldithiocarbamate (ZDEC, Hatano Research Institute) and the negative control was a high-density polyethylene (HDPE) film (Hatano Research Institute). All samples were prepared in triplicates.

The live/dead staining was performed to investigate the direct impact of the electrospun NIPU mats on the cells. The mats were punched, UV-sterilized (150 s, GS Gene Linker,

Bio-rad), washed three times with PBS, clamped in 24 well cell crowns (Sigma), and placed in 24-well plates (Corning). Primary human dermal fibroblasts (hDF) were isolated from foreskin biopsies under the ethics approval no 495/2018BO2 and cultured in Dulbecco's modified Eagle's medium (DMEM) supplemented with FBS (10%), L-Glutamine (4 mM), sodium pyruvate (1 mM), and penicillin−streptomycin (1%, ThermoFisher). Human epithelial cells (MeT-5A, ATCC) from the pleural mesothelium were cultured in the DMEM/F12 medium (ThermoFisher) supplemented with FBS (10%) and penicillin−streptomycin (1%). Both cell types were cultured at 37 °C in a 5% CO_2 atmosphere. Cells were removed from cell culture flasks with trypsin/EDTA (0.25%) and their concentration was adjusted so 4×10^4 hDFs or 6×10^4 MeT-5A cells were seeded on each mat. The positive control (nonadherent) was Parafilm as a highly hydrophobic surface and the negative control was glass. After 24 h or 7 days, the live/dead staining was done with calcein (Invitrogen) and propidium iodide (PI, Sigma-Aldrich) serving as the live and dead markers, respectively. All samples were prepared in triplicates.

Immunohistochemical staining was done to assess the adhesion of collagen I on the biofunctionalized electrospun NIPU mats. Briefly, the biofunctionalized mats were blocked for 30 min with goat block, that is, goat serum (2%), Triton X-100 (0.1%), Tween 20 (0.05%), cold-water fish skin gelatine (0.1%), and bovine serum albumin (BSA, 1%) in DPBS, washed three times with Tween 20 in DPBS (0.05%), and incubated with a mouse anti-Col I primary antibody (1:500) at 4 °C overnight in DPBS buffer containing Triton X-100 (0.1%), Tween 20 (0.05%), cold-water fish skin gelatine (0.1%), and BSA (1%). Immunofluorescence labeling was performed with a goat anti-mouse IgG Alexa-Fluor 546 secondary antibody (1:250) for 30 min at room temperature in the same buffer as the primary antibody. Bare mats served as a control. To test for unspecific binding of the secondary antibody, a control without the primary collagen antibody was included as well. Samples were imaged through a 20× objective with a spinning disk laser microscope (Zeiss). Mean gray-value intensities (GVI) of three images per sample were extracted with ImageJ software.

3. RESULTS AND DISCUSSION

3.1. Polymerization of NIPUs. In general, two bis-carbamates are utilized for the transurethanization reaction; (1) bis-hydroxyalkylcarbamate formed by the reaction of ethylene carbonate with diamines[14] and (2) bis-alkylcarbamate generated from the reaction of DMC with diamines.[13,15] In this study, a bis-methylcarbamate, 1,6-HDC, was prepared from the reaction of DMC and 1,6-HDA (Scheme 1). 1,6-HDC was later reacted with PCDLs using TBT as a catalyst at 170 °C to prepare NIPUs through the transurethanization reaction.

To facilitate the electrospinning process, the resulting NIPU should also have a sufficiently high molecular weight. Therefore, several NIPUs were synthesized employing PCDLs with different molecular weights (500, 1000, and 2000 g/mol) at various stoichiometry ratios, TBT concentrations, temperatures, and vacuum pressures. Generally, PCDLs and 1,6-HDC were heated at 170 °C and stirred mechanically to form a homogeneous melt, first under an N_2 atmosphere and then under a vacuum. Later, the reaction mixture was transferred to a vacuum oven and heated at 170

Scheme 1. Synthesis Route for NIPUs
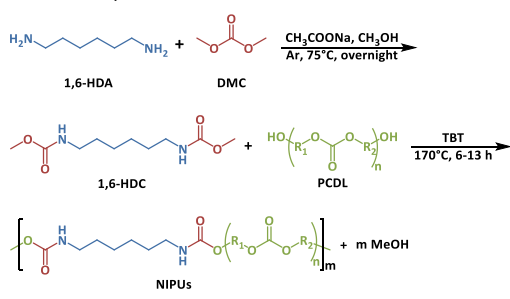
Figure 1. FTIR spectra of 1,6-HDC, PCDL500, and NIPU-D.

°C under a dynamic vacuum. The reaction parameters for selected samples are summarized in Table S1.

The molecular weights of NIPUs were evaluated via GPC (Table 1). The transurethanization reaction between PCDLs and 1,6-HDC generated methanol as a by-product, which should be eliminated from the reaction mixture to reach high-molecular-weight NIPUs. Initially, the reaction mixture was stirred mechanically under an atmospheric pressure for 3−4 h and then kept in a vacuum oven for 2−3 h, which led to a higher molecular weight for NIPU-A, based on PCDL500, compared to NIPU-B and NIPU-C, based on PCDL1000 and PCDL2000 (Table 1). The low viscosity of PCDL500 (100 cP at 75 °C) compared to PCDL1000 and PCDL2000 (410 and 2300 cP at 75 °C) resulted in a low viscose reaction mixture, which facilitated the removal of methanol and consequently the yield of the transurethanization reaction. To further improve the elimination of methanol and hence the molecular weight of NIPUs, the reaction mixtures were stirred under vacuum pressure (600 mbar) for another hour, which led to NIPU-D with almost double molecular weight compared to NIPU-A.

It is worth mentioning that employing stronger vacuums could vaporize the unreacted PCDL500 and even 1,6-HDC and thus change the stoichiometry ratio within the reaction mixture and yield insoluble samples (Table S1). The reason behind the insolubility is the cross-linking of NIPU chains through the condensation reaction of urethane N−H groups arising from NIPU oligomers or unreacted 1,6-HDC with extra methylcarbamate ($COOCH_3$) groups.[13]

The progress of the transurethanization reaction was monitored via FTIR spectroscopy (Figure 1). The broad peak at 3349 cm^{-1} in the FTIR spectrum of PCDL500, attributed to the stretching vibration of O−H bonds, significantly decreased (almost disappeared) in the FTIR spectrum of NIPU-D, preventatively, which means the consumption of the majority of hydroxyl groups in the course of the transurethanization reaction. The FTIR spectrum of NIPU-D displayed the characteristic peaks at 1732 and 1682
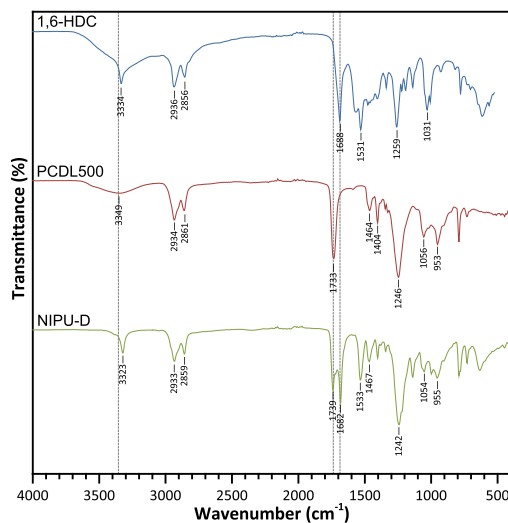
cm^{-1} arising from the stretching vibration of C=O bonds of urethane and carbonate moieties in its backbone.

The chemical structure of NIPU-D was preventatively studied by NMR spectroscopy (Figures 2 and S1, S2 in Electronic Supporting Information, ESI). All peaks are assigned with the corresponding protons or carbons in the embedded molecular structure of NIPU-D. The protons of urethane moieties yielded a signal at 6.95 ppm. The protons at both α-positions of urethane moieties, that is, CH_2NHCO and $NHCOCH_2$, appeared at 3.06 and 3.97 ppm, respectively. Meanwhile, the carbons of urethane and carbonate moieties led to signals at 156.97 and 155.28 ppm. The carbons at both α-positions of urethane moieties, that is, CH_2NHCO and $NHCOCH_2$, appeared at 40.53 and 63.84 ppm, respectively. The NMR spectra confirmed the successful synthesis of NIPUs.

The thermal transitions of NIPUs were determined by DSC (Table 1 and Figure S3 in ESI). NIPUs displayed the thermal profile of semicrystalline polymers including glass transition, crystallization, and melting. The T_g of NIPUs was decreased from −28 to −41 °C by employing higher molecular weight PCDLs, which resulted in lower hard segment (urethane moieties) contents. The hard segments could physically cross-link the soft segments (carbonate moieties) through hydrogen bonds and limit their chain dynamics and free volume. NIPU-A and NIPU-D based on the lowest molecular weight PCDL and thus highest hard segment content displayed higher T_c and T_m values than NIPU-B and NIPU-C. The higher enthalpy

Table 1. GPC and DSC Data for NIPUs

NIPU	MW of PCDL (g/mol)	GPC			DSC						
		M_n (g/mol)	M_w (g/mol)	PDI	T_g (°C)	T_c (°C)	ΔH_c (J/g)	T_{cc} (°C)	ΔH_{cc} (J/g)	T_m (°C)	ΔH_m (J/g)
NIPU-A	500	14,200	26,200	1.85	−28	56	31.6	No	No	108	23.5
NIPU-D	500	24,300	58,600	2.41	−27	53	30.5	No	No	107	37.5
NIPU-B	1000	8800	14,500	1.64	−40	24	25.3	No	No	64	19.1
NIPU-C	2000	10,400	18,700	1.80	−41	−4	3.6	7	19.5	44	27.8
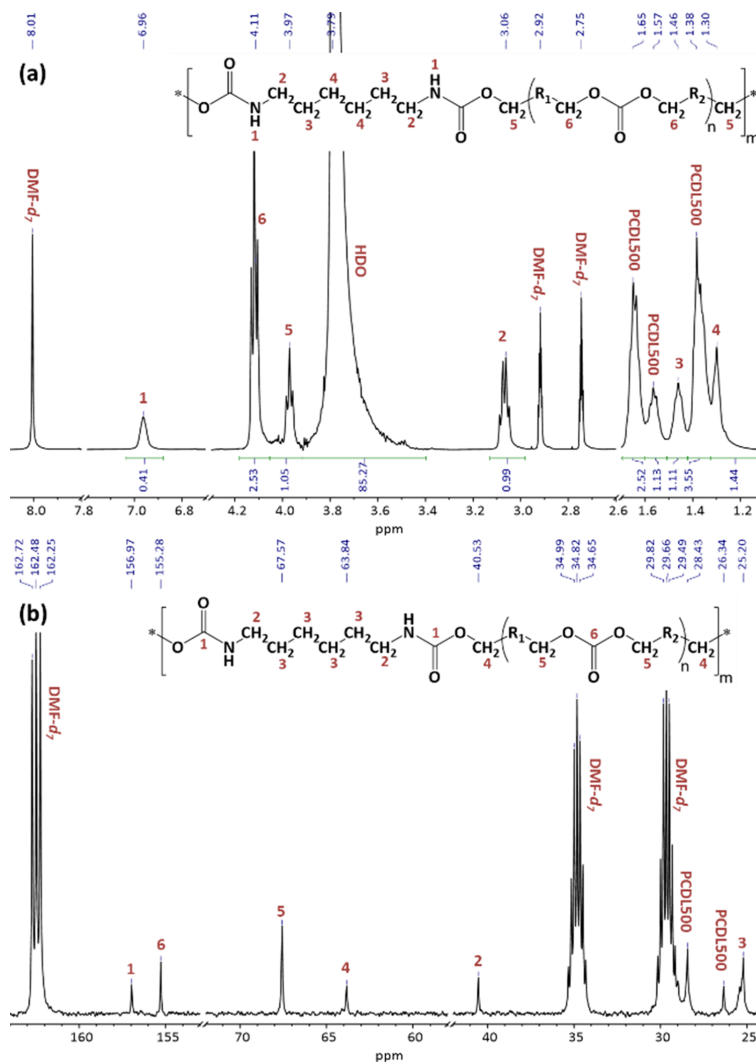
Figure 2. ^{1}H-NMR (a) and ^{13}C-NMR (b) spectra of NIPU-D in DMF-d_7.

(ΔH_c and ΔH_m) values for NIPU-A and NIPU-D displayed their higher crystallinity compared to NIPU-B and NIPU-C. NIPU-C, based on the highest molecular weight PCDL and hence with the lowest hard segment content, showed a low crystallization affinity because a very small crystallization peak (ΔH_c = 3.6 J/g) was detected during its cooling cycle and it mainly crystallized during the second heating cycle (ΔH_{cc} = 19.5 J/g). The double molecular weight of NIPU-D compared to NIPU-A did not significantly change the transition temperatures (T_g, T_c, and T_m) but improved its crystallinity (ΔH_m = 37.5 J/g compared to ΔH_m = 23.5 J/g, respectively). All NIPUs presented two melting peaks in the first heating cycle and one melting peak in the second heating cycle (Figure S3 in ESI). It means the carbonate and urethane moieties

phase-separated over time to generate soft segments with lower T_m values (48−64 °C) and hard segments with higher T_m values (57−115 °C), respectively.

3.2. Electrospinning of NIPUs. Before electrospinning, the solubility of the NIPUs was tested. All NIPUs were soluble in DMF, THF, and HFIP: those with an M_w below 30,000 g/mol (NIPU-A, NIPU-B, and NIPU-C) up to a concentration of 50 wt % and those with a higher molecular weight (NIPU-D) usually up to 35 wt %. Meanwhile, NIPU-A and NIPU-D, both based on PCDL500, had a higher solubility in HFIP compared to DMF and THF. In the first step to establishing a stable electrospinning process, the electrospinnability of NIPU-A, NIPU-B, and NIPU-C was investigated in combination with different solvents (Figure S4 in ESI). Although the electro-

Table 2. Overview of the Established Electrospinning Parameters and Resulting Fiber Diameters[a]

samples			electrospinning parameters						fiber diameter	
NIPU	conc.	salt	U (kV)	φ (mL/h)	CID (mm)	rH (%)	T (°C)	d (cm)	average (μm)	spread (μm)
NIPU-A	50%	no	20	0.1	0.5	30	40	25	$-^b$	$-^b$
NIPU-D	30%	no	19−24	0.2	0.5	30	40	28	1.05 ± 0.23	0.46
NIPU-D	35%	no	24	0.2	0.5	30	40	28	2.42 ± 0.01	0.59
NIPU-D	25%	yes	23	0.4	0.5	20	35	28	1.11 ± 0.03	0.34
NIPU-D	30%	yes	22	0.4	0.5	20	35	28	1.23 ± 0.23	0.36
NIPU-D	35%	yes	23	0.4	0.5	20	35	28	2.53 ± 0.27	0.76

[a]U: electrical potential, φ: flow speed, CID: cannula inner diameter, rH: relative humidity, T: temperature, and d: tip-to-collector distance. The average values refer to the mean of the fiber diameters and the inter-sample standard deviation ($n = 3$) and the spread refers to the mean of the standard deviation of the intra-sample fiber distributions. [b]The electrospun sample contained beads.
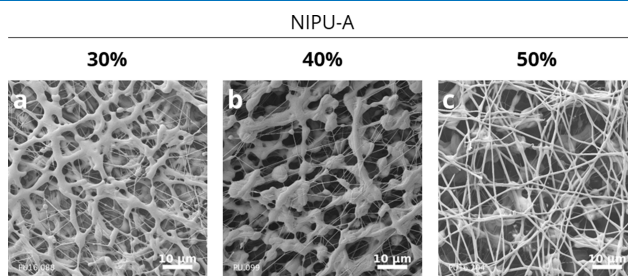
Figure 3. SEM micrographs of electrospun NIPU-A mats electrospun at 30 wt % (a), 40 wt % (b), and 50 wt % (c) in HFIP.
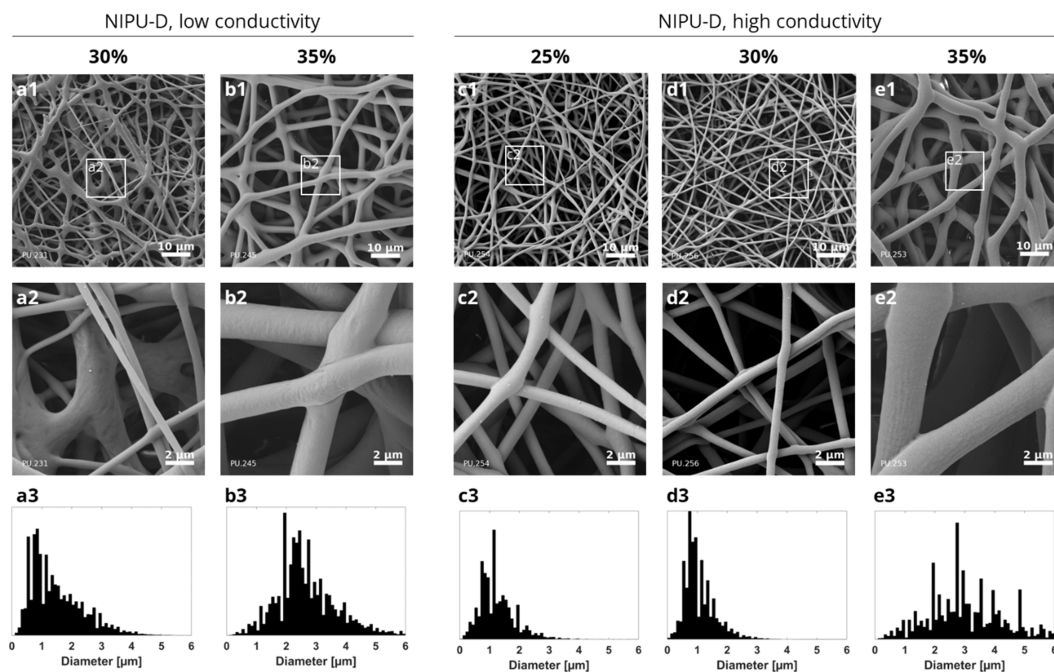
Figure 4. SEM micrographs and the corresponding intra-sample distribution of the fiber diameters of electrospun NIPU-D mats, which were electrospun at a concentration of 30 wt % (a) and 35 wt % (b) in HFIP with low conductivity (<0.1 μS/cm) and of those which were electrospun at a concentration of 25 wt % (c), 30 wt % (d), and 35 wt % (e) in HFIP with high conductivity (10 μS/cm).
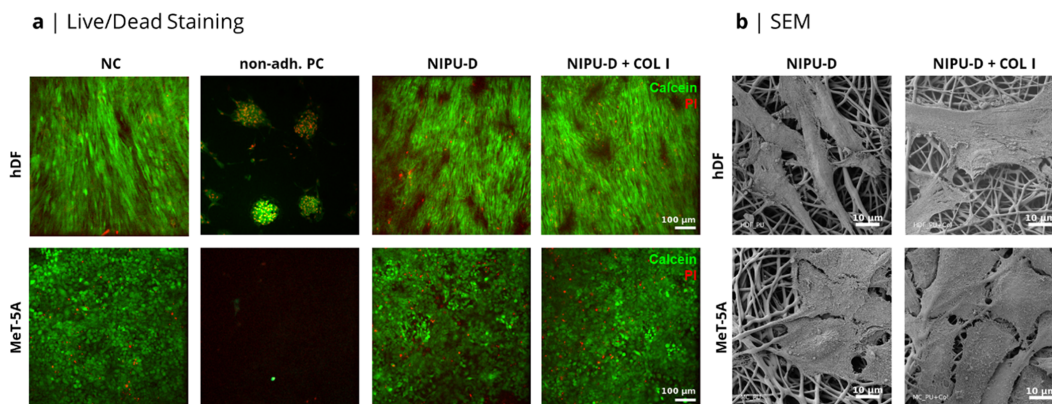
Figure 5. (a) Live/dead staining of hDFs and MeT-5A cells on electrospun NIPU-D mats after 7 days of static cell culture. (b) SEM images of hDFs and MeT-5A cells on electrospun NIPU-D mats after 24 h of static cell culture. NC: glass, non-adh. PC: Parafilm. Representative images from three independent experiments (n = 3).

spinning of NIPUs in DMF solutions yielded a small Taylor cone and a thin stable fiber (Figure S4b in ESI), there was no sign of a fibrous microstructure on the collector (Figure S4e in ESI). The electrospinning of NIPUs in THF solutions was considered to be unviable, as the relatively high vapor pressure of THF caused the solidification of the solutions at the tip of the cannula (Figure S4c in ESI), which prematurely halted the electrospinning process. Only electrospinning of NIPUs in HFIP solutions resulted in a partially fibrous scaffold (Figure S4d in ESI) when dissolved at concentrations of over 30 wt %. Because the electrospinning of NIPU-A based on PCDL 500 and with the highest molecular weight (M_w = 26,200 g/mol) in HFIP had shown the most promising results, further optimization of the electrospinning process was only conducted with HFIP as an electrospinning solvent.

High-molecular-weight NIPU-A (M_w = 26,200 g/mol) and NIPU-D (M_w = 58,600 g/mol), both based on PCDL500, were successfully electrospun into fibrous mats. An overview of the established electrospinning parameters that resulted in a stable fiber-yielding process and the corresponding average fiber diameters and spreads is listed in Table 2.

The formation of fibers during the electrospinning of NIPU-A started at a solution concentration of 30 wt % and improved with increasing the solution concentration up to 50 wt %, whilst the number of beads decreased (Figure 3). At the highest achieved concentration of 50 wt %, the NIPU-A mats were not bead-free. At higher concentrations (>50 wt %), the NIPU-A solutions became too viscous for electrospinning.

The first signs of fibers in NIPU-D mats started at a solution concentration of 30 wt % with an average fiber diameter of 1.05 ± 0.23 μm. At a higher concentration (35 wt %), the fiber diameter increased to 2.42 ± 0.01 μm and the fiber morphology improved, as the formation of molten junctions decreased (Figure 4a,b). The reduction of bead formation and the increase in the fiber diameter in NIPUs with a higher molecular weight and solution concentration can be attributed to the rheological properties of the electrospinning solution, which have already been observed in the electrospinning of traditional TPUs[43] as well as other polymers.[44−46] Moreover, the fibers in the NIPU-D mats had a more defined morphology compared to those in NIPU-A mats, which

strengthens the premise that higher molecular weights improve the electrospinnability of NIPUs. By increasing the solution conductivity to 10 μS/cm, via supplementing HFIP with sodium carbonate salt, the formation of fibers started at 25 wt % and slightly thickened at 30 wt % with fiber diameters being 1.11 ± 0.03 μm and 1.23 ± 0.28 μm. Compared to the NIPU mats electrospun out of unsupplemented HFIP, fibers were more separated and had more well-defined round cross-sections (Figure 4c,d). Furthermore, the intra-sample fiber diameter spread was narrowed and the fibrous mats contained a few molten fibers up to a concentration of 30 wt %. Because electrospinning of NIPU-D at 25 wt % in supplemented HFIP was found to be the most stable electrospinning process with the smallest intra-sample fiber diameter spread (0.34 ± 0.01 μm), these process parameters (Table 2) were selected for the creation of electrospun mats for biocompatibility tests.

3.3. Biocompatibility of Electrospun Mats. To assess the suitability of electrospun NIPU mats as a possible pericardial substitute in cardiac tissue engineering, the ability of the mats to facilitate the adhesion and proliferation of fibroblasts and epithelial cells was investigated in vitro. The relative viabilities for the L929 cells cultured in NIPUs' medium extracts were over 70% (Figure S5 in ESI); therefore, none of the synthesized NIPUs were considered to be cytotoxic. The electrospinning of NIPUs did not negatively affect the relative viability of the L929 cells in the medium extracts. It means that vacuum drying was sufficient to remove any remaining HFIP residues.

Most TPUs are known to be hydrophobic with no natural recognition sites for cells, which can hinder their application in tissue engineering. Therefore, their surfaces are commonly modified through the surface immobilization of biomolecules to improve the interfacial properties.[47] Here, the electrospun NIPU-D mats were functionalized with collagen to investigate the effect of biofunctionalization on biocompatibility. The collagen functionalization only minimally decreased the contact angle of mats from 101 ± 6° to 98 ± 2° (Figure S6 in ESI), although the immunological staining against collagen I confirmed the successful surface adsorption of collagen on the fibers (Figure S7 in ESI). The performance of the bare and collagen-functionalized electrospun NIPU-D mats was eval-

uated after 24 h and 7 days of static culture employing live/dead staining with calcein and PI (Figure 5a). The used MeT-5A (epithelial cells) originated from the pleural mesothelial membrane, comprising squamous epithelial cells. The same simple squamous epithelial cells line the outermost pericardial layer toward the serous cavity.[48−50] After 24 h, both fibroblasts and epithelial cells stained predominantly positive for calcein, except for some scarcely distributed PI-positive epithelial cells on the bare mats. (Figure S8 in ESI). After 7 days, both cell types formed almost confluent cell layers and were almost exclusively stained calcein-positive on both mats.

Furthermore, the morphology and the arrangement of both cell types on the bare and collagen-functionalized electrospun NIPU mats reflected those on the negative control (glass) by this time point. The hDFs presented an almost confluent layer of spindle-shaped fibroblasts, whereas the MeT-5A cells showed an anticipated cobblestone morphology in a closely packed arrangement. As expected, the cells barely adhered to the nonadherent positive control (Parafilm). Both cell types displayed adhesion and interaction with the bare and collagen-functionalized electrospun NIPU mats by using their filopodia, which is observed in the SEM images (Figure 5b). Moreover, the SEM images revealed the cobblestone morphology of the epithelial cells and the tendency to form a closely packed single-cell layer. Despite the high contact angles, both mats provided a highly biocompatible substrate for the cultured cells. More specifically, the bare mats performed as well as the biofunctionalized mats, which shows that the electrospun NIPU mats can be very well employed as a three-dimensional scaffold without further processing. These biocompatibility studies indicate that the bare electrospun NIPU mats do not pose any adverse effects on cell proliferation and are an interesting candidate for use in tissue engineering applications. Although the comparison against a commercially available TPU was not considered in the present study, live/dead staining may not reveal increased biocompatibility in a direct comparison between NIPUs and conventional TPUs.[8] TPUs generally owe their biocompatibility to their high stability, unless their hard-segment chemistry is modified to be more prone to hydrolytic degradation.[51,52] Implanted biomaterials usually become subject to such hydrolytic activities during inflammatory responses, for example, through cholesterol esterase.[53−55] To prevent the release of potentially harmful hard-segment degradation products, attempts have been made to replace aromatic diisocyanates in favor of aliphatic diisocyanates, for example, 1,6-butane diisocyanate (BDI), that are expected to yield naturally occurring degradation products, such as putrescine (1,4-butane diamine).[56] However, the use of aliphatic isocyanates, including BDI, highly increases the hydrolytic degradation rate, and the use of diisocyanates in the synthesis still poses a major health concern. Here, we showed that isocyanates and tin-based catalysts can be entirely eliminated in the production chain of electrospun TPU grafts, while the easy processability of TPU in electrospinning is retained. Still, the solubilization of these NIPUs required the use of HFIP, a fluorinated solvent, which is not quite devoid of safety concerns. Further risk reduction can be achieved by exploring electrospinning processes that do not require fluorinated solvents, such as solvent-free melt electrowriting, and hence further improve the sustainability of TPU graft production.

4. CONCLUSIONS

To reduce the environmental and human health dangers in the production of nonwoven PC-based TPU mats, it is key to establish a green synthesis route, which eliminates the use of isocyanates and tin-based catalysts. Here, we demonstrated a synthesis route through transurethanization with the use of 1,6-HDC and PCDLs with different molecular weights. The lower viscosity of PCDL500 and continuous stirring under reduced pressure aided the extraction of methanol and allowed for the synthesis of NIPUs with the highest molecular weights. The highest achieved molecular weight (M_w) was 58,600 g/mol, which proved to be sufficiently high for a fiber-yielding electrospinning process. Fiber formation was observed in PCDL500-based NIPUs with an M_w starting at 26,200 g/mol with increasing solution concentration and considerably improved in NIPU-D with an even higher M_w of 58,600 g/mol. Despite high water contact angles, the bare electrospun NIPU mats did not underperform in comparison to collagen-functionalized mats because both fibroblasts and epithelial cells displayed good adhesion and proliferation. These in vitro investigations of the electrospun NIPU mats showed that they bear great potential in biomimetic cardiac scaffolds.

■ ASSOCIATED CONTENT

ⓢ Supporting Information

The Supporting Information is available free of charge at https://pubs.acs.org/doi/10.1021/acsomega.2c03731.

> ^{1}H-NMR spectrum for PCDL500 in CDCl$_3$; ^{1}H-NMR spectrum for 1,6-HDC in CDCl$_3$; reaction parameters for the synthesis of NIPUs; DSC curves of NIPUs; optical and SEM images for the electrospinning of NIPUs with different electrospinning solvents; relative viability of L929 cells in medium extracts of NIPUs assessed using MTT assay; contact angle for water droplets on electrospun NIPU-D mats; and collagen immunostaining and live/dead staining (PDF)

■ AUTHOR INFORMATION

Corresponding Authors

Dmitri Visser − NMI Natural and Medical Science Institute at the University of Tübingen, 72770 Reutlingen, Germany; ⓞ orcid.org/0000-0002-8868-9265; Phone: +49 (0) 7121 51530-292; Email: dmitri.visser@nmi.de

Hadi Bakhshi − Department of Life Science and Bioprocesses and Department of Functional Polymer Systems, Fraunhofer Institute for Applied Polymer Research IAP, 14476 Potsdam, Germany; Phone: +49 (0) 331-568-1425; Email: hadi.bakhshi@iap.fraunhofer.de

Authors

Katharina Rogg − NMI Natural and Medical Science Institute at the University of Tübingen, 72770 Reutlingen, Germany

Ellena Fuhrmann − NMI Natural and Medical Science Institute at the University of Tübingen, 72770 Reutlingen, Germany

Franziska Wieland − Department of Functional Polymer Systems, Fraunhofer Institute for Applied Polymer Research IAP, 14476 Potsdam, Germany

Katja Schenke-Layland − NMI Natural and Medical Science Institute at the University of Tübingen, 72770 Reutlingen, Germany; Institute of Biomedical Engineering, Dept. for Medical Technologies and Regenerative Medicine and Cluster

of Excellence iFIT (EXC 2180) "Image-Guided and Functionally Instructed Tumor Therapies", Eberhard Karls University Tübingen, 72076 Tübingen, Germany; orcid.org/0000-0001-8066-5157

Wolfdietrich Meyer − *Department of Life Science and Bioprocesses and Department of Functional Polymer Systems, Fraunhofer Institute for Applied Polymer Research IAP, 14476 Potsdam, Germany;* orcid.org/0000-0003-1330-2887

Hanna Hartmann − *NMI Natural and Medical Science Institute at the University of Tübingen, 72770 Reutlingen, Germany;* orcid.org/0000-0001-9643-998X

Complete contact information is available at:
https://pubs.acs.org/10.1021/acsomega.2c03731

Notes

The authors declare no competing financial interest.
hDFs were isolated from juvenile foreskin under ethics approval no 495/2018BO2 from the University Hospital of Tübingen, Germany.

REFERENCES

(1) Lockey, J. E.; Redlich, C. A.; Streicher, R.; Pfahles-Hutchens, A.; Hakkinen, P. J.; Ellison, G. L.; Harber, P.; Utell, M.; Holland, J.; Comai, A.; White, M. Isocyanates and human health: Multi-stakeholder information needs and research priorities. *J. Occup. Environ. Med.* **2015**, *57*, 44.

(2) Redlich, C.; Bello, D.; Wisnewski, A.; Health effects of isocyanates. In *Environmental and occupational medicine*, 4th ed.; Rom, W.; Markowitz, S., Eds.; Lippincott Williams & Wilkins, 2007; pp 502−515.

(3) Allport, D. C.; Gilbert, D. S.; Outterside, S.; *MDI and TDI: safety, health and the environment: a source book and practical guide.* John Wiley & Sons, 2003.

(4) Gagné, S.; Lesage, J.; Ostiguy, C.; Van Tra, H. Determination of unreacted 2,4-toluene diisocyanate (2,4TDI) and 2,6-toluene diisocyanate (2,6TDI) in foams at ultratrace level by using HPLC-CIS-MS-MS. *Analyst* **2003**, *128*, 1447−1451.

(5) Krone, C. A.; Ely, J. T. A.; Klingner, T.; Rando, R. J. Isocyanates in flexible polyurethane foams. *Bull. Environ. Contam. Toxicol.* **2003**, *70*, 328−335.

(6) Nath, M. Toxicity and the cardiovascular activity of organotin compounds: A review. *Appl. Organomet. Chem.* **2008**, *22*, 598−612.

(7) Tanzi, M. C.; Verderio, P.; Lampugnani, M. G.; Resnati, M.; Dejana, E.; Sturani, E. Cytotoxicity of some catalysts commonly used in the synthesis of copolymers for biomedical use. *J. Mater. Sci.: Mater. Med.* **1994**, *5*, 393−396.

(8) Aduba, D. C.; Zhang, K.; Kanitkar, A.; Sirrine, J. M.; Verbridge, S. S.; Long, T. E. Electrospinning of plant oil-based, non-isocyanate polyurethanes for biomedical applications. *J. Appl. Polym. Sci.* **2018**, *135*, 46464.

(9) Pramanik, S. K.; Sreedharan, S.; Singh, H.; Khan, M.; Tiwari, K.; Shiras, A.; Smythe, C.; Thomas, J. A.; Das, A. Mitochondria targeting non-isocyanate-based polyurethane nanocapsules for enzyme-triggered drug release. *Bioconjugate Chem.* **2018**, *29*, 3532−3543.

(10) Zhao, Y.; Xia, X.; Zhou, J.; Huang, Z.; Lei, F.; Tan, X.; Yu, D.; Zhu, Y.; Xu, H. Thermoresponsive behavior of non-isocyanate poly(hydroxy)urethane for biomedical composite materials. *Adv. Compos. Hybrid Mater.* **2021**, *5*, 843−852.

(11) Ghasemlou, M.; Daver, F.; Ivanova, E. P.; Adhikari, B. Synthesis of green hybrid materials using starch and non-isocyanate polyurethanes. *Carbohydr. Polym.* **2020**, *229*, No. 115535.

(12) Matsumoto, K.; Kokai, A.; Endo, T. Synthesis and properties of novel poly(hydroxyurethane) from difunctional alicyclic carbonate and m-xylylenediamine and its possibility as gas barrier materials. *Polym. Bull.* **2016**, *73*, 677−686.

(13) Shen, Z.; Zhang, J.; Zhu, W.; Zheng, L.; Li, C.; Xiao, Y.; Liu, J.; Wu, S.; Zhang, B. A solvent-free route to non-isocyanate poly-(carbonate urethane) with high molecular weight and competitive mechanical properties. *Eur. Polym. J.* **2018**, *107*, 258−266.

(14) Deng, Y.; Li, S.; Zhao, J.; Zhang, Z.; Zhang, J.; Yang, W. Crystallizable and tough aliphatic thermoplastic poly(ether urethane)s synthesized through a non-isocyanate route. *RSC Adv.* **2014**, *4*, 43406−43414.

(15) Wołosz, D.; Parzuchowski, P. G.; Świderska, A. Synthesis and characterization of the non-isocyanate poly(carbonate-urethane)s obtained via polycondensation route. *Eur. Polym. J.* **2021**, *155*, No. 110574.

(16) Khan, I.; Smith, N.; Jones, E.; Finch, D. S.; Cameron, R. E. Analysis and evaluation of a biomedical polycarbonate urethane tested in an in vitro study and an ovine arthroplasty model. Part I: Materials selection and evaluation. *Biomaterials* **2005**, *26*, 621−631.

(17) Doshi, J.; Reneker, D. H. Electrospinning process and applications of electrospun fibers. *J. Electrost.* **1995**, *35*, 151−160.

(18) Liu, Y.; Teng, H.; Hou, H.; You, T. Nonenzymatic glucose sensor based on renewable electrospun Ni nanoparticle-loaded carbon nanofiber paste electrode. *Biosens. Bioelectron.* **2009**, *24*, 3329−3334.

(19) Lee, J. S.; Kwon, O. S.; Park, S. J.; Park, E. Y.; You, S. A.; Yoon, H.; Jang, J. Fabrication of ultrafine metal-oxide-decorated carbon nanofibers for DMMP sensor application. *ACS Nano* **2011**, *5*, 7992−8001.

(20) Mercante, L. A.; Scagion, V. P.; Migliorini, F. L.; Mattoso, L. H. C.; Correa, D. S. Electrospinning-based (bio)sensors for food and agricultural applications: A review. *TrAC, Trends Anal. Chem.* **2017**, *91*, 91−103.

(21) Lu, T.; Cui, J.; Qu, Q.; Wang, Y.; Zhang, J.; Xiong, R.; Ma, W.; Huang, C. Multistructured electrospun nanofibers for air filtration: a review. *ACS Appl. Mater. Interfaces* **2021**, *13*, 23293−23313.

(22) Lv, D.; Zhu, M.; Jiang, Z.; Jiang, S.; Zhang, Q.; Xiong, R.; Huang, C. Green electrospun nanofibers and their application in air filtration. *Macromol. Mater. Eng.* **2018**, *303*, No. 1800336.

(23) Khorshidi, S.; Solouk, A.; Mirzadeh, H.; Mazinani, S.; Lagaron, J. M.; Sharifi, S.; Ramakrishna, S. A review of key challenges of electrospun scaffolds for tissue-engineering applications. *J. Tissue Eng. Regener. Med.* **2016**, *10*, 715−738.

(24) Arab-Ahmadi, S.; Irani, S.; Bakhshi, H.; Atyabi, F.; Ghalandari, B. Immobilization of cobalt-loaded laponite/carboxymethyl chitosan on polycaprolactone nanofiber for improving osteogenesis and angiogenesis activities. *Polym. Adv. Technol.* **2021**, *32*, 4362−4372.

(25) Arab-Ahmadi, S.; Irani, S.; Bakhshi, H.; Atyabi, F.; Ghalandari, B. Immobilization of carboxymethyl chitosan/laponite on polycaprolactone nanofibers as osteoinductive bone scaffolds. *Polym. Adv. Technol.* **2021**, *32*, 755−765.

(26) Orafa, Z.; Irani, S.; Zamanian, A.; Bakhshi, H.; Nikukar, H.; Ghalandari, B. Coating of laponite on PLA nanofibrous for bone tissue engineering application. *Macromol. Res.* **2021**, *29*, 191−198.

(27) Lamba, N. M. K.; Woodhouse, K. A.; Cooper, S. L.; The Chemistry of Polyurethane Copolymers. In *Polyurethanes in Biomedical Applications*, 1st ed.; CRC Press, 2017; pp 5−25.

(28) Kucinska-Lipka, J.; Gubanska, I.; Janik, H.; Sienkiewicz, M. Fabrication of polyurethane and polyurethane based composite fibres by the electrospinning technique for soft tissue engineering of cardiovascular system. *Mater. Sci. Eng., C* **2015**, *46*, 166−176.

(29) Kidoaki, S.; Kwon, I. K.; Matsuda, T. Mesoscopic spatial designs of nano-and microfiber meshes for tissue-engineering matrix and scaffold based on newly devised multilayering and mixing electrospinning techniques. *Biomaterials* **2005**, *26*, 37−46.

(30) Baudis, S.; Ligon, S. C.; Seidler, K.; Weigel, G.; Grasl, C.; Bergmeister, H.; Schima, H.; Liska, R. Hard-block degradable thermoplastic urethane-elastomers for electrospun vascular prostheses. *J. Polym. Sci., Part A: Polym. Chem.* **2012**, *50*, 1272−1280.

(31) Daum, R.; Visser, D.; Wild, C.; Kutuzova, L.; Schneider, M.; Lorenz, G.; Weiss, M.; Hinderer, S.; Stock, U. A.; Seifert, M.; Schenke-Layland, K. Fibronectin adsorption on electrospun synthetic vascular grafts attracts endothelial progenitor cells and promotes endothelialization in dynamic in vitro culture. *Cell* **2020**, *9*, 778.

(32) Stankus, J. J.; Guan, J.; Fujimoto, K.; Wagner, W. R. Microintegrating smooth muscle cells into a biodegradable, elastomeric fiber matrix. *Biomaterials* **2006**, *27*, 735−744.

(33) Uttayarat, P.; Perets, A.; Li, M.; Pimton, P.; Stachelek, S. J.; Alferiev, I.; Composto, R. J.; Levy, R. J.; Lelkes, P. I. Micropatterning of three-dimensional electrospun polyurethane vascular grafts. *Acta Biomater.* **2010**, *6*, 4229−4237.

(34) Amoroso, N. J.; D'Amore, A.; Hong, Y.; Rivera, C. P.; Sacks, M. S.; Wagner, W. R. Microstructural manipulation of electrospun scaffolds for specific bending stiffness for heart valve tissue engineering. *Acta Biomater.* **2012**, *8*, 4268−4277.

(35) Puperi, D. S.; Kishan, A.; Punske, Z. E.; Wu, Y.; Cosgriff-Hernandez, E.; West, J. L.; Grande-Allen, K. J. Electrospun polyurethane and hydrogel composite scaffolds as biomechanical mimics for aortic valve tissue engineering. *ACS Biomater. Sci. Eng.* **2016**, *2*, 1546−1558.

(36) Motiwale, S.; Russell, M. D.; Conroy, O.; Carruth, J.; Wancura, M.; Robinson, A.; Cosgriff-Hernandez, E.; Sacks, M. S. Anisotropic elastic behavior of a hydrogel-coated electrospun polyurethane: Suitability for heart valve leaflets. *J. Mech. Behav. Biomed. Mater.* **2022**, *125*, No. 104877.

(37) Şenel Ayaz, H. G.; Perets, A.; Ayaz, H.; Gilroy, K. D.; Govindaraj, M.; Brookstein, D.; Lelkes, P. I. Textile-templated electrospun anisotropic scaffolds for regenerative cardiac tissue engineering. *Biomaterials* **2014**, *35*, 8540−8552.

(38) D'Amore, A.; Yoshizumi, T.; Luketich, S. K.; Wolf, M. T.; Gu, X.; Cammarata, M.; Hoff, R.; Badylak, S. F.; Wagner, W. R. Bi-layered polyurethane − Extracellular matrix cardiac patch improves ischemic ventricular wall remodeling in a rat model. *Biomaterials* **2016**, *107*, 1−14.

(39) Tao, Z. W.; Jarrell, D. K.; Robinson, A.; Cosgriff-Hernandez, E. M.; Jacot, J. G. A prevascularized polyurethane-reinforced fibrin patch improves regenerative remodeling in a rat right ventricle replacement model. *Adv. Healthcare Mater.* **2021**, *10*, No. 2101018.

(40) Sun, D. L.; Xie, S. J.; Deng, J. R.; Huang, C. J.; Ruckenstein, E.; Chao, Z. S. CH3COONa as an effective catalyst for methoxycarbonylation of 1,6-hexanediamine by dimethyl carbonate to dimethylhexane-1,6-dicarbamate. *Green Chem.* **2010**, *12*, 483−449.

(41) Stadelmann, K.; Weghofer, A.; Urbanczyk, M.; Maulana, T. I.; Loskill, P.; Jones, P. D.; Schenke-Layland, K. Development of a bi-layered cryogenic electrospun polylactic acid scaffold to study calcific aortic valve disease in a 3D co-culture model. *Acta Biomater.* **2022**, *140*, 364−378.

(42) Murphy, R.; Turcott, A.; Banuelos, L.; Dowey, E.; Goodwin, B.; Cardinal, K. O. SIMPoly: A matlab-based image analysis tool to measure electrospun polymer scaffold fiber diameter. *Tissue Eng., Part C* **2020**, *26*, 628−636.

(43) Mi, H.-Y.; Jing, X.; Jacques, B. R.; Turng, L.-S.; Peng, X.-F. Characterization and properties of electrospun thermoplastic polyurethane blend fibers: Effect of solution rheological properties on fiber formation. *J. Mater. Res.* **2013**, *28*, 2339−2350.

(44) Veleirinho, B.; Rei, M. F.; Lopes-Da-Silva, J. A. Solvent and concentration effects on the properties of electrospun poly(ethylene terephthalate) nanofiber mats. *J. Polym. Sci., Part B: Polym. Phys.* **2008**, *46*, 460−471.

(45) Filip, P.; Peer, P. Characterization of poly(ethylene oxide) nanofibers—mutual relations between mean diameter of electrospun nanofibers and solution characteristics. *Processes* **2019**, *7*, 948.

(46) Kim, K. W.; Lee, K. H.; Khil, M. S.; Ho, Y. S.; Kim, H. Y. The effect of molecular weight and the linear velocity of drum surface on the properties of electrospun poly (ethylene terephthalate) nonwovens. *Fibers Polym.* **2004**, *5*, 122−127.

(47) Ren, X.; Feng, Y.; Guo, J.; Wang, H.; Li, Q.; Yang, J.; Hao, X.; Lv, J.; Ma, N.; Li, W. Surface modification and endothelialization of biomaterials as potential scaffolds for vascular tissue engineering applications. *Chem. Soc. Rev.* **2015**, *44*, 5680−5742.

(48) Whitaker, D.; Papadimitriou, J. M.; Walters, M. N. I. The mesothelium and its reactions: A review. *Crit. Rev. Toxicol.* **1982**, *10*, 81−144.

(49) Mutsaers, S. E. The mesothelial cell. *Int. J. Biochem. Cell Biol.* **2004**, *36*, 9−16.

(50) Lachaud, C. C.; Rodriguez-Campins, B.; Hmadcha, A.; Soria, B. Use of mesothelial cells and biological matrices for tissue engineering of simple epithelium surrogates. *Front. Bioeng. Biotechnol.* **2015**, *3*, 117.

(51) Tanzi, M. C.; Mantovani, D.; Petrini, P.; Guidoin, R.; Laroche, G. Chemical stability of polyether urethanes versus polycarbonate urethanes. *J. Biomed. Mater. Res.* **1997**, *36*, 550−559.

(52) Santerre, J.; Woodhouse, K.; Laroche, G.; Labow, R. Understanding the biodegradation of polyurethanes: from classical implants to tissue engineering materials. *Biomaterials* **2005**, *26*, 7457−7470.

(53) Christenson, E. M.; Patel, S.; Anderson, J. M.; Hiltner, A. Enzymatic degradation of poly (ether urethane) and poly (carbonate urethane) by cholesterol esterase. *Biomaterials* **2006**, *27*, 3920−3926.

(54) Labow, R. S.; Meek, E.; Santerre, J. P. Synthesis of cholesterol esterase by monocyte-derived macrophages: a potential role in the biodegradation of poly (urethane) s. *J. Biomater. Appl.* **1999**, *13*, 187−205.

(55) Tang, Y.; Labow, R.; Santerre, J. Enzyme-induced biodegradation of polycarbonate-polyurethanes: Dependence on hard-segment chemistry. *J. Biomed. Mater. Res.* **2001**, *57*, 597−611.

(56) Guan, J.; Fujimoto, K. L.; Sacks, M. S.; Wagner, W. R. Preparation and characterization of highly porous, biodegradable polyurethane scaffolds for soft tissue applications. *Biomaterials* **2005**, *26*, 3961−3971.

S1

Supplementary Information

for

Green Chemistry for Biomimetic Materials: Synthesis and Electrospinning of High-Molecular-Weight Polycarbonate-Based Non-Isocyanate Polyurethanes

Dmitri Visser[a,*], Hadi Bakhshi[b,c,*], Katharina Rogg[a], Ellena Fuhrmann[a], Franziska Wieland[c], Katja Schenke-Layland[a,d,e], Wolfdietrich Meyer[b,c], Hanna Hartmann[a]
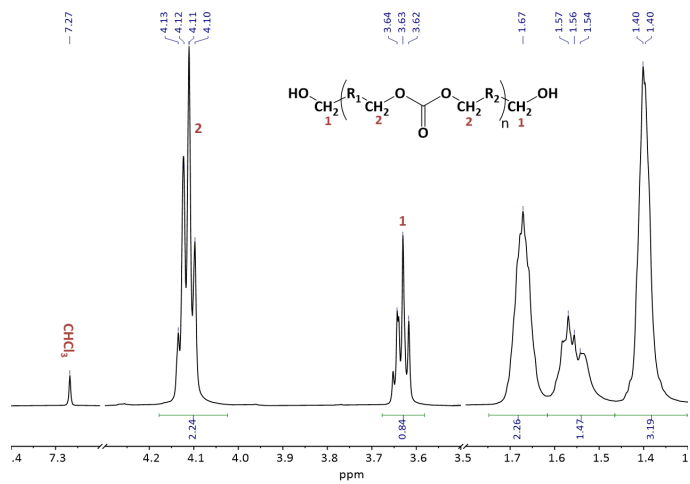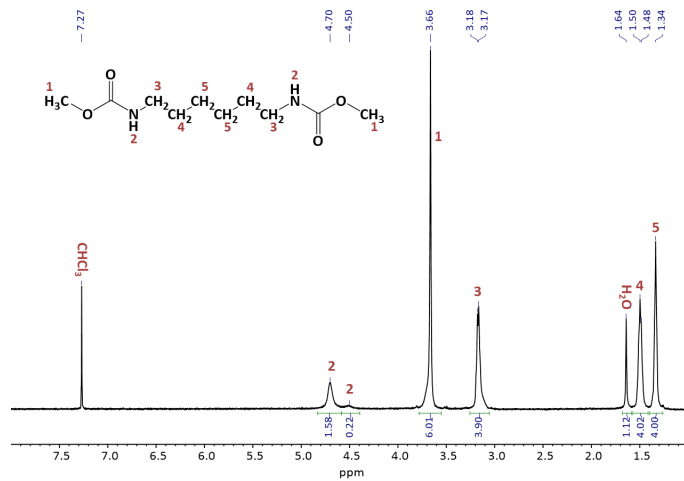
[a] NMI Natural and Medical Science Institute at the University of Tübingen, Markwiesenstrasse 55, 72770 Reutlingen, Germany

[b] Department of Life Science and Bioprocesses, Fraunhofer Institute for Applied Polymer Research IAP, Geiselbergstraße 69, 14476 Potsdam, Germany

[c] Department of Functional Polymer Systems, Fraunhofer Institute for Applied Polymer Research IAP, Geiselbergstraße 69, 14476 Potsdam, Germany

[d] Institute of Biomedical Engineering, Dept. for Medical Technologies and Regenerative Medicine, Eberhard Karls University Tübingen, 72076 Tübingen, Germany

[e] Cluster of Excellence iFIT (EXC 2180) "Image-Guided and Functionally Instructed Tumor Therapies", Eberhard Karls University Tübingen, 72076 Tübingen, Germany

*Corresponding authors: DV: E-mail: dmitri.visser@nmi.de, Tel: +49 (0) 7121 51530-292; HB: E-mail: hadi.bakhshi@iap.fraunhofer.de, Tel: +49 (0) 331-568-1425

Contents:

S2

Figure S1. ^{1}H-NMR spectrum for PCDL500 in CDCl$_3$.

Figure S2. ^{1}H-NMR spectrum for 1,6-HDC in CDCl3.

S3

Table S1. Reaction parameters for the synthesis of NIPUs.

| Run	MW of PCDL (g/mol)	PCDL (mmol)	1,6-HDC (mmol)	TBT (wt%)	Reaction parameters	GPC			
						M_n (g/mol)	M_w (g/mol)	M_p (g/mol)	PDI
500-1 (NIPU-A)	500	43.05	43.05	0.2-0.3	1. Mechanical stirring at 170°C for 4 h	–	–	–	–
					2. Keeping in a vacuum oven at 170°C for 2 h	14,200	26,200	20,900	1.85
500-7	500	43.05	43.05	0.2-0.3	1. Mechanical stirring at 170°C for 3 h	17,400	46,400	42,900	2.67
					2. Mechanical stirring at 170°C and 85 mbar for 1 h	–	–	–	–
					3. Keeping in a vacuum oven at 170°C for 3 h	The sample was insoluble in DMF.			
500-8 (NIPU-D)	500	43.05	43.05	0.2-0.3	1. Mechanical stirring at 170°C for 3 h	20,200	44,200	42,900	2.18
					2. Mechanical stirring at 170°C and 600 mbar for 1 h	19,700	48,400	37,700	2.46
					3. Keeping in a vacuum oven at 170°C for 3 h	24,300	58,600	42,200	2.41
1000-3 (NIPU-B)	1000	43.05	43.05	0.2-0.3	1. Mechanical stirring at 170°C for 3 h	–	–	–	–
					2. Keeping in a vacuum oven at 170°C for 3 h	8,800	14,500	12,100	1.60
2000-1 (NIPU-C)	2000	30.14	30.14	0.2-0.3	1. Mechanical stirring at 170°C for 2 h	–	–	–	–
					2. Keeping in a vacuum oven at 170°C for 3 h	10,400	18,700	15,000	1.80

S4
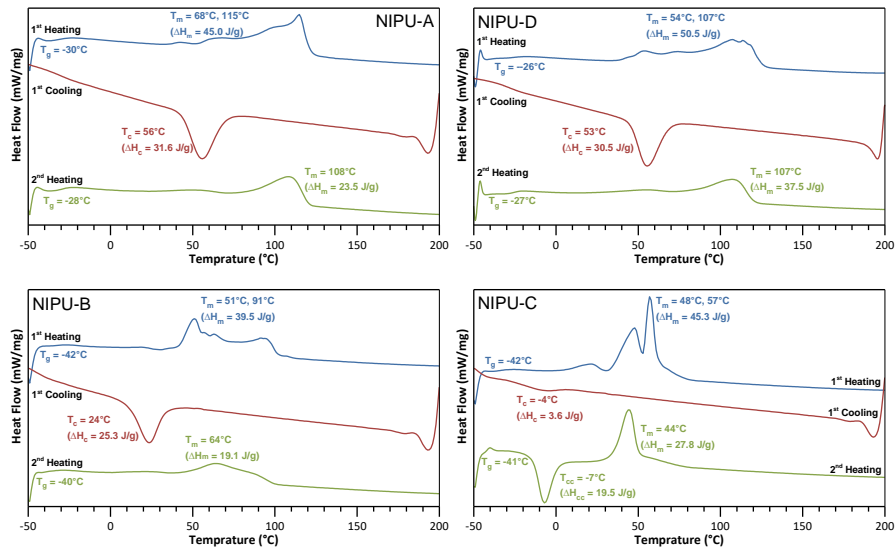
Figure S3. DSC curves of NIPUs
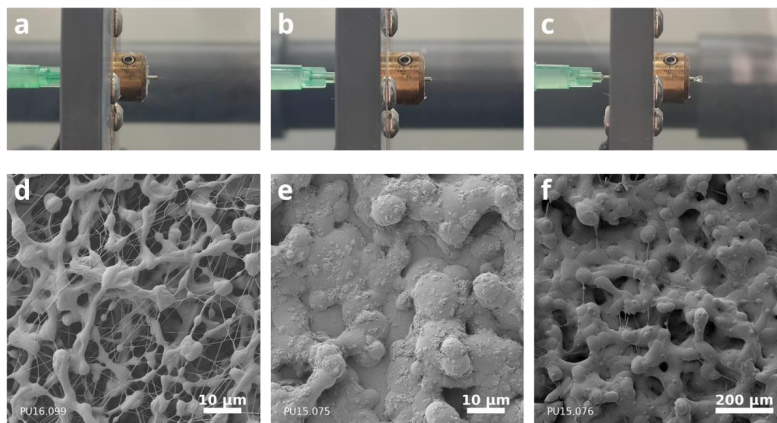
Figure S4. Representative optical and SEM images for the electrospinning of NIPUs with different electrospinning solvents: NIPU-A in HFIP (40 wt%) at 37°C (a and d), NIPU-B in DMF (40 wt%) at 23°C (b and e), and NIPU-B in THF (40 wt%) at 23°C (c and f). All solutions were electrospun using a 21G cannula corresponding to an inner diameter of 0.5 mm, an electrical potential of 23 kV, and a tip-to-collector distance of 25 cm.
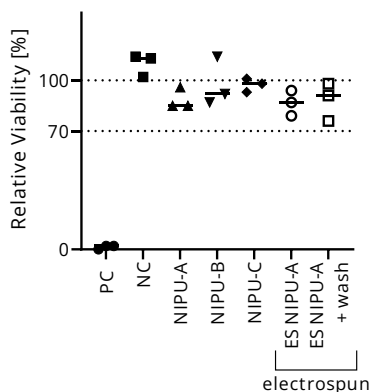
S5

Figure S5. Relative viability (normalized to blanks without material) of L929 cells in undiluted medium extracts of NIPUs assessed using MTT assay. PC: TPU film containing ZDEC (0.1%). NC: HDPE film.
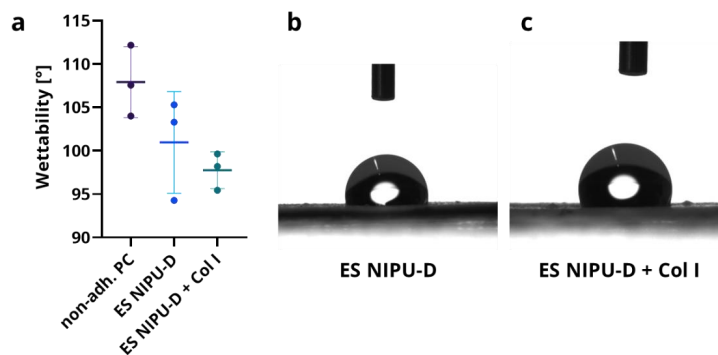

Figure S6. (a) Mean contact angle for water droplet after 20 seconds on bare electrospun NIPU-D mats (ES NIPU-D) and biofunctionalized electrospun NIPU-D mats (ES NIPU-D + Col I). Results are presented as mean ± SD (n = 3). The unpaired, two-sided t-test between ES NIPU-D and ES NIPU-D+Col I did not yield a statistically significant difference. Representative images of contact angle measurements of ES NIPU-D (b) and ES NIPU-D + Col I (c) were taken with an integrated drop shape analyzer camera system.
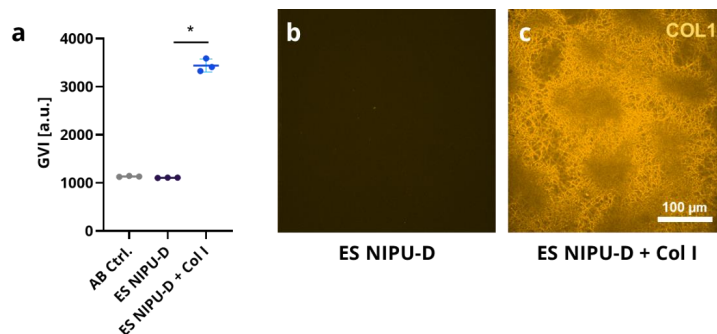
S6

Figure S7. (a) Mean gray-value intensities (GVI) of collagen immunostaining on bare electrospun NIPU-D mats (ES NIPU-D) and biofunctionalized electrospun NIPU-D mats (ES NIPU-D + Col I). To test the unspecific binding of the secondary antibody, a control without the primary collagen antibody was included as well (AB Ctrl.). Results are presented as mean ± SD (n = 3). The unpaired, two-sided t-test between ES NIPU-D and ES NIPU-D+Col I yielded a statistically significant difference (*: $p < 0.05$). Representative immunostaining images of collagen I on ES NIPU-D (b) and ES NIPU-D + Col I (c) were taken with a 20x objective.
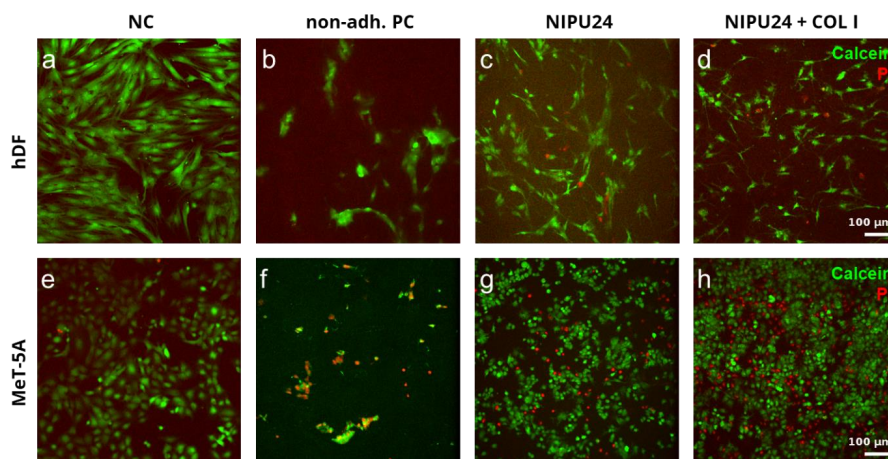

Figure S8. Live/Dead staining of hDFs (a-b) and MeT-5A (e-f) cells on electrospun NIPU-D mats after 24 hours of static cell culture. NC: glass, non-adh. PC: Parafilm. Representative images from three independent experiments (n=3).

Journal of Materials Chemistry B

PAPER

Electrospinning of collagen: enzymatic and spectroscopic analyses reveal solvent-independent disruption of the triple-helical structure†

Q1

Dmitri Visser, [ID] [a] Katharina Rogg,[a] Ellena Fuhrmann,[a] Julia Marzi,[abc] Katja Schenke-Layland [ID] [abc] and Hanna Hartmann*[a]

Electrospinning has become a well-established method for creating nanofibrous meshes for tissue-engineering applications. The incorporation of natural extracellular components, such as electrospun pure collagen nanofibers, has proven to be particularly challenging, as electrospun collagen nanofibers do not constitute native collagen fibers anymore. In this study, we show that this detrimental effect is not only limited to fluorinated solvents, as previously thought. Rat tail collagen was dissolved in acetic acid and ethanol and electrospun at various temperatures. Electrospun collagen mats were analyzed using circular dichroism, enzymatic digestion, SDS-PAGE, western blotting, and Raman spectroscopy and compared to heat-denatured and electrospun collagen in HFIP. Our data suggest that even non-fluorinated electrospinning solvents, such as acid-based solvents, do not yield structurally intact fibers. Interestingly, neither epithelial cells nor fibroblasts displayed a different cellular response to electrospun collagen compared to collagen-coated polyurethane scaffolds in F-actin staining and metabolic analysis using fluorescent lifetime imaging. The disruption of the structural integrity of collagen might therefore be underestimated based on the cell–material interactions alone. These observations expose the larger than anticipated vulnerability of collagen in the electrospinning process. Based on these findings, the influence of the electrospinning process on the distinct biochemical properties of collagen should always be considered, when ECM-mimicking fibrous constructs are manufactured.

Introduction

Collagen, the most abundant protein in all animals, is an extracellular protein, which plays the role of the major stress-bearing component of connective tissues.[1] Of all collagens found in the body, fibril-forming collagens are quantitatively the most important of the collagen family, including collagen type I, which accounts for over 70% of the total collagen.[2] Collagen is characterized by its unique supercoiled triple-helical arrangement of three alpha chains, stabilized by hydrogen bonds between hydroxyproline in adjacent chains.[3–6] The fibrous collagen found in skin and tendons additionally comprises intermolecular aldimine-type cross-links, which are easily broken in dilute acidic solvents.[7] Hence, these tissue types are often used to extract collagen for biomedical applications, as under appropriate *in vitro* conditions, the extracted collagen fibrils will self-assemble and return to insoluble collagen fibrils in aqueous media.[8,9]

Over the last two decades, electrospinning has emerged as a promising versatile technique to process a wide range of polymers into fibrous constructs for tissue engineering applications.[10] These fibrous scaffolds can have fiber diameters ranging from a few microns down to the submicron range, making electrospun materials ideal candidates to mimic the native extracellular matrix (ECM).[10] For this reason, electrospinning also has great potential in mimicking native collagen fibrils, as collagen fibrils found *in vivo* have diameters ranging from 20 nm to 40 μm.[2,11] Initial efforts to electrospin collagen were made using highly volatile fluorinated solvents, such as hexafluoroisopropanol (HFIP) and trifluoroethanol (TFE).[12–15] However, the use of fluorinated solvents has raised concerns

[a] MI Natural and Medical Sciences Institute at the University of Tübingen, Markwiesenstrasse 55, 72770 Reutlingen, Germany.
E-mail: hanna.hartmann@nmi.de; Tel: +49 (0) 7121 51530-872

[b] Institute of Biomedical Engineering, Department for Medical Technologies & Regenerative Medicine, Eberhard Karls University Tübingen, 72076 Tübingen, Germany

[c] Cluster of Excellence iFIT (EXC 2180) ''Image-Guided and Functionally Instructed Tumor Therapies'', Eberhard Karls University Tübingen, 72076 Tübingen, Germany

† Electronic supplementary information (ESI) available. See DOI: https://doi.org/10.1039/d2tb02602c

87

regarding the potential denaturation of the native structure of collagen.[16] One study reported by Zeugolis *et al.* showed that rat-tail collagen lost its crystalline and fibrillary structure after solubilization in HFIP and subsequent electrospinning, resulting in a water-soluble product that more closely resembled gelatin.[17]

Recent efforts have focused on the substitution of fluorinated solvents in favor of gentler solvents to retain the integrity of collagen.[18–22] Most of these substitutes were binary solvents, consisting of ethanol and a concentrated buffered saline,[23–26] acetic acid,[19,23] or hydrochloric acid.[27,28] Only a few studies, however, thoroughly addressed the collagen structure after electrospinning. Promising advances have been presented by Dems *et al*, who reported the preservation of the native triple helical structure by electrospinning collagen in a mixture of hydrochloric acid and ethanol and treating the product with ammonia vapor.[27] Some studies included cross-linking with glutaraldehyde or carbodiimides after electrospinning, which more or less disproves the success of the use of alternative solvents in the first place.[21,25,29] Solution viscosity and solvent volatility are two key conditions that should be satisfied for a stable electrospinning process. Although ethanol is understandably used in an attempt to increase the required solvent volatility, evidence exists that it might affect the native triple-helical structure of collagen.[30] Initial proof-of-principles and *in vitro* biocompatibility tests might not suffice to prove this, as the structural change of collagen does not directly impair cell–material interactions in *in vitro* or *in vivo* studies. However, assurance of the structural integrity of collagen is of high importance when collagen-containing tissue-engineered constructs enter market approval. The current state of the art of electrospun ECM-mimicking constructs raises the question of whether the electrospinning of pure collagen nanofibers remains an effective approach, if the biochemical properties of collagen are to be preserved.

In this study, acid-soluble rat tail collagen was directly electrospun in ethanol-containing binary solvents and consecutively characterized with a focus on the triple-helical structure, proteolytic resistance, and cell–material interactions. Using a climate-controlled chamber, we asserted that collagen was not subject to thermal denaturation in this process and limited the scope to solvent-related effects. We aimed to investigate the impact of solubilization and electrospinning on collagen and to examine whether the results from *in vitro* cell–material interaction studies correlate with a benign and successful electrospinning of collagen, using gentle electrospinning solvents.

Experimental

Materials

Glacial acetic acid and blotting grade powdered milk were obtained from Carl Roth (Karlsruhe, Germany). Ethanol absolute (>99%) from Fisher Scientific (Pittsburgh, PA, US). Hexafluoroisopropanol (HFIP) was obtained from Iris Biotech GmbH (Marktredwitz, Germany). Dulbecco's modified phosphate-buffered saline (DPBS) from Gibco (Thermo Fisher Scientific, Waltham, MA, US). Sodium dodecyl sulfate (SDS) electrophoresis supplies, including Bis-Tris gels, dithiothreitol (DTT) reducing agent, anti-oxidant, and MES SDS running buffer were obtained from Invitrogen (Thermo Fisher Scientific). Instant-Blue Coomassie protein stain was obtained from Abcam (Cambridge, UK). The nitrocellulose blotting membrane was obtained from GE Healthcare. Mouse anti-collagen I (NB600-450) primary antibody from Novus and AlexaFluor 647 donkey anti-mouse from Invitrogen (Thermo Fisher Scientific). All other materials were obtained from Sigma Aldrich (St. Louis, MO, US).

Collagen extraction

Collagen type I was isolated using an acid-based extraction from rat tail tendons, generously provided by the University Hospital of Tübingen. After extraction, the obtained collagen suspensions were lyophilized and stored at 4 °C until use.

Preparation of collagen solutions

Lyophilized rat tail collagen I foam was solubilized at various concentrations in different solvents (10x PBS/ethanol (1 : 1), 5 M acetic acid/ethanol (1 : 1 and 1 : 2), 30 mM hydrochloric acid/ethanol (1 : 3), and 5 M acetic acid/isopropanol (1 : 1), or HFIP). For collagen solutions in ethanol-containing binary solvents, collagen was first solubilized in the acid or DPBS at 4 °C overnight and, consecutively, ethanol was slowly added under continuous stirring to prevent precipitation. These solutions would then be spun to test the spinnability of collagen in different solvents.

To assess the impact of solubilization in acetic acid with ethanol, rat tail collagen was first solubilized in one part 5 M acetic acid, then two parts ethanol were added until a final collagen concentration between 22 and 33 mg mL^{-1} was obtained. As a control, rat tail collagen foam was dissolved at 4 wt% in HFIP. All solutions for electrospinning were prepared fresh.

Electrospinning procedure

The electrospinning process was performed using a climate-controlled EC-CLI electrospinning setup (IME Technologies, Waalre, The Netherlands) with a flat collector plate.

For the comparison of the spinnability of collagen in various solvents, the temperature and the relative humidity of the electrospinning chamber were varied between 20 and 37 °C and 5 and 20%, respectively.

The electrospinning samples for the investigation of collagen denaturation were spun with collagen in 5 M acetic acid/ethanol (1 : 2). To assess the impact of the environmental electrospinning parameters, this collagen solution was spun at 20, 25, and 30 °C (ES-HAc/EtOH-20, ES-HAc/EtOH-25, and ES-HAc/EtOH-30). The electrospinning chamber was additionally fed with nitrogen supply to obtain a relative air humidity of <10%. All experiments were conducted with a 21G cannula corresponding to an inner diameter of 0.5 mm and tip-to-

collector distance of 20 cm. The remaining electrospinning parameters (voltage and flow rate) were varied until a stable, fiber-yielding process was established. The control (ES-HFIP) was spun out of a 4 wt% collagen solution in HFIP.

Circular dichroism

Circular dichroism (CD) of collagen was measured with a J-720 spectropolarimeter (Jasco Co., Tokyo, Japan). Samples of both lyophilized and electrospun rat tail collagen type I were solubilized in 0.1 M acetic acid under continuous stirring at 4 °C overnight to get 1 mg mL^{-1} stock solutions. The final concentration of the samples was adjusted to 0.33 mg mL^{-1} by diluting the stock solution with 0.1 M acetic acid. Spectra were recorded between 250 and 195 nm at 0.2 nm intervals, made from five repeated scans at a scan rate of 20 nm min^{-1}, 4 s response time, and 1 nm bandwidth. Estimation of the folded fraction (θ) of collagen was obtained according to the following definition presented in Bürck et al.

$$\theta = \frac{\theta_{\text{obs}} - \theta_{\text{u}}}{\theta_{\text{t}} - \theta_{\text{u}}} \qquad (1)$$

where θ_{obs} is the observed maximal ellipticity and θ_{t} and θ_{u} represent the maximal ellipticity of collagen at 222 nm in an ordered and unordered state, respectively.[23] θ_{t} and θ_{u} were obtained from collagen samples, which had been solubilized in 0.1 M acetic acid under stirring for three hours at 4 °C and 70 °C respectively.

Enzymatic digestion, SDS-PAGE and western blotting

For enzymatic digestion, a 0.1 mg mL^{-1} alpha-chymotrypsin solution in DPBS was prepared. Collagen samples were dissolved at 1 mg mL^{-1} for digestion at 37 °C under agitation at 400 RPM for 10 minutes. Samples were denatured in DTT and boiled for 7 minutes. An equal amount of each sample was loaded onto a 4–12% Bis-Tris gel and analyzed using electrophoresis. Additionally, a prestained protein size marker, PageRulerPlus (Thermo Scientific), was loaded to estimate the apparent size of the collagen fragments. Protein bands were visualized with InstantBlue Coomassie Protein Stain overnight. The gel was briefly destained in distilled water for 10 minutes and imaged using an Odyssee Imager (LI-COR, Lincoln, NE, USA). Proteins were transferred in western blotting following the semi-wet procedure. In short, blotting was performed at 300 mA for 140 minutes. Consecutively, collagen type I was stained with mouse anti-collagen alpha I (NB600-450, Novus) and AF647 donkey anti-mouse (A-31571, Invitrogen). The membrane was scanned in a Typhoon Trio (GE Healthcare, Chicago, IL, USA) using an excitation wavelength of 633 nm.

Raman spectroscopy

Molecular fingerprinting of collagen foams and collagen mats was conducted with an alpha 300R inverse Raman microspectrometer (WITec), using an LD EC Epiplan-Neofluor 50× objective (Zeiss). Samples were excited with a 532 nm laser operating at 50 mW. At least 10 spectra were sampled at random locations of every sample by the accumulation of 5 measurements integrated over 0.5 seconds. Spectroscopic data were preprocessed using Project FIVE 5.2 (WITec) and analyzed by means of principal component analysis (PCA) in MATLAB using the nonlinear iterative partial least squares (NIPALS) algorithm. The source code of the MATLAB analysis package can be retrieved from GitHub (github.com/ksllabtue/ramat).

Cell culture

To facilitate the handling of the electrospun mats, while minimizing the required amount of collagen for the production of these mats, collagen was processed into collagen-polyurethane bilayer mats (ES-PUCOL). Briefly, a thin layer of collagen was spun atop fibrous non-isocyanate polyurethane mats (ES-PU), which provided structural support and had been produced and tested for biocompatibility as described previously.[31] The rat tail collagen was spun out of a 33 g L^{-1} collagen solution in 5 M acetic acid/ethanol (1:2) at a flow rate of 0.3 mL h^{-1} and voltage of 21 kV. To separate the effects of morphology and material, some ES-PU mats were coated with rat tail collagen to obtain coated biofunctionalized electrospun polyurethane mats (ES-PU + Col). All electrospun mats were then punched and clamped into 24 well cell crowns (Sigma Aldrich). ES-PUCOL mats were additionally cross-linked for 4 hours at RT in a 50 mM 1-ethyl-3-(3-dimethylaminopropyl)carbodiimide (EDC, Iris Biotech) and 20 mM N-hydroxysulfosuccinimide (Sulfo-NHS, BLDpharm) under tension in non-swelling acetonitrile (Fisher Chemical) solution and consecutively washed twice in the crosslinker-free solvent.[32] All electrospun mats were sterilized under UV light for 150 s and washed three times with DPBS+ prior to cell seeding. Primary human dermal (foreskin) fibroblasts (hDFs) and human epithelial cells (MeT-5A, ATCC) were cultured and seeded onto the scaffolds as described previously.[31] Briefly, hDFs were isolated from foreskin biopsies under approval by the local ethics committee at the Tübingen University Hospital (495/2018BO2 approved on 19th October, 2018). hDFs were seeded at $2.67 \cdots 10^5$ cells per cm^2 and hMCs were seeded at $4.00 \cdots 10^5$ cells per cm^2. Additionally, cells cultured on glass in regular cell culture media and in medium with 10% DMSO served as the negative (NC) and positive control (PC), respectively.

Microscopy

A Live/Dead staining using calcein (Invitrogen) and propidium iodide (PI, Sigma Aldrich) was performed 24 hours and 7 days after cell seeding. At the same time points, triplicates of each condition were fixed in 4% paraformaldehyde (PFA).

Cell morphology was then visualized by Phalloidin staining of F-actin fibers and with 4′,6-diamidino-2-phenylindole (DAPI) staining of cell nuclei and captured using a spinning-disk confocal microscope (Zeiss) through a 63× oil immersion objective.

Cell proliferation and metabolic activity of cells on the electrospun mats were assessed by means of fluorescence lifetime imaging microscopy (FLIM). Nicotinamide adenine dinucleotide (NADH) and flavin adenine dinucleotide (FAD) autofluorescence in living cultured cells was induced by two-photon excitation at a wavelength of 700 nm using a femtosecond pulsing Mai Tai laser (Spectra-Physics). The

This journal is © The Royal Society of Chemistry 2023

J. Mater. Chem. B, 2023, 00, 1–12 | 3

Paper

1 superpositioned decay curves of NAD(P)H and FAD were
acquired with a laser scanning microscope (LSM880, Zeiss)
through a $63\times$ objective. The fluorescence lifetimes of these
two components were estimated by bi-exponential decay fitting
5 using a weighted least-squares algorithm in SPCImage (Beck-
er&Hickl GmbH), yielding the relative concentration and
fluorescence lifetime of the free (α_1 and τ_1) and bound compo-
nent (α_2 and τ_2), as given in eqn (2).

$$I = \alpha_1 e^{-\frac{t}{\tau_1}} + \alpha_2 e^{-\frac{t}{\tau_2}} \qquad (2)$$

10 Analogously, this assay was performed 24 hours and 7 days
after the initial cell seeding.

Loss of the second harmonics generation (SHG) activity of
the collagen after electrospinning was exemplarily confirmed
by the aforementioned femtosecond pulsing laser set-up, using
excitation wavelengths of 864 nm and 936 nm. These two
wavelengths ensured that the SHG signal was observed at
halved wavelengths irrespective of the excitation wavelengths.

SEM analysis

Cell-loaded samples for SEM imaging were fixed in a three-step
process; first with 4% PFA in DPBS+ for 30 minutes, thereafter in
4% PFA and 2% glutaraldehyde (in DPBS-) for one hour, and
consecutively dehydrated with isopropanol through critical point
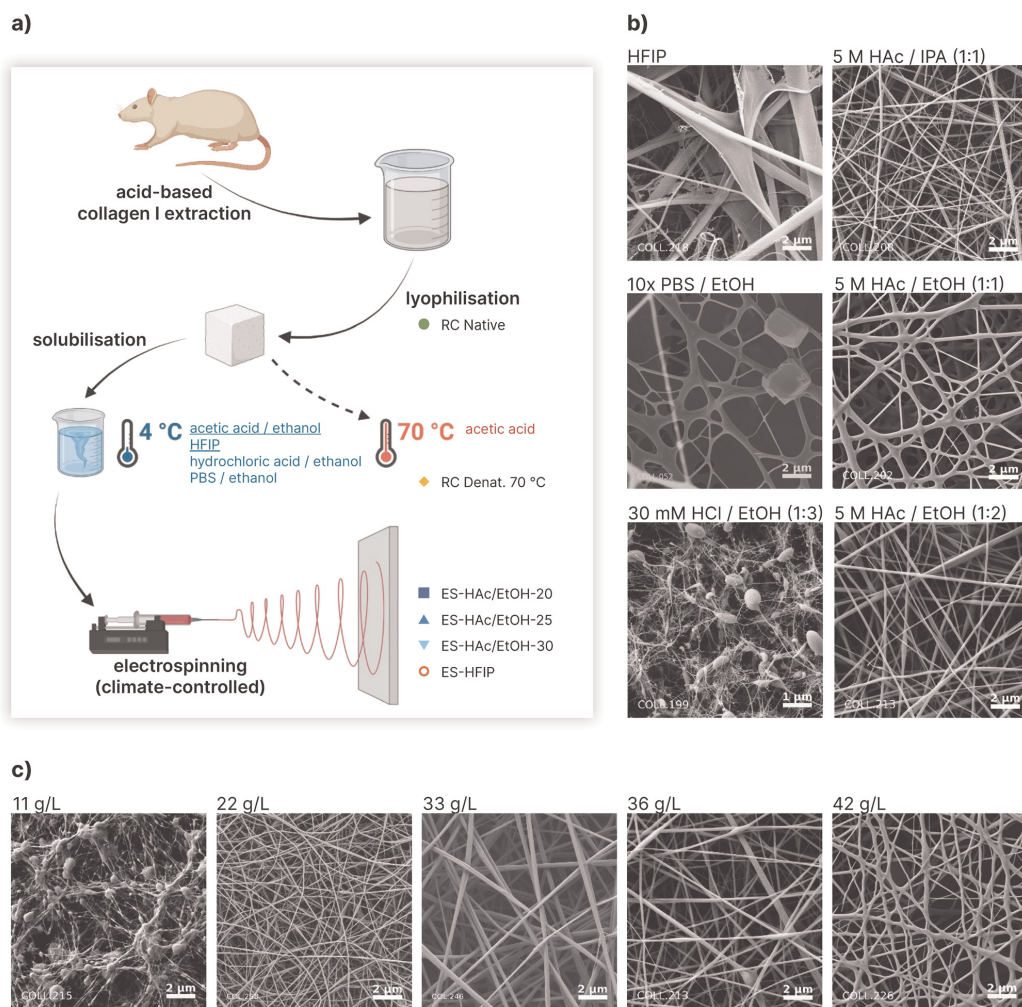

Fig. 1 Electrospinning of rat tail collagen I in various solvents. (a) Experimental overview and respective samples. (b) Solvent comparison between HFIP, $10\times$ PBS/ethanol, 30 mM hydrochloric acid/ethanol in a 1:3 ratio, acetic acid/isopropanol, 5 M acetic acid/ethanol in a 1:1 ratio and 5 M acetic acid/ethanol in a 1:2 ratio. (c) Comparison of different collagen concentrations in 5 M acetic acid/ethanol (1:2).

drying. The samples were coated with gold–palladium in a sputtering system (Balzers, SCD-040) for 20 seconds before microscopy. The morphology of electrospun samples was studied on a scanning electron microscope (SEM, Auriga 40, Zeiss) operating at an electron gun voltage of 3 kV using a secondary electron detector.

Statistical analyses

Data are represented as mean $\pm$ standard deviation of the biological replicates. Experiments were performed at least in biological triplicates ($n \geq 3$). For FLIM, fiber-containing parts of the images were masked, the medians of the fitted coefficients of eqn (2) for the remaining part of the microscopic image were taken as one technical replicate, every biological replicate consisted of multiple technical replicates. Differences between groups were assessed by the analysis of variance (ANOVA), p-values of 0.05 or less were considered statistically significant. GraphPad Prism 9 was used for all statistical analyses.

Results

Electrospinning of rat-tail collagen I

Acid-extracted and lyophilized rat-tail collagen I was solubilized in a number of solvents at various concentrations. These

collagen solutions were consecutively electrospun, whilst the electrospinning parameters were varied until a stable electrospinning process was achieved. SEM analysis revealed a greatly varying micromorphology, depending on the chosen solvent system shown in Fig. 1b. Collagen fibers spun at a concentration of 4 wt% in HFIP generally had low uniformity. Collagen fibers spun at 4 wt% in a mixture of $10\times$ PBS and ethanol, albeit more uniformly shaped, were partially molten together and contained salt crystals. The latter solvent system proved to be particularly challenging in the optimization of the electrospinning process, as droplets were frequently seen on the collector. The binary solvents with acetic acid and either ethanol or isopropanol yielded much more uniformly shaped collagen fibers, whilst also providing a sufficient evaporation rate to enable electrospinning, especially when the ethanol content was increased to a 1:2 ratio (Fig. 1c). The most uniformly distributed round fibers were achieved by electrospinning collagen in a combination of 5 M acetic acid with ethanol (1:2). This combination was the most versatile solvent for collagen, as it provided much room for tailoring the electrospinning parameters. It was found, that decreasing the temperature and relative humidity below 25 $^\circ$C and 6%, respectively, also enabled electrospinning at lower collagen concentrations down to 11 g L^{-1}.
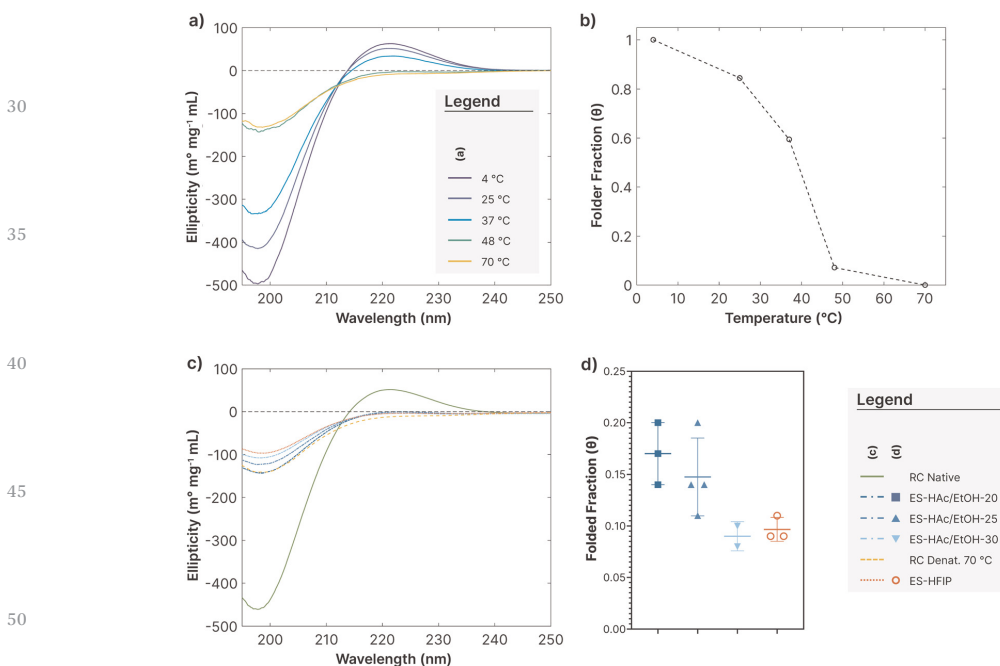
Fig. 2 CD Analysis of electrospun rat tail collagen type I. (a) CD spectra of rat tail collagen type I solubilized in 0.1 M acetic acid at different temperatures between 4 and 70 $^\circ$C, plotted as the ellipticity [m$^\circ$ mL mg^{-1}] as a function of the excitation wavelength [nm]. (b) Results from (a) plotted as the folded PP-II fraction as a function of solubilization temperature [$^\circ$C]. (c) CD spectra of collagen foam (RC Native) and electrospun (ES) collagen. ES-HAc/EtOH was spun with 5 M acetic acid/ethanol (1:2) at different temperatures. All samples were solubilized in 0.1 M acetic acid at 4 $^\circ$C, plotted as the ellipticity as a function of the excitation wavelength. (d) Results from (c), plotted as the folded PP-II fraction.

Circular dichroism

The CD spectra of native rat tail collagen, type I, solubilized at temperatures between 4 and 70 °C in 0.1 M acetic acid are displayed in Fig. 2a. The spectrum of collagen dissolved at 4 °C exhibited a characteristic sinusoidal curve, with a strong negative ellipticity band at 195 nm and a slightly weaker band at 220 nm. These bands got attenuated with increasing solubilization temperature. The folded polyproline-II (PP-II) fraction is given by eqn (1) and plotted in Fig. 2b.

Analogously, the CD spectra of electrospun collagen, electrospun in either 5 M acetic acid/ethanol (1 : 2) (ES-HAc/EtOH) at different temperatures (20, 25, and 30 °C) or HFIP (ES HFIP) and consecutively solubilized at 4 °C in 0.1 M acetic acid, are presented in Fig. 2c. with corresponding folded PP-II fractions in Fig. 2d. A similar attenuating effect with increasing temperature was observed in the CD spectra and the calculated folded PP-II fraction. However, electrospun collagen had only retained $15.7 \pm 2.0\%$ to $8.0 \pm 1.1\%$ of the triple helix in the folded state, when spun at 20 and 30 °C respectively. The majority of the collagen is, thus, in an unordered state, with increased unfolding at higher electrospinning temperatures.

Sodium dodecyl sulfate-polyacrylamide gel electrophoresis (SDS-PAGE)

After incubation with α-chymotrypsin, collagen samples were investigated by SDS-PAGE. The bands of the lyophilized, native rat tail collagen foam (RC Native in Fig. 3a) acted as a reference pattern in the SDS-PAGE analysis. The α_1(I) and α_2(I) bands are clearly visible at approximately 130 and 120 kDa, respectively. At higher molecular weights, dimers, β(I), and trimers, γ(I), were also clearly distinguishable. These bands were still visible in electrospun collagen (ES-HAc/EtOH), although the intensity of the bands was increasingly attenuated with increasing electrospinning temperatures (20, 25 and 30 °C). The native collagen control was not affected by the brief α-chymotrypsin digestion. However, electrospun collagen samples showed a significant loss in collagen α_1(I) and α_2(I) chains after 10 minutes of α-chymotrypsin digestion. In particular, the electrospun collagen samples of 25 and 30 °C and HFP-spun collagen did not have any clearly distinguishable protein bands over 115 kDa after digestion. Western blotting (Fig. 3b) confirmed aforementioned observations. Analogously, loss of α_1(I) chains was observed in electrospun collagen preparations, which had been spun at higher temperatures. Acid-spun collagen at 30 °C (ES HAc/EtOH, 30 °C), as well as HFIP-spun collagen (ES HFIP), did not stain positive for α_1(I). After digestion, intact α_1(I) chains were only observed in native collagen.

Raman spectroscopy

Collagen foams, both right after collagen extraction and after heat-induced denaturation at 70 °C, as well as electrospun collagen were analyzed by Raman spectroscopy (Fig. 4). Peak assignments with corresponding references are listed in Table 1. The three amide bands (amide I, II, and III) were observed in all analyzed samples with maximum intensities at wavelengths of 1664–1668, 1449–1453, and 1244–1249 cm^{-1}, respectively. Typical spectral markers for the primary structure of collagen were observed, including ν(C–C) in the proline and hydroxyproline ring at 814, 854–858, and 923–940 cm^{-1}, ring breathing of tyrosine at 854–858 cm^{-1}, and ν(C–C) in the phenylalanine ring at 1005 and 1030–1034 cm^{-1}.

In processed collagen samples, the maximum height of the amide III band was attenuated, its center shifted to higher wavenumbers and its width due to the formation of shoulders increased, when compared to native collagen (Fig. 4b, c). The height ratio between the amide III and amide II band decreased from 0.89 ± 0.02 in native collagen (RC Native) to 0.77 ± 0.2 in ES-HAc/EtOH-20, even lower than 0.78 ± 0.05 in heat-denatured collagen (RC Denat.) (Fig. 4c). The maximum of the amide III peak had shifted from 1244 cm^{-1} in native collagen to higher wavenumbers after electrospinning or heat denaturation (Fig. 4b). The formation of a shoulder at 1310–1323 cm^{-1} was clearly visible in the averaged Raman spectra of most processed collagen samples. Multivariate data analysis using principal component analysis (PCA) also underlined this observation (Fig. 4d, e). All processed collagen samples were significantly ($p < 0.01$) separated from native collagen by PC2 (Fig. 4e).
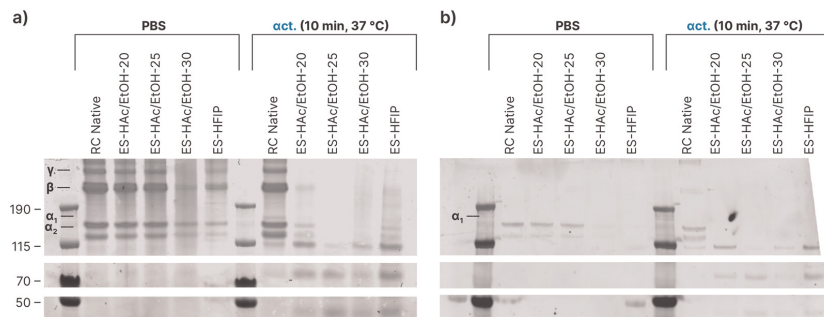

Fig. 3 Coomassie-stained SDS-PAGE analysis (a) and corresponding western blot against collagen α_1(I) (b) of PBS-solubilized and α-chymotrypsin-digested rat tail collagen, type I preparations. RC Native samples were not processed. Acid-spun collagen (ES-HAc/EtOH) was electrospun in 5 M acetic acid/ethanol (1 : 2). ES-HFIP collagen samples were spun in HFIP.
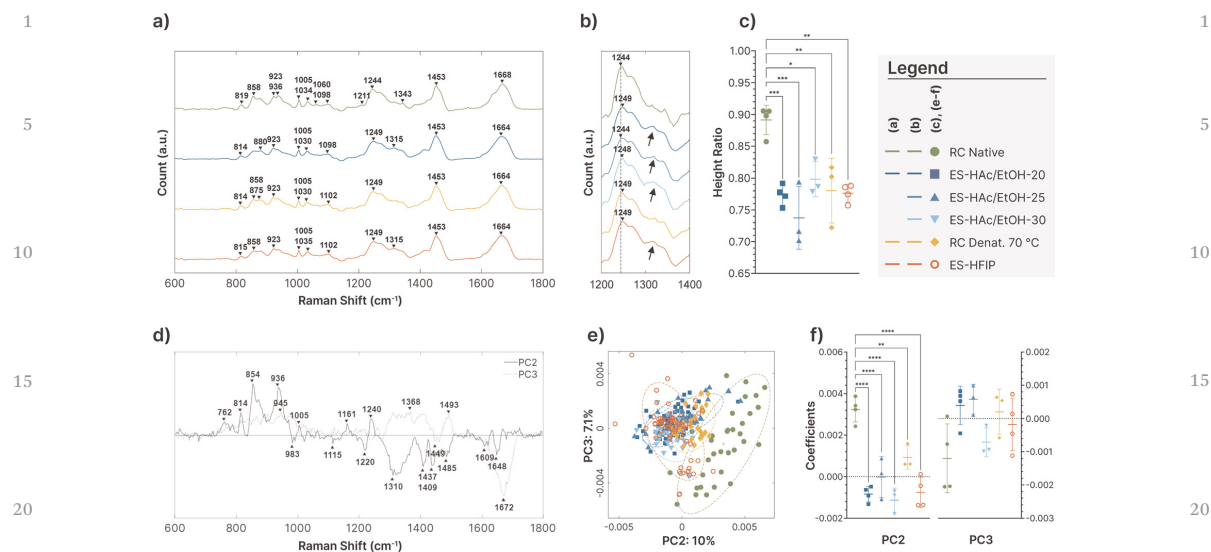
6 | *J. Mater. Chem. B*, 2023, **00**, 1–12

This journal is © The Royal Society of Chemistry 2023

Fig. 4 Raman spectroscopic analysis of native collagen I (RC Native), acid-spun collagen (ES-HAc), heat-denatured collagen (RC Denat.), and HFIP-spun collagen (ES-HFIP). (a) Averaged Raman spectra of selected samples and prominent peaks. Every condition was prepared at least in (biological) triplicate ($n > 3$). Multiple spectra were acquired for every replicate ($n_{tr} > 10$). (b) Changes in the amide III band, shoulder formation is indicated by the arrows. (c) Maximum height ratio between the amide III and amide II bands. (d–f) Results of the multivariate data analysis using principal component analysis (PCA) of the spectra between 600 and 1800 cm^{-1}, comprising the PCA spectral loadings of PC2 and PC3 in (d) and spectral scores (coefficients) in (e) and (f). Ellipses in (e) show 95% confidence intervals.

Table 1 Raman peak assignments with corresponding references

Raman shift	Assignment	Ref.
Proline and hydroxyproline region		
814	Proline, hydroxyproline	33
854	Ring breathing, tyrosine, ν(C–C), proline	34
858	Proline, hydroxyproline	33
858	Tyrosine	34 and 35
875, 880	ν(C–C), hydroxyproline	36
923	ν(C–C), proline, hydroxyproline	34, 37 and 38
936	C–C vibrations, carbonyl	39 and 40
936	ν(C–C), proline, α-helix	36
936	ν(C–C), α-helix, proline, hydroxyproline	33 and 38
1005	ν_s(C–C), phenylalanine	35
1030, 1035	Phenylalanine	33 and 35
Amide region		
1220	Amide III, β-sheet	34
1240–1248	Amide III, α-helix	41 and 42
1310–1368	Amide III shoulder, γ(CH$_3$, CH$_2$)	41
1409	Heat denaturation in cartilage	39
1453	Amide II, ν(C–N), N–H bending	38
1440–1444	δ(CH3, CH2) in collagen	43
1648	Amide I, α-helix	34 and 44
1668	Amide I, α-helix	35 and 36
1672	Amide I, β-sheet	44 and 45

Strong negative loadings for PC2 at 1220 and 1310 cm^{-1} and for PC3 around 1368 cm^{-1} indicate that amide III shoulders are absent in native rat tail collagen and only appear after electrospinning (Fig. 4d). PCA loading also indicate a loss of peaks at 814, 854 and 936 cm^{-1} in PC2. PC3 prominently discriminated the overall intensity at 1672 cm^{-1}, but samples were not statistically separated in this principal component.

Cell culture and cell-material interaction

F-actin staining, SEM, Live/Dead staining and FLIM were performed to analyze the cell interaction with collagen material after different processing, comparing electrospun polyurethane without collagen (ES-PU), with collagen coating (ES-PU + COL) or with collagen electrospun on top (ES-PUCOL). Uniform fiber morphology directly after carbodiimide crosslinking (Fig. S2b, ESI†) and retention of the collagen fiber morphology after 24 hours (Fig. S2c, ESI†) and 7 days (Fig. S2d, ESI†) of cell culture was confirmed through SEM. Microscopic pictures of F-actin/DAPI staining clearly visualize the development of cell morphology over time (Fig. 5a and b). After 24 hours, fibroblasts displayed mostly dendritic and heterogeneous organization on ES-PU mats. Fibroblasts on glass (control) and ES-PUCOL appeared slightly larger with more elongated nuclei. After 7 days, this contrast was no longer noticeable and the fibroblasts had adapted a distinctly polar and oriented morphology on all mats, similar to those on glass. Epithelial clustering of MeT-5A cells was observed after 24 hours, with cells on ES-PUCOL being slightly larger and more evenly spread than those on the polyurethane mats. After 7 days, this difference had largely disappeared, and all epithelial cell cultures had reached confluency on all mats.
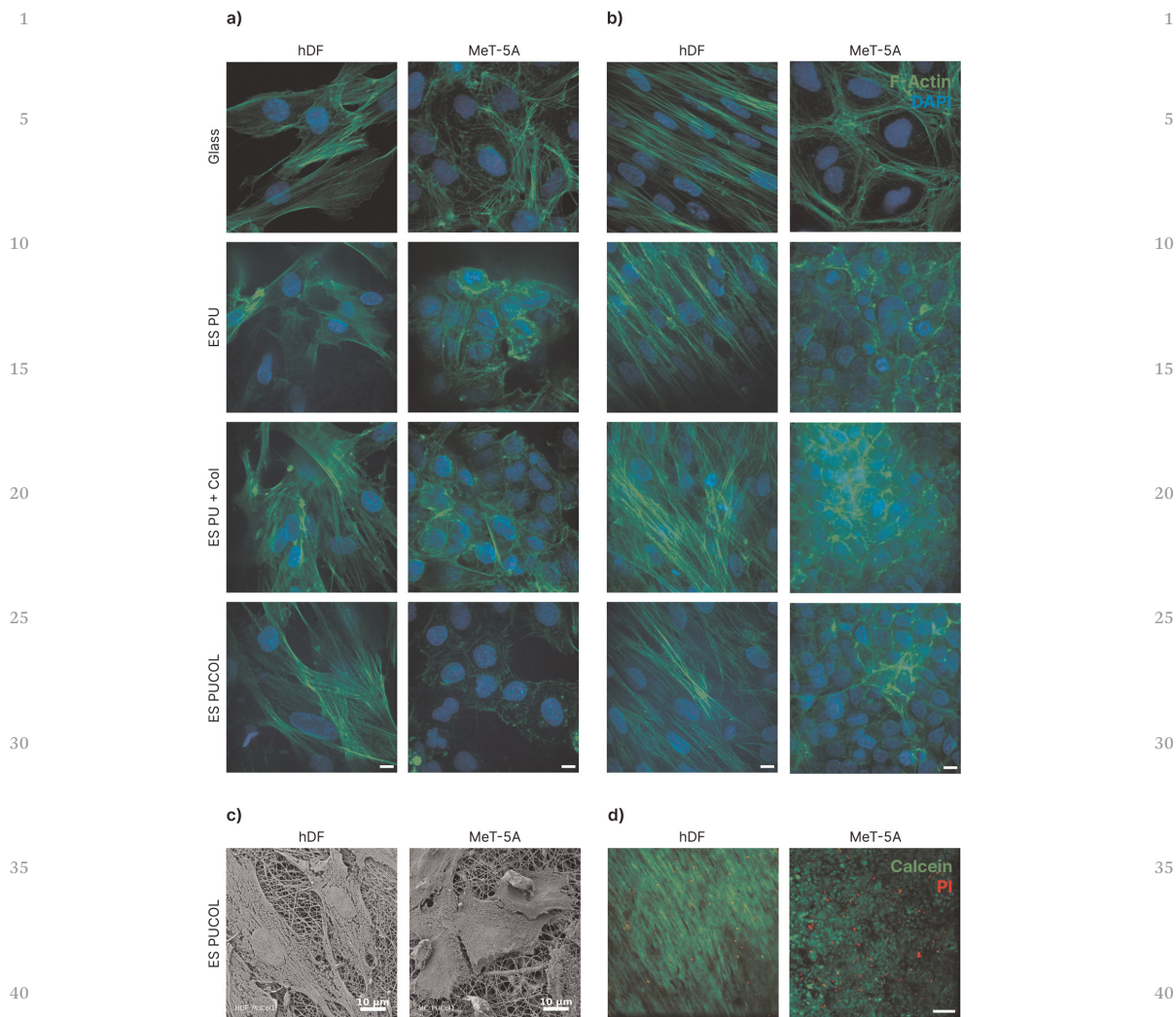
Fig. 5 Microscopic examination of cell-material interaction on electrospun mats. F-actin/DAPI staining of hDFs and MeT-5A on glass, electrospun polyurethane without (ES-PU) and with collagen coating (ES-PU + Col), and the electrospun combination of both (ES-PUCOL) after 24 hours (a) and 7 days (b). F-Actin (Phalloidin) in green, nuclei (DAPI) in blue. Scalebars in the F-Actin/DAPI stainings equal to 10 μm. (c) Scanning electron microscopy images of hDFs and MeT-5A cells on ES PUCOL after 24 hours. (d) Calcein/PI staining of hDFs and MeT-5A cells on electrospun polyurethane/collagen mats (ES PUCOL) after 7 days. Scalebar in the Live/Dead staining corresponds to 100 μm. Calcein in green, PI in red.

The nanoscale collagen fibers and the physical cell–material interaction through filopodia are visible in the SEM images in Fig. 5c. The slightly elongated nuclei of hDFs, as previously seen in the F-Actin/DAPI stainings were visible here as well. Live/Dead Staining with calcein and PI showed that both cell cultures retained a high viability on ES-PUCOL mats after 7 days of cell culture (Fig. 5d). The cells stained predominantly positive for calcein and only a few cells were stained positive for PI, indicating a high percentage of viable cells.

Cell response to different substrates was further analyzed by the changes in the metabolic state of cultured cells with FLIM. Photons originating from the electrospun substrate were successfully removed from the time-correlated single-photon counts using phasor masking (Fig. 6a and e). Second-order multiexponential decay fits yielded the relative concentration and fluorescence lifetime of free (α_1 and τ_1) and bound NAD(P)H (α_2 and τ_2). A significant difference in free NAD(P)H and fluorescence lifetime of free NAD(P)H in both cell types

8 | *J. Mater. Chem. B*, 2023, **00**, 1–12

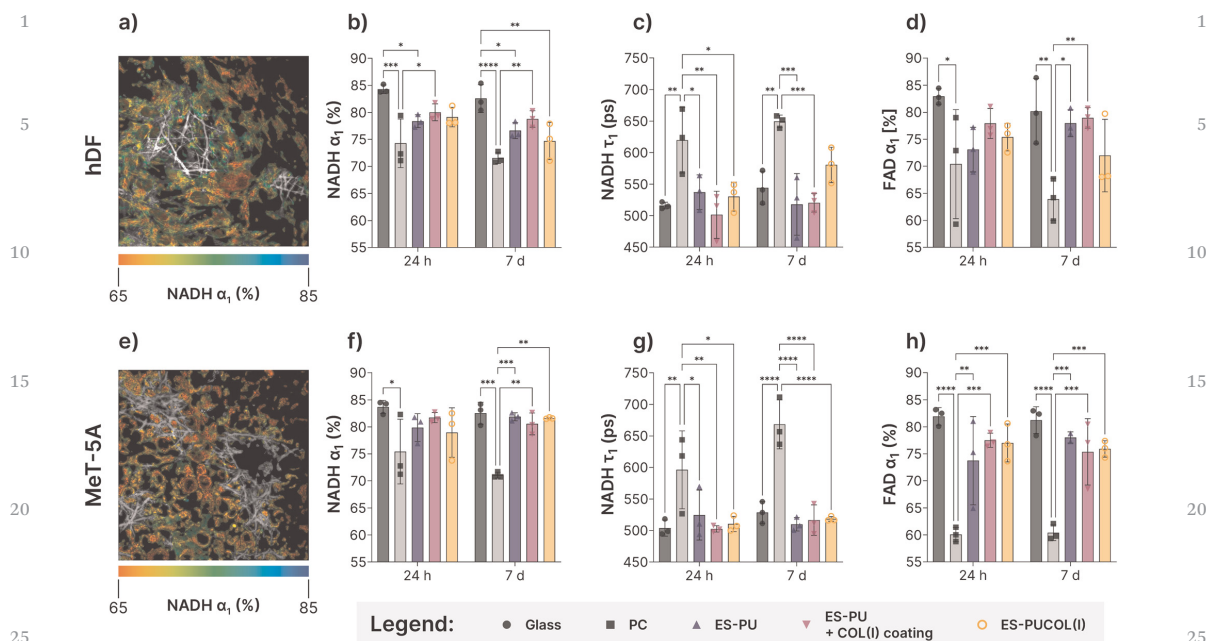This journal is © The Royal Society of Chemistry 2023

Paper

Fig. 6 Analysis of metabolic changes of cells on electrospun scaffolds using FLIM. To exclude the effects of the electrospun scaffolds on the mean values, photons from the scaffolds (white) were masked (a) and (e). Displayed are the mean values of NADH α_1, NADH τ_1, and FAD α_1 of hDFs in (b), (c), and (d), respectively and those of MeT-5A cells in (f), (g), (h) on glass, in the positive control with DMSO (PC), on electrospun PU without (ES-PU) and with collagen I (ES-PU + COL(I)) coating, and on electrospun collagen (ES-PUCOL). $n = 3$ of independent biological replicates, matched two-way ANOVA.

with respect to glass was only observed in the positive control. Free NAD(P)H (α_1) was lower in fibroblasts on ES-PUCOL than on glass after 24 hours (79.1 $\pm$ 1.8%, $p < 0.05$) and after 7 days (74.7 $\pm$ 3.4%, $p < 0.001$). Significant differences in fluorescence lifetime (τ_1) in fibroblasts were neither observed after 24 hours (530.3 $\pm$ 23.0 ps) nor after 7 days (580.4 $\pm$ 28.0 ps). The results suggest a slightly higher cellular stress response on ES-PUCOL than on the collagen-coated ES-PU + Col (higher τ_1 and lower α_1), but differences were not significant. Epithelial cells did not show any signs of an altered metabolic state on ES-PUCOL with respect to glass. The relative amount of free NAD(P)H in MeT-5A cells was 78.9 $\pm$ 4.6% after 24 hours and 81.6 $\pm$ 0.1% after 7 days. Fluorescence lifetime τ_1 was 510.3 $\pm$ 12.3 ps and 518.4 $\pm$ 3.8 ps after 24 hours and 7 days, respectively.

Discussion

The rediscovery of the electrospinning method by Doshi and Reneker in 1995[46] has brought forth a large collection of studies on the use of electrospinning for tissue engineering and, more specifically, the mimicking of the extracellular matrix (ECM). However, the use of natural ECM components themselves, such as collagen, is not always free of concern. The study by Zeugolis *et al.* demonstrated that collagen needs crosslinking and loses its crystalline structure when fluorinated solvents are used.[17] Many solvent substitutes have been proposed and demonstrated in proof-of-principles, showing that collagen can be well spun into fibrous meshes using other solvents.[19–29,47–51] Still, unambiguous evidence for the preservation of the structural integrity and proteolytic resistance of collagen after electrospinning is not presented in most of these studies, neither is a possible mechanism underlying collagen denaturation proposed, when results indicate that collagen was compromised in the process.

In the present work, indeed, we confirm that collagen can be spun out of an array of 'gentle' solvents. Acidic solvent blends with ethanol seem to be particularly well suited to achieve viscous collagen solutions, which yield well-separated and bead-free collagen mats. The evaporation rates of acidic solvent blends often become a limiting factor, which is either increased by creating very concentrated (> 10 wt%) collagen solutions[20,51] or by creating a very dry atmosphere with the help of synthetic dry air.[27] Here, we opted for the latter approach, as very concentrated collagen solutions require thermal or mechanical input during solubilization.

Although these alternative recipes have rapidly gained interest, it has remained unquestioned to crosslink the otherwise water-insoluble collagen after electrospinning.[21,22,24,25,28,29] This necessity suggests an underlying structural change of

collagen. Studies by Liu *et al.* and Kazanci *et al.* showed that electrospun collagen from 40 wt% acetic acid and HFIP had barely discernible circular dichroism spectra, indicating that both solvents caused conformational changes.[20,22] We similarly observed an attenuating effect of electrospinning on the optical activity of collagen. Although the combination of acetic acid and ethanol never unfolded collagen more than HFIP, even electrospinning in acetic acid/ethanol at the lowest achieved temperature of 20 °C only left 15.7 ± 2.0% of the polyproline-II helix in the folded state. This fraction is lower than the reported values by Bürck *et al.*, but still underlines their conclusion that electrospinning in acetic acid, as well as in HFIP, unfolds collagen, albeit to a lesser extent.[23] These observations can also be interpreted as a lowering of the denaturation temperature due to the addition of ethanol or the introduction of the electrospinning process. The thermal stability of collagen is influenced by multiple factors, as the denaturation temperature of collagen varies greatly depending on its organizational state, which in turn also influences the collagen's potential to refold and renature.[52]

The denaturation temperature of collagen also correlates with its proteolytic resistance, antigenic properties, and cell–material interaction.[52] We therefore also investigated native and electrospun collagen using gel electrophoresis and included a comparison of the enzymatic digestion resistance. Collagen monomers, in contrast to gelatin monomers, are expected to display a clearly distinguishable and narrow molar distribution.[53] The α_1- and α_2-monomers could be observed in all electrospun collagen samples. Without testing for enzymatic resistance, this evidence is, however, not sufficient to prove the preservation of triple helices.[51] Under conditions, which do not disrupt the triple-helical structure, α-chymotrypsin is only able to cleave the non-helical telopeptides.[54] In our study, only native collagen I preserved clearly distinguishable monomers after a brief α-chymotrypsin digestion. The digestion fragments with lower molecular weights in electrospun collagen samples indicate that collagen has attained accessible cleavage sites within the helical domain, which can be explained by a disrupted helical structure.[55] The observed loss in the SHG signal after electrospinning (Fig. S1 in ESI†) strengthens the hypothesis of the transition into an unorderly state.[56,57]

Raman spectroscopic analysis underlined the observation of conformational changes. Lowering, shifting and widening of the amide III band, as observed in all processed collagen samples, have been linked to conformational changes of the alpha helix and collagen heat denaturation.[41] Spectroscopic examinations of collagen have attributed the formation of shoulders of amide III at around 1220 cm^{-1} to a conformational change of polypeptide chains from α-helices to β-sheets.[34] Also the amide II region confirms similar denaturation-related changes at 1409 cm^{-1}.[39] Within the proline and hydroxyproline region, the decrease of the bands between 936 and 940 cm^{-1}, which have been assigned to C–C vibrations adjacent to carbonyl, is indicative of heat-induced denaturation.[39] An interesting observation is that these aforementioned denaturation modes occur irrespective of the electrospinning solvent, as the samples are not separated in the principal components. The denaturation need not be solely attributed to the solvent, but rather to both the solvent and the electrospinning process even in the absence of fluorinated solvents or heat.[20]

The high ethanol content seems to be a common factor in the studies that present a denaturated collagen product, but has also proven to be beneficial for the direct electrospinning of pure collagen fibers. Gopinath *et al.* showed that aqueous ethanol solutions can lower the denaturation temperatures based on the ellipticity at 222 nm from 40 to 34 °C, when the ethanol content is increased to 40%.[30] However, most binary solvent electrospinning recipes comprise even higher ethanol contents from 60%[23] to 75%,[27] including the procedure in our study. Wakuda *et al.* have proposed an alternative two-step approach that omits ethanol as electrospinning solvent without compromising the spinnability.[48] This method comprised the core–shell electrospinning of collagen with a polyvinylpyrrolidone (PVP) shell that was subsequently removed to expose the pure collagen core fibers. However, CD measurements showed that the ethanol-containing washing buffer still significantly lowered the triple helix content, which decreased with increasing ethanol content. Other recent core–shell electrospinning studies support the finding that mostly ethanol and to a lesser extent heat likely contributes to the denaturation of electrospun collagen,[49,50] although preservation of the triple helix was recently reported for an ethanol content as high as 75% with hydrochloric acid.[27] Our data indicate that electrospinning of collagen can cause far reaching denaturation when acid/ethanol mixtures are used. It is likely that this process is dominated by the dehydration by ethanol, breakage of hydrogen bonds, and the alteration of the structure of collagen at multiple levels of its hierarchy that collectively result in the loss of protection against peptide scission.[30,58]

Electrospun collagen has often been studied for use in tissue-engineered constructs. *In vitro* cell-material interaction studies and *in vivo* implant trials often emphasized the potential benefits of the three-dimensionality of electrospun scaffolds, citing the improved cell penetration, vascularization potential, and ECM-mimicking microenvironment as the main factors.[59–62] However, how can the improved cell-material interaction be ascribed to this imitation of the ECM, if the electrospun collagen does not biochemically represent native collagen anymore? As our data suggest, cell–material interaction studies on electrospun scaffolds are unlikely to unravel the inflicted damage on the triple-helical structure of collagen. Both epithelial cells and fibroblasts attained structured cytoskeletal organization after 7 days of cell culture on electrospun collagen and electrospun polyurethane. Live/Dead stainings confirmed high viability of cultured cells on electrospun collagen with and without collagen coating. Live cell examination of the metabolic state of cultured cells proved even more profoundly that electrospinning of pure collagen nanofibers does not yield any benefit over a synthetic electrospun substrate. The ratio of unbound to bound NAD(P)H in the cytoplasm of epithelial cells was not affected by any of the

electrospun scaffolds, neither was its fluorescence lifetime. Fibroblasts even displayed slightly more signs of metabolic stress on electrospun collagen than on collagen-coated scaffolds, although differences were not significant. Effects observed in cell–material interaction studies on electrospun pure collagen fibers do not allow for any attribution other than to the three-dimensional morphology of the fibrous mesh. Unless an application requires a specific morphology or mechanical characteristics of the nanofibers, which can only be achieved by electrospinning pure collagen, it is advised to resort to biofunctionalization by coating of electrospun materials. This observation underlines previously made recommendations for the production of three-dimensional ECM-mimicking substrates.[17] Based on our data, this recommendation holds true and the triple helix content of collagen should be assessed after the direct electrospinning of collagen, despite a more diverse choice of electrospinning solvents.

Conclusion

In the present study, we employed physiochemical analyses alongside cell-material interaction studies to thoroughly address the impact of solvents and electrospinning on the collagen integrity. Although acetic acid and ethanol can be used as electrospinning solvents to process collagen into nanofibers, our data suggest that these nanofibers do not constitute native collagen fibers anymore. Biochemical and spectroscopic analyses of the electrospun nanofibers indicate a disturbed triple helix structure, which closely resembles that of heat-denatured collagen. In addition to that, electrospun synthetic polymers, such as polyurethane, do not provide a less compatible substrate for cultured cells. A significantly different cell response is unlikely to be detected in cell–material interaction studies.

Ethical approval

hDFs were isolated from juvenile foreskin under ethics approval no 495/2018BO2 from the University Hospital of Tübingen, Germany.

Conflicts of interest

There are no conflicts to declare.

Acknowledgements

Q3

References

1 T. Linsenmayer, in *Cell biology of extracellular matrix*, ed. E. D. Hay, Springer, 1991, pp. 7–44.

2 C. M. Kielty and M. E. Grant, *Connective tissue and its heritable disorders: molecular, genetic, and medical aspects*, 2002, pp. 159–221.

3 M. van der Rest, R. Garrone and D. Herbage, *Adv. Mol. Cell Biol.*, 1993, **6**, 1–67.

4 C. Cohen and R. S. Bear, *J. Am. Chem. Soc.*, 1953, **75**, 2783–2784.

5 R. Fraser, T. MacRae and E. Suzuki, *J. Mol. Biol.*, 1979, **129**, 463–481.

6 A. Rich and F. Crick, *J. Mol. Biol.*, 1961, **3**, 483–IN484.

7 R. L. Trelstad, in *Immunochemistry of the extracellular matrix*, ed. H. Furthmayr, CRC Press, Boca Raton, FL, 1982, vol. 1, pp. 32–39.

8 D. Holmes, H. Graham, J. Trotter and K. Kadler, *Micron*, 2001, **32**, 273–285.

9 F. H. Silver and D. E. Birk, *Int. J. Biol. Macromol.*, 1984, **6**, 125–132.

10 S. Khorshidi, A. Solouk, H. Mirzadeh, S. Mazinani, J. M. Lagaron, S. Sharifi and S. Ramakrishna, *J. Tissue Eng. Regener. Med.*, 2016, **10**, 715–738.

11 F. H. Silver, J. W. Freeman and G. P. Seehra, *J. Biomech.*, 2003, **36**, 1529–1553.

12 J. A. Matthews, G. E. Wnek, D. G. Simpson and G. L. Bowlin, *Biomacromolecules*, 2002, **3**, 232–238.

13 T. A. Telemeco, C. Ayres, G. L. Bowlin, G. E. Wnek, E. D. Boland, N. Cohen, C. M. Baumgarten, J. Mathews and D. G. Simpson, *Acta Biomater.*, 2005, **1**, 377–385.

14 L. Huang, K. Nagapudi, R. P. Apkarian and E. L. Chaikof, *J. Biomater. Sci., Polym. Ed.*, 2001, **12**, 979–993.

15 S. Heydarkhan-Hagvall, K. Schenke-Layland, A. P. Dhanasopon, F. Rofail, H. Smith, B. M. Wu, R. Shemin, R. E. Beygui and W. R. MacLellan, *Biomaterials*, 2008, **29**, 2907–2914.

16 D.-P. Hong, M. Hoshino, R. Kuboi and Y. Goto, *J. Am. Chem. Soc.*, 1999, **121**, 8427–8433.

17 D. I. Zeugolis, S. T. Khew, E. S. Yew, A. K. Ekaputra, Y. W. Tong, L. Y. Yung, D. W. Hutmacher, C. Sheppard and M. Raghunath, *Biomaterials*, 2008, **29**, 2293–2305.

18 D. A. Castilla-Casadiego, C. A. Rivera-Martínez, B. A. Quiñones-Colón and J. Almodóvar, *Electrospun Biomaterials and Related Technologies*, 2017, , DOI: **10.1007/978-3-319-70049-6_2**, ch. 2, pp. 21–55.

19 G. Montalbano, C. Tomasina, S. Fiorilli, S. Camarero-Espinosa, C. Vitale-Brovarone and L. Moroni, *Materials*, 2021, **14**. Q4

20 M. Kazanci, *Mater. Lett.*, 2014, **130**, 223–226.

21 A. Elamparithi, A. M. Punnoose and S. Kuruvilla, *Artif. Cells, Nanomed., Biotechnol.*, 2016, **44**, 1318–1325.

22 T. Liu, W. K. Teng, B. P. Chan and S. Y. Chew, *J. Biomed. Mater. Res., Part A*, 2010, **95**, 276–282.

23 J. Burck, S. Heissler, U. Geckle, M. F. Ardakani, R. Schneider, A. S. Ulrich and M. Kazanci, *Langmuir*, 2013, **29**, 1562–1572.

24 J. Baek, X. Chen, S. Sovani, S. Jin, S. P. Grogan and D. D. D'Lima, *J. Orthop. Res.*, 2015, **33**, 572–583.

25 J. Baek, S. Sovani, N. E. Glembotski, J. Du, S. Jin, S. P. Grogan and D. D. D'Lima, *Tissue Eng., Part A*, 2016, **22**, 436–448.

26 B. Dong, O. Arnoult, M. E. Smith and G. E. Wnek, *Macromol. Rapid Commun.*, 2009, **30**, 539–542.

27 D. Dems, J. Rodrigues da Silva, C. Hélary, F. Wien, M. Marchand, N. Debons, L. Muller, Y. Chen, M.-C. Schanne-Klein, C. Laberty-Robert, N. Krins and C. Aimé, *ACS Appl. Bio Mater.*, 2020, **3**, 2948–2957.

28 Q. Jiang, N. Reddy, S. Zhang, N. Roscioli and Y. Yang, *J. Biomed. Mater. Res. Part A*, 2012, **101**, 1237–1247.

29 D. A. Castilla-Casadiego, H. V. Ramos-Avilez, S. Herrera-Posada, B. Calcagno, L. Loyo, J. Shipmon, A. Acevedo, A. Quintana and J. Almodovar, *Macromol. Mater. Eng.*, 2016, **301**, 1064–1075.

30 A. Gopinath, S. M. Reddy, B. Madhan, G. Shanmguam and J. R. Rao, *Eur. Biophys. J.*, 2014, **43**, 643–652.

31 D. Visser, H. Bakhshi, K. Rogg, E. Fuhrmann, F. Wieland, K. Schenke-Layland, W. Meyer and H. Hartmann, *ACS Omega*, 2022, DOI: **10.1021/acsomega.2c03731**. [Q5]

32 C. E. Campiglio, S. Ponzini, P. De Stefano, G. Ortoleva, L. Vignati and L. Draghi, *Polymers*, 2020, **12**, 2472.

33 W. T. Cheng, M. T. Liu, H. N. Liu and S. Y. Lin, *Microsc. Res. Tech.*, 2005, **68**, 75–79.

34 N. Stone, C. Kendall, J. Smith, P. Crow and H. Barr, *Faraday Discuss.*, 2004, **126**, 141–157.

35 A. Rygula, K. Majzner, K. M. Marzec, A. Kaczor, M. Pilarczyk and M. Baranska, *J. Raman Spectrosc.*, 2013, **44**, 1061–1076.

36 Z. Huang, A. McWilliams, H. Lui, D. I. McLean, S. Lam and H. Zeng, *Int. J. Cancer*, 2003, **107**, 1047–1052.

37 N. Stone, C. Kendall, N. Shepherd, P. Crow and H. Barr, *J. Raman Spectrosc.*, 2002, **33**, 564–573.

38 A. C. S. Talari, Z. Movasaghi, S. Rehman and I. U. Rehman, *Appl. Spectrosc. Rev.*, 2014, **50**, 46–111.

39 M. Fields, N. Spencer, J. Dudhia and P. F. McMillan, *Biopolymers*, 2017, **107**. [Q6]

40 Q. Zhang, K. L. Andrew Chan, G. Zhang, T. Gillece, L. Senak, D. J. Moore, R. Mendelsohn and C. R. Flach, *Biopolymers*, 2011, **95**, 607–615.

41 B. G. Frushour and J. L. Koenig, *Biopolymers*, 1975, **14**, 379–391.

42 J. L. Lippert, D. Tyminski and P. J. Desmeules, *J. Am. Chem. Soc.*, 1976, **98**, 7075–7080.

43 R. Dong, X. Yan, X. Pang and S. Liu, *Spectrochim. Acta, Part A*, 2004, **60**, 557–561.

44 I. H. McColl, E. W. Blanch, A. C. Gill, A. G. Rhie, M. A. Ritchie, L. Hecht, K. Nielsen and L. D. Barron, *J. Am. Chem. Soc.*, 2003, **125**, 10019–10026.

45 C. Gullekson, L. Lucas, K. Hewitt and L. Kreplak, *Biophys. J.*, 2011, **100**, 1837–1845.

46 J. Doshi and D. H. Reneker, *J. Electrost.*, 1995, **35**, 151–160.

47 J. Bürck, O. Aras, L. Bertinetti, C. A. Ilhan, M. A. Ermeydan, R. Schneider, A. S. Ulrich and M. Kazanci, *J. Mol. Struct.*, 2018, **1151**, 73–80.

48 Y. Wakuda, S. Nishimoto, S. I. Suye and S. Fujita, *Sci. Rep.*, 2018, **8**, 6248.

49 J. M. Anaya Mancipe, L. C. Boldrini Pereira, P. G. de Miranda Borchio, M. L. Dias and R. M. da Silva Moreira Thiré, *J. Biomed. Mater. Res., Part B*, 2023, **111**, 366–381.

50 J. M. Anaya Mancipe, M. Lopes Dias and R. M. D. S. Moreira Thiré, *Polym.-Plast. Technol. Mater.*, 2022, **61**, 846–860.

51 K. H. Sizeland, K. A. Hofman, I. C. Hallett, D. E. Martin, J. Potgieter, N. M. Kirby, A. Hawley, S. T. Mudie, T. M. Ryan, R. G. Haverkamp and M. H. Cumming, *Materialia*, 2018, **3**, 90–96.

52 M. Meyer, *Biomed. Eng. Online*, 2019, **18**, 24.

53 M. Meyer and B. Morgenstern, *Biomacromolecules*, 2003, **4**, 1727–1732.

54 P. Bornstein, A. H. Kang and K. A. Piez, *Biochemistry*, 1966, **5**, 3803–3812.

55 S. B. Deak, M. Van Der Rest and D. J. Prockop, *Collagen Relat. Res.*, 1985, **5**, 305–313.

56 Y. Sun, W.-L. Chen, S.-J. Lin, S.-H. Jee, Y.-F. Chen, L.-C. Lin, P. T. C. So and C.-Y. Dong, *Biophys. J.*, 2006, **91**, 2620–2625.

57 B.-M. Kim, J. Eichler, K. M. Reiser, A. M. Rubenchik and L. B. Da Silva, *Lasers Surg. Med.*, 2000, **27**, 329–335.

58 O. S. Rabotyagova, P. Cebe and D. L. Kaplan, *Mater. Sci. Eng.: C*, 2008, **28**, 1420–1429.

59 A. P. Kishan and E. M. Cosgriff-Hernandez, *J. Biomed. Mater. Res., Part A*, 2017, **105**, 2892–2905.

60 T. J. Sill and H. A. von Recum, *Biomaterials*, 2008, **29**, 1989–2006.

61 A. Hasan, A. Memic, N. Annabi, M. Hossain, A. Paul, M. R. Dokmeci, F. Dehghani and A. Khademhosseini, *Acta Biomater.*, 2014, **10**, 11–25.

62 L. Salvatore, N. Gallo, M. L. Natali, A. Terzi, A. Sannino and M. Madaghiele, *Front. Bioeng. Biotechnol.*, 2021, **9**. [Q7]

12 | *J. Mater. Chem. B*, 2023, **00**, 1–12

This journal is © The Royal Society of Chemistry 2023

cells

Article

Fibronectin Adsorption on Electrospun Synthetic Vascular Grafts Attracts Endothelial Progenitor Cells and Promotes Endothelialization in Dynamic In Vitro Culture

Ruben Daum [1], Dmitri Visser [1], Constanze Wild [2], Larysa Kutuzova [3], Maria Schneider [2], Günter Lorenz [3], Martin Weiss [1,4], Svenja Hinderer [1], Ulrich A. Stock [5], Martina Seifert [2] and Katja Schenke-Layland [1,4,6,7,*]

[1] NMI Natural and Medical Sciences Institute at the University of Tübingen, 72770 Reutlingen, Germany; ruben.daum@nmi.de (R.D.); dmitri.visser@nmi.de (D.V.); martin.weiss@med.uni-tuebingen.de (M.W.); hinderer@polymedics.de (S.H.)

[2] Institute of Medical Immunology and BIH Center for Regenerative Therapies (BCRT), Charité-Universitätsmedizin Berlin, Corporate Member of Freie Universität Berlin, Humboldt-Universität zu Berlin, and Berlin Institute of Health, 13353 Berlin, Germany; constanze.wild@charite.de (C.W.); maria.schneider@charite.de (M.S.); martina.seifert@charite.de (M.S.)

[3] Applied Chemistry, University of Reutlingen, 72762 Reutlingen, Germany; larysa.kutuzova@reutlingen-univeristy.de (L.K.); guenter.lorenz@reutlingen-university.de (G.L.)

[4] Department of Women's Health, Research Institute for Women's Health, Eberhard-Karls-University Tübingen, 72076 Tübingen, Germany

[5] Department of Cardiothoracic Surgery, Royal Brompton and Harefield Foundation Trust, Harefield Hospital Hill End Rd, Harefiled UB9 6JH, UK; u.stock@rbht.nhs.uk

[6] Cluster of Excellence iFIT (EXC 2180) "Image-Guided and Functionally Instructed Tumor Therapies", Eberhard-Karls-University Tübingen, 72076 Tübingen, Germany

[7] Department of Medicine/Cardiology, Cardiovascular Research Laboratories, David Geffen School of Medicine at UCLA, Los Angeles, CA 90095, USA

* Correspondence: katja.schenke-layland@med.uni-tuebingen.de; Tel.: +49-707-1298-5205

check for updates

Abstract: Appropriate mechanical properties and fast endothelialization of synthetic grafts are key to ensure long-term functionality of implants. We used a newly developed biostable polyurethane elastomer (TPCU) to engineer electrospun vascular scaffolds with promising mechanical properties (E-modulus: 4.8 ± 0.6 MPa, burst pressure: 3326 ± 78 mmHg), which were biofunctionalized with fibronectin (FN) and decorin (DCN). Neither uncoated nor biofunctionalized TPCU scaffolds induced major adverse immune responses except for minor signs of polymorph nuclear cell activation. The in vivo endothelial progenitor cell homing potential of the biofunctionalized scaffolds was simulated in vitro by attracting endothelial colony-forming cells (ECFCs). Although DCN coating did attract ECFCs in combination with FN (FN + DCN), DCN-coated TPCU scaffolds showed a cell-repellent effect in the absence of FN. In a tissue-engineering approach, the electrospun and biofunctionalized tubular grafts were cultured with primary-isolated vascular endothelial cells in a custom-made bioreactor under dynamic conditions with the aim to engineer an advanced therapy medicinal product. Both FN and FN + DCN functionalization supported the formation of a confluent and functional endothelial layer.

Keywords: vascular graft; endothelialization; tissue engineering; decorin; fibronectin; electrospinning; endothelial progenitor cells; bioreactor; biostable polyurethane

---

99

1. Introduction

Atherosclerotic cardiovascular disease is one of the leading causes of death worldwide [1,2]. It includes all medical conditions, where blood flow to organs and limbs is reduced due to plaque deposition. Surgical intervention is required to reopen or replace the defective vessel. The use of autografts, like the saphenous vein or mammary artery, are still the standard clinical approach for the replacement of small diameter blood vessels [3]. However, mechanical or size mismatches, and mainly the scarce availability make alternative grafts necessary [4,5]. In this context, two strategies have emerged in recent years: synthetic substitutes and biological grafts [4]. Although large-diameter synthetic substitutes (>6 mm) are successfully used, small diameter grafts (<6 mm) show low patency rates due to their tendency to elicit thrombosis and the formation of intimal hyperplasia [6–8]. Appropriate mechanical properties and biocompatibility of the synthetic graft as well as a fast endothelialization after implantation are key properties to ensure a long-term functional implant. In addition, the graft should evoke a balanced immune reaction. On the one hand, a moderate immune response is beneficial in order to promote tissue regeneration. On the other hand, chronic immune responses can lead to inflammation, fibrosis, or calcification and should be avoided to ensure long-term function of the vascular graft [9].

Electrospinning has proven to be a suitable method for the fabrication of fibrous scaffolds and vascular constructs as it mimics the highly porous structure and physical properties of the extracellular matrix (ECM) of the native tissue. Due to their high porosity, pore interconnectivity, and large surface area, the fibrous scaffolds are able to promote cell adhesion, cell alignment, and cell proliferation [10–13]. In addition, in order to elicit in situ endothelialization in the body, the material surface can be functionalized with bioactive molecules. A central challenge in this context is the attraction, adhesion, and proliferation of endothelial progenitor cells (EPCs) or endothelial cells (ECs) to form a complete endothelium. Several strategies to address this issue have been described: immobilization of antibodies targeting markers for EPCs such as vascular endothelial growth factor receptor 2 (VEGFR2) and platelet endothelial cell adhesion molecule (PECAM-1) [14,15]; modification of the surface with peptides such as the Arg-Gly-Asp (RGD) or Cys-Ala-Gly (CAG) sequence [16,17]; immobilization of growth factors such as the vascular endothelial growth factor (VEGF) or stromal cell-derived factor-1 (SDF-1) [18,19]; immobilization of oligonucleotides and aptamers [20,21]; and surface modification with oligosaccharides and phospholipids [22,23]. However, it is necessary to develop surfaces with improved biocompatible, bioactive, targeted, and stable biofunctionalization [24].

A recent study described the attraction of EPCs by immobilized recombinant human decorin (DCN) [25]. The small leucine-rich proteoglycan plays a pivotal role in the ECM [26]. It is named after its first known function as a modulator of collagen fibrillogenesis [27]. In recent years, it has been shown that DCN influences a variety of biological processes in addition to its structural function. It is involved in cell attachment [28–30], proliferation [31,32], and migration [28,29,31,33]. Furthermore, it has been described that DCN inhibits the proliferation and migration of vascular smooth muscle cells but does not affect ECs [28,31]. With a proportion of 22% of all proteoglycans in the vessel wall, it also influences many biological processes in vascular homeostasis and angiogenesis [34–36]. Depending on the molecular environment, it can act pro-angiogenic or antiangiogenic [26,34]. For instance, DCN was shown to interact antagonistically with the mesenchymal epithelial transition factor (c-MET) and the VEGFR2, which significantly influences angiogenesis [26,34,37,38]. In addition, DCN binds to the transforming growth factor β (TGF-β), which in turn has an inhibiting effect on the endothelial-mesenchymal transition and fibrosis [26,39,40]. These properties make the protein a promising candidate for improving the endothelialization of a vascular graft. Another highly relevant ECM protein is fibronectin (FN). Since FN interacts with cells via the integrins $\alpha_5\beta_1$ or $\alpha_v\beta_3$, it is a suitable protein for bioactivating a material surface [41–44]. It is of interest with regard to endothelialization, as it plays a pivotal role in wound healing [45,46]. Several studies described the coating of FN in combination with collagens type I [47] and type IV [48], with fibrinogen and tropoelastin [49], hepatocyte growth factor [50], heparin,

and VEGF [51] and with SDF-1α [19] to improve reendothelialization. However, it has never been used in combination with DCN before.

Tissue engineering can be used as an alternative strategy to obtain a functional endothelium in a synthetic graft utilizing a patient's own cells [52]. After implantation, the tissue-engineered vascular graft (TEVG) is replaced by the host's cells and ECM and is thereby degraded [4]. However, the loss of mechanical properties due to a too rapid degradation and unfavorable biological reactions to the degradation products remain a major challenge [1,53]. A recent study addressed this problem by producing a TEGV that consists of a combination of a biodegradable and biostable polymer [54].

In our study, a newly developed biostable polyurethane elastomer was used to develop an electrospun scaffold with mechanical properties that are comparable to native vascular tissues, and a bioactive surface that attracts endothelial progenitor cells or promotes endothelialization [55]. For this purpose, planar and tubular electrospun scaffolds (Figure 1a) were biofunctionalized with FN, DCN, or FN and DCN in combination (FN + DCN; Figure 1b,c). The influence of the FN- and DCN-coated scaffolds on human immune cell features was examined (Figure 1d). Subsequently, the functionality of the electrospun scaffolds was further investigated. First, endothelial progenitor cell homing was simulated in vitro by attracting endothelial colony forming cells (ECFCs) with a potent angiogenic capacity and the capability to support vascular repair (Figure 1e,f). Secondly, in a classical TEVG approach primary-isolated vascular endothelial cells (vECs) were cultured in a custom-made bioreactor to create an advanced therapy medicinal product (ATMP) (Figure 1g).
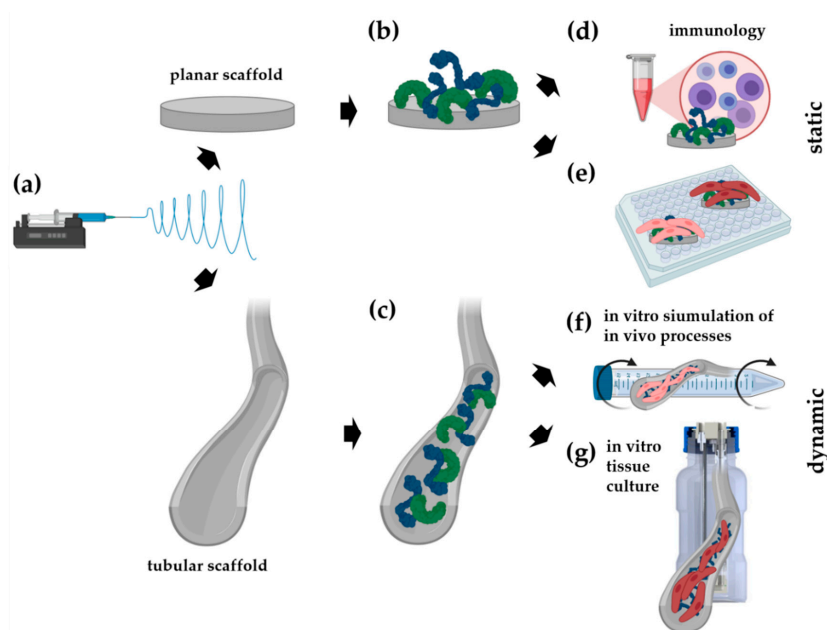

Figure 1. A newly developed polyurethane is used to produce planar and tubular electrospun scaffolds (**a**), which are biofunctionalized with either fibronectin (FN) or decorin (DCN) or with both extracellular matrix (ECM) proteins in combination (**b**,**c**). Besides investigating the immunology (**d**) and endothelial colony forming cell (ECFC) behavior on either planar (**e**) or in tubular scaffolds (**f**), the tubular scaffolds were also cultured with primary-isolated vascular endothelial cells (vECs) in an tissue-engineered vascular graft (TEVG) approach (**g**) in order to assess an ECM protein-improved endothelialization.

2. Materials and Methods

2.1. Electrospun Scaffold Fabrication

Planar and tubular scaffolds were produced by electrospinning of soft thermoplastic polycarbonate-urethane (TPCU). This elastomeric material was synthesized in our laboratory for special medical applications using the multistep one-pot approach [56], which gives good control of the polymer architecture in catalyst-free systems. In more detail, a long-chain aliphatic polycarbonate with more than 72% (*w/w*) in the TPCU formulation provides an additional crystallization of the soft segment, which enhances biostability of the implantable material as well as improves its mechanical properties. In vitro biostability of the TPCU was studied previously from a mechanical point of view under long-term oxidative treatment [55]. Cytocompatibility of the TPCU material was also demonstrated [57]. By adjusting the respective parameters to achieve a stable process and appropriate mechanical properties of the scaffold (Figure S1a), 0.1 g/mL of the polymer was dissolved in 1,1,1,3,3,3 hexafluoro-2-propanol (804515, Merck, Darmstadt, Germany) and electrospun with the process conditions summarized in Table 1. The electrospinning process was carried out in a temperature- and humidity-controlled electrospinning apparatus (EC-CLI, IME Technologies, Eindhoven, Netherlands).

Table 1. Process conditions for electrospinning planar and tubular scaffolds.

Description	Value
Distance	25 cm
Needle i.d.	0.4 mm
Voltage	18 kV/−0.2 kV (needle/collector)
Temperature	23 °C
Humidity	40%
Mandrel diameter [1]	6 mm
Mandrel rotation speed [1]	2000 rpm
Needle translation distance [1]	80 mm
Volume	6 mL
Flow rate	4 mL/h

i.d.= inner diameter; [1] tubular scaffolds.

2.2. Biofunctionalization of the Scaffolds

Before biofunctionalization, the appropriate disinfection method was investigated. Since ethanol did not affect the scaffold in terms of its mechanical properties (Figure S1b), the constructs were disinfected with 70% ethanol for 20 min and afterwards washed three times for 10 min with phosphate-buffered saline (PBS). Microbiological studies were carried out on the scaffolds to investigate the effectiveness of the disinfection method (Figure S3). The scaffolds were functionalized by protein adsorption. They were incubated for 2 h at 37 °C with 20 µg/mL human plasma FN (F1056, Sigma-Aldrich, St. Louis, USA) or 20 µg/mL recombinant full-length human DCN [25], individually or in combination. Excess protein was removed by washing the scaffolds with PBS.

2.3. Morphological and Mechanical Characterization of the Electrospun Scaffolds

For the morphological characterization, punches from the electrospun scaffolds were examined by scanning electron microscopy (SU8030, Hitachi, Tokyo, Japan) followed by the analysis using ImageJ and the DiameterJ package [58] to assess the pore and fiber sizes. For the investigation of the mechanical properties, a ring tensile test was performed based on the methods described by Laterreur et al. [59] in order to determine the circumferential tensile strength and burst pressure. Briefly, the tubular scaffolds were cut into pieces with the length $L_0 = 7$ mm, clamped into a uniaxial tensile testing device (Zwick Roell, Ulm, Germany), and stretched over a distance s with a velocity of 50 mm/min until rupture.

On the basis of the stress–strain curves (Figure S1c), the burst pressure P_b was then calculated by relating the registered force at rupture F_b to the elongation s_b as follows:

$$P_b = \frac{F_b \pi}{L_0 d_{pin}(\pi + 2) + 2L_0 s_b} \tag{1}$$

where d_{pin} represents the diameter of the pins that were used in the ring tensile test. A derivation of Equation (1) is provided by Lattereur et al. [59]. Using an OCA40 (DataPhysics Instruments GmbH, Filderstadt, Germany), the wettability of the scaffolds was analyzed as previously described [60]. A waterdrop with a volume of 2 μL was placed onto the scaffold and measured using the SCA20 software (DataPhysics Instruments, Filderstadt, Germany). The water absorption ability was determined by weighing the specimens in their dry and wet states after submerging the specimens in water for 1 h. The relative weight increase is referred to as the swelling ratio.

2.4. Immune Cell/Scaffold Co-Culture Assays

Polymorph nuclear cells (PMNs) were isolated from freshly donated human blood and peripheral blood mononuclear cells (PBMCs) from buffy coats according to the ethical approval by the local ethics committee at the Charité Berlin (EA2/139/10 approved on 10th December 2010; EA1/226/14 approved on 24th July 2014) and as recently described [61]. Monocytes were magnetically sorted via CD14 beads (130-050-201, Miltenyi Biotec, Bergisch Gladbach, Germany) from PBMCs as previously described [62]. Monocytes were differentiated into M0 macrophages by adding 50 ng/mL of macrophage colony-stimulating factor (M-CSF) (130-096-491, Miltenyi Biotec) to the culture medium for 7 days. All immune cell co-cultures were performed in Roswell Park Memorial Institute (RPMI) 1640 medium (F1415, Biochrom GmbH, Berlin, Germany) with 10% human serum type AB (H4522, Sigma-Aldrich), 1% L-glutamine (25030-024, Thermo Fisher Scientific, Waltham, MA, USA), and 1% penicillin/streptomycin (15140-122, Thermo Fisher Scientific).

First, the scaffold punches were incubated with 100 μg/mL of recombinant full-length human DCN [25] or 20 μg/mL of FN (F1056, Sigma-Aldrich) at 37 °C for 4 h. Next, punches were washed with PBS (L1825, Biochrom GmbH), placed into a well of a 48-well plate, and kept in place with a silicon ring (Ismatec, Wertheim, Germany). Thereafter, the different immune cell types were applied as follows:

Human PMNs were cultured on the uncoated, DCN- or FN-coated scaffolds; 0.2×10^6 PMNs in 200 μL of complete RPMI were seeded directly on the scaffold punches. Unstimulated cells were used as a negative control, and PMNs that were stimulated with 500 ng/mL of lipopolysaccharide (LPS; 297-473-0, Sigma-Aldrich) served as a positive control. LPS is a component of the bacterial cell membrane that triggers the activation of immune cells. After 4 h of culture, cells were harvested only by careful resuspension, stained with human-specific antibodies for CD11b (1:100; 557701, BD Bioscience, San Jose, CA, USA) and CD66b (1:200; 305107, BioLegend, Fell, Germany), and measured by flow cytometry (CytoFLEX LX, Beckman Coulter, Inc., Brea, CA, USA) as described recently [61]. The determined mean fluorescence intensities (MFIs) of marker expression were normalized to the MFI of unstimulated PMNs directly after isolation.

Human monocytes or M0 macrophages were cultured on the uncoated, DCN- or FN-coated scaffolds; 0.2×10^6 cells in 350 μL of complete RPMI were seeded directly on the scaffold punches. Monocytes that were stimulated with 100 ng/mL of LPS served as a positive control, and unstimulated monocytes served as a negative control. Macrophages cultured without any stimulus were used as negative control. To induce the polarization into the M1 phenotype, 20 ng/mL of IFNγ (130-096-486, Miltenyi Biotec) and 100 ng/mL of LPS were added to the medium of M0 macrophages. After two days of culture, monocytes/macrophages were harvested, stained with human-specific antibodies for CD80 (1:20; 305208, BioLegend) and human leukocyte antigen DR isotype (HLA-DR) (1:200; 307616, BioLegend), and measured by flow cytometry. Cells were detached by adding 100 μL of Accutase (A11105-01, Thermo Fisher Scientific) and incubating the cells at 37 °C for 30 min. The determined MFIs of the marker expression were normalized to the MFI of the unstimulated cells.

PBMCs were cultured on the uncoated, DCN- or FN-coated scaffolds; 0.3×10^6 cells were seeded in 400 µL of complete RPMI directly on the scaffold punches. Unstimulated PBMCs served as a negative control. For the positive controls, PBMCs were stimulated with anti-CD28 (556620, BD Bioscience)/anti-CD3 (OKT3, Janssen-Cilag, Neuss, Germany) antibodies. After three days of culture, PBMCs were harvested, stained with human-specific antibodies for CD69 (1:50; 310926 BioLegend), CD25 (1:50; 302605, BioLegend) and HLA-DR (1:100; 307640, BioLegend), and measured by flow cytometry. PBMCs were detached by adding 100 µL of Accutase and by incubating the cells at 37 °C for 30 min. After gating for single and living cells the CD14− and CD14+ populations were defined. For CD3+ cells, the MFI of the activation markers CD25, CD69, and HLA-DR was determined. The determined MFIs of the marker expression were normalized to the MFI of unstimulated PBMCs.

Co-culture supernatants of monocytes and macrophages were collected and the tumor necrosis factor alpha (TNFα) concentration was analyzed by ELISA (430205, BioLegend) according to the manufacturer´s instructions.

2.5. Cell Culture of Primary Endothelial Cells and Endothelial Colony Forming Cells

Human primary-isolated vECs were isolated from foreskin biopsies under the ethics approval no 495/2018BO2 by enzymatic digestion with dispase and trypsin as previously described [63]. The vECs were cultured in endothelial cell growth medium and SupplementMix (C-22020, PromoCell, Heidelberg, Germany), supplemented with 1% penicillin-streptomycin (15140122, Thermo Fisher Scientific).

Human ECFCs (00189423, Lonza, Basel, Switzerland) were cultured in endothelial cell growth medium-2 with supplements (CC-3162, Lonza). Instead of the supplied fetal bovine serum, 5% of human serum (H4522, Sigma-Aldrich) was used. In addition, 1% L-Glutamine (21051024, Thermo Fisher Scientific) and 1% penicillin-streptomycin (15140122, Thermo Fisher Scientific) were added to the cell culture medium.

Both cell types were cultured at 37 °C and 5% CO_2 and passaged at approximately 80% confluence. The vECs were used for the experiment after 2–4 passages.

2.6. Cell Seeding and Culture on Planar Scaffolds

Prior to cell culture experiments, general biocompatibility of the electrospun scaffolds was examined with a cytotoxicity test based on EN ISO 10993-5 [64]. Briefly, the scaffolds were incubated for 72 h at 37 °C and 5% CO_2 in 1 mL endothelial cell growth medium supplemented with 1% penicillin-streptomycin at an extraction ratio of 0.1 mg/mL; 2×10^4 vECs seeded in a 96-well plate were then exposed for 24 h to the extracts supplied with the cell culture medium supplements. Endothelial cell growth medium without the scaffolds served as a negative control. Cells exposed to 1% SDS served as positive control. The extraction and control medium were removed, and an MTS (3-(4,5-dimethylthiazol-2-yl)-5-(3-carboxymethoxyphenyl)-2-(4-sulfophenyl)-2H-tetrazolium) assay (CellTiter 96Aqueous One Solution Cell Proliferation Assay, Promega, Madison, WI, USA) was performed according to the manufacturer's protocol; 20 µL MTS solution and 100 µL cell culture medium were added to each well. After 30 min of incubation at 37 °C, the absorbance of each well was measured at 450 nm using a microplate reader (PHERAstar, BMG Labtech, Ortenberg, Germany). Cell viability was determined by the absorbance of the samples relative to the negative control. No toxic effect of the material was observed (Figure S2a). Biofunctionalization of the scaffolds was then carried out as described above. Cells were seeded afterwards onto the biofunctionalized scaffolds with a diameter of 6 mm, which were placed in a 96-well plate. For the vECs, 5×10^3 cells/well and, for the ECFCs, 1×10^4 cells/well were seeded in 150 µL of the appropriate medium. If required, media change was carried out every 3 days.

2.7. Endothelial Colony Forming Cells (ECFC) Seeding Under Dynamic Conditions

The tubular electrospun scaffolds were cut to 6 cm length and biofunctionalized with FN and DCN alone or in combination as described above. A cell suspension of 4×10^5 ECFCs/mL was pipetted

into the tubular constructs. Afterwards, the constructs were closed at both ends and put in 15-mL centrifuge tubes filled with the corresponding cell culture medium. Placed on a roller mixer (RM5, CAT, Ballrechten-Dottingen, Germany), the tubes were rotated with 60 rpm for 24 h at 37 °C and 5% CO_2. For cell number analysis, the attached cells were stained with 4′,6-diamidino-2-phenylindole (DAPI) (1:50, 10236276001, Roche Diagnostics, Mannheim, Germany) and counted.

2.8. Development of a Bioreactor System for Tissue-Engineered Vascular Graft (TEVG) Culture

The TEVG approach was performed with a custom-made bioreactor setup. The culture chamber consists of a 250-mL glass bottle (Schott Duran, Wertheim, Germany) and encloses a removable custom-designed graft frame that holds the vascular graft. A computer-aided design (CAD) model for the graft frame was created in Solidworks (Dassault Systèmes, Vélizy-Villacoublay, France) and milled out of polyether ether ketone (PEEK; ADS Kunststofftechnik, Ahaus, Germany) using a 2.5-axis flatbed milling setup (Isel, Eichenzell, Germany) with computer numerical control (CNC). The constructed parts were subjected to the aforementioned cytotoxicity test to ensure no toxic leachables are released into the medium under culture (Figure S2b). The modular design of the culture chamber allows for a toolless assembly of the bioreactor system under a sterile bench.

The graft frame—once inserted into the culture chamber—is connected to medium reservoirs and a bubble trap with flexible silicone tubing. Sterile gas exchange is facilitated by sterile filters connected to the medium reservoirs. The entire setup is driven by a multichannel roller pump (Ismatec) (Figure 2).

The flow rates Q for dynamic culture were determined with a derived formulation of the Hagen–Poiseuille equation for laminar flow in straight circular pipes with internal radius r:

$$\tau = \frac{4\mu Q}{\pi r^3} \tag{2}$$

where μ denotes the dynamic viscosity. This gave an analytical approximation of the achieved wall shear stress (τ) within the cultured vascular graft. To validate this approximation and the assumption of a laminar regime within the vascular graft, in silico simulations were used to assess the local fluid dynamics within the vascular graft and graft frame interior. Briefly, the CAD model of the graft frame was meshed and exported to a computational fluid dynamics (CFD) solver (ANSYS Fluent). Dynamic culture with a wide range of flow rates was simulated under steady-state flow and Newtonian rheological conditions, after which the calculated wall shear stress on the interior graft wall was analyzed and compared to the aforementioned analytical solution (Figures S4 and S5).

2.9. Tissue Culture of Vascular Endothelial Cells Under Dynamic Conditions

Tubular electrospun scaffolds were cut to 7.5 cm length and biofunctionalized with 20 µg/mL FN as described previously. After inserting the graft frame into the culture chamber, 2×10^6 vECs/mL were seeded into the tubular scaffold. In order to achieve homogeneous cell adhesion across the entire tube, the culture chamber was placed horizontally and rotated every 15 minutes over 45 ° for 3 h at 37 °C and 5% CO_2. The culture chamber was consecutively connected to the rest of the bioreactor setup and filled with 70 mL culture medium, supplemented with 1% penicillin-streptomycin and 1% PrimocinTM (ant-pm-1, InvivoGen, San Diego, CA, USA). The seeded cells were allowed to proliferate under static conditions during the first three days, after which the flow rate was slowly increased over the course of two days, as shown in Figure 2e. Subsequently, the tubular construct was cultured under constant flow for seven days.
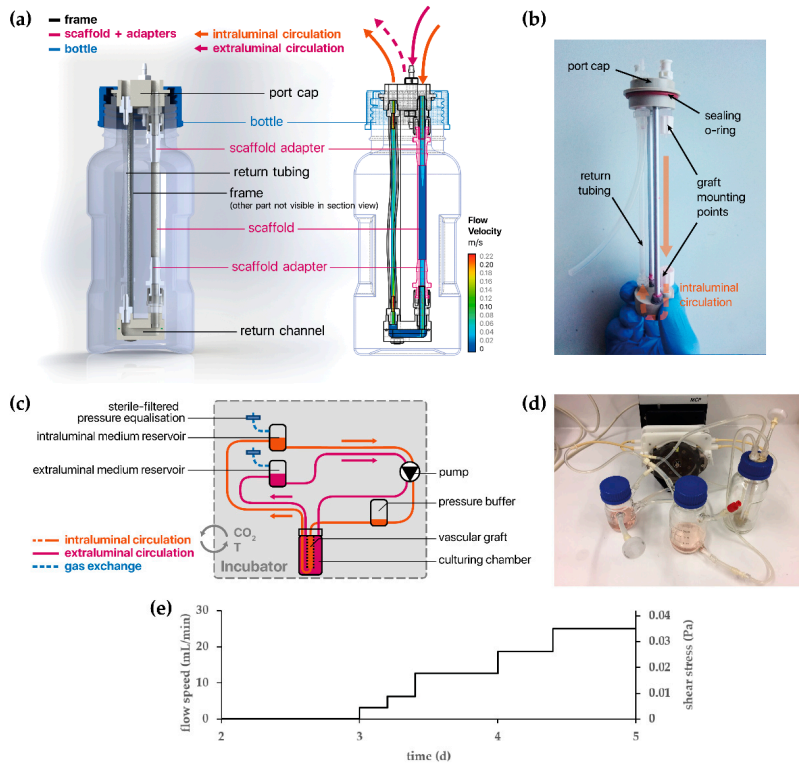
Figure 2. (**a**) A cross-sectional schematic representation of the culturing chamber and its parts. The wireframe model on the right is overlaid by the results of an in silico simulation and shows the flow velocity when the system is perfused with a flow rate of Q = 20 mL/min. (**b**) This photograph shows the graft frame (without scaffold), once it is taken out of the culturing chamber. (**c**) A schematic representation of the entire bioreactor setup, showing the circulation and connections to the medium reservoirs and pressure buffer/bubble trap. (**d**) A photograph showing the assembled bioreactor setup with all the components for the intraluminal circulation. (**e**) Applied perfusion flow speed as function of time with the corresponding wall shear stress.

2.10. Immunofluorescence Staining

In order to examine the protein coating, the biofunctionalized scaffolds were stained using DCN mouse monoclonal IgG_1 (1:200; sc-73896, Santa Cruz Biotechnology, Dallas, TX, USA) and FN polyclonal rabbit IgG (1:500; F3648, Sigma-Aldrich) antibodies. For fluorescence labeling, AlexaFluor 488 anti-mouse IgG (1:250; A-11001, Thermo Fisher Scientific) and AlexaFluor 546 anti-rabbit IgG (1:250; A-11035, Thermo Fisher Scientific) were used as secondary antibodies.

Cells cultured on the scaffolds were stained as follows: after washing once with PBS, the cell-seeded scaffolds were fixed with 4% paraformaldehyde (P6148, Sigma-Aldrich). In order to reduce nonspecific binding, the samples were incubated with 2% goat serum-containing block solution for 30 min. Afterwards, the cells were incubated over night at 4 °C with the following antibodies: Vascular endothelial cadherin (VE-cadherin) monoclonal mouse IgG_{2B} (1:500, MAB9381, R&D systems, Minneapolis, MN, USA), VEGFR2 polyclonal rabbit IgG (1:75, ab2349, Abcam, Cambridge, UK), PECAM-1 monoclonal mouse IgG_1 (1:100, sc-71872, Santa Cruz), von Willebrand factor (vWF)

polyclonal rabbit IgG (1:200, A0082, Dako, Glostrup, Denmark), and vinculin monoclonal mouse IgG$_1$ (1:500, MAP3574, Millipore, Burlington, MA, USA). F-actin was stained for 45 min in the dark with Alexa Fluor 647 Phalloidin (1:500, A22287, Thermo Fisher Scientific). Subsequently, samples were incubated with the appropriate secondary antibodies (AlexaFluor 488 anti-mouse IgG, AlexaFluor 546 anti-rabbit IgG, and AlexaFluor 488 anti-mouse IgG2b (all 1:250; Thermo Fisher Scientific)).

Finally, nuclei were stained with DAPI (1:50) for 15 min in the dark. Images were obtained by using a fluorescence microscope (Cell Observer, Carl Zeiss AG, Oberkochen, Germany).

2.11. Examination of the Cell Coverage on the Tubular Scaffolds

The cell coverage of the inner wall of the tubular constructs was investigated using MTT (3-(4,5-dimethylthiazol-2-yl)-2,5-diphenyltetrazolium bromide) (M2128-1G, Sigma-Aldrich). After culturing with vECs, the constructs were incubated for 20 min with 1 mg/mL MTT at 37 °C and 5% CO_2. The insoluble purple formazan produced by the cellular reduction of MTT was then examined macroscopically.

2.12. Image Analysis

FN and DCN coating were quantified by measuring the relative pixel intensity (RPI) of the immunofluorescence images. To assess protein expression in the experiments, the area within a defined fluorescence intensity threshold was measured and normalized to the cell number. The cell count in the static experiments was quantified by counting the DAPI-stained cell nuclei per area. The quantification of the adherent ECFCs in the dynamic experiment was performed by measuring the DAPI-stained area normalized to the total area. All images were analyzed using ImageJ [58].

2.13. Scanning Electron Microscopy of Cells

Prior to SEM imaging of the scaffolds with cells, a critical point drying step was performed. First, cells were fixed for 60 min with 4% paraformaldehyde (PFA)/25% glutaraldehyde in PBS. Subsequently, a series of ethanol solutions in ascending concentration up to 100% was carried out to remove water. Critical point drying was done with a CPD 030 (Bal-Tec AG, Balzers, Liechtenstein) according to the manufacturer's protocol. Prior to imaging, the specimens were platina-coated (SCD050, Bal-Tec AG) for one minute at 0.05 mbar and rinsed with Argon after the coating process. SEM imaging was performed with a SU8030 (Hitachi, Tokyo, Japan) and an Auriga® 40 (Zeiss, Oberkochen, Germany).

For SEM imaging of the monocytes and macrophages, the cells were cultured for two days on uncoated (w/o), DCN- or FN-coated scaffolds, followed by preparation (as described in Reference [62]) and imaging with a JCM 6000 Benchtop (JEOL, Freising, Germany).

2.14. Statistical Analysis

Except stated otherwise, data are presented as mean ± standard deviation. For the immune data, GraphPad Prism (GraphPad Software, San Diego, CA, USA) was used to determine statistical significance between two groups using a one-way ANOVA/Kruskal–Wallis test. For the other data, a one-way ANOVA/Fisher's Least Significant Difference test was performed. A Welch's t-test was performed to compare between two data groups using OriginPro (OriginLab, Northampton, MA, USA). Probability values of 95%, 99%, 99.9%, and 99.99% were used to determine significance.

3. Results

3.1. Biofunctionalization Does Not Impact the Mechanical Properties of Electrospun Tubular Constructs

Electrospinning was used to fabricate 110-mm long tubular scaffolds with an inner diameter of 5 mm and a thickness of 0.40 ± 0.06 mm (Figure 3a). In order to modulate the cell–material interaction, the surface was biofunctionalized with FN, DCN, or FN + DCN. The impact of the biofunctionalization on the morphological and mechanical properties of the material was investigated (Figure 3). Fiber and

pore size analysis of the SEM images revealed no significant alteration due to protein adsorption (Figure 3e). Higher magnifications of the SEM images showed distribution of the proteins on the fibers. While DCN formed randomly distributed aggregates on the TPCU scaffolds, FN coating showed a network-like deposition in the nanometer range, which was also seen in the FN + DCN-coated samples, in which clearly recognizable aggregates were deposited on the protein network (Figure 3b, white arrows). Biofunctionalization utilizing both proteins individually and in combination was confirmed by IF staining. DCN IF staining revealed a more heterogeneous distribution of DCN in combination with FN than alone (Figure 3c, white arrows). The contact angle of the scaffolds was not significantly changed by the adsorption of either FN or DCN in comparison with the uncoated scaffolds. A significantly higher swelling ratio was observed of scaffolds that had been coated with FN + DCN (Figure 3e; control: 93.7% ± 7.7% versus FN + DCN: 117.1% ± 8.7%, $p < 0.05$). Overall, biofunctionalization had no significant influence on the mechanical properties (Figure 3e). The ultimate tensile strength ranged from 21.1 ± 3.5 MPa (DCN) to 22.1 ± 3.7 MPa (FN). Burst pressures were in the range between 3124 ± 466 mmHg (FN + DCN) to 3326 ± 78 mmHg (controls). Interestingly, the elastic modulus of the samples coated with FN + DCN showed a lower value compared to the controls, although this was not statistically significant (3.7 ± 0.5 MPa FN + DCN versus 4.8 ± 0.6 MPa controls, $p = 0.125$).

We compared the mechanical properties (elastic modulus and burst pressure) of our electrospun scaffolds with autologous grafts, which are today's gold standard for vascular bypass surgeries, using data obtained from literature (Table 2) [65]. The elastic modulus of our constructs (4.8 ± 0.6 MPa) was slightly higher than that of saphenous veins (2.25–4.2 MPa) [66,67] and of iliofemoral arteries (1.54 MPa) and veins (3.11 MPa) [68]. However, compared with an internal mammary artery (8 MPa) and a femoral artery (FA, 10.5 MPa)—used for popliteal bypass surgery—our engineered scaffolds showed a lower elastic modulus [66,69,70]. Regarding the burst pressure, engineered scaffolds (3326 ± 78 mmHg) lied within the range of a saphenous vein (1250–3900 mmHg) [66,67,71,72] and an internal mammary artery (2000–3196 mmHg) [66,71]. Konig et al. recommends for a TEGV a minimum burst pressure of 1700 mmHg [71]. We can therefore argue that our constructs have suitable mechanical properties to serve as a vascular graft or TEGV.

Table 2. Mechanical properties of the electrospun constructs and native blood vessels.

Graft Type	Elastic Modulus (MPa)	Burst Pressure (mmHg)	Ref.
Electrospun vascular graft	4.8 ± 0.6	3326 ± 78	-
Saphenous vein	4.2	1680–3900	[66]
Saphenous vein	2.25	1250	[67]
Saphenous vein	NA	1680	[73]
Saphenous vein	NA	2200	[72]
Saphenous vein	NA	1599	[71]
Internal mammary artery	NA	3196	[71]
Internal mammary artery	8	2000	[66]
Femoral artery	9–12	NA	[69]
Iliofemoral artery	1.54	NA	[68]
Iliofemoral vein	3.11	NA	[68]

Sample	Fiber size	Pore size	Contact angle	Swelling ratio	E-modulus	UTS*	Burst pressure
	nm	*μm²*	*°*	*%*	*MPa*	*MPa*	*mmHg*
control	775.8 ± 162.5	0.09 ± 0.03	98.4 ± 3.7	93.7 ± 7.7	4.8 ± 0.6	21.3 ± 2.1	3326 ± 78
FN	741.3 ± 141.0	0.12 ± 0.05	99.2 ± 2.3	103.3 ± 9.5	5.6 ± 0.9	22.1 ± 3.7	3151 ± 161
DCN	765.3 ± 172.7	0.11 ± 0.04	97.1 ± 7.1	100.1 ± 13.9	5.0 ± 1.1	21.1 ± 3.5	3150 ± 199
FN+DCN	698.7 ± 61.0	0.08 ± 0.01	100.0 ± 5.6	117.1 ± 8.7**	3.7 ± 0.5	21.4 ± 3.0	3124 ± 466

* UTS = Ultimate Tensile Strength
** One-way ANOVA, n=4, p<0.05 vs control

Figure 3. Morphological and mechanical characterization of the tubular biofunctionalized scaffolds: (**a**) Electrospun tubular scaffolds were fabricated with a length of 110 mm, an inner diameter of 5 mm, and a thickness of 0.40 ± 0.06 mm. (**b**) SEM images of control and biofunctionalized scaffolds: Scaffolds coated with FN show a network-like structure on the fibers. Aggregates deposited on the FN + DCN-coated samples are indicated by white arrows. (**c,d**) The coating of FN, DCN, or FN + DCN in combination was confirmed with IF staining: FN (red) and DCN (green). The white arrows indicate aggregates deposited on the FN + DCN-coated samples. Two-tailed *t*-test vs. control, n = 3, RPI = relative pixel intensity. (**e**) Fiber and pore size analysis shows no significant difference between the biofunctionalized scaffolds and the controls. Mechanical properties are not influenced by the protein coating. One-way ANOVA, n = 4, $p < 0.05$ vs. control.

3.2. Decorin and Fibronectin Coating of the Scaffolds Does Not Induce a Disadvantageous Immune Response

The effect of DCN- or FN-coated TPCU scaffolds on immune cells was investigated in order to estimate their suitability as vascular graft material. The immune response of a combination coating

was not required as the immune system would not react differently to the presence of both proteins in one coating. The performed immunological evaluation followed the normal sequence of immune activation [9], starting with PMNs that are followed by monocytes, which differentiate into macrophages at the site of injury, and finally T cells that become activated (Figure 4a).
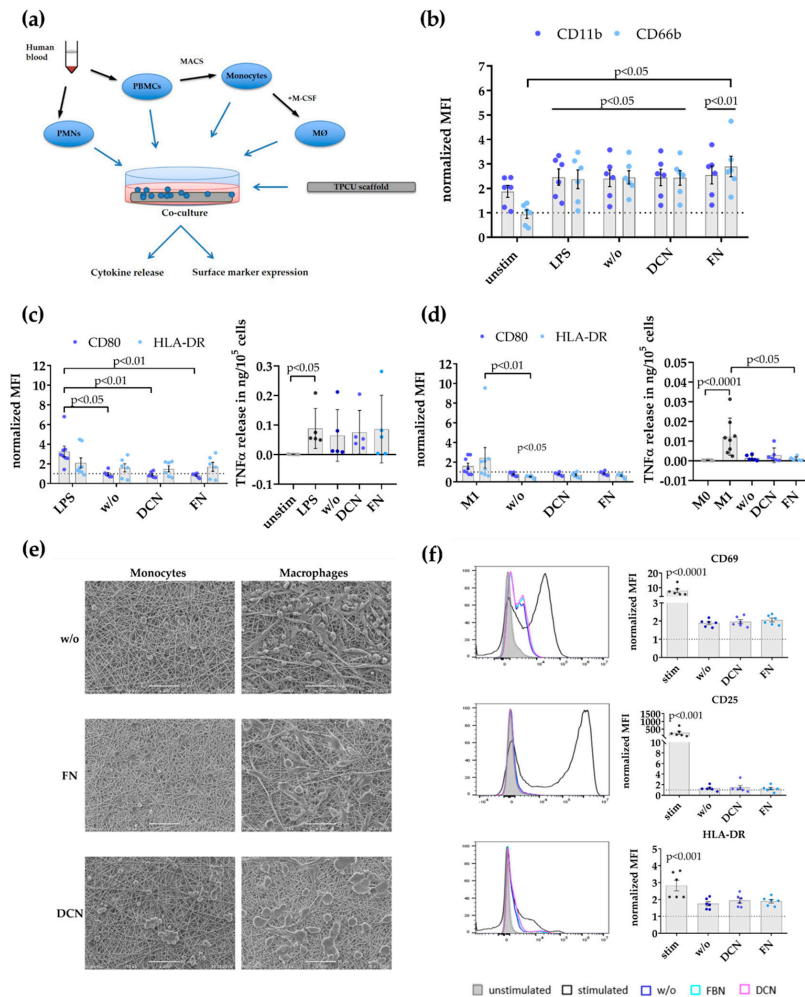

Figure 4. Immune response profile of FN- and DCN-coated planar scaffolds: (**a**) Schematic overview of the analysis steps and used immune cell assays. Polymorph nuclear cells (PMNs) and peripheral blood mononuclear cells (PBMCs) were isolated from human blood. Monocytes were acquired from PBMCs by magnetic separation via CD14 beads. Monocytes were differentiated into M0 macrophages (MØ) by stimulation with 50 ng/mL of macrophage colony-stimulating factor (M-CSF) for 7 days. (**b**) Surface expression of activation markers CD11b and CD66b by PMNs after 4 h: Displayed are the mean fluorescence intensities (MFI) normalized to unstimulated PMNs after isolation as mean ± SEM

(standard error of the mean) for unstimulated (unstim) and lipopolysaccharide (LPS)-stimulated cells, as well as PMNs cultured on the uncoated (w/o), DCN-coated (DCN), and FN-coated (FN) scaffolds determined with flow cytometry. Kruskal–Wallis test, n = 6. (**c**) Surface expression of activation markers CD80 and human leukocyte antigen DR isotype (HLA-DR), and tumor necrosis factor alpha (TNFα) release by monocytes. Shown are the MFI normalized to unstimulated monocytes as mean ± SEM for LPS-stimulated cells as well as monocytes cultured on uncoated (w/o), DCN-coated (DCN), and FN-coated (FN) scaffolds. Kruskal–Wallis test, n = 6–8. The TNF release is depicted in ng/10^5 cells as mean ± SEM for unstimulated (unstim) and LPS-stimulated cells as well as monocytes cultured on the uncoated (w/o), DCN-coated (DCN), and FN-coated (FN) scaffolds. Kruskal–Wallis test, n = 5. (**d**) Surface expression of activation markers CD80 and HLA-DR, and TNFα release by macrophage: Displayed is the MFI normalized to unstimulated M0 macrophages as mean ± SEM for macrophages differentiated to M1 and as well as cells cultured on uncoated (w/o), DCN-coated (DCN), and FN-coated (FN) scaffolds. Kruskal–Wallis test, n = 6–8. The TNFα release is shown in ng/10^5 cells as mean ± SEM for unstimulated M0 macrophages; macrophages differentiated to M1; and as well as cells cultured on the uncoated (w/o), DCN-coated (DCN), and FN-coated (FN) scaffolds. Kruskal–Wallis test, n = 6–9. (**e**) Representative SEM images of monocytes (left) and macrophages (right) on uncoated (w/o) and with biofunctionalized scaffolds (DCN and FN). Scale bars represent 50 μm. (**f**) Expression of activation markers CD69, CD25, and HLA-DR on CD3+ T cells in whole PBMC co-cultures: Shown are representative histograms (left) and the surface expression levels as MFI normalized to unstimulated T cells as mean ± SEM (right) for αCD3/αCD28-stimulated T cells (stim) as well as T cells cultured on uncoated (w/o), DCN-coated, and FN-coated scaffold. Kruskal–Wallis test, n = 6.

Initially, the expression of known PMN activation markers, the integrin CD11b, and the adhesion molecule CD66b was analyzed (Figure 4b). The normalized mean fluorescence intensity (MFI) for CD11b (stim 2.461 ± 0.3323, $p = 0.0179$; w/o 2.406 ± 0.3393, $p = 0.0378$; DCN 2.442 ± 0.3361, $p = 0.0217$; FN 2.549 ± 0.3644, $p < 0.0090$; all versus unstim 0 hours 1 ± 0) and CD66b (stim 2.372 ± 0.3875, $p = 0.0453$; w/o 2.448 ± 0.2728, $p = 0.0414$; DCN 2.431 ± 0.3041, $p = 0.0453$; FN: 2.893 ± 0.4239, $p = 0.0073$; all versus unstim 0 h 1 ± 0) was significantly increased on PMNs after LPS stimulation (positive control) and, after culture on the uncoated/coated scaffolds, compared to the level of PMNs directly after isolation (dotted line, set to 1). Additionally, PMNs on FN-coated TPCU scaffolds displayed a significantly higher CD66b expression compared with the unstimulated controls (FN 2.893 ± 0.4239 versus unstim 4 h 0.9438 ± 0.1723, $p < 0.0345$).

In a next step, monocyte responses were studied by flow cytometry analysis of the activation markers CD80 and HLA-DR (Figure 4c). The expression level for the co-stimulatory molecule CD80 was significantly upregulated only on LPS-stimulated monocytes compared with all other experimental groups (LPS 3.254 ± 0.5533 versus w/o 0.9592 ± 0.1342, $p = 0.0143$; versus DCN 0.8888 ± 0.1209, $p = 0.0046$; versus FN 0.8325 ± 0.08414, $p = 0.0018$). No significant differences in HLA-DR expression were detectable between the tested conditions. Additionally, no enhanced TNFα release of monocytes cultured on the uncoated/coated scaffolds was measured in contrast to a significantly elevated secretion in the LPS-stimulated controls compared to the unstimulated controls (LPS 0.08859 ± 0.03039 versus unstim 0.0005580 ± 0.0002111, $p = 0.0228$).

Then, macrophages (M0 type) generated in vitro by M-CSF were screened for signs of activation or polarization (Figure 4d). M0 (unstimulated) and M1 macrophages (IFNγ/LPS-stimulated) were used as control groups. Enhanced CD80 and HLA-DR expression and increase of TNFα secretion are hallmarks of pro-inflammatory M1 macrophages. There was no difference in the CD80 expression level between M0 macrophages (dotted line, set to 1) and all other experimental groups. The expression of HLA-DR by macrophages on uncoated scaffolds was significantly decreased compared with the M0 and M1 control settings (w/o 0.5220 ± 0.05753 versus M0 1 ± 0, $p = 0.0106$; versus M1 2.453 ± 1.040, $p = 0.0049$). Whereas M1 macrophages significantly elevated their TNFα release compared with M0 macrophages (M1 0.01229 ± 0.003333 versus M0 0.0002707 ± 0.00004142, $p < 0.0001$), no enhancement in pro-inflammatory cytokine release was measurable in all other experimental groups. Macrophages on the FN-coated scaffolds actually decreased their TNFα release compared with the M1 controls

(FN 0.0009826 ± 0.0004063 versus M1 0.01229 ± 0.003333, $p = 0.0432$). Complementary to the analysis of changes in surface marker and pro-inflammatory cytokine release by monocytes and macrophages, scanning electron microscopy was applied to assess the effects of co-culture on their morphology (Figure 4e). Scanning electron microscopy images were taken after the cells were cultured for two days on the different scaffold groups. Monocytes and macrophages on the DCN-coated scaffolds formed clusters of preferentially rounded cells. Macrophages cultured on uncoated or FN-coated scaffolds displayed more diverse shapes in contrast with cells grown on the DCN-coated TPCU scaffolds.

The potential activation of T cells was determined by flow cytometry analysis of known activation markers CD69, CD25, and HLA-DR [74] after culturing complete human PBMCs on either uncoated or coated scaffolds (Figure 4f). However, only anti-CD3/anti-CD28 stimulated T cells (stim; positive control) significantly elevated the expression level for CD69 (stim 7.956 ± 1.319 versus unstim 1 ± 0, $p < 0.0001$), CD25 (stim 265.6 ± 101.5 versus unstim 1 ± 0, $p = 0.0008$), and HLA-DR (stim 2.824 ± 0.3099 versus unstim 1 ± 0, $p = 0.0001$) compared with the level of the unstimulated controls (dotted line, set to 1). No significant increase in T cell activation marker expression was observed in any other experimental group.

3.3. Simulation of Endothelial Progenitor Cell Homing Using Endothelial Colony Forming Cells

3.3.1. ECFCs Show Altered VEGFR2 and PECAM-1 Expression Patterns on FN + DCN-Coated TPCU Scaffolds Under Static Culture Conditions

ECFCs were seeded on the biofunctionalized planar scaffolds and cultured under static conditions for 24 and 48 h. The amount of adherent ECFCs was significantly higher on samples coated with FN (24 h: 257 ± 57 cells/mm^2 versus control with 137 ± 46 cells/mm^2, $p < 0.01$; 48 h: 301 v 64 cells/mm^2 versus control with 52 ± 32 cells/mm^2, $p < 0.001$) and FN + DCN (24 h: 243 ± 63 cells/mm^2 versus control with 137 ± 46 cells/mm^2, $p < 0.01$; 48 h: 292 ± 54 cells/mm^2 versus control with 52 ± 32 cells/mm^2, $p < 0.001$) when compared with the uncoated samples (controls) throughout the entire culture period (Figure 5a). No significant difference of adherent cells was observed between FN coating and FN + DCN coating (24 h: $p = 0.656$; 48 h: $p = 756$). DCN coating did not show any significant difference in cell density in comparison with the uncoated controls (24 h: 105 ± 40 cells/mm^2 versus control with 137 ± 46 cells/mm^2, $p = 0.340$; 48 h: 30 ± 11 cells/mm^2 versus control with 52 ± 32 cells/mm^2, $p = 0.460$).

SEM analyses revealed that the ECFCs on the control and DCN-coated TPCU scaffolds had attained a spherical shape after 24 h whereas those on TPCU scaffolds that were coated with FN and FN + DCN showed a stretched morphology (Figure 5b). Immunofluorescence staining of samples 24 h after seeding (Figure 5c,d) identified a significantly lower PECAM-1 expression in ECFCs on FN + DCN-coated samples in comparison with FN coating (0.64 ± 0.30 versus 0.90 ± 0.25, $p < 0.05$). After 48 h, this effect tended to reverse, although the difference was not significant (0.70 ± 0.15 versus 0.54 ± 0.23, $p = 0.073$). A similar and statistically not significant tendency was detected for the fluorescence intensity of vWF. No significant changes were observed in VE-cadherin or vinculin expression. VEGFR2 expression was significantly decreased in cells cultured on FN-coated scaffolds when compared with cells grown on FN + DCN-coated scaffolds after 24 h (0.64 ± 0.11 versus 0.29 ± 0.16, $p < 0.01$). After 48 h, this effect vanished (0.28 ± 0.17 versus 0.28 ± 0.15, $p = 0.942$).
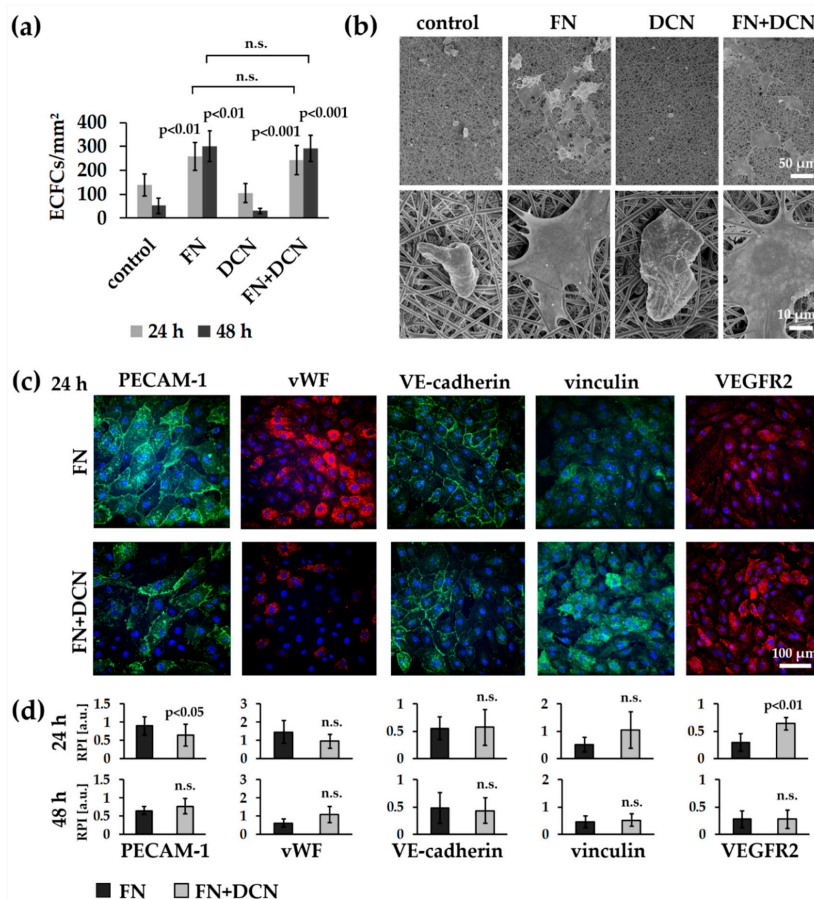
Figure 5. Static experiments of human ECFCs on FN-, DCN-, or FN + DCN-coated scaffolds: (**a**) Attachment and proliferation of the human ECFCs after 24 h and 48 h. Cells on FN and FN + DCN coating show a significantly higher proliferation when compared with cells gown on DCN and controls. Two-tailed *t*-test, compared to controls, n = 5, n.s. = not significant. (**b**) SEM images and (**c**) Immunofluorescence staining of ECFCs 24 h after seeding on ECM protein-coated scaffolds: Cells on FN and FN + DCN show a spread morphology in contrast to DCN coating and controls. (**d**) Semiquantitative fluorescence intensity analysis (relative pixel intensity (arbitrary units)) of cells on FN and FN + DCN shows no significant difference for the endothelial cell type marker von Willebrand factor (vWF) as well as vinculin and vascular endothelial cadherin (VE-cadherin). Platelet endothelial cell adhesion molecule (PECAM-1) expression is significantly decreased and VEGFR2 expression is significantly increased on FN + DCN-coated scaffolds after 24 h. Two-tailed *t*-test, n = 6, n.s. = not significant.

3.3.2. FN + DCN-Coating Attracts ECFCs Under Dynamic Culture Conditions

After ECFC seeding under static conditions, the cell-seeded scaffolds were dynamically cultured on a roller mixer for 24 h (Figure 6a). This approach was performed to reflect more closely the in vivo conditions. The analysis of the adherent cells showed a significantly increased cell number on the

FN + DCN-coated samples when compared with the controls and DCN-coated samples (5.7% ± 4.4% versus DCN coating with 1.0% ± 0.8%, $p < 0.05$ and versus control with 0.6% ± 0.7%, $p < 0.05$). The FN coating led to a nonsignificant decrease of adherent cells compared to FN + DCN coating (Figure 6b; 3.4% ± 1.5% versus 5.7% ± 4.4%, $p = 0.226$). Cells on all samples showed comparable PECAM-1 and vWF expression levels (Figure 6c). Distinct differences were observed in the cell morphology. F-actin staining helped visualizing the spread cells on the FN- and FN + DCN-coated scaffolds and cells with a more rounded morphology on the control samples and DCN-coated scaffolds (Figure 6c).
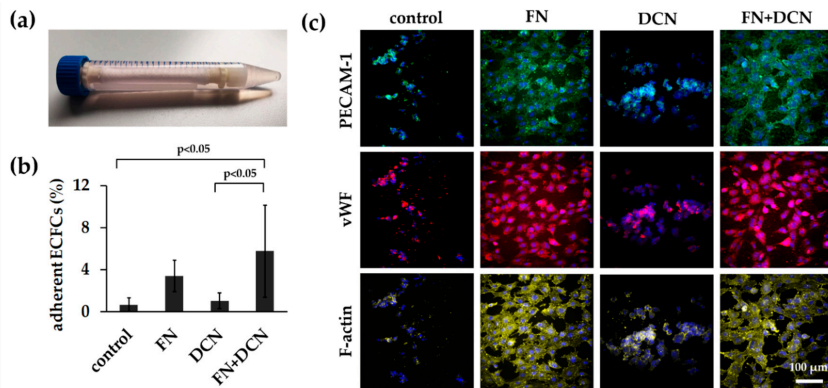
Figure 6. In vitro simulation of in vivo processes: ECFC attraction under dynamic conditions. (**a**) ECFCs were seeded into tubular constructs and cultured for 24 h on a roller mixer. (**b**) Adherent cells after 24 h on control scaffolds and on DCN-, FN-, and FN + DCN-coated scaffolds. FN + DCN coating shows a significantly higher cell number when compared with DCN coating and controls. One-way ANOVA, n = 4. (**c**) PECAM-1 (green), vWF (red), and F-actin (yellow) expression in ECFCs. Cells on FN and FN + DCN show a more spread morphology in contrast to the DCN and control samples.

3.4. In Vitro Tissue Engineering Approach Using Vascular Endothelial Cells

3.4.1. vECs Form an Endothelial Layer on FN- and FN + DCN-Coated Scaffolds Under Static Culture Conditions

vECs were seeded on the biofunctionalized planar constructs and cultured for 1, 4, and 7 days in order to investigate endothelialization (Figure 7a). One day after seeding, the cell number for all conditions was not significantly different. On day 4, vECs significantly increased proliferation on FN coating (78 ± 26 cells/mm^2 versus control with 8 ± 7 cells/mm^2, $p < 0.01$) and FN + DCN coating (55 ± 27 cells/mm^2 versus control with 8 ± 7 cells/mm^2, $p < 0.05$), while the VEC count on the DCN-coated samples had slightly decreased (7 ± 5 cells/mm^2 versus control with 8 ± 7 cells/mm^2, $p < 0.931$). This trend continued until day 7, on which a significantly increased cell count was detected for FN coating (186 ± 47 cells/mm^2 versus control with 16 ± 16 cells/mm^2, $p < 0.001$) and FN + DCN coating (135 ± 50 cells/mm^2 versus control with 16 ± 16 cells/mm^2, $p < 0.01$) in comparison with the uncoated controls. DCN coating of the TPCU scaffolds showed no improvement when compared with the control samples. Over the entire period of the experiment, the cell count was not significantly different between FN and FN + DCN coating.
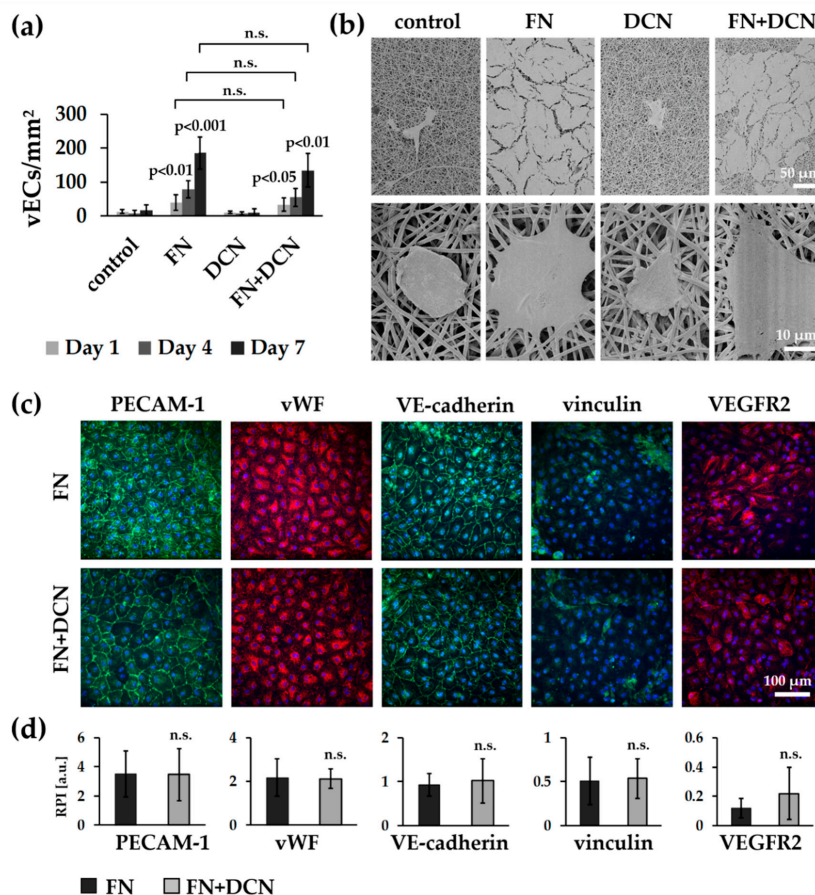
Figure 7. Static cell culture experiments of vECs on FN- and DCN-coated scaffolds: (**a**) Attachment and proliferation of vECs after 1, 4, and 7 days. vECs on FN and FN + DCN coating show a significantly higher proliferation rate compared with cells gown on DCN coating or control scaffolds. Two-tailed *t*-test, compared with control samples, n = 3, n.s. = not significant. (**b**) SEM images and (**c**) IF staining of vECs 7 days after seeding on ECM-coated scaffolds. Cells on FN and FN + DCN coating show a spread morphology in contrast with cells on DCN coating and control samples. (**d**) Semiquantitative fluorescence intensity analysis (relative pixel intensity (a.u.)) of cells on FN and FN + DCN coating shows no significant difference for PECAM-1, vWF, vinculin, or VE-cadherin expression. Two-tailed *t*-test, n = 5, n.s. = not significant.

While vECs on the control and DCN-coated scaffolds showed a spherical shape after 7 days as assessed using SEM, on FN and FN + DCN-coated scaffolds, vECs were stretched out and formed an almost confluent endothelial cell layer (Figure 7b). IF staining confirmed the expression of the endothelial cell type-specific markers PECAM-1, vWF, and VE-cadherin in the vECs on both FN and FN + DCN coating (Figure 7c). Semiquantitative analysis of fluorescence intensities revealed no significant differences of marker expression between FN and FN + DCN coating (Figure 7d). Vinculin expression was comparable in vECs on both coatings. With regard to VEGFR2, an increased fluorescence intensity

in cells grown on the FN + DCN-coated samples was observed. However, due to a high variation in expression levels of individual experiments, no statistical significance between cells grown on FN or FN + DCN coating could be determined.

In summary, our data showed that DCN coating of the TPCU scaffolds did not have a substantial advantage when aiming for an increased VEC proliferation or an improved cell–cell or cell–material interaction. For this reason, only FN biofunctionalized TPCU scaffolds were used for the following in vitro tissue engineering experiments.

3.4.2. vECs Cultured in a Custom-Made Bioreactor Under Flow Form a Confluent and Aligned Cell Layer on FN-Biofunctionalized TPCU

After successful implementation of the developed bioreactor system, we aimed to test whether the FN-biofunctionalized TPCU scaffolds can be endothelialized under dynamic conditions. vECs were seeded into the tubular TPCU scaffolds, and after an initial culture for three days under static conditions to allow cell attachment, a flow was employed that was stepwise increased to 25 mL/min within 1.5 days (Figure 2e). Under this flow, which causes a shear stress of about 0.03 Pa, the vEC-seeded FN-biofunctionalized scaffolds were cultured for seven days. Metabolic activity assessment using an MTT assay showed that a large part of the inner wall of our construct was covered with living cells, as indicated by the purple formazan stain (Figure 8a). IF staining and SEM further revealed a layer of confluent vECs that were aligned in the direction of flow (Figure 8b,c).
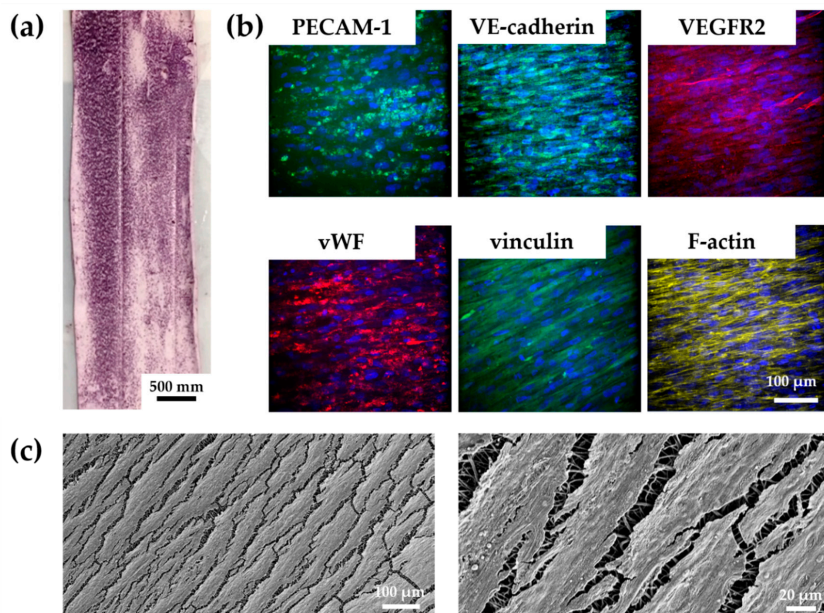

Figure 8. Tissue-engineering approach with vascular endothelial cells cultured for 7 days on FN-biofunctionalized electrospun tubular TPCU scaffolds under dynamic conditions: (**a**) Inner wall of the tubular construct shows living vECs indicated by the purple formazan stain. (**b**) PECAM-1, vWF, VE-cadherin, vinculin, VEGFR2, and F-actin expression were detected. vECs show an aligned morphology. (**c**) SEM confirms vECs that had aligned with the flow to which they were exposed to during the dynamic culture in the bioreactor.

We confirmed the expression of the endothelial cell markers PECAM-1, vWF, and VE-cadherin. However, PECAM-1 and VE-cadherin did not appear to be located on the cell membrane as usual. Vinculin and VEGFR2 were also detected in the cells. Nevertheless, the staining of VEGFR2 showed only a weak signal.

4. Discussion

Due to a proven biocompatibility and biostability at body temperature [55,57], we selected for this study a novel thermoplastic polycarbonate urethane for the fabrication of a TEVG. At first, scaffolds were produced by electrospinning of the TPCU and were disinfected with 70% ethanol. Microbiological studies showed that ethanol treatment did not achieved 100% sterility (Figure S3; 2 out of 9 plates showed germ growth). We are aware that disinfection with ethanol does not necessarily inactivate all forms of microorganisms [75]; therefore, for the clinical translation, a more efficient sterilization method should be considered.

After disinfection, scaffolds were then biofunctionalized by adsorption of FN and DCN, either alone or in combination. The adsorbed proteins did not impact elastic modulus or burst pressure of the tubular constructs (Figure 3). We demonstrated that the biomechanical properties of our constructs were comparable to native vascular tissue (Table 2).

The ability to mimic the nanofibrous topography of the ECM makes electrospinning a powerful method for cardiovascular tissue-engineering applications. Several studies have already described the influence of fiber and pore size on cell adhesion, cell migration, proliferation, and differentiation, as well as cell–cell interaction [76–78]. In native blood vessels, the ECs are located on the basal lamina, a mixture of defined ECM proteins that form a network and bind cells [79]. The literature describes a wide range of pore and fiber diameters (1–1000 nm) from different vessels, depending on the position and physical properties of the vessel [80]. The main collagen component of the basal lamina is collagen type IV. It forms fibers that range from 20 to 52 nm [80–82]. In our study, the fiber diameters were between 699 ± 61 nm and 776 ± 163 nm, which is much higher compared to the collagen type IV fibers in native vessels. However, other studies developing electrospun vascular grafts reported comparable [83] or even larger fiber sizes [84,85] on which a functional endothelium was formed [84]. The pore size strongly depends on the vessel type and ranges between 5 nm and 8 μm [80,82,86–89]. Our constructs showed pore sizes between 0.08 ± 0.01 μm^2 and 0.12 ± 0.05 μm^2, which lies in the range of a native vessel.

Several studies have already described that FN improves the endothelialization of vascular grafts [19,48,49,51]. In our study, we observed a fibrous-like structure of the coated FN (Figure 3b). This phenomenon can be interpreted as material-driven fibrillogenesis, first described by Salmeron-Sanchez et al. [3]. In the human body, FN matrix assembly is a cell-mediated process [90] that influences cell growth, cell differentiation, and cell–cell interaction [76–78,90,91]. It has been shown that the adhesion of FN on poly (ethyl acrylate) (PEA) can lead to a spontaneous organization of FN into protein networks. It has also been shown that cell-free material-induced FN fibrillogenesis influences the maintenance and differentiation of stem cells [3,92]. Furthermore, it was described that the FN network has an increased ability to store growth factors [93]. To the best of our knowledge, our study is the first to show that material-driven fibrillogenesis can be observed on electrospun TPCU fibers. We presume that the surface properties, such as hydrophobicity and polarity, are comparable to those of PEA. Whether the FN network has a significant advantage in terms of cell behavior or growth factor binding compared to dispersed, coated FN molecules would need further investigation.

In addition to FN coating, in this study, we also used DCN coating. We observed that, after coating on the TPCU, DCN was randomly distributed in aggregates on the fibers (Figure 3b). Since DCN does not form fibrils, this coating behavior was expected. Even larger, globular DCN aggregates were observed on the FN + DCN samples (Figure 3b,d). Interestingly, these aggregates were predominantly seen on the FN fibrils and not on the TPCU itself. It is known that DCN interacts with FN [94,95]. Furthermore, the interaction of proteins with materials is determined by the geometrical, chemical,

and electrical properties of the substrate [96]. In this respect, it can be hypothesized that the DCN prefers the FN surface more than the hydrophobic polyurethane surface. Interestingly, we observed a significantly increased swelling ratio for FN + DCN (Figure 3e). This was not the case with individually FN- or DCN-coated TPCU. Depending on the surface properties of the material and the interaction with other proteins, the conformation, orientation, and bioactivity of a protein can also be influenced [96–98]. With this in mind, one can assume that both DCN and FN in combination can have a different bioactivity [99].

In contrast to our previous findings using poly (ethylene glycol) dimethacrylate-poly (L-lactide) (PEGdma-PLA) or a blend of poly-ε-caprolacton and gelatin [25,100], we identified a cell-repellent effect of the DCN-coated TCPU electrospun scaffolds for both human ECFCs and human vECs. As already discussed, cells prefer to adhere to hydrophilic surfaces [101]. Since the TCPU itself is highly hydrophobic (control: 98.4 ± 3.7 °), it can cause a cell-repellent effect. DCN alone was not able to diminish this effect (Figure 5a,b). Cell adhesion is influenced by cell-adhesive peptides such as the RGD sequence. Since DCN does not contain these sequences, as it is the case with FN, we assume that at least this integrin-based cell–material interaction cannot be mediated by DCN. It has been described that DCN can even partially inhibit cell adhesion; however, this has only been observed with fibroblasts and not with endothelial cells [28,102]. Hinderer et al. observed an attraction of ECFCs to DCN-coated PEGdma-PLA [25]. A direct comparison with this study is therefore difficult, since this polymer has different surface properties, which influence the amount and orientation of the adsorbed DCN and thus may have an altered impact on cell behavior [96]. FN coating reversed the cell-repellent effect of the TCPU, both with and without DCN (Figure 5). We can therefore conclude that the cell attraction and proliferation is supported by FN but not affected by DCN [99,103].

Scaffolds should in general exhibit a low immunogenicity and at the same time support tissue regenerative processes. The evaluation of the immune response profiles of the analyzed control and ECM-coated scaffolds excluded any major adverse effects, with only minor innate activation characteristics. Co-culturing PMNs, as the first cells of an innate immune response, induced an activated cell phenotype regarding the expression of CD11b and CD66b. Monocytes were incompletely activated after co-culturing with the scaffold as indicated by only a weak tendency to upregulate the HLA-DR expression and to increase their TNFα release. From the literature, it is well known that the upregulation of CD80 and HLA-DR would be a hallmark of M1 macrophages [62,104] and that the fiber and pore size of electrospun scaffolds could impact the macrophage polarization state [105]. When analyzing the potential impact of the TPCU scaffolds on macrophage polarization, no clear trend to drive the process into a specific macrophage subtype could be determined. Also, the coating by either DCN or FN did not trigger a specific type of macrophage polarization. In contrast, co-culture studies with soluble recombinant DCN demonstrated that macrophages responded with an upregulated CD80 expression as well an increased secretion of TNFα and IL-10 [25]. The absent responses in the present study may result from the far lower amount of protein present on the coated scaffolds in comparison with the high protein amounts available within solutions or even by conformational changes. Not surprisingly, adaptive T cell responses were also not detected. T cells on scaffolds simply showed a trend to upregulate CD69 and HLA-DR without significant changes.

A functional endothelium is mainly characterized by cell–cell junctions [106]. As PECAM-1 is the most abundant component of the EC junction, which contributes to the maintenance of the EC permeability barrier, its expression is essential for a functional EC layer [107]. In our study, the ECFCs on FN coating revealed a significantly increased PECAM-1 expression after 24 h compared with ECFCs cultured on FN + DCN-coated scaffolds. In contrast, the VEGFR2 expression was significantly decreased in the ECFCs on FN coating after 24 h compared with FN + DCN coating. It has been reported that VEGFR2 is highly expressed in early endothelial precursor cells but not in all mature ECs [108,109]. For example, PECAM-1 is less expressed in endothelial progenitor cells, as it is typically associated with a more mature EC phenotype [110]. Interestingly, DCN has been reported to stimulate the maintenance of undifferentiated progenitor cells [111], and FN promotes endothelial

cell differentiation [112]. Therefore, we hypothesize that the FN + DCN coating in our experiments kept the ECFCs in a precursor cell state compared with the culture on only FN. It may also be possible that a direct interaction of DCN with VEGFR2 leads to its upregulation. A positive feedback loop between VEGF and VEGFR2 has been described [113]. Whether DCN has the same effect remains to be confirmed.

Since DCN exerts many other functions, an indirect regulation of VEGFR2 is also conceivable [34,114]. Mazor et al. showed that the matrix metalloproteinase-1 (MMP-1) promotes the expression of VEGFR2 [115]. The core protein of DCN in turn is able to stimulate the expression of MMP-1 [116,117]. Furthermore, Murakami et al. reported that increased concentrations of the fibroblast growth factor (FGF) led to an increase in VEGFR2 levels [118]. DCN, in turn, can bind to FGF and can increase its activity [119]. It was also described that VEGFR2 expression is regulated by the disruption of the c-MET receptor tyrosine kinase [120]. As an antagonistic ligand of c-MET, DCN is able to inhibit its activity and thus might indirectly promote VEGFR2 expression [38]. We have already discussed the hypothesis that DCN in interaction with FN may exhibit an altered bioactivity. This would explain why DCN, which was adsorbed on the TPCU scaffold surface, impacted ECs in combination with FN but did not without [96–98]. The reason for VEGFR2 upregulation can also be due to FN. It might be possible that, in combination with DCN, its conformation and function is also changed [96–98]. It has been shown that conformational remodeling of the FN matrix selectively regulates VEGF signaling [121]. VEGF in turn regulates VEGFR2 expression [113]. By binding to VEGF, FN can promote full phosphorylation and activation of VEGFR2 [122]. Interestingly, after 48 h, the difference between FN and FN + DCN coating for both the PECAM-1 and VEGFR2 expression had vanished (Figure 5d). With regard to VEGFR2, a short half-life of the receptor is described, which enables ECs to adapt quickly to changes in the extracellular environment [118,123]. This leads to the question of how long the biofunctionalized DCN coating was fully biologically active in our study. Due to its natural presence in the body, it can be easily degraded [124]. We showed that DCN acts on ECFCs for at least 24 h under static conditions. The culture of vECs over 7 days under static conditions revealed the same expression of PECAM-1 and VEGFR2 on FN and FN + DCN coating (Figure 7). This observation supports the assumption that the DCN was only active for a short period of time and that its effect had disappeared after 7 days. In addition, it is possible that the vECs are not as sensitive to DCN, as we have observed with the ECFCs. Several studies have described an increase in VEGFR2 expression during differentiation and expansion of endothelial progenitor cells [109,125]. At the same time, VEGFR2 expression was relatively low during the proliferation phase [126]. Since the vECs are mature cells, it can be assumed that the externally changed conditions do not affect the VEFGR2 expression significantly. Nevertheless, in this study, we successfully showed that vECs formed an endothelium on biofunctionalized FN-coated constructs after 7 days of culture whereas DCN-coated TPCU scaffolds did not show a significant effect on cell proliferation.

In our TEVG experiments using a custom-made bioreactor, we observed a unidirectional cell orientation in the direction of the flow. The response of ECs to shear stress is well studied [127–129]. It has been shown that, under flow, the morphology of vECs changes from a cobblestone (static) to an elongated form and that vECs align in the direction of the flow in only 24 h [127]. The hemodynamic forces can modulate not only the phenotype but also the gene expression of the cells. In this context, the correct flow is of great importance for a properly functioning endothelium [130]. In our study, IF staining revealed the expression of vWF, PECAM-1, and VE-cadherin. However, PECAM-1 and VE-cadherin were not located on the cell membrane as usually seen. VEGFR2 expression was quite weak, and the F-actin staining revealed a rather fibroblast-like cell morphology. We hypothesize that the vECs underwent endothelial-mesenchymal transition (EndMT). ECs, which undergo EndMT, lose the expression of the characteristic surface endothelial markers PECAM-1, VE-cadherin, and VEGFR2 [39,131,132]. Mahmoud et al. showed that the EndMT can be induced under low shear stress (0.4 Pa) [133]. In our approach, the cells experienced a wall shear stress of about 0.03 Pa, which is slightly lower than a venous wall shear stress (0.06 Pa) [134]. In silico simulations of our dynamic bioreactor culture

confirmed laminar flow conditions along a large part of the vascular wall using the applied parameters. Another reason for the fibroblast-like phenotype could be that ECs are highly plastic [135,136]. Therefore, culturing ECs in vitro in an artificial environment can lead to cell dedifferentiation [136,137]. This highlights the importance of fine-tuning the culture conditions to create a functional TEGV.

5. Conclusions

In the present study, we successfully engineered a TPCU electrospun vascular graft which combines appropriate mechanical properties with a highly bioactive surface for the attraction of ECs. The FN biofunctionalization was characterized by a material-driven fibrillogenesis, which might have a positive impact on FN functionality [3]. To imitate the physiological conditions of a blood vessel, a bioreactor for in vitro tissue culture was designed and manufactured. vECs seeded on the FN-functionalized constructs formed a confluent and functional endothelium under static and dynamic conditions. In contrast, DCN-biofunctionalized TPCU scaffolds had a cell-repellent effect on vECs and ECFCs, most likely due to the high hydrophobic properties of the TPCU. However, since DCN has been shown to inhibit the adhesion of fibroblasts, it remains a promising protein for the functionalization of vascular grafts [29].

The challenge for the future will be to combine the advantages of different proteins and to thus increase the selectivity, functionality, and stability of a biofunctionalized vascular graft while keeping the complexity of the coating as low as possible.

References

1. Catto, V.; Farè, S.; Freddi, G.; Tanzi, M.C. Vascular Tissue Engineering: Recent Advances in Small Diameter Blood Vessel Regeneration. *ISRN Vasc. Med.* **2014**, *2014*, 923030. [CrossRef]
2. Causes of Death. Available online: https://www.who.int/data/gho/data/themes/topics/causes-of-death/GHO/causes-of-death (accessed on 29 December 2019).
3. Salmerón-Sánchez, M.; Rico, P.; Moratal, D.; Lee, T.T.; Schwarzbauer, J.E.; García, A.J. Role of Material-Driven Fibronectin Fibrillogenesis in Cell Differentiation. *Biomaterials* **2011**, *32*, 2099–2105. [CrossRef] [PubMed]
4. Sánchez, P.F.; Brey, E.M.; Carlos Briceño, J.C. Endothelialization Mechanisms in Vascular Grafts. *J. Tissue Eng. Regen. Med.* **2018**, *12*, 2164–2178. [CrossRef] [PubMed]
5. L'Heureux, N.; Dusserre, N.; Marini, A.; Garrido, S.; De la Fuente, L.; McAllister, T. Technology Insight: The Evolution of Tissue-Engineered Vascular Grafts - From Research to Clinical Practice. *Nat. Clin. Pract. Cardiovasc. Med.* **2007**, *4*, 389–395. [CrossRef] [PubMed]

6. Ercolani, E.; Del Gaudio, C.; Bianco, A. Vascular Tissue Engineering of Small-Diameter Blood Vessels: Reviewing the Electrospinning Approach. *J. Tissue Eng. Regen. Med.* **2015**, *9*, 861–888. [CrossRef] [PubMed]
7. Seifu, D.G.; Purnama, A.; Mequanint, K.; Mantovani, D. Small-Diameter Vascular Tissue Engineering. *Nat. Rev. Cardiol.* **2013**, *10*, 410–421. [CrossRef]
8. Ravi, S.; Qu, Z.; Chaikof, E.L. Polymeric Materials for Tissue Engineering of Arterial Substitutes. *Vascular* **2009**, *17*, S45–S54. [CrossRef]
9. Julier, Z.; Park, A.J.; Briquez, P.S.; Martino, M.M. Promoting Tissue Regeneration by Modulating the Immune System. *Acta Biomater.* **2017**, *53*, 13–28. [CrossRef]
10. Hinderer, S.; Brauchle, E.; Schenke-Layland, K. Generation and Assessment of Functional Biomaterial Scaffolds for Applications in Cardiovascular Tissue Engineering and Regenerative Medicine. *Adv. Healthc. Mater.* **2015**, *4*, 2326–2341. [CrossRef]
11. Ndreu, A.; Nikkola, L.; Ylikauppilar, H.; Ashammakhi, N.; Hasirci, V. Electrospun Biodegradable Nanofibrous Mats for Tissue Engineering. *Nanomedicine* **2008**, *3*, 45–60. [CrossRef]
12. Li, M.; Mondrinos, M.J.; Gandhi, M.R.; Ko, F.K.; Weiss, A.S.; Lelkes, P.I. Electrospun Protein Fibers as Matrices for Tissue Engineering. *Biomaterials* **2005**, *26*, 5999–6008. [CrossRef]
13. Boland, E.D.; Matthews, J.A.; Pawlowski, K.J.; Simpson, D.G.; Wnek, G.E.; Bowlin, G.L. Electrospinning Collagen and Elastin: Preliminary Vascular Tissue Engineering. *Front. Biosci.* **2004**, *9*, 1422–1432. [CrossRef] [PubMed]
14. Zhang, M.; Wang, Z.; Wang, Z.; Feng, S.; Xu, H.; Zhao, Q.; Wang, S.; Fang, J.; Qiao, M.; Kong, D. Immobilization of Anti-CD31 Antibody on Electrospun Poly(E{open}-Caprolactone) Scaffolds through Hydrophobins for Specific Adhesion of Endothelial Cells. *Colloids Surf. B Biointerfaces* **2011**, *85*, 32–39. [CrossRef]
15. Markway, B.D.; McCarty, O.J.T.; Marzec, U.M.; Courtman, D.W.; Hanson, S.R.; Hinds, M.T. Capture of Flowing Endothelial Cells Using Surface-Immobilized Anti-Kinase Insert Domain Receptor Antibody. *Tissue Eng.-Part C Methods* **2008**, *14*, 97–105. [CrossRef]
16. Kanie, K.; Narita, Y.; Zhao, Y.; Kuwabara, F.; Satake, M.; Honda, S.; Kaneko, H.; Yoshioka, T.; Okochi, M.; Honda, H.; et al. Collagen Type IV-Specific Tripeptides for Selective Adhesion of Endothelial and Smooth Muscle Cells. *Biotechnol. Bioeng.* **2012**, *109*, 1808–1816. [CrossRef]
17. Li, J.; Ding, M.; Fu, Q.; Tan, H.; Xie, X.; Zhong, Y. A Novel Strategy to Graft RGD Peptide on Biomaterials Surfaces for Endothelization of Small-Diameter Vascular Grafts and Tissue Engineering Blood Vessel. *J. Mater. Sci. Mater. Med.* **2008**, *19*, 2595–2603. [CrossRef]
18. Edlund, U.; Sauter, T.; Albertsson, A.-C. Covalent VEGF Protein Immobilization on Resorbable Polymeric Surfaces. *Polym. Adv. Technol.* **2011**, *22*, 166–171. [CrossRef]
19. De Visscher, G.; Mesure, L.; Meuris, B.; Ivanova, A.; Flameng, W. Improved Endothelialization and Reduced Thrombosis by Coating a Synthetic Vascular Graft with Fibronectin and Stem Cell Homing Factor SDF-1α. *Acta Biomater.* **2012**, *8*, 1330–1338. [CrossRef] [PubMed]
20. Schleicher, M.; Hansmann, J.; Elkin, B.; Kluger, P.J.; Liebscher, S.; Huber, A.J.T.; Fritze, O.; Schille, C.; Müller, M.; Schenke-Layland, K.; et al. Oligonucleotide and Parylene Surface Coating of Polystyrene and EPTFE for Improved Endothelial Cell Attachment and Hemocompatibility. *Int. J. Biomater.* **2012**, *2012*, 397813. [CrossRef] [PubMed]
21. Strahm, Y.; Flueckiger, A.; Billinger, M.; Meier, P.; Mettler, D.; Weisser, S.; Schaffner, T.; Hess, O. Endothelial-Cell-Binding Aptamer for Coating of Intracoronary Stents. *J. Invasive Cardiol.* **2010**, *22*, 481–487.
22. Suuronen, E.J.; Zhang, P.; Kuraitis, D.; Cao, X.; Melhuish, A.; McKee, D.; Li, F.; Mesana, T.G.; Veinot, J.P.; Ruel, M. An Acellular Matrix-Bound Ligand Enhances the Mobilization, Recruitment and Therapeutic Effects of Circulating Progenitor Cells in a Hindlimb Ischemia Model. *FASEB J.* **2009**, *23*, 1447–1458. [CrossRef] [PubMed]
23. Tardif, K.; Cloutier, I.; Miao, Z.; Lemieux, C.; St-Denis, C.; Winnik, F.M.; Tanguay, J.F. A Phosphorylcholine-Modified Chitosan Polymer as an Endothelial Progenitor Cell Supporting Matrix. *Biomaterials* **2011**, *32*, 5046–5055. [CrossRef] [PubMed]
24. Melchiorri, A.J.; Hibino, N.; Fisher, J.P. Strategies and Techniques to Enhance the in Situ Endothelialization of Small-Diameter Biodegradable Polymeric Vascular Grafts. *Tissue Eng. Part B. Rev.* **2013**, *19*, 292–307. [CrossRef] [PubMed]

25. Hinderer, S.; Sudrow, K.; Schneider, M.; Holeiter, M.; Layland, S.L.; Seifert, M.; Schenke-Layland, K. Surface Functionalization of Electrospun Scaffolds Using Recombinant Human Decorin Attracts Circulating Endothelial Progenitor Cells. *Sci. Rep.* **2018**, *8*, 110. [CrossRef]

26. Zhang, W.; Ge, Y.; Cheng, Q.; Zhang, Q.; Fang, L.; Zheng, J. Decorin Is a Pivotal Effector in the Extracellular Matrix and Tumour Microenvironment. *Oncotarget* **2018**, *9*, 5480–5491. [CrossRef]

27. Chen, S.; Young, M.F.; Chakravarti, S.; Birk, D.E. Interclass Small Leucine-Rich Repeat Proteoglycan Interactions Regulate Collagen Fibrillogenesis and Corneal Stromal Assembly. *Matrix Biol.* **2014**, *35*, 103–111. [CrossRef]

28. Fiedler, L.R.; Schönherr, E.; Waddington, R.; Niland, S.; Seidler, D.G.; Aeschlimann, D.; Eble, J.A. Decorin Regulates Endothelial Cell Motility on Collagen I through Activation of Insulin-like Growth Factor I Receptor and Modulation of A2β1 Integrin Activity. *J. Biol. Chem.* **2008**, *283*, 17406–17415. [CrossRef]

29. Fiedler, L.R.; Eble, J.A. Decorin Regulates Endothelial Cell-Matrix Interactions during Angiogenesis. *Cell Adh. Migr.* **2009**, *3*, 3–6. [CrossRef]

30. Zafiropoulos, A.; Nikitovic, D.; Katonis, P.; Tsatsakis, A.; Karamanos, N.K.; Tzanakakis, G.N. Decorin-Induced Growth Inhibition Is Overcome through Protracted Expression and Activation of Epidermal Growth Factor Receptors in Osteosarcoma Cells. *Mol. Cancer Res.* **2008**, *6*, 785–794. [CrossRef]

31. Nili, N.; Cheema, A.N.; Giordano, F.J.; Barolet, A.W.; Babaei, S.; Hickey, R.; Eskandarian, M.R.; Smeets, M.; Butany, J.; Pasterkamp, G.; et al. Decorin Inhibition of PDGF-Stimulated Vascular Smooth Muscle Cell Function: Potential Mechanism for Inhibition of Intimal Hyperplasia after Balloon Angioplasty. *Am. J. Pathol.* **2003**, *163*, 869–878. [CrossRef]

32. D'Antoni, M.L.; Risse, P.A.; Ferraro, P.; Martin, J.G.; Ludwig, M.S. Effects of Decorin and Biglycan on Human Airway Smooth Muscle Cell Adhesion. *Matrix Biol.* **2012**, *31*, 101–112. [CrossRef]

33. De Lange Davies, C.; Melder, R.J.; Munn, L.L.; Mouta-Carreira, C.; Jain, R.K.; Boucher, Y. Decorin Inhibits Endothelial Migration and Tube-like Structure Formation: Role of Thrombospondin-1. *Microvasc. Res.* **2001**, *62*, 26–42. [CrossRef]

34. Järveläinen, H.; Sainio, A.; Wight, T.N. Pivotal Role for Decorin in Angiogenesis. *Matrix Biol.* **2015**, *43*, 15–26. [CrossRef]

35. Riessen, R.; Isner, J.M.; Blessing, E.; Loushin, C.; Nikol, S.; Wight, T.N. Regional Differences in the Distribution of the Proteoglycans Biglycan and Decorin in the Extracellular Matrix of Atherosclerotic and Restenotic Human Coronary Arteries. *Am. J. Pathol.* **1994**, *144*, 962–974.

36. Salisbury, B.G.; Wagner, W.D. Isolation and Preliminary Characterization of Proteoglycans Dissociatively Extracted from Human Aorta. *J. Biol. Chem.* **1981**, *256*, 8050–8057.

37. Khan, G.A.; Girish, G.V.; Lala, N.; di Guglielmo, G.M.; Lala, P.K. Decorin Is a Novel VEGFR-2-Binding Antagonist for the Human Extravillous Trophoblast. *Mol. Endocrinol.* **2011**, *25*, 1431–1443. [CrossRef]

38. Goldoni, S.; Humphries, A.; Nyström, A.; Sattar, S.; Owens, R.T.; McQuillan, D.J.; Ireton, K.; Iozzo, R.V. Decorin Is a Novel Antagonistic Ligand of the Met Receptor. *J. Cell Biol.* **2009**, *185*, 743–754. [CrossRef]

39. Van Meeteren, L.A.; Ten Dijke, P. Regulation of Endothelial Cell Plasticity by TGF-β. *Cell Tissue Res.* **2012**, *347*, 177–186. [CrossRef]

40. Järvinen, T.A.H.; Ruoslahti, E. Target-Seeking Antifibrotic Compound Enhances Wound Healing and Suppresses Scar Formation in Mice. *Proc. Natl. Acad. Sci. USA* **2010**, *107*, 21671–21676. [CrossRef]

41. Liverani, L.; Killian, M.S.; Boccaccini, A.R. Fibronectin Functionalized Electrospun Fibers by Using Benign Solvents: Best Way to Achieve Effective Functionalization. *Front. Bioeng. Biotechnol.* **2019**, *7*, 68. [CrossRef]

42. Campos, D.M.; Gritsch, K.; Salles, V.; Attik, G.N.; Grosgogeat, B. Surface Entrapment of Fibronectin on Electrospun PLGA Scaffolds for Periodontal Tissue Engineering. *Biores. Open Access* **2014**, *3*, 117–126. [CrossRef]

43. Regis, S.; Youssefian, S.; Jassal, M.; Phaneuf, M.; Rahbar, N.; Bhowmick, S. Integrin A5β1-Mediated Attachment of NIH/3T3 Fibroblasts to Fibronectin Adsorbed onto Electrospun Polymer Scaffolds. *Polym. Eng. Sci.* **2014**, *54*, 2587–2594. [CrossRef]

44. Monchaux, E.; Vermette, P. Effects of Surface Properties and Bioactivation of Biomaterials on Endothelial Cells. *Front. Biosci.-Sch.* **2010**, *2*, 239–255.

45. Lenselink, E.A. Role of Fibronectin in Normal Wound Healing. *Int. Wound J.* **2015**, *12*, 313–316. [CrossRef]

46. Grinnell, F. Fibronectin and Wound Healing. *J. Cell. Biochem.* **1984**, *26*, 107–116. [CrossRef]

47. Sgarioto, M.; Vigneron, P.; Patterson, J.; Malherbe, F.; Nagel, M.D.; Egles, C. Collagen Type I Together with Fibronectin Provide a Better Support for Endothelialization. *Comptes Rendus-Biol.* **2012**, *335*, 520–528. [CrossRef]

48. Ardila, D.; Liou, J.-J.; Maestas, D.; Slepian, M.; Badowski, M.; Wagner, W.; Harris, D.; Vande Geest, J. Surface Modification of Electrospun Scaffolds for Endothelialization of Tissue-Engineered Vascular Grafts Using Human Cord Blood-Derived Endothelial Cells. *J. Clin. Med.* **2019**, *8*, 185. [CrossRef]

49. Tersteeg, C.; Roest, M.; Mak-Nienhuis, E.M.; Ligtenberg, E.; Hoefer, I.E.; de Groot, P.G.; Pasterkamp, G. A Fibronectin-Fibrinogen-Tropoelastin Coating Reduces Smooth Muscle Cell Growth but Improves Endothelial Cell Function. *J. Cell. Mol. Med.* **2012**, *16*, 2117–2126. [CrossRef]

50. Ota, T.; Sawa, Y.; Iwai, S.; Kitajima, T.; Ueda, Y.; Coppin, C.; Matsuda, H.; Okita, Y. Fibronectin-Hepatocyte Growth Factor Enhances Reendothelialization in Tissue-Engineered Heart Valve. *Ann. Thorac. Surg.* **2005**, *80*, 1794–1801. [CrossRef]

51. Wang, X.; Liu, T.; Chen, Y.; Zhang, K.; Maitz, M.F.; Pan, C.; Chen, J.; Huang, N. Extracellular Matrix Inspired Surface Functionalization with Heparin, Fibronectin and VEGF Provides an Anticoagulant and Endothelialization Supporting Microenvironment. *Appl. Surf. Sci.* **2014**, *320*, 871–882. [CrossRef]

52. Hoenig, M.R.; Campbell, G.R.; Campbell, J.H. Vascular Grafts and the Endothelium. *Endothel. J. Endothel. Cell Res.* **2006**, *13*, 385–401. [CrossRef]

53. Matsuzaki, Y.; John, K.; Shoji, T.; Shinoka, T. The Evolution of Tissue Engineered Vascular Graft Technologies: From Preclinical Trials to Advancing Patient Care. *Appl. Sci.* **2019**, *9*, 1274. [CrossRef]

54. Popov, G.; Vavilov, V.; Yukina, G.; Popryadukhin, P.; Dobrovolskaya, I.; Ivan'kova, E.; Yudin, V. Long-Term Functioning Aneurysmal Free Tissue-Engineered Vascular Graft Based on Composite Bi-Layered (PLLA/FPL) Scaffold. *Eur. J. Vasc. Endovasc. Surg.* **2019**, *58*, e817–e818. [CrossRef]

55. Kutuzova, L.; Athanasopulu, K.; Schneider, M.; Kandelbauer, A.; Kemkemer, R.; Lorenz, G. In Vitro Bio-Stability Screening of Novel Implantable Polyurethane Elastomers: Morphological Design and Mechanical Aspects. *Curr. Dir. Biomed. Eng.* **2018**, *4*, 535–538. [CrossRef]

56. Broadwater, S.J.; Roth, S.L.; Price, K.E.; Kobašlija, M.; McQuade, D.T. One-Pot Multi-Step Synthesis: A Challenge Spawning Innovation. *Org. Biomol. Chem.* **2005**, *3*, 2899–2906. [CrossRef]

57. Athanasopulu, K.; Kutuzova, L.; Thiel, J.; Lorenz, G.; Kemkemer, R. Enhancing the Biocompatibility of Siliconepolycarbonate Urethane Based Implant Materials. *Curr. Dir. Biomed. Eng.* **2019**, *5*, 453–455. [CrossRef]

58. Schindelin, J.; Arganda-Carreras, I.; Frise, E.; Kaynig, V.; Longair, M.; Pietzsch, T.; Preibisch, S.; Rueden, C.; Saalfeld, S.; Schmid, B.; et al. Fiji: An Open-Source Platform for Biological-Image Analysis. *Nat. Methods* **2012**, *9*, 676–682. [CrossRef]

59. Laterreur, V.; Ruel, J.; Auger, F.A.; Vallières, K.; Tremblay, C.; Lacroix, D.; Tondreau, M.; Bourget, J.M.; Germain, L. Comparison of the Direct Burst Pressure and the Ring Tensile Test Methods for Mechanical Characterization of Tissue-Engineered Vascular Substitutes. *J. Mech. Behav. Biomed. Mater.* **2014**, *34*, 253–263. [CrossRef]

60. Hinderer, S.; Seifert, J.; Votteler, M.; Shen, N.; Rheinlaender, J.; Schäffer, T.E.; Schenke-Layland, K. Engineering of a Bio-Functionalized Hybrid off-the-Shelf Heart Valve. *Biomaterials* **2014**, *35*, 2130–2139. [CrossRef]

61. Becker, M.; Schneider, M.; Stamm, C.; Seifert, M. A Polymorphonuclear Leukocyte Assay to Assess Implant Immunocompatibility. *Tissue Eng. Part C Methods* **2019**, *25*, 500–511. [CrossRef]

62. Schneider, M.; Stamm, C.; Brockbank, K.G.M.; Stock, U.A.; Seifert, M. The Choice of Cryopreservation Method Affects Immune Compatibility of Human Cardiovascular Matrices. *Sci. Rep.* **2017**, *7*, 1–14. [CrossRef]

63. Pusch, J.; Votteler, M.; Göhler, S.; Engl, J.; Hampel, M.; Walles, H.; Schenke-Layland, K. The Physiological Performance of a Three-Dimensional Model That Mimics the Microenvironment of the Small Intestine. *Biomaterials* **2011**, *32*, 7469–7478. [CrossRef] [PubMed]

64. Piccirillo, G.; Carvajal Berrio, D.A.; Laurita, A.; Pepe, A.; Bochicchio, B.; Schenke-Layland, K.; Hinderer, S. Controlled and Tuneable Drug Release from Electrospun Fibers and a Non-Invasive Approach for Cytotoxicity Testing. *Sci. Rep.* **2019**, *9*, 1–10. [CrossRef] [PubMed]

65. Al-Sabti, H.A.; Al Kindi, A.; Al-Rasadi, K.; Banerjee, Y.; Al-Hashmi, K.; Al-Hinai, A. Saphenous Vein Graft vs. Radial Artery Graft Searching for the Best Second Coronary Artery Bypass Graft. *J. Saudi Heart Assoc.* **2013**, *25*, 247–254. [CrossRef]

66. Stekelenburg, M.; Rutten, M.C.M.; Snoeckx, L.H.E.H.; Baaijens, F.P.T. Dynamic Straining Combined with Fibrin Gel Cell Seeding Improves Strength of Tissue-Engineered Small-Diameter Vascular Grafts. *Tissue Eng. Part A* **2009**, *15*, 1081–1089. [CrossRef]

67. Soletti, L.; Hong, Y.; Guan, J.; Stankus, J.J.; El-Kurdi, M.S.; Wagner, W.R.; Vorp, D.A. A Bilayered Elastomeric Scaffold for Tissue Engineering of Small Diameter Vascular Grafts. *Acta Biomater.* **2010**, *6*, 110–122. [CrossRef]

68. Pukacki, F.; Jankowski, T.; Gabriel, M.; Oszkinis, G.; Krasinski, Z.; Zapalski, S. The Mechanical Properties of Fresh and Cryopreserved Arterial Homografts. *Eur. J. Vasc. Endovasc. Surg.* **2000**, *20*, 21–24. [CrossRef]

69. Porter, T.R.; Taylor, D.O.; Fields, J.; Cycan, A.; Akosah, K.; Mohanty, P.K.; Pandian, N.G. Direct in Vivo Evaluation of Pulmonary Arterial Pathology in Chronic Congestive Heart Failure with Catheter-Based Intravascular Ultrasound Imaging. *Am. J. Cardiol.* **1993**, *71*, 754–757. [CrossRef]

70. Abbott, W.M. Prosthetic Above-Knee Femoral-Popliteal Bypass: Indications and Choice of Graft. *Semin. Vasc. Surg.* **1997**, *10*, 3–7.

71. Konig, G.; McAllister, T.N.; Dusserre, N.; Garrido, S.A.; Iyican, C.; Marini, A.; Fiorillo, A.; Avila, H.; Wystrychowski, W.; Zagalski, K.; et al. Mechanical Properties of Completely Autologous Human Tissue Engineered Blood Vessels Compared to Human Saphenous Vein and Mammary Artery. *Biomaterials* **2009**, *30*, 1542–1550. [CrossRef]

72. Lamm, P.; Juchem, G.; Milz, S.; Schuffenhauer, M.; Reichart, B. Autologous Endothelialized Vein Allograft: A Solution in the Search for Small-Caliber Grafts in Coronary Artery Bypass Graft Operations. *Circulation* **2001**, *104*, I-108. [CrossRef]

73. L'Heureux, N.; Pâquet, S.; Labbé, R.; Germain, L.; Auger, F.A. A Completely Biological Tissue-Engineered Human Blood Vessel. *FASEB J.* **1998**, *12*, 47–56.

74. Caruso, A.; Licenziati, S.; Corulli, M.; Canaris, A.D.; De Francesco, M.A.; Fiorentini, S.; Peroni, L.; Fallacara, F.; Dima, F.; Balsari, A.; et al. Flow Cytometric Analysis of Activation Markers on Stimulated T Cells and Their Correlation with Cell Proliferation. *Cytometry* **1997**, *27*, 71–76. [CrossRef]

75. Lerouge, S. Introduction to Sterilization: Definitions and Challenges. In *Sterilisation of Biomaterials and Medical Devices*; Elsevier: Amsterdam, The Netherlands, 2012; pp. 1–19.

76. Ameer, J.M.; Anil Kumar, P.R.; Kasoju, N. Strategies to Tune Electrospun Scaffold Porosity for Effective Cell Response in Tissue Engineering. *J. Funct. Biomater.* **2019**, *10*, 30. [CrossRef]

77. Bružauskaitė, I.; Bironaitė, D.; Bagdonas, E.; Bernotienė, E. Scaffolds and Cells for Tissue Regeneration: Different Scaffold Pore Sizes—Different Cell Effects. *Cytotechnology* **2016**, *68*, 355–369. [CrossRef]

78. Murphy, C.M.; O'Brien, F.J. Understanding the Effect of Mean Pore Size on Cell Activity in Collagen-Glycosaminoglycan Scaffolds. *Cell Adhes. Migr.* **2010**, *4*, 377–381. [CrossRef]

79. Arends, F.; Lieleg, O. Biophysical Properties of the Basal Lamina: A Highly Selective Extracellular Matrix. In *Composition and Function of the Extracellular Matrix in the Human Body*; InTech: London, UK, 2016.

80. Liliensiek, S.J.; Nealey, P.; Murphy, C.J. Characterization of Endothelial Basement Membrane Nanotopography in Rhesus Macaque as a Guide for Vessel Tissue Engineering. *Tissue Eng. Part A* **2009**, *15*, 2643–2651. [CrossRef]

81. Sage, H. Collagens of Basement Membranes. *J. Investig. Dermatol.* **1982**, *79*, 51s–59s. [CrossRef]

82. Abrams, G.A.; Murphy, C.J.; Wang, Z.Y.; Nealey, P.F.; Bjorling, D.E. Ultrastructural Basement Membrane Topography of the Bladder Epithelium. *Urol. Res.* **2003**, *31*, 341–346.

83. Inoguchi, H.; Kwon, I.K.; Inoue, E.; Takamizawa, K.; Maehara, Y.; Matsuda, T. Mechanical Responses of a Compliant Electrospun Poly(L-Lactide-Co-ε- Caprolactone) Small-Diameter Vascular Graft. *Biomaterials* **2006**, *27*, 1470–1478. [CrossRef]

84. Nottelet, B.; Pektok, E.; Mandracchia, D.; Tille, J.-C.; Walpoth, B.; Gurny, R.; Möller, M. Factorial Design Optimization and *in Vivo* Feasibility of Poly(ε-Caprolactone)-Micro- and Nanofiber-Based Small Diameter Vascular Grafts. *J. Biomed. Mater. Res. Part A* **2009**, *89A*, 865–875. [CrossRef] [PubMed]

85. Vaz, C.M.; van Tuijl, S.; Bouten, C.V.C.; Baaijens, F.P.T. Design of Scaffolds for Blood Vessel Tissue Engineering Using a Multi-Layering Electrospinning Technique. *Acta Biomater.* **2005**, *1*, 575–582. [CrossRef] [PubMed]

86. Hironaka, K.; Makino, H.; Yamasaki, Y.; Ota, Z. Renal Basement Membranes by Ultrahigh Resolution Scanning Electron Microscopy. *Kidney Int.* **1993**, *43*, 334–345. [CrossRef] [PubMed]

87. Takeuchi, T.; Gonda, T. Distribution of the Pores of Epithelial Basement Membrane in the Rat Small Intestine. *J. Vet. Med. Sci.* **2004**, *66*, 695–700. [CrossRef] [PubMed]

88. Yurchenco, P.D.; Ruben, G.C. Basement Membrane Structure in Situ: Evidence for Lateral Associations in the Type IV Collagen Network. *J. Cell Biol.* **1987**, *105*, 2559–2568. [CrossRef]

89. Howat, W.J.; Holmes, J.A.; Holgate, S.T.; Lackie, P.M. Basement Membrane Pores in Human Bronchial Epithelium: A Conduit for Infiltrating Cells? *Am. J. Pathol.* **2001**, *158*, 673–680. [CrossRef]

90. Wierzbicka-Patynowski, I.; Schwarzbauer, J.E. Cell-Surface Transglutaminase Promotes Fibronectin Assembly via Interaction with the Gelatin-Binding Domain of Fibronectin: A Role in TGFbeta-Dependent Matrix Deposition. *J. Cell Sci.* **2003**, *116*, 3269–3276. [CrossRef]

91. Sevilla, C.A.; Dalecki, D.; Hocking, D.C. Regional Fibronectin and Collagen Fibril Co-Assembly Directs Cell Proliferation and Microtissue Morphology. *PLoS ONE* **2013**, *8*, e77316. [CrossRef]

92. Rico, P.; Mnatsakanyan, H.; Dalby, M.J.; Salmerón-Sánchez, M. Material-Driven Fibronectin Assembly Promotes Maintenance of Mesenchymal Stem Cell Phenotypes. *Adv. Funct. Mater.* **2016**, *26*, 6563–6573. [CrossRef]

93. Llopis-Hernández, V.; Cantini, M.; González-García, C.; Cheng, Z.A.; Yang, J.; Tsimbouri, P.M.; García, A.J.; Dalby, M.J.; Salmerón-Sánchez, M. Material-Driven Fibronectin Assembly for High-Efficiency Presentation of Growth Factors. *Sci. Adv.* **2016**, *2*, e1600188. [CrossRef]

94. Schmidt, G.; Hausser, H.; Kresse, H. Interaction of the Small Proteoglycan Decorin with Fibronectin. Involvement of the Sequence NKISK of the Core Protein. *Biochem. J.* **1991**, *280*, 411–414. [CrossRef] [PubMed]

95. Winnemöller, M.; Schmidt, G.; Kresse, H. Influence of Decorin on Fibroblast Adhesion to Fibronectin. *Eur. J. Cell Biol.* **1991**, *54*, 10–17. [PubMed]

96. Dee, K.C.; Puleo, D.A.; Bizios, R. Protein-Surface Interactions. In *An Introduction to Tissue-Biomaterial Interaction*; Wiley: Hoboken, NJ, USA, 2002; pp. 37–51.

97. Thyparambil, A.A.; Wei, Y.; Latour, R.A. Experimental Characterization of Adsorbed Protein Orientation, Conformation, and Bioactivity. *Biointerphases* **2015**, *10*, 019002. [CrossRef] [PubMed]

98. Latour, R.A. Molecular Simulation of Protein-Surface Interactions. In *Biological Interactions on Material Surfaces*; Puleo, D.A., Bizios, R., Eds.; Springer US: Berlin/Heidelberg, Germany, 2009; pp. 73–74.

99. Lebaron, R.G.; Athanasiou, K.A. Extracellular Matrix Cell Adhesion Peptides: Functional Applications in Orthopedic Materials. *Tissue Eng.* **2000**, *6*, 85–103. [CrossRef]

100. Hinderer, S.; Schesny, M.; Bayrak, A.; Ibold, B.; Hampel, M.; Walles, T.; Stock, U.A.; Seifert, M.; Schenke-Layland, K. Engineering of Fibrillar Decorin Matrices for a Tissue-Engineered Trachea. *Biomaterials* **2012**, *33*, 5259–5266. [CrossRef]

101. Ishizaki, T.; Saito, N.; Takai, O. Correlation of Cell Adhesive Behaviors on Superhydrophobic, Superhydrophilic, and Micropatterned Superhydrophobic/Superhydrophilic Surfaces to Their Surface Chemistry. *Langmuir* **2010**, *26*, 8147–8154. [CrossRef]

102. Schmidt, G.; Robenek, H.; Harrach, B.; Glössl, J.; Nolte, V.; Hörmann, H.; Richter, H.; Kresse, H. Interaction of Small Dermatan Sulfate Proteoglycan from Fibroblasts with Fibronectin. *J. Cell Biol.* **1987**, *104*, 1683–1691. [CrossRef]

103. Zhao, J.; Mitrofan, C.G.; Appleby, S.L.; Morrell, N.W.; Lever, A.M.L. Disrupted Endothelial Cell Layer and Exposed Extracellular Matrix Proteins Promote Capture of Late Outgrowth Endothelial Progenitor Cells. *Stem Cells Int.* **2016**, *2016*, 1406304. [CrossRef]

104. Brown, B.N.; Badylak, S.F. Expanded Applications, Shifting Paradigms and an Improved Understanding of Host-Biomaterial Interactions. *Acta Biomater.* **2013**, *9*, 4948–4955. [CrossRef]

105. Wang, Z.; Cui, Y.; Wang, J.; Yang, X.; Wu, Y.; Wang, K.; Gao, X.; Li, D.; Li, Y.; Zheng, X.L.; et al. The Effect of Thick Fibers and Large Pores of Electrospun Poly(ε-Caprolactone) Vascular Grafts on Macrophage Polarization and Arterial Regeneration. *Biomaterials* **2014**, *35*, 5700–5710. [CrossRef]

106. Dejana, E.; Orsenigo, F.; Molendini, C.; Baluk, P.; McDonald, D.M. Organization and Signaling of Endothelial Cell-to-Cell Junctions in Various Regions of the Blood and Lymphatic Vascular Trees. *Cell Tissue Res.* **2009**, *335*, 17–25. [CrossRef] [PubMed]

107. Lertkiatmongkol, P.; Liao, D.; Mei, H.; Hu, Y.; Newman, P.J. Endothelial Functions of Platelet/Endothelial Cell Adhesion Molecule-1 (CD31). *Curr. Opin. Hematol.* **2016**, *23*, 253–259. [CrossRef] [PubMed]

108. Yamaguchi, T.P.; Dumont, D.J.; Conlon, R.A.; Breitman, M.L.; Rossant, J. Flk-1, an Fit-Related Receptor Tyrosine Kinase Is an Early Marker for Endothelial Cell Precursors. *Development* **1993**, *118*, 489–498. [PubMed]

109. Smadja, D.M.; Bièche, I.; Helley, D.; Laurendeau, I.; Simonin, G.; Muller, L.; Aiach, M.; Gaussem, P. Increased VEGFR2 Expression during Human Late Endothelial Progenitor Cells Expansion Enhances in Vitro Angiogenesis with Up-Regulation of Integrin A6. *J. Cell. Mol. Med.* **2007**, *11*, 1149–1161. [CrossRef]

110. Kusuma, S.; Zhao, S.; Gerecht, S. The Extracellular Matrix Is a Novel Attribute of Endothelial Progenitors and of Hypoxic Mature Endothelial Cells. *FASEB J.* **2012**, *26*, 4925–4936. [CrossRef]

111. Ichii, M.; Frank, M.B.; Iozzo, R.V.; Kincade, P.W. The Canonical Wnt Pathway Shapes Niches Supportive of Hematopoietic Stem/Progenitor Cells. *Blood* **2012**, *119*, 1683–1692. [CrossRef]

112. Wijelath, E.S.; Rahman, S.; Murray, J.; Patel, Y.; Savidge, G.; Sobel, M. Fibronectin Promotes VEGF-Induced CD34+ Cell Differentiation into Endothelial Cells. *J. Vasc. Surg.* **2004**, *39*, 655–660. [CrossRef]

113. Shen, B.Q.; Lee, D.Y.; Gerber, H.P.; Keyt, B.A.; Ferrara, N.; Zioncheck, T.F. Homologous Up-Regulation of KDR/Flk-1 Receptor Expression by Vascular Endothelial Growth Factor in Vitro. *J. Biol. Chem.* **1998**, *273*, 29979–29985. [CrossRef]

114. Neill, T.; Schaefer, L.; Iozzo, R.V. Decorin: A Guardian from the Matrix. *Am. J. Pathol.* **2012**, *181*, 380–387. [CrossRef]

115. Mazor, R.; Alsaigh, T.; Shaked, H.; Altshuler, A.E.; Pocock, E.S.; Kistler, E.B.; Karin, M.; Schmid-Schönbein, G.W. Matrix Metalloproteinase-1-Mediated up-Regulation of Vascular Endothelial Growth Factor-2 in Endothelial Cells. *J. Biol. Chem.* **2013**, *288*, 598–607. [CrossRef]

116. Huttenlocher, A.; Werb, Z.; Tremble, P.; Huhtala, P.; Rosenberg, L.; Damsky, C.H. Decorin Regulates Collagenase Gene Expression in Fibroblasts Adhering to Vitronectin. *Matrix Biol.* **1996**, *15*, 239–250. [CrossRef]

117. Schönherr, E.; Schaefer, L.; O'Connell, B.C.; Kresse, H. Matrix Metalloproteinase Expression by Endothelial Cells in Collagen Lattices Changes during Co-Culture with Fibroblasts and upon Induction of Decorin Expression. *J. Cell. Physiol.* **2001**, *187*, 37–47. [CrossRef]

118. Murakami, M.; Nguyen, L.T.; Hatanaka, K.; Schachterle, W.; Chen, P.Y.; Zhuang, Z.W.; Black, B.L.; Simons, M. FGF-Dependent Regulation of VEGF Receptor 2 Expression in Mice. *J. Clin. Investig.* **2011**, *121*, 2668–2678. [CrossRef] [PubMed]

119. Penc, S.F.; Pomahac, B.; Winkler, T.; Dorschner, R.A.; Eriksson, E.; Herndon, M.; Gallo, R.L. Dermatan Sulfate Released after Injury Is a Potent Promoter of Fibroblast Growth Factor-2 Function. *J. Biol. Chem.* **1998**, *273*, 28116–28121. [CrossRef] [PubMed]

120. Chen, T.T.; Filvaroff, E.; Peng, J.; Marsters, S.; Jubb, A.; Koeppen, H.; Merchant, M.; Ashkenazi, A. MET Suppresses Epithelial VEGFR2 via Intracrine VEGF-Induced Endoplasmic Reticulum-Associated Degradation. *EBioMedicine* **2015**, *2*, 406–420. [CrossRef] [PubMed]

121. Chen, S.; Chakrabarti, R.; Keats, E.C.; Chen, M.; Chakrabarti, S.; Khan, Z.A. Regulation of Vascular Endothelial Growth Factor Expression by Extra Domain B Segment of Fibronectin in Endothelial Cells. *Investig. Ophthalmol. Vis. Sci.* **2012**, *53*, 8333–8343. [CrossRef]

122. Wijelath, E.S.; Rahman, S.; Namekata, M.; Murray, J.; Nishimura, T.; Mostafavi-Pour, Z.; Patel, Y.; Suda, Y.; Humphries, M.J.; Sobel, M. Heparin-II Domain of Fibronectin Is a Vascular Endothelial Growth Factor-Binding Domain. *Circ. Res.* **2006**, *99*, 853–860. [CrossRef]

123. Kou, R.; SenBanerjee, S.; Jain, M.K.; Michel, T. Differential Regulation of Vascular Endothelial Growth Factor Receptors (VEGFR) Revealed by RNA Interference: Interactions of VEGFR-1 and VEGFR-2 in Endothelial Cell Signaling. *Biochemistry* **2005**, *44*, 15064–15073. [CrossRef]

124. Scott, R.A.; Paderi, J.E.; Sturek, M.; Panitch, A. Decorin Mimic Inhibits Vascular Smooth Muscle Proliferation and Migration. *PLoS ONE* **2013**, *8*, e82456. [CrossRef]

125. Harding, A.; Cortez-Toledo, E.; Magner, N.L.; Beegle, J.R.; Coleal-Bergum, D.P.; Hao, D.; Wang, A.; Nolta, J.A.; Zhou, P. Highly Efficient Differentiation of Endothelial Cells from Pluripotent Stem Cells Requires the MAPK and the PI3K Pathways. *Stem Cells* **2017**, *35*, 909–919. [CrossRef]

126. Bryan, B.A.; Walshe, T.E.; Mitchell, D.C.; Havumaki, J.S.; Saint-Geniez, M.; Maharaj, A.S.; Maldonado, A.E.; D'Amore, P.A. Coordinated Vascular Endothelial Growth Factor Expression and Signaling during Skeletal Myogenic Differentiation. *Mol. Biol. Cell* **2008**, *19*, 994–1006. [CrossRef] [PubMed]

127. Zeng, Y.; Zhang, X.F.; Fu, B.M.; Tarbell, J.M. The Role of Endothelial Surface Glycocalyx in Mechanosensing and Transduction. In *Advances in Experimental Medicine and Biology*; Springer New York LLC: New York, NY, USA, 2018; Volume 1097, pp. 1–27.

128. Ballermann, B.J.; Dardik, A.; Eng, E.; Liu, A. Shear Stress and the Endothelium. *Kidney Int.* **1998**, *54*, S100–S108. [CrossRef] [PubMed]

129. Sato, M.; Kataoka, N.; Ohshima, N. Response of Vascular Endothelial Cells to Flow Shear Stress: Phenomenological Aspect. In *Biomechanics*; Springer Japan: Tokyo, Japan, 1996; pp. 3–27.

130. Zhou, J.; Li, Y.S.; Chien, S. Shear Stress-Initiated Signaling and Its Regulation of Endothelial Function. *Arterioscler. Thromb. Vasc. Biol.* **2014**, *34*, 2191–2198. [CrossRef]
131. Sánchez-Duffhues, G.; García de Vinuesa, A.; ten Dijke, P. Endothelial-to-Mesenchymal Transition in Cardiovascular Diseases: Developmental Signaling Pathways Gone Awry. *Dev. Dyn.* **2018**, *247*, 492–508. [CrossRef] [PubMed]
132. Moonen, J.R.A.J.; Lee, E.S.; Schmidt, M.; Maleszewska, M.; Koerts, J.A.; Brouwer, L.A.; Van Kooten, T.G.; Van Luyn, M.J.A.; Zeebregts, C.J.; Krenning, G.; et al. Endothelial-to-Mesenchymal Transition Contributes to Fibro-Proliferative Vascular Disease and Is Modulated by Fluid Shear Stress. *Cardiovasc. Res.* **2015**, *108*, 377–386. [CrossRef]
133. Mahmoud, M.M.; Serbanovic-Canic, J.; Feng, S.; Souilhol, C.; Xing, R.; Hsiao, S.; Mammoto, A.; Chen, J.; Ariaans, M.; Francis, S.E.; et al. Shear Stress Induces Endothelial-To-Mesenchymal Transition via the Transcription Factor Snail. *Sci. Rep.* **2017**, *7*, 1–12. [CrossRef]
134. Melchiorri, A.J.; Bracaglia, L.G.; Kimerer, L.K.; Hibino, N.; Fisher, J.P. In Vitro Endothelialization of Biodegradable Vascular Grafts Via Endothelial Progenitor Cell Seeding and Maturation in a Tubular Perfusion System Bioreactor. *Tissue Eng.-Part C Methods* **2016**, *22*, 663–670. [CrossRef]
135. Dejana, E.; Hirschi, K.K.; Simons, M. The Molecular Basis of Endothelial Cell Plasticity. *Nat. Commun.* **2017**, *8*, 1–11. [CrossRef]
136. Lacorre, D.A.; Baekkevold, E.S.; Garrido, I.; Brandtzaeg, P.; Haraldsen, G.; Amalric, F.; Girard, J.P. Plasticity of Endothelial Cells: Rapid Dedifferentiation of Freshly Isolated High Endothelial Venule Endothelial Cells Outside the Lymphoid Tissue Microenvironment. *Blood* **2004**, *103*, 4164–4172. [CrossRef]
137. Nguyen, M.T.X.; Okina, E.; Chai, X.; Tan, K.H.; Hovatta, O.; Ghosh, S.; Tryggvason, K. Differentiation of Human Embryonic Stem Cells to Endothelial Progenitor Cells on Laminins in Defined and Xeno-Free Systems. *Stem Cell Rep.* **2016**, *7*, 802–816. [CrossRef]